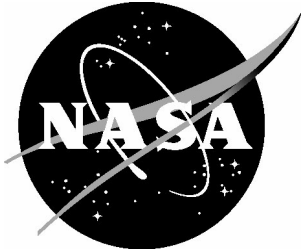


NASA/TM-20230001707



Experimental Investigation of Block-TPS Fence/Gap Roughness Effects on Transition Onset and Turbulent Heating Augmentation at Mach 6

Brian R. Hollis
Langley Research Center, Hampton, Virginia

Kevin E. Hollingsworth
Jacobs Technologies, Inc, Hampton, Virginia

February 2023

NASA STI Program Report Series

Since its founding, NASA has been dedicated to the advancement of aeronautics and space science. The NASA scientific and technical information (STI) program plays a key part in helping NASA maintain this important role.

The NASA STI program operates under the auspices of the Agency Chief Information Officer. It collects, organizes, provides for archiving, and disseminates NASA's STI. The NASA STI program provides access to the NTRS Registered and its public interface, the NASA Technical Reports Server, thus providing one of the largest collections of aeronautical and space science STI in the world. Results are published in both non-NASA channels and by NASA in the NASA STI Report Series, which includes the following report types:

- **TECHNICAL PUBLICATION.** Reports of completed research or a major significant phase of research that present the results of NASA Programs and include extensive data or theoretical analysis. Includes compilations of significant scientific and technical data and information deemed to be of continuing reference value. NASA counterpart of peer-reviewed formal professional papers but has less stringent limitations on manuscript length and extent of graphic presentations.
- **TECHNICAL MEMORANDUM.** Scientific and technical findings that are preliminary or of specialized interest, e.g., quick release reports, working papers, and bibliographies that contain minimal annotation. Does not contain extensive analysis.
- **CONTRACTOR REPORT.** Scientific and technical findings by NASA-sponsored contractors and grantees.

- **CONFERENCE PUBLICATION.** Collected papers from scientific and technical conferences, symposia, seminars, or other meetings sponsored or co-sponsored by NASA.
- **SPECIAL PUBLICATION.** Scientific, technical, or historical information from NASA programs, projects, and missions, often concerned with subjects having substantial public interest.
- **TECHNICAL TRANSLATION.** English-language translations of foreign scientific and technical material pertinent to NASA's mission.

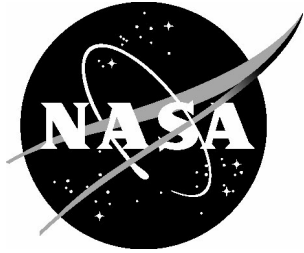
Specialized services also include organizing and publishing research results, distributing specialized research announcements and feeds, providing information desk and personal search support, and enabling data exchange services.

For more information about the NASA STI program, see the following:

- Access the NASA STI program home page at <http://www.sti.nasa.gov>
- Help desk contact information:

<https://www.sti.nasa.gov/sti-contact-form/>
and select the "General" help request

NASA/TM-20230001707



Experimental Investigation of Block-TPS Fence/Gap Roughness Effects on Transition Onset and Turbulent Heating Augmentation at Mach 6

Brian R. Hollis
Langley Research Center, Hampton, Virginia

Kevin E. Hollingsworth
Jacobs Technologies, Inc, Hampton, Virginia

National Aeronautics and
Space Administration

Langley Research Center
Hampton, Virginia 23681-2199

February 2023

The use of trademarks or names of manufacturers in this report is for accurate reporting and does not constitute an official endorsement, either expressed or implied, of such products or manufacturers by the National Aeronautics and Space Administration.

Available from:

NASA STI Program / Mail Stop 148
NASA Langley Research Center
Hampton, VA 23681-2199
Fax: 757-864-6500

Table of Contents

Table of Contents.....	i
List of Tables	ii
Abstract.....	1
Symbols	2
Subscripts and Superscripts	2
Acronyms.....	2
Introduction.....	3
Background.....	3
Experimental Tools and Methods	4
Wind Tunnel Models	4
Model Geometries.....	4
Model Fabrication.....	4
Wind Tunnel Test Facility	5
Facility Description.....	5
Facility Operating Conditions.....	5
Experimental Data	6
Data Acquisition and Reduction	6
Data Mapping and Presentation.....	6
Phosphor Thermography Data Quality	7
Heat Transfer Data Uncertainty.....	8
Calibration Correction for Heat Transfer Data.....	8
Computational Tools and Methods	9
Flow Field Solver.....	9
Boundary-Layer Parameters	10
Experimental Data Analysis	11
Reynolds Number Effects on Heating and Transition	11
Gap Depth / Fence Height Effects on Heating and Transition	11
General Reynolds Number and Fence/Gap Size Trends	11
Transition Onset Correlation	12
Fence/Gap Heating Augmentation.....	12
Summary.....	13
References.....	13
Appendix A. Sphere-cone Geometry Global Heating Images.....	120
Appendix B. Spherical-Cap Geometry Global Heating Images.....	148

List of Tables

Table 1. Wind tunnel model geometry parameters.	15
Table 2. Wind tunnel model fence / gap location parameters.....	15
Table 3. Wind tunnel model fence / gap geometry parameters.	15
Table 4. Averaged Nominal Conditions for 20-Inch Mach 6 Air Tunnel Test 7036.....	16
Table 5. Averaged Nominal Conditions for 20-Inch Mach 6 Air Tunnel Test 7057.....	16
Table 6. CFD Conditions for 20-Inch Mach 6 Air Tunnel Tests 7036 and 7057.	16
Table 7. 20-Inch Mach 6 Air Tunnel Test 7036 run matrix.....	17
Table 8. 20-Inch Mach 6 Air Tunnel Test 7057 run matrix.....	19

List of Figures

Figure 1. Discrete surface roughness types.....	21
Figure 2. Distributed surface roughness types.....	21
Figure 3. Sphere-cone geometry.....	22
Figure 4. Spherical-cap geometry.....	22
Figure 5. Sphere-cone fence / gap layout.....	23
Figure 6. Spherical-cap fence / gap layout.....	23
Figure 7. Fence / gap dimensions.....	24
Figure 8. Fence / gap size comparisons.....	24
Figure 9. Sample fence model photographs (Spherical-cap, 12-mil fence).....	25
Figure 10. Sample gap model photographs (Sphere-cone, 24-mil gap).....	25
Figure 11. Fence model fabrication errors.....	26
Figure 12. Schematic of Langley Research Center 20-Inch Mach 6 Air Tunnel.....	27
Figure 13. Langley Research Center 20-Inch Mach 6 Air Tunnel test section.....	27
Figure 14. Sample phosphor thermography 2-D image data.....	28
Figure 15. Sample 3-D mapping of phosphor thermography data.....	28
Figure 16. Streamlines for data extraction on sphere-cone geometry.....	29
Figure 17. Streamlines for data extraction on spherical-cap geometry.....	29
Figure 18. Illustration of camera field-of-view for hemisphere model in 20-Inch Mach 6 Air Tunnel.....	30
Figure 19. CFD predictions for hemisphere heating at wind tunnel conditions.....	31
Figure 20. Measured stagnation point heating for pretest calibrations for Test 7036.....	31
Figure 21. Measured stagnation point heating for pretest calibrations for Test 7057.....	31
Figure 22. Centerline profiles of roughness effects on k/δ , sphere-cone geometry with fences.....	32
Figure 23. Centerline profiles of roughness effects on k/δ , spherical-cap geometry with fences.....	33
Figure 24. Centerline profiles of roughness effects on Re_{k+} , sphere-cone geometry with fences.....	34
Figure 25. Centerline profiles of roughness effects on Re_{k+} , spherical-cap geometry.....	35
Figure 26. Reynolds Number effects, smooth sphere-cone model images.....	36
Figure 27. Reynolds number effects, smooth sphere-cone model plots.....	37
Figure 28. Reynolds Number effects, sphere-cone 3-mil gap model images.....	38
Figure 29. Reynolds Number effects, sphere-cone 3-mil gap model plots.....	39
Figure 30. Reynolds Number effects, sphere-cone 6-mil gap model images.....	40
Figure 31. Reynolds Number effects, sphere-cone 6-mil gap model plots.....	41
Figure 32. Reynolds Number effects, sphere-cone 12-mil gap model images.....	42
Figure 33. Reynolds Number effects, sphere-cone 12-mil gap model plots.....	43
Figure 34. Reynolds Number effects, sphere-cone 24-mil gap model images.....	44
Figure 35. Reynolds Number effects, sphere-cone 24-mil gap model plots.....	45
Figure 36. Reynolds Number effects, sphere-cone 3-mil fence model images.....	46
Figure 37. Reynolds Number effects, sphere-cone 3-mil fence model plots.....	47
Figure 38. Reynolds Number effects, sphere-cone 6-mil fence model images.....	48
Figure 39. Reynolds Number effects, sphere-cone 6-mil fence model plots.....	49
Figure 40. Reynolds Number effects, sphere-cone 12-mil fence model images.....	50
Figure 41. Reynolds Number effects, sphere-cone 12-mil fence model plots.....	51
Figure 42. Reynolds Number effects, sphere-cone 24-mil fence model images.....	52
Figure 43. Reynolds Number effects, sphere-cone 24-mil fence model plots.....	53
Figure 44. Reynolds Number effects, spherical-cap smooth model images.....	54
Figure 45. Reynolds Number effects, spherical-cap smooth model plots.....	55
Figure 46. Reynolds Number effects, spherical-cap 3-mil gap model images.....	56
Figure 47. Reynolds Number effects, spherical-cap 3-mil gap model plots.....	57
Figure 48. Reynolds Number effects, spherical-cap 6-mil gap model images.....	58

Figure 49. Reynolds Number effects, spherical-cap 6-mil gap model plots.....	59
Figure 50. Reynolds Number effects, spherical-cap 12-mil gap model images.....	60
Figure 51. Reynolds Number effects, spherical-cap 12-mil gap model plots.....	61
Figure 52. Reynolds Number effects, spherical-cap 24-mil gap model images.....	62
Figure 53. Reynolds Number effects, spherical-cap 24-mil gap model plots.....	63
Figure 54. Reynolds Number effects, spherical-cap 3-mil fence model images.....	64
Figure 55. Reynolds Number effects, spherical-cap 3-mil fence model plots.....	65
Figure 56. Reynolds Number effects, spherical-cap 6-mil fence model images.....	66
Figure 57. Reynolds Number effects, spherical-cap 6-mil fence model plots.....	67
Figure 58. Reynolds Number effects, spherical-cap 12-mil fence model images.....	68
Figure 59. Reynolds Number effects, spherical-cap 12-mil fence model plots.....	69
Figure 60. Reynolds Number effects, spherical-cap 24-mil fence model images.....	70
Figure 61. Reynolds Number effects, spherical-cap 24-mil fence model plots.....	71
Figure 62. Gap depth effects, sphere-cone geometry, $Re_\infty = 2.1 \times 10^6$ /ft images.....	72
Figure 63. Gap depth effects, sphere-cone geometry, $Re_\infty = 2.1 \times 10^6$ /ft plots.....	73
Figure 64. Gap depth effects, sphere-cone geometry, $Re_\infty = 3.0 \times 10^6$ /ft images.....	74
Figure 65. Gap depth effects, sphere-cone geometry, $Re_\infty = 3.0 \times 10^6$ /ft plots.....	75
Figure 66. Gap depth effects, sphere-cone geometry, $Re_\infty = 5.0 \times 10^6$ /ft images.....	76
Figure 67. Gap depth effects, sphere-cone geometry, $Re_\infty = 5.0 \times 10^6$ /ft plots.....	77
Figure 68. Gap depth effects, sphere-cone geometry, $Re_\infty = 6.6 \times 10^6$ /ft images.....	78
Figure 69. Gap depth effects, sphere-cone geometry, $Re_\infty = 6.6 \times 10^6$ /ft plots.....	79
Figure 70. Gap depth effects, sphere-cone geometry, $Re_\infty = 7.5 \times 10^6$ /ft images.....	80
Figure 71. Gap depth effects, sphere-cone geometry, $Re_\infty = 7.5 \times 10^6$ /ft plots.....	81
Figure 72. Gap depth effects, sphere-cone geometry, $Re_\infty = 8.3 \times 10^6$ /ft images.....	82
Figure 73. Gap depth effects, sphere-cone geometry, $Re_\infty = 8.3 \times 10^6$ /ft images.....	83
Figure 74. Fence height effects, sphere-cone geometry, $Re_\infty = 2.1 \times 10^6$ /ft images.....	84
Figure 75. Fence height effects, sphere-cone geometry, $Re_\infty = 2.1 \times 10^6$ /ft images.....	85
Figure 76. Fence height effects, sphere-cone geometry, $Re_\infty = 3.0 \times 10^6$ /ft images.....	86
Figure 77. Fence height effects, sphere-cone geometry, $Re_\infty = 3.0 \times 10^6$ /ft images.....	87
Figure 78. Fence height effects, sphere-cone geometry, $Re_\infty = 5.0 \times 10^6$ /ft images.....	88
Figure 79. Fence height effects, sphere-cone geometry, $Re_\infty = 5.0 \times 10^6$ /ft images.....	89
Figure 80. Fence height effects, sphere-cone geometry, $Re_\infty = 6.6 \times 10^6$ /ft images.....	90
Figure 81. Fence height effects, sphere-cone geometry, $Re_\infty = 6.6 \times 10^6$ /ft images.....	91
Figure 82. Fence height effects, sphere-cone geometry, $Re_\infty = 7.5 \times 10^6$ /ft images.....	92
Figure 83. Fence height effects, sphere-cone geometry, $Re_\infty = 7.5 \times 10^6$ /ft images.....	93
Figure 84. Fence height effects, sphere-cone geometry, $Re_\infty = 8.3 \times 10^6$ /ft images.....	94
Figure 85. Fence height effects, sphere-cone geometry, $Re_\infty = 8.3 \times 10^6$ /ft images.....	95
Figure 86. Gap depth effects, spherical-cap geometry, $Re_\infty = 2.1 \times 10^6$ /ft images.....	96
Figure 87. Gap depth effects, spherical-cap geometry, $Re_\infty = 2.1 \times 10^6$ /ft plots.....	97
Figure 88. Gap depth effects, spherical-cap geometry, $Re_\infty = 3.0 \times 10^6$ /ft images.....	98
Figure 89. Gap depth effects, spherical-cap geometry, $Re_\infty = 3.0 \times 10^6$ /ft plots.....	99
Figure 90. Gap depth effects, spherical-cap geometry, $Re_\infty = 5.0 \times 10^6$ /ft images.....	100
Figure 91. Gap depth effects, spherical-cap geometry, $Re_\infty = 5.0 \times 10^6$ /ft plots.....	101
Figure 92. Gap depth effects, spherical-cap geometry, $Re_\infty = 6.6 \times 10^6$ /ft images.....	102
Figure 93. Gap depth effects, spherical-cap geometry, $Re_\infty = 6.6 \times 10^6$ /ft plots.....	103
Figure 94. Gap depth effects, spherical-cap geometry, $Re_\infty = 7.5 \times 10^6$ /ft images.....	104
Figure 95. Gap depth effects, spherical-cap geometry, $Re_\infty = 7.5 \times 10^6$ /ft plots.....	105
Figure 96. Gap depth effects, spherical-cap geometry, $Re_\infty = 8.3 \times 10^6$ /ft images.....	106
Figure 97. Gap depth effects, spherical-cap geometry, $Re_\infty = 8.3 \times 10^6$ /ft images.....	107
Figure 98. Fence height effects, spherical-cap geometry, $Re_\infty = 2.1 \times 10^6$ /ft images.....	108
Figure 99. Fence height effects, spherical-cap geometry, $Re_\infty = 2.1 \times 10^6$ /ft images.....	109

Figure 100. Fence height effects, spherical-cap geometry, $Re_\infty = 3.0 \times 10^6$ /ft images.....	110
Figure 101. Fence height effects, spherical-cap geometry, $Re_\infty = 3.0 \times 10^6$ /ft images.....	111
Figure 102. Fence height effects, spherical-cap geometry, $Re_\infty = 5.0 \times 10^6$ /ft images.....	112
Figure 103. Fence height effects, spherical-cap geometry, $Re_\infty = 5.0 \times 10^6$ /ft images.....	113
Figure 104. Fence height effects, spherical-cap geometry, $Re_\infty = 6.6 \times 10^6$ /ft images.....	114
Figure 105. Fence height effects, spherical-cap geometry, $Re_\infty = 6.6 \times 10^6$ /ft images.....	115
Figure 106. Fence height effects, spherical-cap geometry, $Re_\infty = 7.5 \times 10^6$ /ft images.....	116
Figure 107. Fence height effects, spherical-cap geometry, $Re_\infty = 7.5 \times 10^6$ /ft images.....	117
Figure 108. Fence height effects, spherical-cap geometry, $Re_\infty = 8.3 \times 10^6$ /ft images.....	118
Figure 109. Fence height effects, spherical-cap geometry, $Re_\infty = 8.3 \times 10^6$ /ft images.....	119
Figure 110. Test 7036, Run 50, $Re_\infty = 2.1 \times 10^6$ /ft, sphere-cone, smooth OML.....	121
Figure 111. Test 7036, Run 51, $Re_\infty = 3.0 \times 10^6$ /ft, sphere-cone, smooth OML.....	121
Figure 112. Test 7036, Run 52, $Re_\infty = 5.0 \times 10^6$ /ft, sphere-cone, smooth OML.....	122
Figure 113. Test 7036, Run 53, $Re_\infty = 6.6 \times 10^6$ /ft, sphere-cone, smooth OML.....	122
Figure 114. Test 7036, Run 54, $Re_\infty = 7.5 \times 10^6$ /ft, sphere-cone, smooth OML.....	123
Figure 115. Test 7036, Run 55, $Re_\infty = 8.3 \times 10^6$ /ft, sphere-cone, smooth OML.....	123
Figure 116. Test 7036, Run 26, $Re_\infty = 2.1 \times 10^6$ /ft, sphere-cone 3 mil gap.....	124
Figure 117. Test 7036, Run 27, $Re_\infty = 3.0 \times 10^6$ /ft, sphere-cone 3 mil gap.....	124
Figure 118. Test 7036, Run 28, $Re_\infty = 5.0 \times 10^6$ /ft, sphere-cone 3 mil gap.....	125
Figure 119. Test 7036, Run 29, $Re_\infty = 6.6 \times 10^6$ /ft, sphere-cone 3 mil gap.....	125
Figure 120. Test 7036, Run 30, $Re_\infty = 7.5 \times 10^6$ /ft, sphere-cone 3 mil gap.....	126
Figure 121. Test 7036, Run 31, $Re_\infty = 8.3 \times 10^6$ /ft, sphere-cone 3 mil gap.....	126
Figure 122. Test 7036, Run 62, $Re_\infty = 2.1 \times 10^6$ /ft, sphere-cone 6 mil gap.....	127
Figure 123. Test 7036, Run 63, $Re_\infty = 3.0 \times 10^6$ /ft, sphere-cone 6 mil gap.....	127
Figure 124. Test 7036, Run 64, $Re_\infty = 5.0 \times 10^6$ /ft, sphere-cone 6 mil gap.....	128
Figure 125. Test 7036, Run 65, $Re_\infty = 6.6 \times 10^6$ /ft, sphere-cone 6 mil gap.....	128
Figure 126. Test 7036, Run 66, $Re_\infty = 7.5 \times 10^6$ /ft, sphere-cone 6 mil gap.....	129
Figure 127. Test 7036, Run 67, $Re_\infty = 8.3 \times 10^6$ /ft, sphere-cone 6 mil gap.....	129
Figure 128. Test 7036, Run 56, $Re_\infty = 2.1 \times 10^6$ /ft, sphere-cone 12 mil gap.....	130
Figure 129. Test 7036, Run 57, $Re_\infty = 3.0 \times 10^6$ /ft, sphere-cone 12 mil gap.....	130
Figure 130. Test 7036, Run 58, $Re_\infty = 5.0 \times 10^6$ /ft, sphere-cone 12 mil gap.....	131
Figure 131. Test 7036, Run 59, $Re_\infty = 6.6 \times 10^6$ /ft, sphere-cone 12 mil gap.....	131
Figure 132. Test 7036, Run 60, $Re_\infty = 7.5 \times 10^6$ /ft, sphere-cone 12 mil gap.....	132
Figure 133. Test 7036, Run 61, $Re_\infty = 8.3 \times 10^6$ /ft, sphere-cone 12 mil gap.....	132
Figure 134. Test 7036, Run 7, $Re_\infty = 2.1 \times 10^6$ /ft, sphere-cone 24 mil gap.....	133
Figure 135. Test 7036, Run 2, $Re_\infty = 3.0 \times 10^6$ /ft, sphere-cone 24 mil gap.....	133
Figure 136. Test 7036, Run 1, $Re_\infty = 5.0 \times 10^6$ /ft, sphere-cone 24 mil gap.....	134
Figure 137. Test 7036, Run 3, $Re_\infty = 6.6 \times 10^6$ /ft, sphere-cone 24 mil gap.....	134
Figure 138. Test 7036, Run 4, $Re_\infty = 7.5 \times 10^6$ /ft, sphere-cone 24 mil gap.....	135
Figure 139. Test 7036, Run 5, $Re_\infty = 8.3 \times 10^6$ /ft, sphere-cone 24 mil gap.....	135
Figure 140. Test 7036, Run 20, $Re_\infty = 2.1 \times 10^6$ /ft, sphere-cone 3 mil fence.....	136
Figure 141. Test 7036, Run 21, $Re_\infty = 3.0 \times 10^6$ /ft, sphere-cone 3 mil fence.....	136
Figure 142. Test 7036, Run 22, $Re_\infty = 5.0 \times 10^6$ /ft, sphere-cone 3 mil fence.....	137
Figure 143. Test 7036, Run 23, $Re_\infty = 6.6 \times 10^6$ /ft, sphere-cone 3 mil fence.....	137
Figure 144. Test 7036, Run 24, $Re_\infty = 7.5 \times 10^6$ /ft, sphere-cone 3 mil fence.....	138
Figure 145. Test 7036, Run 25, $Re_\infty = 8.3 \times 10^6$ /ft, sphere-cone 3 mil fence.....	138
Figure 146. Test 7036, Run 46, $Re_\infty = 2.1 \times 10^6$ /ft, sphere-cone 6 mil fence.....	139
Figure 147. Test 7036, Run 45, $Re_\infty = 3.0 \times 10^6$ /ft, sphere-cone 6 mil fence.....	139
Figure 148. Test 7036, Run 44, $Re_\infty = 5.0 \times 10^6$ /ft, sphere-cone 6 mil fence.....	140
Figure 149. Test 7036, Run 47, $Re_\infty = 6.6 \times 10^6$ /ft, sphere-cone 6 mil fence.....	140
Figure 150. Test 7036, Run 48, $Re_\infty = 7.5 \times 10^6$ /ft, sphere-cone 6 mil fence.....	141

Figure 151. Test 7036, Run 49, $Re_\infty = 8.3 \times 10^6/\text{ft}$, sphere-cone 6 mil fence.....	141
Figure 152. Test 7036, Run 68, $Re_\infty = 2.1 \times 10^6/\text{ft}$, sphere-cone 12 mil fence.....	142
Figure 153. Test 7036, Run 69, $Re_\infty = 3.0 \times 10^6/\text{ft}$, sphere-cone 12 mil fence.....	142
Figure 154. Test 7036, Run 70, $Re_\infty = 5.0 \times 10^6/\text{ft}$, sphere-cone 12 mil fence.....	143
Figure 155. Test 7036, Run 71, $Re_\infty = 6.6 \times 10^6/\text{ft}$, sphere-cone 12 mil fence.....	143
Figure 156. Test 7036, Run 72, $Re_\infty = 7.5 \times 10^6/\text{ft}$, sphere-cone 12 mil fence.....	144
Figure 157. Test 7036, Run 73, $Re_\infty = 8.3 \times 10^6/\text{ft}$, sphere-cone 12 mil fence.....	144
Figure 158. Test 7036, Run 13, $Re_\infty = 2.1 \times 10^6/\text{ft}$, sphere-cone 24 mil fence.....	145
Figure 159. Test 7036, Run 14, $Re_\infty = 3.0 \times 10^6/\text{ft}$, sphere-cone 24 mil fence.....	145
Figure 160. Test 7036, Run 15, $Re_\infty = 5.0 \times 10^6/\text{ft}$, sphere-cone 24 mil fence.....	146
Figure 161. Test 7036, Run 16, $Re_\infty = 6.6 \times 10^6/\text{ft}$, sphere-cone 24 mil fence.....	146
Figure 162. Test 7036, Run 17, $Re_\infty = 7.5 \times 10^6/\text{ft}$, sphere-cone 24 mil fence.....	147
Figure 163. Test 7036, Run 18, $Re_\infty = 8.3 \times 10^6/\text{ft}$, sphere-cone 24 mil fence.....	147
Figure 164. Test 7057, Run 7, $Re_\infty = 2.1 \times 10^6/\text{ft}$, spherical-cap, smooth OML.....	149
Figure 165. Test 7057, Run 8, $Re_\infty = 3.0 \times 10^6/\text{ft}$, spherical-cap, smooth OML.....	149
Figure 166. Test 7057, Run 9, $Re_\infty = 5.0 \times 10^6/\text{ft}$, spherical-cap, smooth OML.....	150
Figure 167. Test 7057, Run 10, $Re_\infty = 6.6 \times 10^6/\text{ft}$, spherical-cap, smooth OML.....	150
Figure 168. Test 7057, Run 11, $Re_\infty = 7.5 \times 10^6/\text{ft}$, spherical-cap, smooth OML.....	151
Figure 169. Test 7057, Run 12, $Re_\infty = 8.3 \times 10^6/\text{ft}$, spherical-cap, smooth OML.....	151
Figure 170. Test 7057, Run 158, $Re_\infty = 2.1 \times 10^6/\text{ft}$, spherical-cap 3 mil gap.....	152
Figure 171. Test 7057, Run 159, $Re_\infty = 3.0 \times 10^6/\text{ft}$, spherical-cap 3 mil gap.....	152
Figure 172. Test 7057, Run 162, $Re_\infty = 5.0 \times 10^6/\text{ft}$, spherical-cap 3 mil gap.....	153
Figure 173. Test 7057, Run 163, $Re_\infty = 6.6 \times 10^6/\text{ft}$, spherical-cap 3 mil gap.....	153
Figure 174. Test 7057, Run 164, $Re_\infty = 7.5 \times 10^6/\text{ft}$, spherical-cap 3 mil gap.....	154
Figure 175. Test 7057, Run 165, $Re_\infty = 8.3 \times 10^6/\text{ft}$, spherical-cap 3 mil gap.....	154
Figure 176. Test 7057, Run 61, $Re_\infty = 2.1 \times 10^6/\text{ft}$, spherical-cap 6 mil gap.....	155
Figure 177. Test 7057, Run 62, $Re_\infty = 3.0 \times 10^6/\text{ft}$, spherical-cap 6 mil gap.....	155
Figure 178. Test 7057, Run 63, $Re_\infty = 5.0 \times 10^6/\text{ft}$, spherical-cap 6 mil gap.....	156
Figure 179. Test 7057, Run 64, $Re_\infty = 6.6 \times 10^6/\text{ft}$, spherical-cap 6 mil gap.....	156
Figure 180. Test 7057, Run 65, $Re_\infty = 7.5 \times 10^6/\text{ft}$, spherical-cap 6 mil gap.....	157
Figure 181. Test 7057, Run 66, $Re_\infty = 8.3 \times 10^6/\text{ft}$, spherical-cap 6 mil gap.....	157
Figure 182. Test 7057, Run 85, $Re_\infty = 2.1 \times 10^6/\text{ft}$, spherical-cap 12 mil gap.....	158
Figure 183. Test 7057, Run 86, $Re_\infty = 3.0 \times 10^6/\text{ft}$, spherical-cap 12 mil gap.....	158
Figure 184. Test 7057, Run 87, $Re_\infty = 5.0 \times 10^6/\text{ft}$, spherical-cap 12 mil gap.....	159
Figure 185. Test 7057, Run 88, $Re_\infty = 6.6 \times 10^6/\text{ft}$, spherical-cap 12 mil gap.....	159
Figure 186. Test 7057, Run 89, $Re_\infty = 7.5 \times 10^6/\text{ft}$, spherical-cap 12 mil gap.....	160
Figure 187. Test 7057, Run 90, $Re_\infty = 8.3 \times 10^6/\text{ft}$, spherical-cap 12 mil gap.....	160
Figure 188. Test 7057, Run 91, $Re_\infty = 2.1 \times 10^6/\text{ft}$, spherical-cap 24 mil gap.....	161
Figure 189. Test 7057, Run 92, $Re_\infty = 3.0 \times 10^6/\text{ft}$, spherical-cap 24 mil gap.....	161
Figure 190. Test 7057, Run 93, $Re_\infty = 5.0 \times 10^6/\text{ft}$, spherical-cap 24 mil gap.....	162
Figure 191. Test 7057, Run 94, $Re_\infty = 6.6 \times 10^6/\text{ft}$, spherical-cap 24 mil gap.....	162
Figure 192. Test 7057, Run 95, $Re_\infty = 7.5 \times 10^6/\text{ft}$, spherical-cap 24 mil gap.....	163
Figure 193. Test 7057, Run 96, $Re_\infty = 8.3 \times 10^6/\text{ft}$, spherical-cap 24 mil gap.....	163
Figure 194. Test 7057, Run 67, $Re_\infty = 2.1 \times 10^6/\text{ft}$, spherical-cap 3 mil fence.....	164
Figure 195. Test 7057, Run 68, $Re_\infty = 3.0 \times 10^6/\text{ft}$, spherical-cap 3 mil fence.....	164
Figure 196. Test 7057, Run 69, $Re_\infty = 5.0 \times 10^6/\text{ft}$, spherical-cap 3 mil fence.....	165
Figure 197. Test 7057, Run 70, $Re_\infty = 6.6 \times 10^6/\text{ft}$, spherical-cap 3 mil fence.....	165
Figure 198. Test 7057, Run 71, $Re_\infty = 7.5 \times 10^6/\text{ft}$, spherical-cap 3 mil fence.....	166
Figure 199. Test 7057, Run 72, $Re_\infty = 8.3 \times 10^6/\text{ft}$, spherical-cap 3 mil fence.....	166
Figure 200. Test 7057, Run 73, $Re_\infty = 2.1 \times 10^6/\text{ft}$, spherical-cap 6 mil fence.....	167
Figure 201. Test 7057, Run 74, $Re_\infty = 3.0 \times 10^6/\text{ft}$, spherical-cap 6 mil fence.....	167

Figure 202. Test 7057, Run 75, $Re_\infty = 5.0 \times 10^6/\text{ft}$, spherical-cap 6 mil fence.....	168
Figure 203. Test 7057, Run 76, $Re_\infty = 6.6 \times 10^6/\text{ft}$, spherical-cap 6 mil fence.....	168
Figure 204. Test 7057, Run 77, $Re_\infty = 7.5 \times 10^6/\text{ft}$, spherical-cap 6 mil fence.....	169
Figure 205. Test 7057, Run 78, $Re_\infty = 8.3 \times 10^6/\text{ft}$, spherical-cap 6 mil fence.....	169
Figure 206. Test 7057, Run 48, $Re_\infty = 2.1 \times 10^6/\text{ft}$, spherical-cap 12 mil fence.....	170
Figure 207. Test 7057, Run 49, $Re_\infty = 3.0 \times 10^6/\text{ft}$, spherical-cap 12 mil fence.....	170
Figure 208. Test 7057, Run 50, $Re_\infty = 5.0 \times 10^6/\text{ft}$, spherical-cap 12 mil fence.....	171
Figure 209. Test 7057, Run 51, $Re_\infty = 6.6 \times 10^6/\text{ft}$, spherical-cap 12 mil fence.....	171
Figure 210. Test 7057, Run 52, $Re_\infty = 7.5 \times 10^6/\text{ft}$, spherical-cap 12 mil fence.....	172
Figure 211. Test 7057, Run 53, $Re_\infty = 8.3 \times 10^6/\text{ft}$, spherical-cap 12 mil fence.....	172
Figure 212. Test 7057, Run 97, $Re_\infty = 2.1 \times 10^6/\text{ft}$, spherical-cap 24 mil fence.....	173
Figure 213. Test 7057, Run 98, $Re_\infty = 3.0 \times 10^6/\text{ft}$, spherical-cap 24 mil fence.....	173
Figure 214. Test 7057, Run 99, $Re_\infty = 5.0 \times 10^6/\text{ft}$, spherical-cap 24 mil fence.....	174
Figure 215. Test 7057, Run 100, $Re_\infty = 6.6 \times 10^6/\text{ft}$, spherical-cap 24 mil fence.....	174
Figure 216. Test 7057, Run 101, $Re_\infty = 7.5 \times 10^6/\text{ft}$, spherical-cap 24 mil fence.....	175
Figure 217. Test 7057, Run 102, $Re_\infty = 8.3 \times 10^6/\text{ft}$, spherical-cap 24 mil fence.....	175

Abstract

An experimental investigation of boundary-layer transition and convective surface heating on wind tunnel models that simulated aeroshells comprised of multiple blocks of thermal protection system (TPS) material has been performed. Two representative entry vehicle geometries, a sphere-cone aeroshell and a spherical-cap aeroshell, were considered. Multiple cast ceramic models of each geometry were fabricated with varying fence heights or gap depths to represent gap fillers that either protrude above, or are recessed below, the TPS blocks due to differential ablation during reentry. Wind tunnel testing was performed at Mach 6 over a range of Reynolds numbers sufficient to produce laminar, transitional, and turbulent flow. Convective surface heating and boundary-layer transition onset data were obtained using global phosphor thermography. The experimental heating data are presented herein, as are comparisons to laminar and turbulent smooth-wall heat transfer distributions from computational flow field simulations.

Symbols

H_F, H_G	fence height or gap depth
H_0	tunnel total (reservoir) enthalpy
H_{AW}	adiabatic wall enthalpy
H_W	wall enthalpy
H_{300K}	wall enthalpy at 300 K
h	measured heat-transfer film coefficient
h_{FR}	Fay-Riddell theory heat-transfer film coefficient
M_e	boundary-layer edge Mach number
M_∞	free stream Mach number
q	heat transfer rate
r_{stag}	approximate radius of edge Mach cutoff region
R	model radius
R_F, R_G	model fence or gap fillet radius
R_N	model nose radius
R_C	model corner radius
Re_θ	boundary-layer momentum thickness Reynolds number
Re_∞	free stream unit Reynolds number
s/R	normalized surface running length from edge Mach cutoff
s_0/R	normalized surface running length from stagnation point
$T_{w,AVG}$	average wall temperature
T_∞	free stream temperature
U_∞	free stream velocity
W_F, W_G	model fence gap depth
x, y, z	Cartesian coordinates
α	angle of attack
β	model spherical nose included angle
β_F, β_G	model fence or gap fillet radius
ϕ	streamline angular coordinate identifier
ρ_∞	free stream density
θ	boundary-layer momentum thickness

Subscripts and Superscripts

∞	wind tunnel free stream condition
0	wind tunnel stagnation or reservoir condition
e	boundary layer edge condition
f	fence
g	gap
w	model wall condition

Acronyms

CFD	Computational Fluid Dynamics
IHEAT	Imaging for Hypersonic Experimental Aerothermodynamic Testing
LAL	Langley Aerothermodynamics Laboratory
LaRC	Langley Research Center

LAURA	Langley Aerothermodynamic Upwind Relaxation Algorithm
OML	Outer Mold Line
TPS	Thermal Protection System

Introduction

This report documents an experimental dataset of discrete fence and gap surface roughness effects on boundary-layer transition and heating augmentation on blunt body entry vehicle configurations. The data were obtained through hypersonic wind tunnel testing of two representative entry vehicle aeroshell geometries with roughness patterns that simulated fences or gaps produced by differential ablation of thermal protection system (TPS) blocks and the gap fillers between them. This reference document can be used as the basis for future detailed analyses of the heat-transfer distributions and boundary-layer transition onset locations measured in the test program. The current study is a direct follow-on to previous studies of ablated TPS with both distributed sand-grain roughness (Refs. 1) and hexcomb pattern roughness (Refs. 2–3) on the same aeroshell geometries. Another related study (Refs. 4–5) was also conducted on the effects of distributed sand-grain surface roughness on hemispherical nose tips, rather than these aeroshell geometries.

Background

“Roughness” is a generic term in aerospace literature that encompasses many types of surface features that deviate from that of a smooth outer mold line (OML). Roughness can be divided into two general types, discrete and distributed. Discrete roughness (Figure 1) includes surface features such as: a) protruding compression pads or recessed cavities at mechanical attachment points; b) fences or gaps between heat shield blocks or tiles resulting from differential ablation TPS and the filler material between them; and c) physical damage to a TPS. Distributed roughness (Figure 2) includes features such as: a) regular patterns resulting from ablation of hexcomb-structure TPS; b) irregular deflections of a flexible TPS under aerodynamic loading; c) random “sand-grain” features resulting from ablation of a monolithic TPS; or d) the texture of overlapping fibers on a woven TPS.

Data on the effects of surface roughness are valuable because the roughness of an entry vehicle’s TPS can promote earlier boundary-layer transition and produce higher turbulent heating (and shear) levels than would be expected based on an idealized, smooth-wall analysis. However, due to the complexities of roughness effects, a vehicle’s TPS is typically designed using analytical, computational, and/or experimental techniques that are based on the assumption of a smooth surface. The effects of roughness on the aerothermodynamic environment can then be included through approximate engineering and methods.

The purpose of this test program was to obtain data on the effects of fences or gaps produced by the differential ablation of TPS blocks and gap fillers. Examples of ablating TPS that produce such patterns include the PICA material used on the Mars Science Laboratory and Mars 2020 entry vehicles and the Artemis EM-1 flight test vehicle, and also the PICA-X derivative employed on the SpaceX Dragon capsules. Another related example is the TPS of the Shuttle Orbiter – although this TPS was non-ablating, fences or gaps were still produced when the gap fillers between the tiles came loose and either fell out – leaving a gap – or were left sticking out above the tiles to form fences.

The data obtained in this test program are intended for use in the development and/or validation of engineering correlations for the effects of fence/gap roughness on boundary-layer transition and turbulent heat transfer. These data can also serve as the basis for development and/or validation of higher-fidelity,

numerical flow field simulation models for roughness effects.

Experimental Tools and Methods

Wind Tunnel Models

Model Geometries

Roughness effects data were obtained on two representative entry vehicle geometries: a sphere-cone geometry (Figure 3) and a spherical-cap geometry (Figure 4). The spherical-cap geometry is similar to that of the Mercury – Gemini – Apollo – Orion/Artemis family of entry vehicles employed in NASA’s crewed space program. The sphere-cone geometry is similar to that of the Mars Viking – Mars Pathfinder – Mars Exploration Rover – Mars Phoenix – Mars Science Laboratory – Mars 2020 family of entry vehicles used in NASA’s robotic Mars exploration program. Geometric parameters for both configurations are listed in Table 1. Multiple models of each configuration were fabricated with a range of fence heights and gap depths between the TPS blocks.

A generic pattern of TPS blocks was developed that was similar to those employed in flight vehicles, but that can be represented by a simple set of geometric parameters. This block TPS layout consists of a single circular block at the geometric center of the aeroshell that is surrounded by four concentric rings of blocks. Each ring is comprised of a different number of arc-sector geometry blocks arrayed around the center of the aeroshell. These patterns are shown in Figure 5 for the sphere-cone aeroshell and in Figure 6 for the spherical-cap aeroshell. These blocks are separated by either fence or gap patterns referred to as “ribs”, which are the concentric fences or gaps between each ring of blocks and “spars”, which are the radial fences or gaps that connect the rings. The geometric definitions of these rings and spars are provided in Table 2. The patterns on the sphere-cone and spherical-cap aeroshells are almost identical, with only slight differences required to fit the patterns onto models with the same overall 6-in. diameter but with different shoulder radii.

Four models with different fence heights and four models with different gap depths were defined for each aeroshell geometry. The fence and gap cross-sections are shown in Figure 7 and the geometric information is provided in Table 3. The fence and gap cross-sections are identical except they are mirrored across the surface of the geometry. The different fence height and gap depth geometries are also identical except in their scale. A visual comparison between the different fence and gap scales is shown in Figure 8. The fences or gaps were blended into each aeroshell geometry to have a surface normal (positive or negative, respectively) orientation with respect to the center of the cross-section.

Model Fabrication

The fabrication process for a ceramic model is documented in Ref. 6. The first step in fabrication of a model is the production of a rapid prototype pattern of the geometry using a three-dimensional wax printer. The pattern is then hand-worked (if necessary) to a smooth surface finish to remove any printing artifacts. A multiple-piece injection mold is then built around the wax pattern. A silica ceramic shell model is then slip-cast in the shell mold. Then, the ceramic model is removed from the mold, dried, and sintered. The finished ceramic model is then back-filled with a hydraulically setting magnesia ceramic for strength and support and mounted on a stainless-steel cylindrical sting. Finally, the model is coated with a mixture of phosphors that luminesce under ultraviolet lighting. Sample photographs of a cast ceramic fence and gap model are shown in Figure 9.

After fabrication was completed, problems were found with the sphere-cone 24-mil fence model and the spherical-cap 24-fence model. As illustrated in Figure 11, several of the fence segments were damaged or missing from these models. These segments are shown in red in the diagram. Additionally, on the 24-mil fence spherical-cap model, a CAD error resulted in the second set of spars being rotated approximately 15-deg counter-clockwise from the intended location. Schedule limitations precluded rebuilding these models, so the “as-built” configurations were tested and the data are included herein for completeness. There is nothing inherently wrong with the data from these models with damaged or mislocated fences and the results are still valid as long as these issues are noted.

Wind Tunnel Test Facility

Facility Description

Wind tunnel testing was performed at the Langley Aerothermodynamics Laboratory (LAL) in the 20-Inch Mach 6 Air Tunnel. This wind tunnel is described in brief below and more detailed information on the LAL facilities can be found in Refs. 7-8.

The NASA LaRC 20-Inch Mach 6 Air Tunnel (Figure 12 - Figure 13) is a blow-down facility in which heated, dried, and filtered air is used as the test gas. The tunnel has a two-dimensional contoured nozzle that opens into a 20.5 in. × 20.0 in. test section. The tunnel is equipped with a bottom-mounted injection system with a -5-deg to +55-deg pitch range and ±5-deg yaw range that can transfer a model from a sheltered model box to the tunnel centerline in less than 0.5 sec. Run times of up to 15 minutes are possible in this facility, although for aeroheating studies, run times of only a few seconds are typically required. The nominal reservoir conditions of this facility produce perfect-gas free stream flows with Mach numbers between 5.8 and 6.1 and unit Reynolds numbers of $0.5 \times 10^6/\text{ft}$ to $8.3 \times 10^6/\text{ft}$. With its wide Reynolds number operating range capable of producing laminar, transitional, or turbulent flow on most geometries, this tunnel is primarily used for heat-transfer and boundary-layer transition studies.

Facility Operating Conditions

Data were obtained in the 20-Inch Mach 6 Air Tunnel Tests 7036 and 7057 at six unit Reynolds numbers from $Re_\infty = 2.1 \times 10^6/\text{ft}$ to $8.1 \times 10^6/\text{ft}$. The nominal conditions defined by the average of all runs at each operating point are listed in Table 4 for Test 7036 and in Table 5 for Test 7057. The variation of conditions from run-to-run was less than ±0.5%. Smooth-surface CFD simulations from previous testing of these aeroshells geometries (but using wind tunnel models with different roughness types) were employed in this study for comparisons with the data. These simulations were performed at slightly different conditions, as given in Table 6. However, this slight mismatch in conditions has no impact on the nondimensionalized film coefficient comparisons between prediction and measurements.

The complete test matrices with individual run conditions are listed in Table 7 for Test 7036, in which the sphere-cone geometry was used and in Table 8 for Test 7057, in which the spherical-cap geometry was used. Entries in these tables are sorted first by fence or gap dimension, and then by free stream unit Reynolds number. All sphere-cone data were obtained at $\alpha = 16$ deg. and all spherical-cap data were obtained at $\alpha = 28$ deg. The values were selected for continuity with data obtained in prior roughness tests of these geometries (Refs. 1–3).

Free stream velocity (U_∞), density (ρ_∞), temperature (T_∞), unit Reynolds number (Re_∞), and Mach number (M_∞) are provided in these tables. Additionally, an average model surface temperature (T_w), enthalpy difference (ΔH_{tot}), and reference Fay-Riddell heat transfer film-coefficient value (h_{FR}) are

provided. This wall temperature is the average over the model surface when the thermographic phosphor image was obtained and is provided because boundary-layer transition is known to be sensitive to wall temperature. The enthalpy term is defined as the difference $H_0 - H_{300K}$ between the free stream total enthalpy and the wall enthalpy at cold wall (300 K) conditions. The film coefficient is the value from the Fay-Riddell theory (Ref. 9) for a hemispherical radius at cold wall conditions, where the radius is the nose radius of the respective model geometry.

Experimental Data

Data Acquisition and Reduction

Aeroheating data were obtained using the two-color, relative-intensity, global phosphor thermography method (Refs. 10-11) and reduced using the IHEAT (Imaging for Hypersonic Experimental Aerothermodynamic Testing) code (Ref. 12). In this method, a model is illuminated by ultraviolet light sources that induce temperature-dependent fluorescence of the phosphor coating during a run. Fluorescent intensity images of a model are taken in the tunnel before and during a run using a three-color, charge-coupled device camera and the images are processed to determine heat-transfer distributions. The intensity data are then converted to temperatures using pretest calibrations of the data acquisition system.

Heat-transfer film coefficients are determined by assuming a step function in the film coefficient from the prerun temperature to the run temperature, which corresponds to a parabolic temperature-time history. The heating data are typically reported in terms of the ratio h/h_{FR} where the heat-transfer film coefficient, h , is defined in terms of enthalpy via Eq. (1) as:

$$h = q/\Delta H_{TOT} = q/(H_{AW} - H_w) \cong q/(H_0 - H_w) \quad (1)$$

In the calculation of the heat-transfer film coefficient, it is assumed that for a blunt-body, the adiabatic wall enthalpy H_{AW} is equal to the free stream total enthalpy of the tunnel, H_0 . This heat transfer coefficient definition provides a theoretically near-constant value over the course of a run since the decrease in time of the heat transfer rate in the numerator as the model surface becomes hotter is balanced by the decrease of the enthalpy-difference term in the denominator. Additionally, the ratio h/h_{FR} is invariant with Reynolds number for laminar, perfect-gas flow such as produced in the LAL wind tunnels.

Data Mapping and Presentation

The two-dimensional (2-D) image data output from IHEAT (Figure 14) were transformed to account for optical perspective effects and mapped to a three-dimensional (3-D) CAD surface of the smooth-surface (no blocks, steps or gaps) wind tunnel model (Figure 15). To accomplish this mapping, perspective, translational, and rotational transformations are first performed on the 3-D CAD surface until its 2-D projection matches that of the 2-D image data. The image data are then assigned transformed (x, y, z) coordinates based on interpolation between the image and surface geometry. Finally, the transformation is inverted to obtain an orthographic, 3-D heating distribution map of the experimental data.

The mapped data from all runs are collected in the Appendices and presented therein as large, high-resolution images. These images are ordered by model geometry, fence or gap dimension, and Reynolds numbers. Smaller images will be shown in the body of the report along with streamline-based heating

distributions.

An additional data manipulation step was performed to extract the streamline-based heating distributions from the mapped wind tunnel data set. These streamline-based data sets can be used in boundary-layer transition analyses and for comparisons of Reynolds number and fence/gap roughness effects. For each run, streamlines were defined based on the boundary-layer edge velocity vectors from the computed flow fields (to be discussed in the next section). Thirty-six streamline termini were established at locations spaced in 10-deg increments around the circumference of the geometry and the streamlines were then traced backward from each terminus toward the flow field stagnation point. The resulting streamlines are shown in Figure 16 for the sphere-cone geometry and in Figure 17 for the spherical-cap geometry. Each streamline is identified by the angular location, ϕ , of its terminus. The geometric definition (x, y, z) of each streamline was then interpolated onto the 3-D mapped image and experimental data were extracted along each streamline in terms of h/h_{FR} vs. s/R , where s/R is the normalized streamline distance from the stagnation point. Additionally, the predicted flow field quantities (surface heating, boundary-layer height, momentum-thickness Reynold number, etc.) were also extracted along these streamlines and combined with the wind tunnel data set to enable direct comparisons and analyses.

One complication needs to be noted with respect to extraction of data along streamlines. The extraction algorithm tended to fail near the stagnation point where the velocity vectors approach zero; essentially the physical location becomes indeterminate, resulting in unreliable path-lengths through the stagnation region. This problem was resolved by stopping the reverse tracing of the streamlines from the outer edge of the model toward that stagnation point at the location where the edge Mach number, M_e , dropped below 0.025. The “true” streamline length value, s_0 was determined via from an estimate of the physical length Δs from the M_e cutoff to the stagnation region as a function of the streamline terminus angular location ϕ and the approximate radius of the stagnation region, r_{stag} :

$$s_0 = s + \Delta s \quad (2)$$

$$\Delta s = \cos(2\phi) \times r_{stag}/3 + r_{stag}, \text{ where } r_{stag} \cong 0.003 \text{ m} \quad (3)$$

In the body of this report, plotted data will be shown in terms of s/R , as that is the quantity in which the data were extracted along streamlines. However, the estimated actual distance, s_0/R , can be determined using Eqs. (2) – (3).

Phosphor Thermography Data Quality

An important factor that influences the quality of phosphor thermography data is the local surface inclination at a given point on the model with respect to both the camera and the UV lights. Phosphor thermography provides the best result when the surface to be imaged is normal to the camera, which reduces perspective distortion and image smearing, and when the surface is well illuminated, which induces the best temperature response of the phosphor coating. Because of the three-dimensional nature of a wind tunnel model, the entire surface of a model cannot be optimally imaged, or in some cases cannot even be viewed. For blunt bodies such as those in this test, the windward centerline region of the model – the ‘bottom’ of the model with respect to the view orientation - is the area where the data quality is most affected. This

situation is illustrated for a simple hemispherical model in Figure 18. Because of this limitation, windward centerline region data are only regarded as qualitative, not quantitative. Although image data from this region will be shown, quantitative plotted data will not be provided for the streamlines originating from the 160-deg through 200-deg termini.

Another issue with respect to data quality is the calibration range of the thermographic phosphor systems, which is roughly from 275 K to 460 K. At certain test conditions (generally the nominal Reynolds numbers of $5 \times 10^6/\text{ft}$ to $7 \times 10^6/\text{ft}$) for models with large roughness elements, the heating augmentation is great enough that the surface temperatures are elevated beyond the range of the phosphor calibration. For such cases, the data are not usable and are represented by white regions on the heating images shown herein.

Heat Transfer Data Uncertainty

The experimental uncertainty for convective heat transfer measurements on a *smooth, blunt body geometry* model in the 20-Inch Mach 6 Air Tunnel is quantified as a function of the net uncertainties resulting from: the data acquisition method ($\pm 10\%$); flow quality and test-condition repeatability ($\pm 5\%$); and the accuracy of the 3D mapping process ($\pm 10\%$), which results in an overall root-sum-squared value of $\pm 15\%$. Experience with this technique indicates that these values are usually conservative and as will be shown later, the predicted and measured heating distributions were in close agreement (generally less than $\pm 5\%$) for laminar, smooth-wall cases. It is assumed that the fence/gap patterns introduced additional uncertainties for three reasons. First, the fence and gap geometries are three-dimensional so the one-dimensional surface-normal heat conduction assumption is only approximately correct. Second, the dimensions of the smaller fence/gap patterns approach the fidelity limit of the wax printing and ceramic casting processes. Third, the fences and gaps produced very detailed heating patterns, which in some cases, were smaller than the resolution of the camera system; thus, measurements in such areas are, in effect, a spatial average rather than a point measurement. Quantification of such errors on a macro-scale is not possible because of the localized and position/pattern/orientation dependency of fence/gap features but these errors are probably on the order of $\pm 10\text{--}20\%$. Taken together with the smooth-wall uncertainty, the uncertainty in heating on fence/gap models is estimated to be in the $\pm 18\text{--}25\%$ range.

Calibration Correction for Heat Transfer Data

A central premise in the analysis of wind tunnel heating data is that for a given Mach number, the normalized heat transfer film coefficient, h/h_{FR} , at any point on a geometry remains constant with varying Reynolds number at perfect gas conditions for attached flow over a blunt body. This behavior is demonstrated through CFD simulations for a 2-inch diameter hemisphere over the current range of test conditions. As shown in Figure 19, laminar simulations using the LAURA code (see section below on Computational Tools and Methods) predict a constant value of $h/h_{FR} = 1.06$ at the hemisphere stagnation point for all test condition Reynolds numbers. The fact that the ratio is not exactly 1 is due to the differences between a modern CFD prediction for the film coefficient at perfect-gas wind tunnel conditions and the semiempirical Fay-Riddell correlation for the film coefficient based on approximate boundary-layer solutions for reacting-gas flight conditions. The fact that the two predictions are so close is a testament to the utility of the original Fay-Riddell method that was developed in the 1950s.

While the CFD predictions do indeed demonstrate a constant value of h/h_{FR} for the wind tunnel conditions, the same result was not obtained during the test program; rather, a small dependency on Reynolds number was observed in the experimental data. This dependency is illustrated by stagnation point heating data from pretest checkout and calibration runs on a phosphor-coated, 2-in radius hemisphere shown in Figure 20 for Test 7036 and Figure 21 for Test 7057. Instead of a constant value for stagnation point

h/h_{FR} at all Reynolds numbers, values at lower Reynolds numbers were observed to be at or below the predicted value for the computations, while values at higher Reynolds numbers were observed to be greater than the predicted value. Second-order polynomial fits to the measured heating values that reflect these variations are also shown in the figures.

There are several potential sources of uncertainty that could be producing this dependency, including variations in the bulk materials used to cast the ceramic wind tunnel models, the consistency of the thermographic phosphor mixtures used to coat the models, the fidelity of the phosphor intensity/temperature calibrations, degradation of the UV lighting or imaging camera, and/or the flow quality of the wind tunnel. However, it was beyond the scope of this study to resolve whether any, or all, of these factors influenced the experimental data.

Because the differences in predicted and measured stagnation point film-coefficient ratios for the calibration hemisphere tests fell within the estimated uncertainty of $\pm 18\text{--}25\%$ range cited in the previous section, these results were considered acceptable from an experimental perspective. However, since the differences can be represented by a bias function that depends on Reynolds number, as opposed to a random dispersion, an additional data processing step was conducted to correct the heating data based on the hemisphere calibration run data. The original data were modified using the polynomial curve fits as per Eqs. (4)–(6) and all data and results presented herein reflect this calibration correction.

$$\left(\frac{h}{h_{FR}}\right)_{exp,corr} = \left(\frac{h}{h_{FR}}\right)_{exp} \times \left(\frac{h_{CFD}}{h_{FR}}\right)_{hemi-stag} \times \phi_{corr} \quad (4)$$

where:

$$\left(\frac{h_{CFD}}{h_{FR}}\right)_{hemi-stag} = 1.06 \quad (5)$$

$$\begin{aligned} \phi_{corr} &= 1/(A + Bx + Cx^2), \text{ and } x = Re_{\infty}/1,000,000 \\ \text{Test 7036: } &A = 0.8279 \quad B = 0.09120 \quad C = -7.583 \times 10^{-3} \\ \text{Test 7057: } &A = 0.9971 \quad B = 0.03163 \quad C = -2.034 \times 10^{-3} \end{aligned} \quad (6)$$

Computational Tools and Methods

Flow Field Solver

Flow field solutions were generated using the LAURA (Langley Aerothermodynamic Upwind Relaxation Algorithm) code. LAURA (Refs. 13–14) is a three-dimensional, structured-grid, finite-volume solver that includes perfect-gas and nonequilibrium chemistry options, a variety of turbulence models, and ablation and radiative transport capabilities. LAURA solutions were used for comparisons of predicted heating levels with the measured data and to define the streamlines along which to extract the mapped experimental data, as described above. The solutions employed herein were taken from previous studies of the same aeroshell geometries (but with different roughness types) at the same nominal test conditions, as per Table 6.

Solutions were computed on multiblock grids of each geometry with a smooth (no fences or gaps) outer

mold line. Grid adaption was performed to align the grid outer boundary with the bow shock and to cluster cells near the surface to produce wall cell Reynolds numbers on the order of 1 to 10. For these wind tunnel conditions, the perfect-gas air option was used. Both laminar and turbulent solutions were generated. Turbulent cases were computed using the Cebeci-Smith algebraic model with fully turbulent flow over the entire geometry. Because the computations were performed on a smooth geometry, they are not quantitatively comparable to the actual wind tunnel tests performed on these rough-surface models with heating augmentation, but are still as basis for evaluation the roughness effects with respect to a smooth-OML.

For the wall temperature boundary condition, a change in the normal practice for wind tunnel simulations of setting this value to a “cold-wall” ambient temperature (allowable because of the very small variation in heat-transfer coefficient with temperature) was employed. Literature on roughness effects indicates a dependence of transition onset location on the ratio of boundary-layer edge temperature to wall temperature T_e/T_w . To approximately account for this effect (which was expected to be small, but non-negligible, for these test conditions), the computations were performed using a uniform “hot-wall” wall temperature set to the average of the measured surface temperature on the model for each run. These values varied between ~ 325 K to 420 K, depending on fence/gap dimensions and Reynolds number. These hot-wall solutions were performed using the original cold-wall simulations from previous tests as a starting points and then running them to convergence at the new temperatures.

Boundary-Layer Parameters

The flow field solutions also provide boundary-layer information, such as boundary-layer height parameters, boundary-layer Reynolds number parameters, and other flow field variables such as velocity vectors, temperature and density. This information can be used in the correlation of transition and heating augmentation data, extrapolation of wind tunnel data to flight condition, or (as noted previously) in the mapping of streamlines for comparison with experimental data

The ratio of the physical roughness height to that of the boundary-layer has a first-order influence on transition onset. Centerline distributions of k/δ for the range of fence heights and free stream Reynolds number conditions are presented in Figure 22 for the sphere-cone geometry and in Figure 23 for the spherical-cap geometry. In these figures, k represents the fence height and δ is the physical height of the boundary layer. Values of k/δ vary over more than two orders of magnitude depending on fence height and Reynolds numbers. The smaller fences (3 mil and 6 mil) remain within the boundary layer, while the larger fences (12 mil and 24 mil) are taller than the boundary layer height. It is unclear at this stage what (if any) height parameter would be useful in the correlation of gap transition effects so no plots are provide for the gap cases.

The turbulent roughness height Reynolds number, Re_{k+} as per Eq. (7), can be used as a correlation parameter for turbulent roughness heating augmentation. Centerline distributions of Re_{k+} are presented in Figure 24 for the sphere-cone geometry and in Figure 25 for the spherical-cap geometries for the range of fence heights and free stream Reynolds number conditions. Values of Re_{k+} also vary over more than two orders of magnitude, indicative of laminar flow at the lowest levels and roughness-augmented turbulent flow at the highest levels.

$$Re_{k+} = \rho_w U_\tau k_F / \mu_w, \text{ where } U_\tau = \sqrt{\tau_w / \rho_w} \quad (7)$$

Experimental Data Analysis

Reynolds Number Effects on Heating and Transition

The effects of Reynolds number on the heating levels and boundary-layer transition onset locations are illustrated for each fence height or gap depth in Figure 26 through Figure 43 for the sphere-cone geometry and in Figure 44 through Figure 61 for the spherical-cap geometry. Two figures are provided for each case: in the first figure, global heating images are shown for each Reynolds number, ordered left-to-right, top-to-bottom in terms of increasing Reynolds number; in the second figure, line plots of h/h_{FR} vs. s/R are shown, ordered left-to-right, top-to-bottom in terms of streamline angular coordinate. For brevity, all of the extracted streamlines are not shown in these figures. Instead, streamlines are shown at 30-deg increments from 0-deg to 150-deg. As noted earlier, the data for streamlines between 160-deg and 200-deg are considered to be qualitative, not quantitative. Data for streamlines from 210-deg to 360-deg are nominally symmetric with the data from 0-deg to 150-deg, although in practice, model surface irregularities can cause asymmetric behavior. Such local asymmetries can be observed in the images that accompany the line plots.

In these line-plots, the CFD predictions for smooth-wall, laminar and turbulent heating levels are also shown. Because the laminar heat-transfer film coefficient ratio, h/h_{FR} , remains nearly constant with Reynolds number, only the lowest Reynolds number laminar prediction is shown for each case. However, since this invariance does not hold for turbulent flow, turbulent predictions are shown for the different Reynolds numbers. As noted previously, turbulent cases were treated as fully-turbulent flow over the entire geometry. These turbulent cases are shown as limiting bounds, since the actual transition occurred at different locations for each test condition / model geometry.

Gap Depth / Fence Height Effects on Heating and Transition

The same data are shown in the next group of figures, but they are reordered to show the effects of the fence height or gap depth on transition and heating at each Reynolds number. The sphere-cone data are shown in Figure 62 through Figure 85 and the spherical-cap data are shown in Figure 86 through Figure 109. Two figures are provided for each case: in the first figure, global heating images are shown for each Reynolds number, ordered left-to-right, top-to-bottom in terms of increasing gap height or fence depth; in the second figure, line plots of h/h_{FR} vs. s/R are shown, ordered left-to-right, top-to-bottom in terms of streamline angular coordinate. As with the Reynold number effects plot set, both laminar and turbulent CFD heating predictions are shown in the figures. It is assumed that facility noise effects on transition are minimal in these data because the surface OML roughness features (step or gaps) promotes a “bypass transition” mode (Ref. 15) that is separate from the small disturbance growth modes of conventional stability theory analyses.

General Reynolds Number and Fence/Gap Size Trends

In these line-plots for Reynolds number and roughness pattern effects, the laminar CFD predictions shown allow for baseline assessment of the computational accuracy through comparisons with the smooth-OML and low-Reynolds number, small fence height / gap depth cases for which boundary-layer transition did not occur. In general, good agreement between data and predictions was observed for all laminar cases. However, the turbulent predictions are shown only for illustrative purposes since the fully-turbulent, smooth-wall computations do not account for roughness effects on transition location or heating augmentation.

Reynolds-number and fence/gap roughness effects on transition and heating follow expected trends. As

Reynolds number is increased, the transition onset location moves upstream toward the stagnation point of the model. The transition onset location also moves upstream as fence height or gap depth is increased and the measured rough-wall turbulent heating levels grow increasingly greater than the predicted smooth-wall turbulent heating levels. The data also show that for equivalent fence height and gap depth values, fences produce much greater heating augmentation and promote transition much earlier than gaps.

Transition Onset Correlation

In previous roughness studies (e.g., Refs. 1–5), empirical transition correlations were developed to model the influence of different roughness types (hexcomb patterns and distributed sand-grain) on boundary-layer transition. Such correlations were suitable because of the continuous and isotropic influence of these roughness types on transition. In both the hexcomb and sand-grain roughness studies, the elements were tightly-packed and covered the entire model surface – thus boundary-layer disturbances travelling along a streamline were continuously reinforced without any smooth intervals between elements that would allow the disturbances to dissipate. And the roughness influence on transition showed no directional dependency with respect to the relative orientation of the elements to the streamlines crossing them.

In contrast, for the current fence/gap roughness study, the effects are both discontinuous and anisotropic. The ribs and spars of the fence/gap roughness patterns are (relatively) widely spaced, thus there is some streamline running length downstream of each element over which boundary-layer disturbances can dissipate (partially or fully depending on the feature dimension and flow conditions) before encountering the next element. And the influence of each element on transition appears to be dependent on the relative orientation of the element toward the streamline. Additionally, different streamlines can cross both single fence/gap elements and “T-junctions” where the streamline encounters a junction between a circumferential rib and a radial spar.

It appears unlikely that a universal transition correlation can be developed for fence/gap roughness, as such a correlation would need to include not just the local boundary-layer conditions, but the individual element physical dimensions, the spacing between elements, and the orientation of the element with respect to the streamline, as well as whether the element is a single rib/spar or a T-junction. A limited empirical correlation could possibly be developed from these data for a specific subset of variables, for instance at each element along the centerline of a model, where the streamline would only pass over single fence/gap ribs orientated normal to the streamline direction. However, the application of such a correlation would be limited only to very similar vehicle geometries and fence/gap patterns. Such an exercise is deferred pending a future mission/geometry specific requirement.

Fence/Gap Heating Augmentation

In this report, analysis of the heating augmentation due to the fences and gaps is limited to the expected observation that heating levels increase with fence height or gap depth and fence/gap width and that the effects of fences are greater than that of gaps. This limitation is due to the complexities of the problem and the intent of quickly releasing this data set as a basis for further analysis. For any given fence/gap location and orientation and Reynolds number, the heating augmentation with respect to smooth-wall laminar or turbulent predictions can be determined through reference to the data and figures presented herein. However, the development of engineering correlations or numerical models for simulation of these data would depend on not just modeling the effects of the fences or gaps on the flow field and surface heating, but also modeling their effects on transition onset. That is, it is not possible to accurately predict turbulent heating augmentation without first developing a transition model to predict the influence of each fence or

gap. Computational model development is beyond the scope of this study, but the data presented herein would be valuable for such activities.

Summary

The effects of fences or gaps produced by differential ablation of TPS blocks and gap fillers on boundary-layer transition and turbulent heating have been investigated through hypersonic wind tunnel testing of two representative entry vehicle geometry models with generic block TPS layouts and a wide range of fence heights and gap depths. Surface heating and boundary-layer transition onset data were obtained at Mach 6 over a range of free stream Reynolds numbers sufficient to produce laminar, transitional and turbulent flow, depending on fence/gap dimensions. Heating distributions have been provided in the form of both streamline plots and global surface heating images. It was found that the effects of boundary-layer transition and heating augmentation were dependent not just on local conditions flow field conditions, but on the orientation and spacing of the fence/gap elements.

References

1. Hollis, B. R. and Hollingsworth, K. E., "Experimental Investigation of Distributed Sand-Grain Roughness Effects on Transition Onset and Turbulent Heating Augmentation at Mach 6," NASA/TM-2022-0005643, April 2022.
2. Hollis, B. R., "Hexcomb-Pattern Roughness Effects on Blunt-Body Transition and Heating," *Journal of Spacecraft and Rockets*, Vol. 58, No. 6, November-December 2021, pp. 1612-1635.
3. Hollis, B. R., "Experimental Investigation of Hexcomb-Pattern Roughness Effects on Transition Onset and Turbulent Heating Augmentation at Mach 6," NASA/TM-2019-220424, November 2019.
4. Hollis, B. R., "Correlation of Recent and Historical Hemispherical Nose Tip Distributed Roughness Transition Data," *Journal of Spacecraft and Rockets*, Vol. 56, No. 5, May-June 2019, pp. 664-686.
5. Hollis, B. R., "Experimental Investigation of Roughness Effects on Transition Onset and Turbulent Heating Augmentation at Mach 6 and Mach 10," NASA/TM-2017-219613, May 2017.
6. Buck, G. M., "Rapid Model Fabrication and Testing for Aerospace Vehicles," AIAA Paper 2000-0826, 38th AIAA Aerospace Sciences Meeting and Exhibit, Reno, NV, January 10-13, 2000.
7. Berger, K., Rufer, S., Hollingsworth, K. and Wright, S., "NASA Langley Aerothermodynamic Laboratory: Hypersonic Testing Capabilities," AIAA Paper 2015-1337, 53rd AIAA Aerospace Sciences Meeting, Kissimmee, FL, January 5-9, 2015.
8. Hollis, B. R., Berger, K. T., Berry, S. A., Brauckmann, G. J., et al, "Entry, Descent, and Landing Aerothermodynamics: NASA Langley Experimental Capabilities and Contributions," AIAA Paper 2014-1154, AIAA 52nd Aerospace Science Meeting, National Harbor, MD, January 13-17, 2014.
9. Fay, J. A., and Riddell, F. R., "Theory of Stagnation Point Heat Transfer in Dissociated Air," *Journal of Aeronautical Sciences*, Vol. 25, No. 2., February 1958, pp. 73-85.
10. Buck, G. M., "Surface Temperature/Heat Transfer Measurement Using a Quantitative Phosphor Thermography System," AIAA Paper 91-0064, 29th Aerospace Sciences Meeting, Reno, NV, January 7-10, 1991.
11. Merski, N. R., "Global Aeroheating Wind-Tunnel Measurements Using Improved Two-Color Phosphor Thermography Methods," *Journal of Spacecraft and Rockets*, Vol. 36, No. 2, March-April 1999, pp. 160-170.

12. Mason, M. L. and Rufer, S. J., "Imaging for Hypersonic Experimental Aeroheating Testing (IHEAT) version 4.0: User Manual," NASA/TM-2018-220113, November 2018.
13. Gnoffo, P. A., "An Upwind-Biased, Point-Implicit Algorithm for Viscous, Compressible Perfect-Gas Flows," NASA TP-2953, February 1990.
14. Mazaheri, A., Gnoffo, P. A., Johnston, C. O., and Kleb, B., "LAURA User's Manual: 5.5-65135," NASA TM-2013-217800, February 2013.
15. Morkovin, M. V., "Critical Evaluation of Transition from Laminar to Turbulent Shear Layers with Emphasis on Hypersonically Travelling Blunt Bodies", Air Force Flight Dynamics Laboratory, AFFDL-TR-68-1949, March 1969.

Table 1. Wind tunnel model geometry parameters.

Model geometry	Model radius, R		Nose radius, R_n		Shoulder radius, R_s		Nose included angle, β	R_n/R	R_s/R
	in.	m	in.	m	in.	m	deg		
Spherical-cap	3.000	0.0762	7.200	0.1829	0.3000	0.00762	23.04	2.4	0.100
Sphere-cone	3.000	0.0762	1.500	0.0371	0.1500	0.00381	20.00	0.5	0.050

Table 2. Wind tunnel model fence / gap location parameters.

Fence / Gap rib #	Sphere-cone rib radius		Spherical-cap rib radius		Spar separation
	in.	m	in.	m	deg
1	0.5130	0.01303	0.5636	0.01432	60
2	1.1010	0.02797	1.1272	0.02863	45
3	1.7072	0.04336	1.6907	0.04294	30
4	2.3042	0.05853	2.2543	0.05726	22.5
5	2.9013	0.07369	2.8179	0.07157	N/A

Table 3. Wind tunnel model fence / gap geometry parameters.

Model ID	Fence height / Gap depth H_F/H_G		Fence / Gap half-width W_F/W_G		Fence / Gap fillet radius R_F/R_G		Fence / Gap turning angle β_F/β_G
	in.	m	in.	m	in.	m	deg
24-fence / 24-gap	0.024	6.096E-04	0.024	6.096E-04	0.00600	1.524E-04	75
12-fence / 12-gap	0.012	3.048E-04	0.012	3.048E-04	0.00300	7.620E-05	75
6-fence / 6-gap	0.006	1.524E-04	0.006	1.524E-04	0.00150	3.810E-05	75
3-fence / 3-gap	0.003	7.620E-05	0.003	7.620E-05	0.00075	1.905E-05	75

Table 4. Averaged Nominal Conditions for 20-Inch Mach 6 Air Tunnel Test 7036.

Re_∞ (1/ft)	Re_∞ (1/m)	M_∞	T_∞ (K)	ρ_∞ (kg/m ³)	U_∞ (m/s)	ΔH (J/kg)	h_{FR} (kg/m ² -s) sphere-cone	
2.066E+06	6.777E+06	5.97	63.13	3.2331E-02	949.76	2.135E+05	2.536E-01	
2.980E+06	9.777E+06	6.00	63.44	4.6557E-02	956.32	2.200E+05	3.072E-01	
4.963E+06	1.628E+07	6.03	63.72	7.7376E-02	962.73	2.264E+05	3.992E-01	
6.487E+06	2.128E+07	6.04	63.51	1.0086E-01	962.17	2.257E+05	4.555E-01	
7.206E+06	2.364E+07	6.05	63.49	1.1194E-01	962.47	2.259E+05	4.800E-01	
8.162E+06	2.678E+07	6.03	59.15	1.2272E-01	924.17	1.852E+05	4.781E-01	

Table 5. Averaged Nominal Conditions for 20-Inch Mach 6 Air Tunnel Test 7057.

Re_∞ (1/ft)	Re_∞ (1/m)	M_∞	T_∞ (K)	ρ_∞ (kg/m ³)	U_∞ (m/s)	ΔH (J/kg)	h_{FR} (kg/m ² -s) spherical-cap	
2.034E+06	6.673E+06	5.97	62.74	3.172E-02	947.14	2.106E+05	1.144E-01	
3.004E+06	9.856E+06	6.00	63.08	4.677E-02	953.95	2.174E+05	1.401E-01	
4.969E+06	1.630E+07	6.03	63.72	7.744E-02	963.06	2.268E+05	1.824E-01	
6.491E+06	2.130E+07	6.04	63.44	1.008E-01	962.08	2.255E+05	2.078E-01	
7.192E+06	2.360E+07	6.05	63.47	1.117E-01	962.85	2.263E+05	2.189E-01	
8.110E+06	2.661E+07	6.04	59.27	1.220E-01	925.72	1.868E+05	2.180E-01	

Table 6. CFD Conditions for 20-Inch Mach 6 Air Tunnel Tests 7036 and 7057.

Re_∞ (1/ft)	Re_∞ (1/m)	M_∞	T_∞ (K)	ρ_∞ (kg/m ³)	U_∞ (m/s)	ΔH (J/kg)	h_{FR} (kg/m ² -s)	
							sphere-cone	spherical-cap
2.099E+06	6.885E+06	5.96	61.88	3.253E-02	939.54	2.0257E+05	2.513E-01	1.147E-01
3.034E+06	9.954E+06	5.99	62.53	4.708E-02	948.65	2.1182E+05	3.059E-01	1.396E-01
5.042E+06	1.654E+07	6.02	63.24	7.843E-02	957.52	2.2096E+05	3.993E-01	1.822E-01
6.631E+06	2.176E+07	6.04	62.57	1.023E-01	954.55	2.1741E+05	4.543E-01	2.074E-01
7.455E+06	2.446E+07	6.04	62.52	1.150E-01	953.64	2.1646E+05	4.811E-01	2.196E-01
8.335E+06	2.734E+07	6.03	58.59	1.249E-01	918.19	1.7913E+05	4.785E-01	2.184E-01

Table 7. 20-Inch Mach 6 Air Tunnel Test 7036 run matrix.

Run	Geometry	Fence / Gap	α_∞ (deg)	Re_∞ (1/ft)	M_∞	T_∞ (K)	ρ_∞ (kg/m ³)	U_∞ (m/s)	ΔH (J/kg)	h_{FR} (kg/m ² -s)	$T_{w,avg}$ (K)
50	sphere-cone	Smooth	16	2.02E+06	5.96	62.9	3.161E-02	948.0	2.116E+05	2.505E-01	331
51	sphere-cone	Smooth	16	2.96E+06	6.00	63.4	4.629E-02	956.1	2.198E+05	3.062E-01	342
52	sphere-cone	Smooth	16	4.96E+06	6.03	63.7	7.733E-02	962.4	2.262E+05	3.990E-01	359
53	sphere-cone	Smooth	16	6.47E+06	6.04	63.6	1.007E-01	962.7	2.262E+05	4.554E-01	371
54	sphere-cone	Smooth	16	7.23E+06	6.05	63.4	1.122E-01	961.5	2.248E+05	4.799E-01	378
55	sphere-cone	Smooth	16	8.13E+06	6.03	59.2	1.224E-01	924.8	1.859E+05	4.778E-01	368
26	sphere-cone	3-mil gap	16	2.02E+06	5.97	63.1	3.166E-02	949.2	2.130E+05	2.511E-01	332
27	sphere-cone	3-mil gap	16	2.98E+06	6.00	63.4	4.655E-02	955.7	2.193E+05	3.069E-01	343
28	sphere-cone	3-mil gap	16	4.96E+06	6.03	63.7	7.732E-02	962.3	2.260E+05	3.989E-01	359
29	sphere-cone	3-mil gap	16	6.49E+06	6.04	63.7	1.011E-01	963.6	2.272E+05	4.568E-01	368
30	sphere-cone	3-mil gap	16	7.24E+06	6.05	63.4	1.124E-01	961.5	2.249E+05	4.804E-01	374
31	sphere-cone	3-mil gap	16	8.26E+06	6.03	58.7	1.238E-01	920.3	1.812E+05	4.776E-01	359
62	sphere-cone	6-mil gap	16	2.02E+06	5.97	63.1	3.159E-02	949.6	2.134E+05	2.509E-01	331
63	sphere-cone	6-mil gap	16	2.99E+06	6.00	63.4	4.668E-02	955.7	2.194E+05	3.074E-01	342
64	sphere-cone	6-mil gap	16	4.94E+06	6.03	63.9	7.716E-02	963.9	2.277E+05	3.993E-01	359
65	sphere-cone	6-mil gap	16	6.47E+06	6.04	63.5	1.006E-01	962.4	2.260E+05	4.549E-01	370
66	sphere-cone	6-mil gap	16	7.23E+06	6.05	63.4	1.123E-01	961.4	2.248E+05	4.800E-01	376
67	sphere-cone	6-mil gap	16	8.23E+06	6.03	59.0	1.236E-01	922.9	1.839E+05	4.789E-01	363
56	sphere-cone	12-mil gap	16	2.03E+06	5.97	63.0	3.169E-02	948.4	2.120E+05	2.509E-01	334
57	sphere-cone	12-mil gap	16	2.98E+06	6.00	63.3	4.656E-02	955.3	2.189E+05	3.068E-01	345
58	sphere-cone	12-mil gap	16	4.94E+06	6.03	63.8	7.704E-02	963.1	2.269E+05	3.986E-01	363
59	sphere-cone	12-mil gap	16	6.55E+06	6.04	63.2	1.015E-01	959.2	2.225E+05	4.552E-01	385
60	sphere-cone	12-mil gap	16	7.22E+06	6.05	63.5	1.121E-01	962.3	2.257E+05	4.802E-01	392
61	sphere-cone	12-mil gap	16	8.07E+06	6.03	59.6	1.217E-01	928.0	1.892E+05	4.785E-01	380
6	sphere-cone	24-mil gap	16	2.03E+06	5.97	63.1	3.173E-02	949.6	2.133E+05	2.514E-01	338
2	sphere-cone	24-mil gap	16	2.97E+06	5.99	63.7	4.644E-02	957.7	2.216E+05	3.074E-01	346
1	sphere-cone	24-mil gap	16	4.92E+06	6.05	63.5	7.636E-02	964.6	2.281E+05	3.975E-01	369
3	sphere-cone	24-mil gap	16	6.47E+06	6.04	63.7	1.008E-01	963.0	2.266E+05	4.558E-01	390
4	sphere-cone	24-mil gap	16	7.22E+06	6.05	63.4	1.121E-01	961.6	2.250E+05	4.798E-01	398
5	sphere-cone	24-mil gap	16	8.13E+06	6.03	59.3	1.223E-01	925.4	1.865E+05	4.781E-01	385
20	sphere-cone	3-mil fence	16	1.99E+06	5.97	63.4	3.128E-02	951.9	2.159E+05	2.504E-01	334
21	sphere-cone	3-mil fence	16	2.98E+06	6.00	63.5	4.653E-02	957.0	2.208E+05	3.074E-01	345
22	sphere-cone	3-mil fence	16	4.94E+06	6.03	63.9	7.717E-02	963.9	2.278E+05	3.993E-01	362
23	sphere-cone	3-mil fence	16	6.51E+06	6.04	63.4	1.011E-01	961.6	2.251E+05	4.557E-01	378
24	sphere-cone	3-mil fence	16	7.21E+06	6.05	63.5	1.121E-01	962.9	2.264E+05	4.805E-01	390
25	sphere-cone	3-mil fence	16	8.16E+06	6.03	59.1	1.228E-01	924.0	1.851E+05	4.780E-01	377
46	sphere-cone	6-mil fence	16	2.03E+06	5.97	62.9	3.175E-02	947.4	2.110E+05	2.508E-01	337
45	sphere-cone	6-mil fence	16	3.00E+06	6.00	63.1	4.672E-02	953.9	2.174E+05	3.068E-01	349
44	sphere-cone	6-mil fence	16	4.98E+06	6.03	63.6	7.765E-02	961.7	2.254E+05	3.994E-01	383
47	sphere-cone	6-mil fence	16	6.42E+06	6.04	63.8	1.000E-01	964.4	2.281E+05	4.549E-01	401
48	sphere-cone	6-mil fence	16	7.22E+06	6.05	63.5	1.121E-01	962.2	2.257E+05	4.802E-01	404
49	sphere-cone	6-mil fence	16	8.18E+06	6.03	59.1	1.230E-01	924.1	1.852E+05	4.785E-01	389

Table 7 continued.

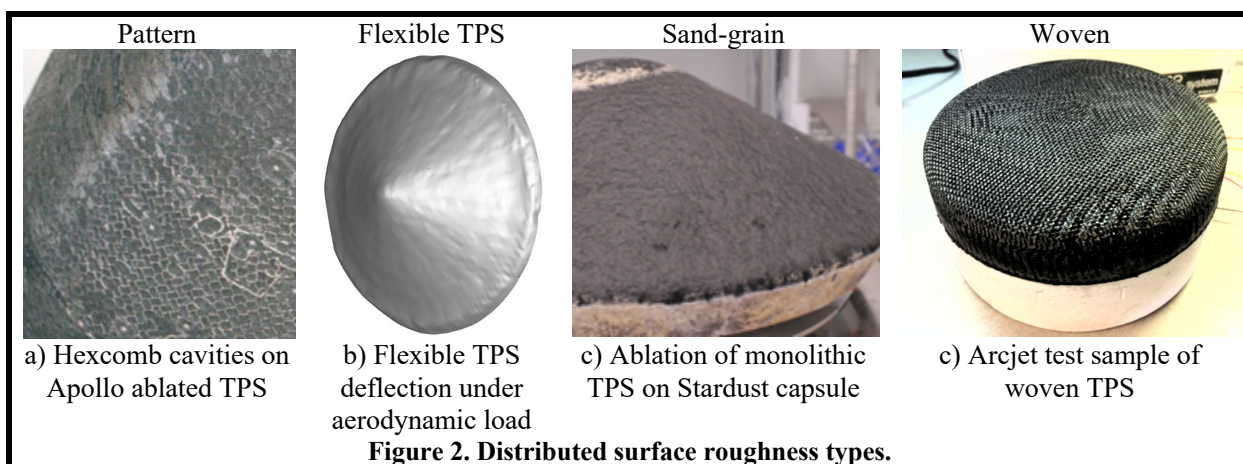
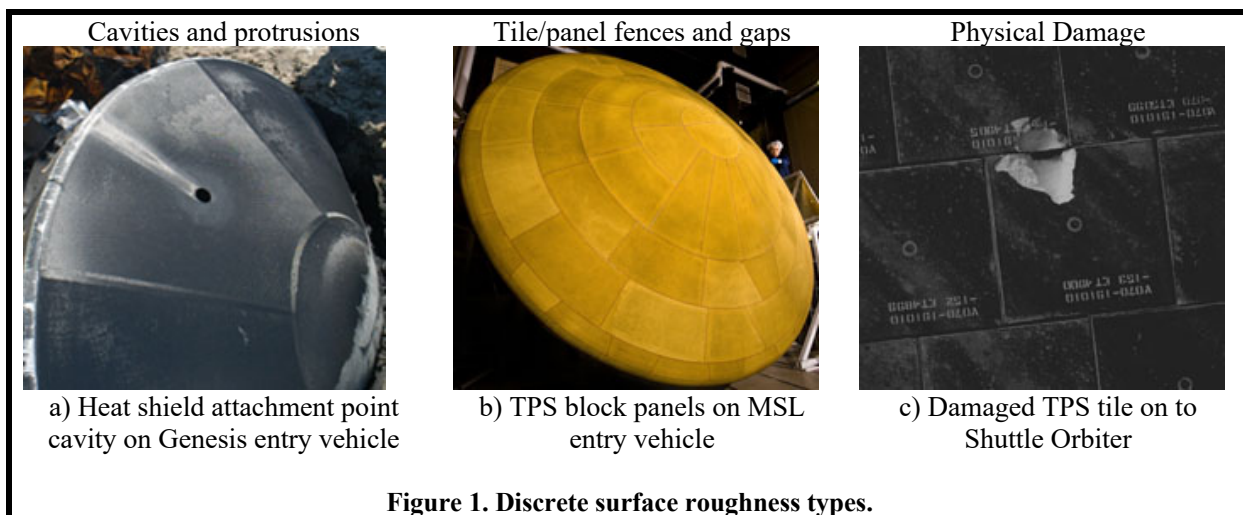
Run	Geometry	Fence / Gap	α_∞ (deg)	Re_∞ (1/ft)	M_∞	T_∞ (K)	ρ_∞ (kg/m ³)	U_∞ (m/s)	ΔH (J/kg)	h_{FR} (kg/m ² -s)	$T_{w,avg}$ (K)
68	sphere-cone	12-mil fence	16	2.02E+06	5.97	63.2	3.164E-02	950.4	2.142E+05	2.514E-01	346
69	sphere-cone	12-mil fence	16	2.98E+06	6.00	63.4	4.655E-02	956.1	2.198E+05	3.071E-01	367
70	sphere-cone	12-mil fence	16	4.99E+06	6.03	63.5	7.770E-02	961.0	2.246E+05	3.992E-01	395
71	sphere-cone	12-mil fence	16	6.50E+06	6.04	63.4	1.009E-01	961.4	2.248E+05	4.551E-01	408
72	sphere-cone	12-mil fence	16	7.13E+06	6.05	63.8	1.110E-01	965.1	2.288E+05	4.796E-01	411
73	sphere-cone	12-mil fence	16	8.21E+06	6.03	59.0	1.234E-01	922.7	1.837E+05	4.784E-01	16
13	sphere-cone	24-mil fence	16	2.02E+06	5.97	63.0	3.160E-02	948.8	2.125E+05	2.507E-01	2.02E+06
14	sphere-cone	24-mil fence	16	2.98E+06	6.00	63.5	4.656E-02	957.2	2.210E+05	3.076E-01	2.98E+06
15	sphere-cone	24-mil fence	16	5.00E+06	6.03	63.5	7.776E-02	960.3	2.238E+05	3.990E-01	5.00E+06
16	sphere-cone	24-mil fence	16	6.55E+06	6.04	63.2	1.017E-01	959.8	2.231E+05	4.559E-01	6.55E+06
17	sphere-cone	24-mil fence	16	7.23E+06	6.05	63.4	1.123E-01	961.5	2.249E+05	4.802E-01	7.23E+06
18	sphere-cone	24-mil fence	16	8.13E+06	6.03	59.2	1.223E-01	925.0	1.861E+05	4.778E-01	8.13E+06

Table 8. 20-Inch Mach 6 Air Tunnel Test 7057 run matrix.

Run	Geometry	Fence / Gap	α_∞ (deg)	Re_∞ (1/ft)	M_∞	T_∞ (K)	ρ_∞ (kg/m ³)	U_∞ (m/s)	ΔH (J/kg)	h_{FR} (kg/m ² -s)	$T_{w,avg}$ (K)
7	Spherical-cap	smooth	28	2.04E+06	5.97	62.6	3.178E-02	946.0	2.094E+05	9.900E-02	332
8	Spherical-cap	smooth	28	3.01E+06	6.00	63.0	4.676E-02	953.4	2.168E+05	1.212E-01	342
9	Spherical-cap	smooth	28	5.03E+06	6.03	63.4	7.821E-02	960.8	2.243E+05	1.583E-01	357
10	Spherical-cap	smooth	28	6.52E+06	6.04	63.3	1.011E-01	960.6	2.239E+05	1.799E-01	366
11	Spherical-cap	smooth	28	7.28E+06	6.05	63.0	1.126E-01	959.1	2.223E+05	2.188E-01	364
12	Spherical-cap	smooth	28	8.02E+06	6.04	59.5	1.208E-01	928.0	1.892E+05	2.176E-01	356
158	Spherical-cap	3-mil gap	28	2.02E+06	5.97	62.9	3.148E-02	948.2	2.118E+05	1.141E-01	331
159	Spherical-cap	3-mil gap	28	3.01E+06	6.00	63.0	4.683E-02	953.4	2.168E+05	1.401E-01	341
162	Spherical-cap	3-mil gap	28	4.93E+06	6.03	64.0	7.704E-02	965.7	2.296E+05	1.825E-01	358
163	Spherical-cap	3-mil gap	28	6.50E+06	6.04	63.3	1.008E-01	960.9	2.243E+05	2.075E-01	382
164	Spherical-cap	3-mil gap	28	7.21E+06	6.05	63.2	1.118E-01	960.9	2.242E+05	2.185E-01	396
165	Spherical-cap	3-mil gap	28	8.14E+06	6.04	59.1	1.223E-01	924.6	1.856E+05	2.179E-01	383
61	Spherical-cap	6-mil gap	28	2.04E+06	5.97	62.8	3.176E-02	947.4	2.109E+05	1.145E-01	330
62	Spherical-cap	6-mil gap	28	3.01E+06	6.00	63.0	4.678E-02	953.8	2.172E+05	1.401E-01	334
63	Spherical-cap	6-mil gap	28	4.98E+06	6.03	63.8	7.765E-02	964.1	2.279E+05	1.829E-01	352
64	Spherical-cap	6-mil gap	28	6.43E+06	6.05	63.8	1.001E-01	965.3	2.290E+05	2.080E-01	362
65	Spherical-cap	6-mil gap	28	7.15E+06	6.05	63.7	1.112E-01	964.7	2.283E+05	2.190E-01	367
66	Spherical-cap	6-mil gap	28	8.03E+06	6.04	59.7	1.212E-01	929.7	1.909E+05	2.184E-01	357
85	Spherical-cap	12-mil gap	28	2.03E+06	5.97	62.6	3.163E-02	946.0	2.094E+05	1.141E-01	332
86	Spherical-cap	12-mil gap	28	3.01E+06	6.00	62.9	4.673E-02	952.8	2.161E+05	1.398E-01	343
87	Spherical-cap	12-mil gap	28	5.03E+06	6.03	63.2	7.809E-02	958.5	2.218E+05	1.821E-01	352
88	Spherical-cap	12-mil gap	28	6.47E+06	6.04	63.6	1.007E-01	963.8	2.273E+05	2.081E-01	380
89	Spherical-cap	12-mil gap	28	7.15E+06	6.05	63.8	1.112E-01	965.5	2.291E+05	2.192E-01	395
90	Spherical-cap	12-mil gap	28	8.09E+06	6.04	59.4	1.218E-01	927.1	1.883E+05	2.182E-01	381
91	Spherical-cap	24-mil gap	28	2.04E+06	5.97	62.8	3.177E-02	947.4	2.109E+05	1.145E-01	330
92	Spherical-cap	24-mil gap	28	3.01E+06	6.00	63.1	4.680E-02	954.4	2.179E+05	1.402E-01	341
93	Spherical-cap	24-mil gap	28	4.95E+06	6.03	63.8	7.722E-02	963.4	2.272E+05	1.822E-01	375
94	Spherical-cap	24-mil gap	28	6.51E+06	6.04	63.4	1.011E-01	961.6	2.250E+05	2.080E-01	392
95	Spherical-cap	24-mil gap	28	7.19E+06	6.05	63.5	1.117E-01	963.2	2.267E+05	2.191E-01	400
96	Spherical-cap	24-mil gap	28	8.10E+06	6.04	59.3	1.219E-01	926.5	1.876E+05	2.181E-01	384
67	Spherical-cap	3-mil fence	28	2.04E+06	5.97	62.7	3.187E-02	946.6	2.100E+05	1.146E-01	339
68	Spherical-cap	3-mil fence	28	3.01E+06	6.00	63.1	4.687E-02	954.6	2.181E+05	1.404E-01	339
69	Spherical-cap	3-mil fence	28	5.01E+06	6.03	63.6	7.794E-02	962.2	2.259E+05	1.828E-01	357
70	Spherical-cap	3-mil fence	28	6.52E+06	6.04	63.2	1.011E-01	960.2	2.235E+05	2.076E-01	377
71	Spherical-cap	3-mil fence	28	7.22E+06	6.05	63.3	1.120E-01	961.2	2.245E+05	2.188E-01	386
72	Spherical-cap	3-mil fence	28	8.13E+06	6.04	59.2	1.222E-01	925.2	1.863E+05	2.180E-01	374
73	Spherical-cap	6-mil fence	28	2.06E+06	5.97	62.6	3.202E-02	946.2	2.096E+05	1.148E-01	327
74	Spherical-cap	6-mil fence	28	2.99E+06	6.00	63.3	4.657E-02	955.4	2.190E+05	1.401E-01	338
75	Spherical-cap	6-mil fence	28	4.93E+06	6.03	64.1	7.708E-02	966.6	2.306E+05	1.828E-01	364
76	Spherical-cap	6-mil fence	28	6.57E+06	6.04	63.1	1.017E-01	959.1	2.223E+05	2.080E-01	383
77	Spherical-cap	6-mil fence	28	7.18E+06	6.05	63.4	1.115E-01	962.5	2.259E+05	2.187E-01	393
78	Spherical-cap	6-mil fence	28	8.10E+06	6.04	59.3	1.218E-01	925.7	1.868E+05	2.179E-01	381

Table 8 continued.

Run	Geometry	Fence / Gap	α_∞ (deg)	Re_∞ (1/ft)	M_∞	T_∞ (K)	ρ_∞ (kg/m ³)	U_∞ (m/s)	ΔH (J/kg)	h_{FR} (kg/m ² -s)	$T_{w,avg}$ (K)
48	Spherical-cap	12-mil fence	28	2.02E+06	5.97	62.9	3.150E-02	948.6	2.122E+05	1.142E-01	342
49	Spherical-cap	12-mil fence	28	2.99E+06	6.00	63.3	4.671E-02	956.1	2.197E+05	1.404E-01	363
50	Spherical-cap	12-mil fence	28	4.93E+06	6.03	63.8	7.681E-02	963.4	2.272E+05	1.817E-01	392
51	Spherical-cap	12-mil fence	28	6.52E+06	6.04	63.3	1.012E-01	961.2	2.245E+05	2.080E-01	407
52	Spherical-cap	12-mil fence	28	7.27E+06	6.05	63.2	1.126E-01	960.3	2.235E+05	2.191E-01	410
53	Spherical-cap	12-mil fence	28	8.14E+06	6.04	59.2	1.223E-01	925.1	1.861E+05	2.181E-01	392
97	Spherical-cap	24-mil fence	28	2.03E+06	5.97	62.7	3.171E-02	947.2	2.107E+05	1.144E-01	353
98	Spherical-cap	24-mil fence	28	2.98E+06	6.00	63.0	4.638E-02	953.5	2.169E+05	1.394E-01	368
99	Spherical-cap	24-mil fence	28	4.95E+06	6.03	63.7	7.717E-02	963.1	2.268E+05	1.821E-01	397
100	Spherical-cap	24-mil fence	28	6.52E+06	6.04	63.4	1.012E-01	961.8	2.253E+05	2.081E-01	412
101	Spherical-cap	24-mil fence	28	7.12E+06	6.05	63.7	1.108E-01	965.0	2.286E+05	2.187E-01	418
102	Spherical-cap	24-mil fence	28	8.14E+06	6.04	59.2	1.223E-01	924.9	1.859E+05	2.180E-01	398



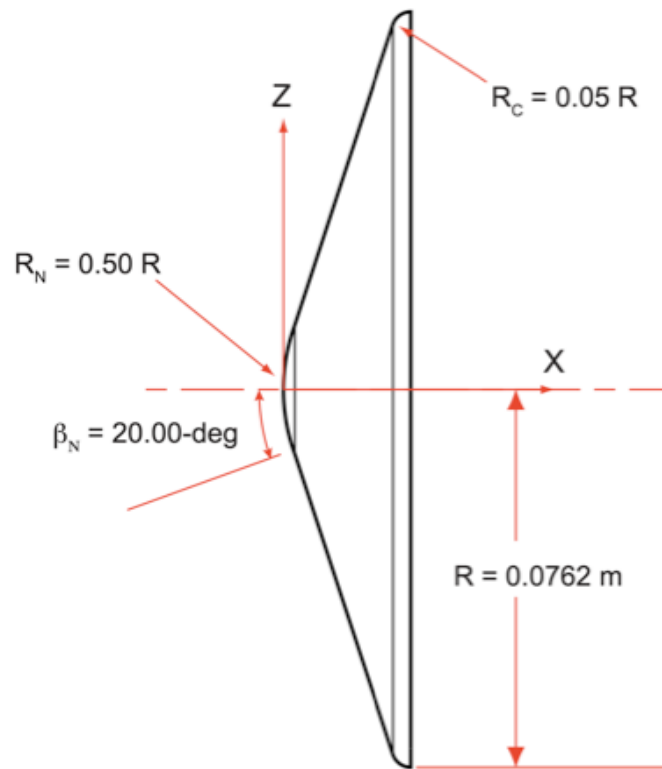


Figure 3. Sphere-cone geometry.

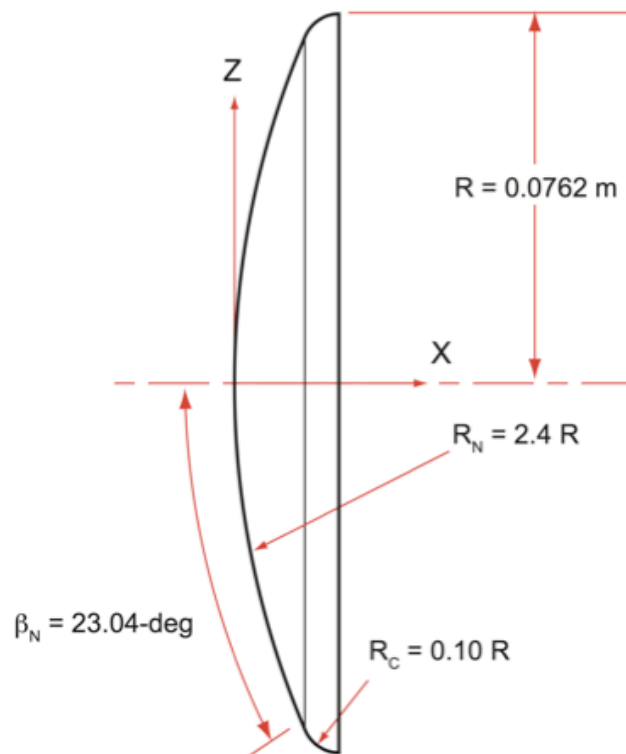


Figure 4. Spherical-cap geometry.

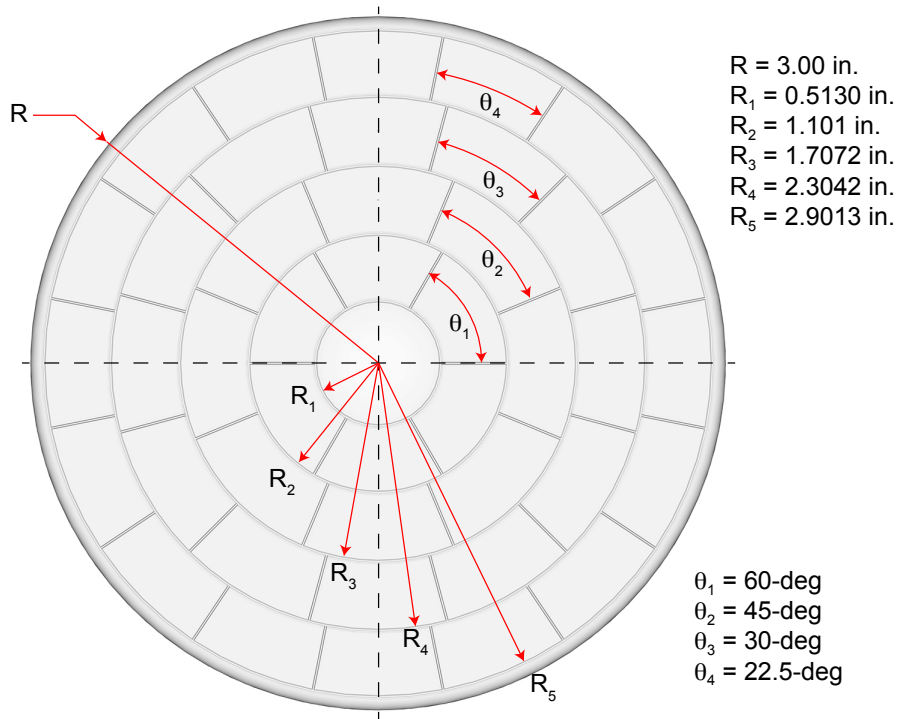


Figure 5. Sphere-cone fence / gap layout.

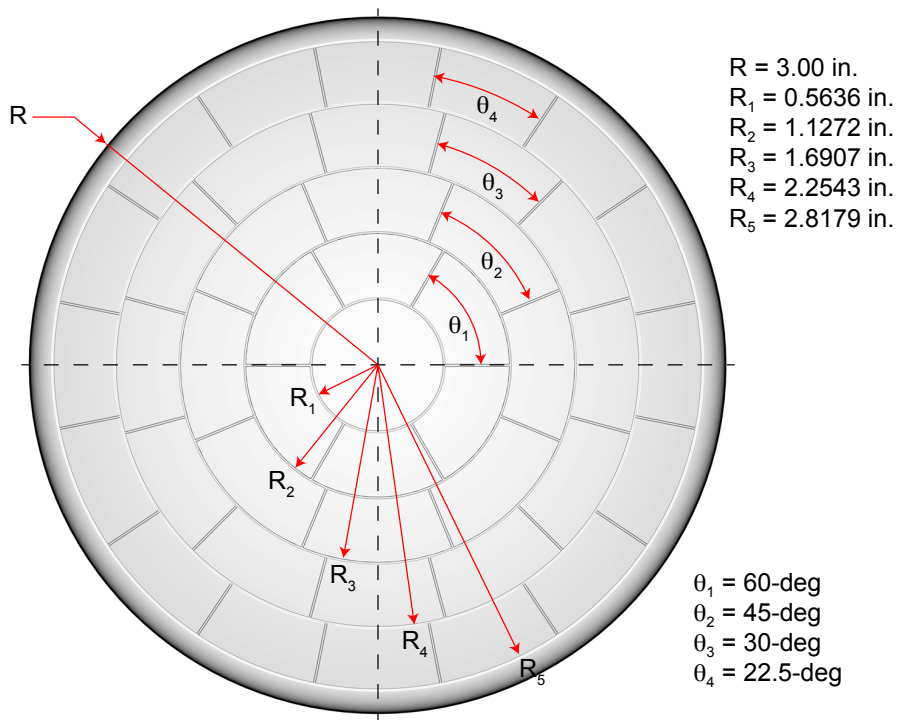
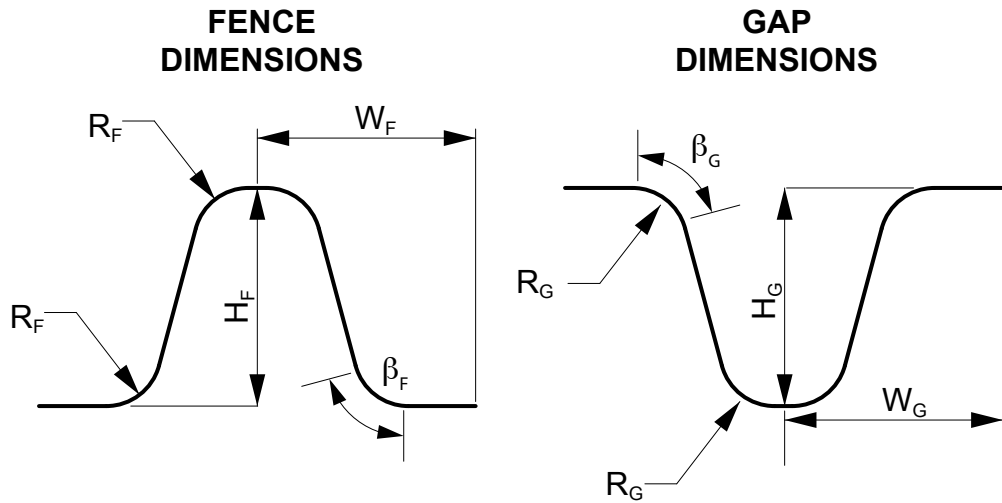


Figure 6. Spherical-cap fence / gap layout.



Model	$H_{F/G}$ (in)	$W_{F/G}$ (in)	$R_{F/G}$ (in)	$\beta_{F/G}$ (deg)
24-Fence/Gap	0.024	0.024	0.00600	75.0
12-Fence/Gap	0.012	0.012	0.00300	75.0
06-Fence/Gap	0.006	0.006	0.00150	75.0
03-Fence/Gap	0.003	0.003	0.00075	75.0

Figure 7. Fence / gap dimensions.

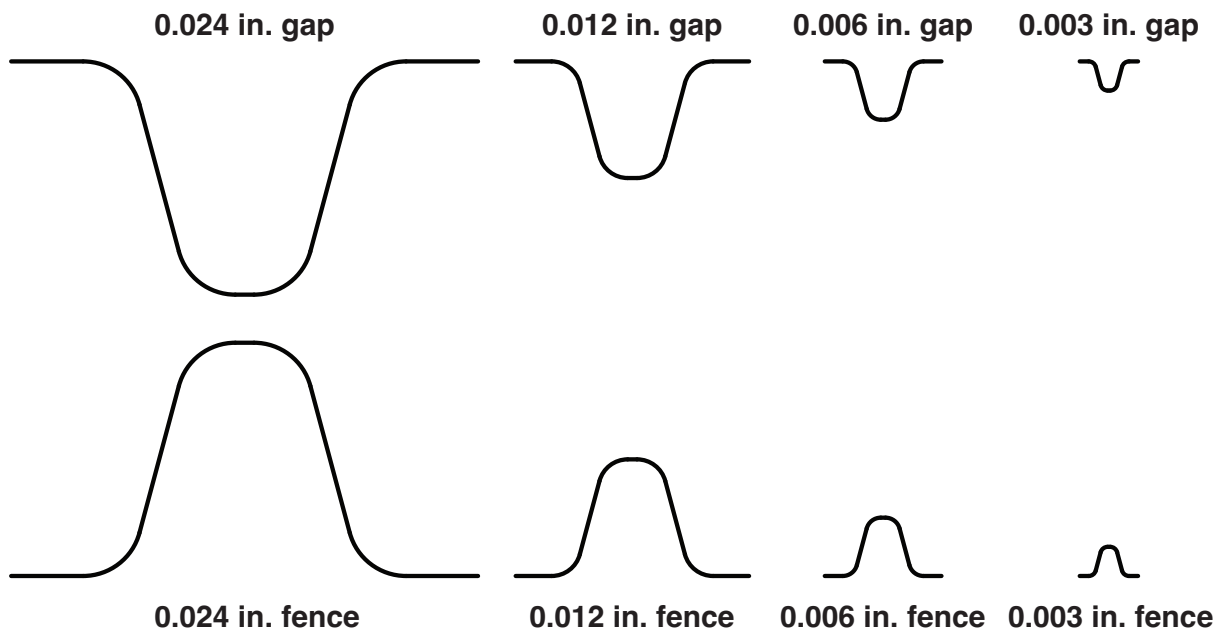


Figure 8. Fence / gap size comparisons.

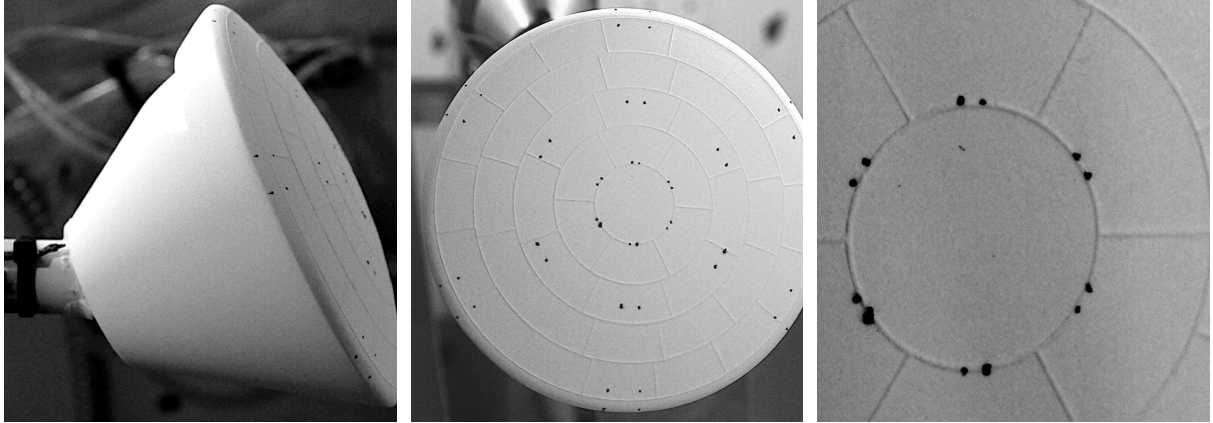


Figure 9. Sample fence model photographs (Spherical-cap, 12-mil fence).

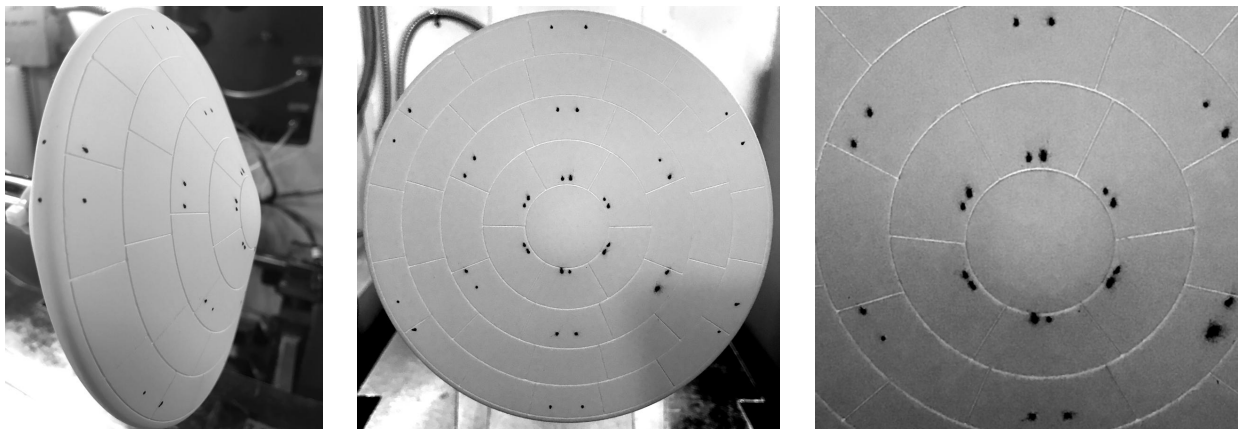
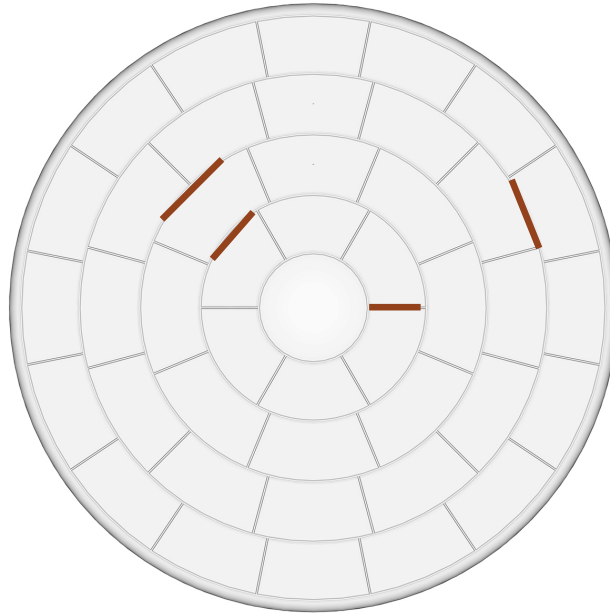
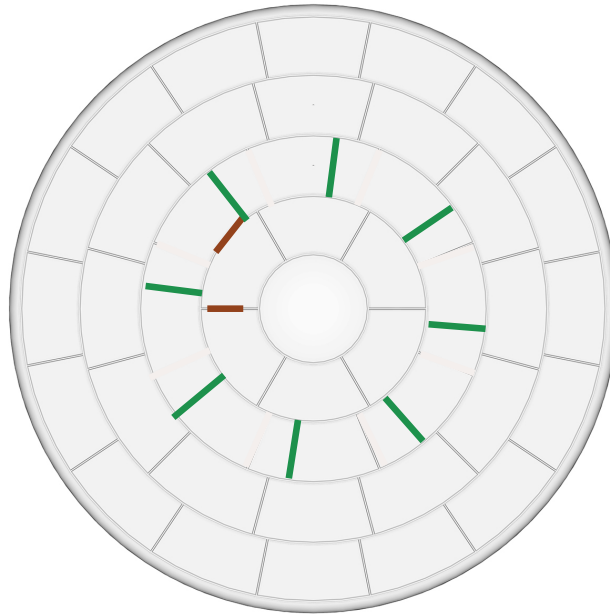


Figure 10. Sample gap model photographs (Sphere-cone, 24-mil gap).

Sphere-cone, 24-fence



Spherical-cap, 24-fence



- Fence element damaged/missing in casting
- Fence element misaligned in CAD

Figure 11. Fence model fabrication errors.

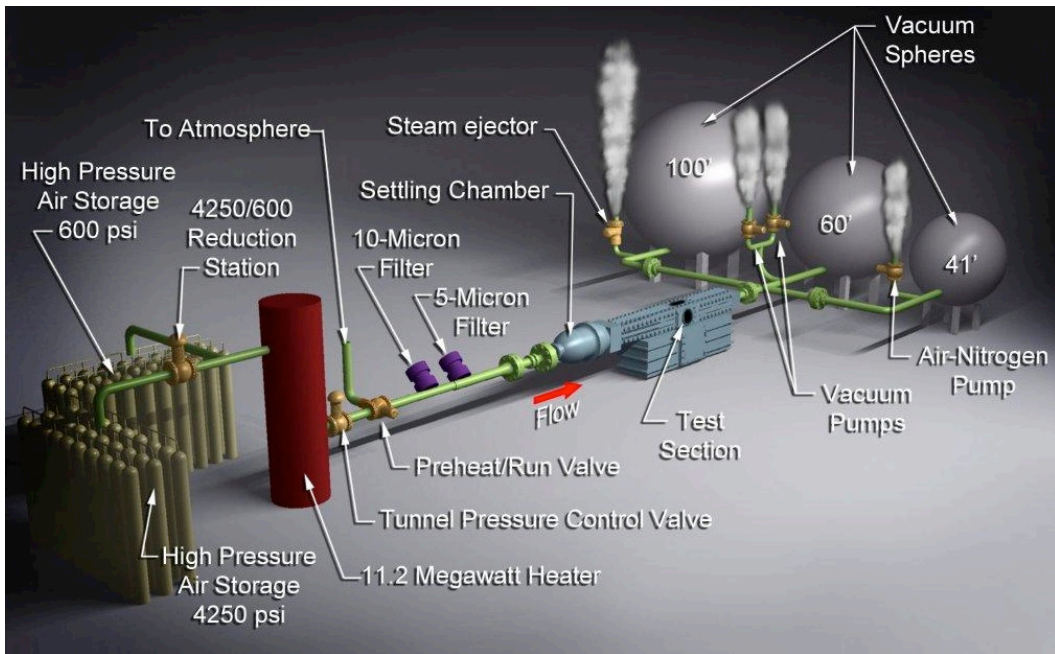


Figure 12. Schematic of Langley Research Center 20-Inch Mach 6 Air Tunnel.



Figure 13. Langley Research Center 20-Inch Mach 6 Air Tunnel test section.

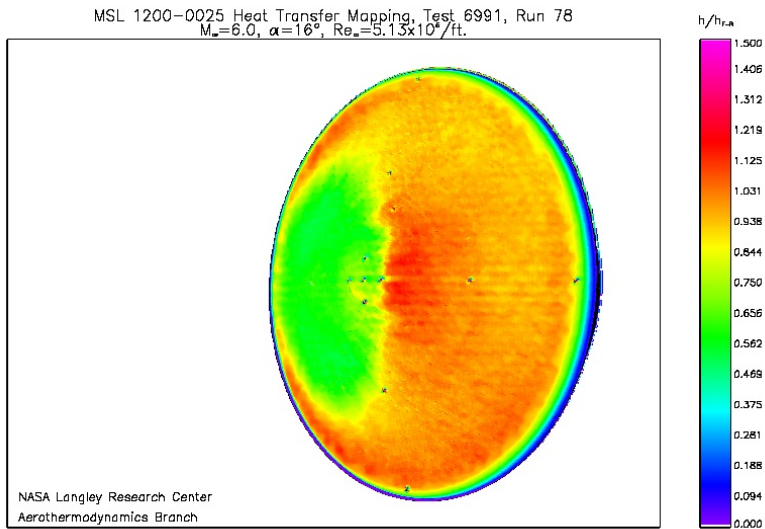


Figure 14. Sample phosphor thermography 2-D image data.

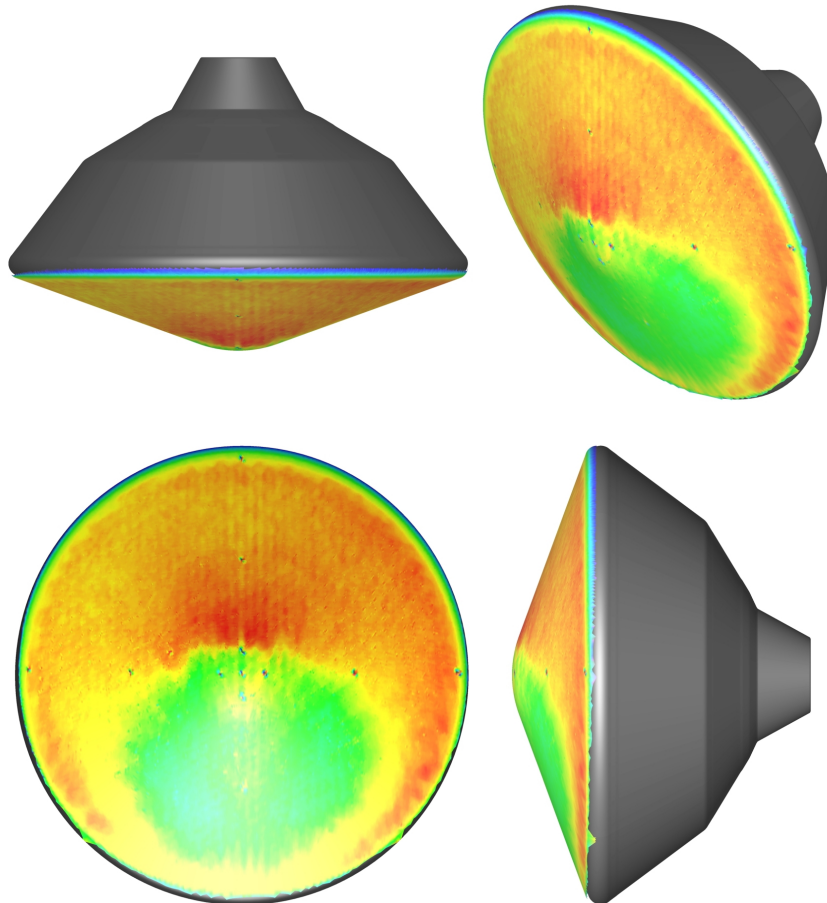


Figure 15. Sample 3-D mapping of phosphor thermography data.

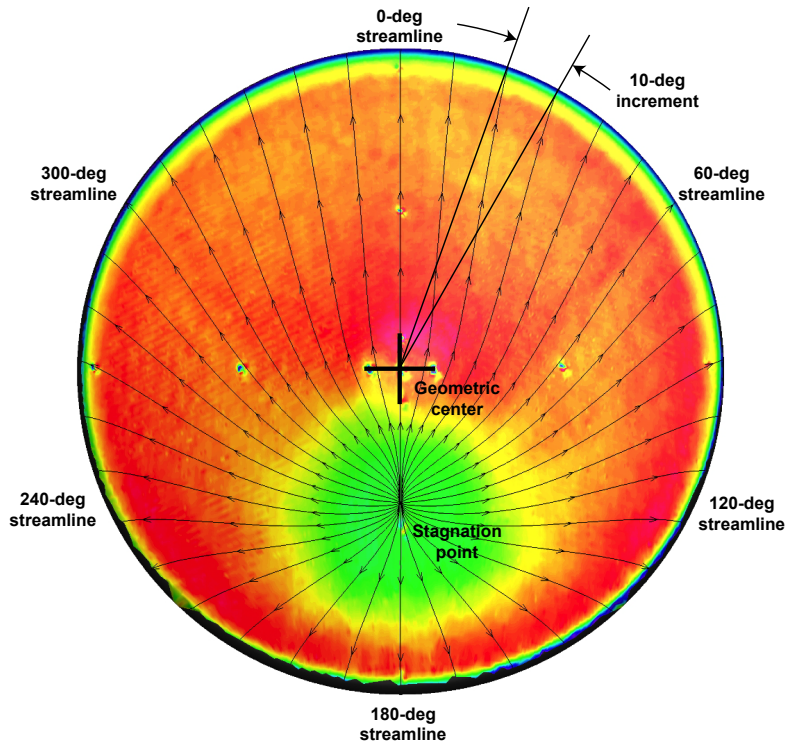


Figure 16. Streamlines for data extraction on sphere-cone geometry.

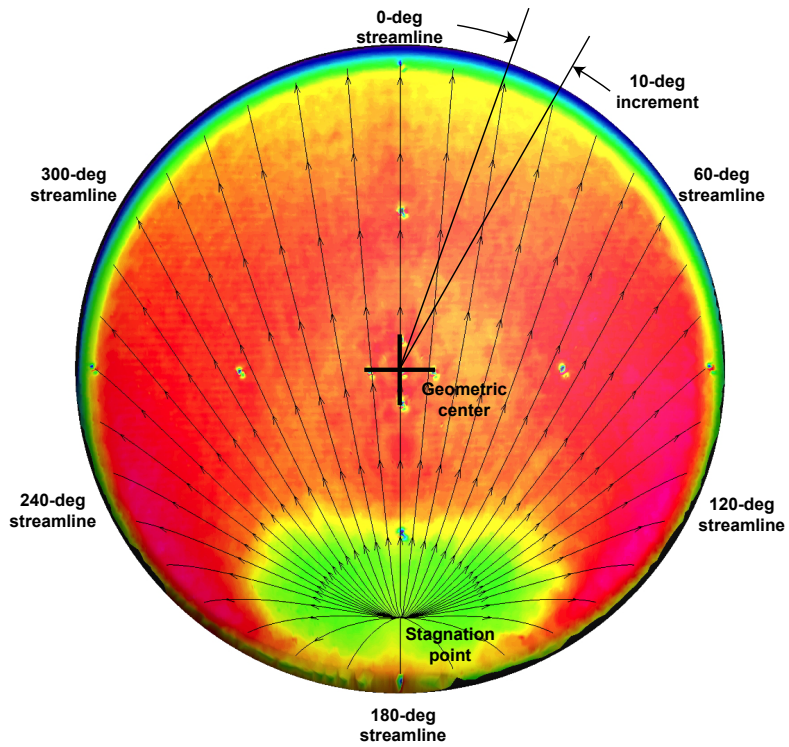


Figure 17. Streamlines for data extraction on spherical-cap geometry.

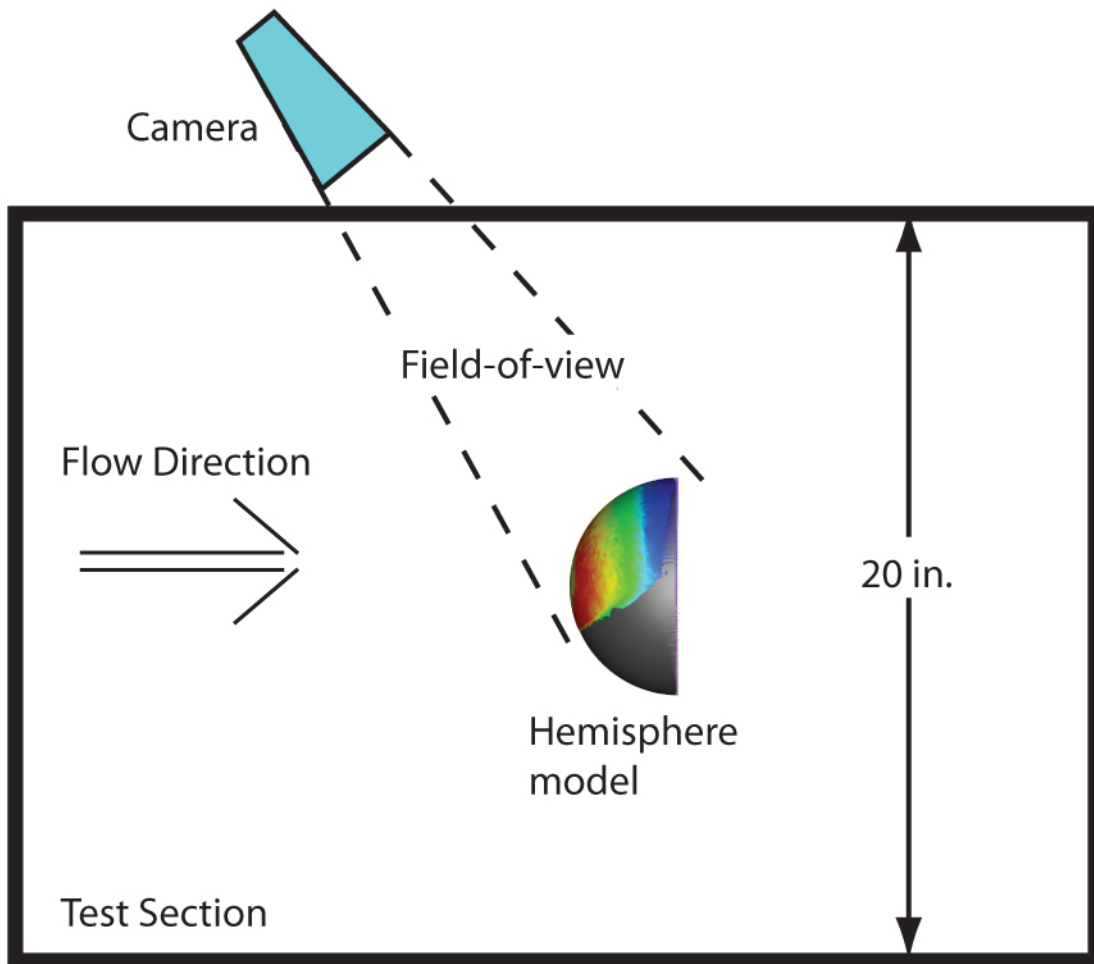


Figure 18. Illustration of camera field-of-view for hemisphere model in 20-Inch Mach 6 Air Tunnel.

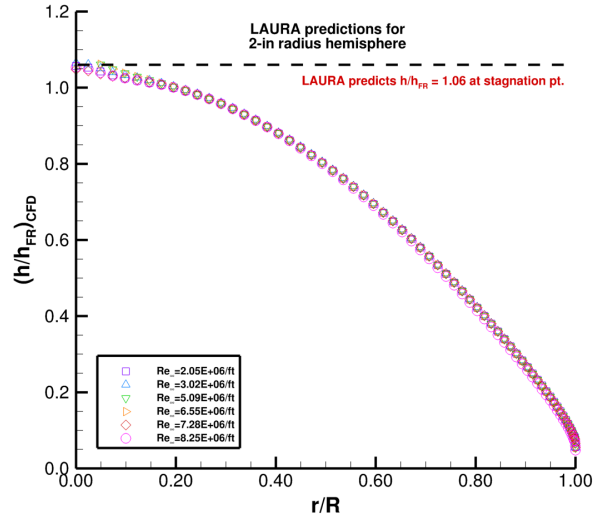


Figure 19. CFD predictions for hemisphere heating at wind tunnel conditions.

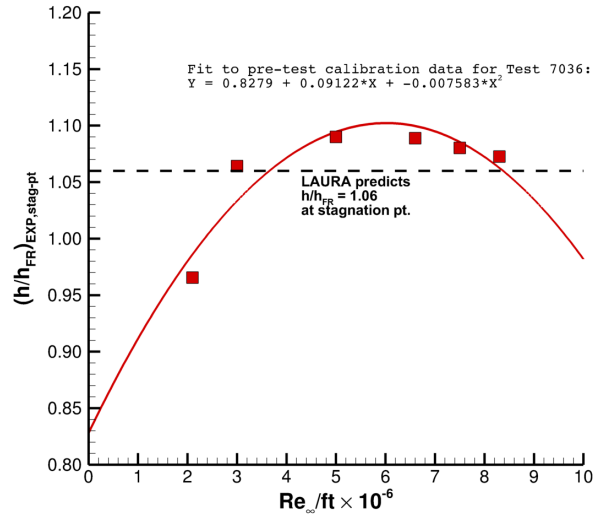


Figure 20. Measured stagnation point heating for pretest calibrations for Test 7036.

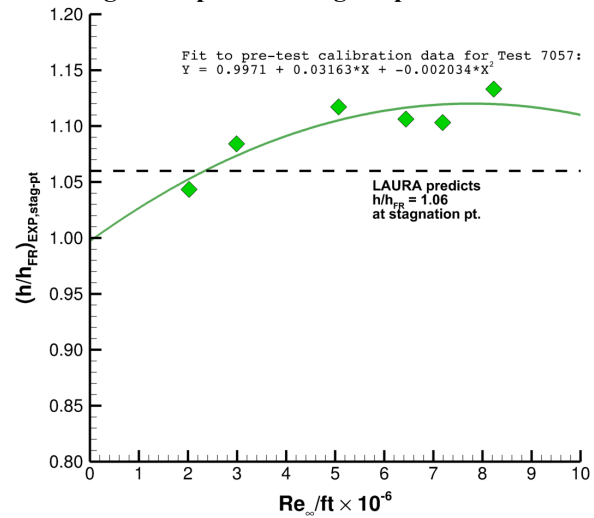


Figure 21. Measured stagnation point heating for pretest calibrations for Test 7057.

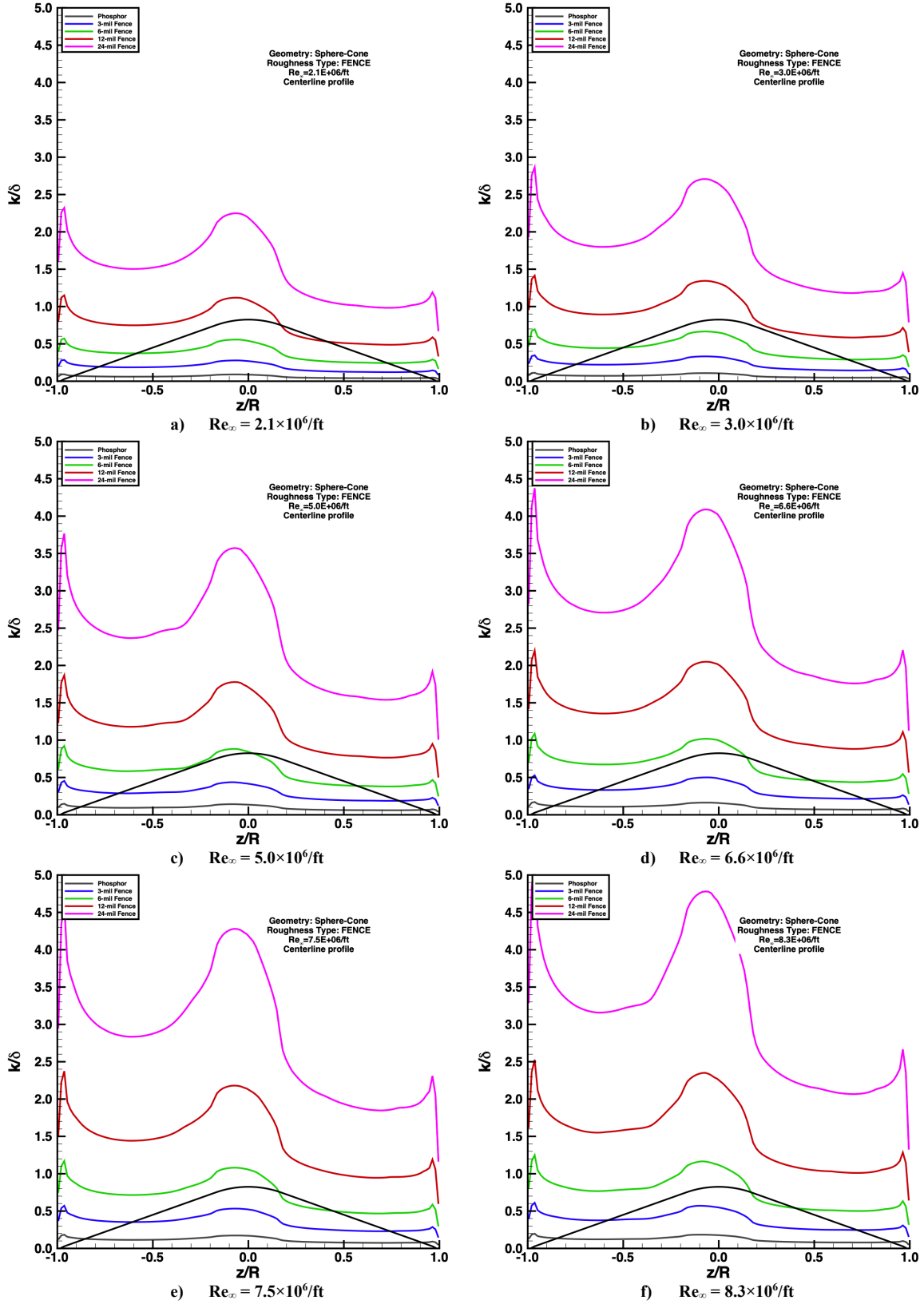


Figure 22. Centerline profiles of roughness effects on k/δ , sphere-cone geometry with fences.

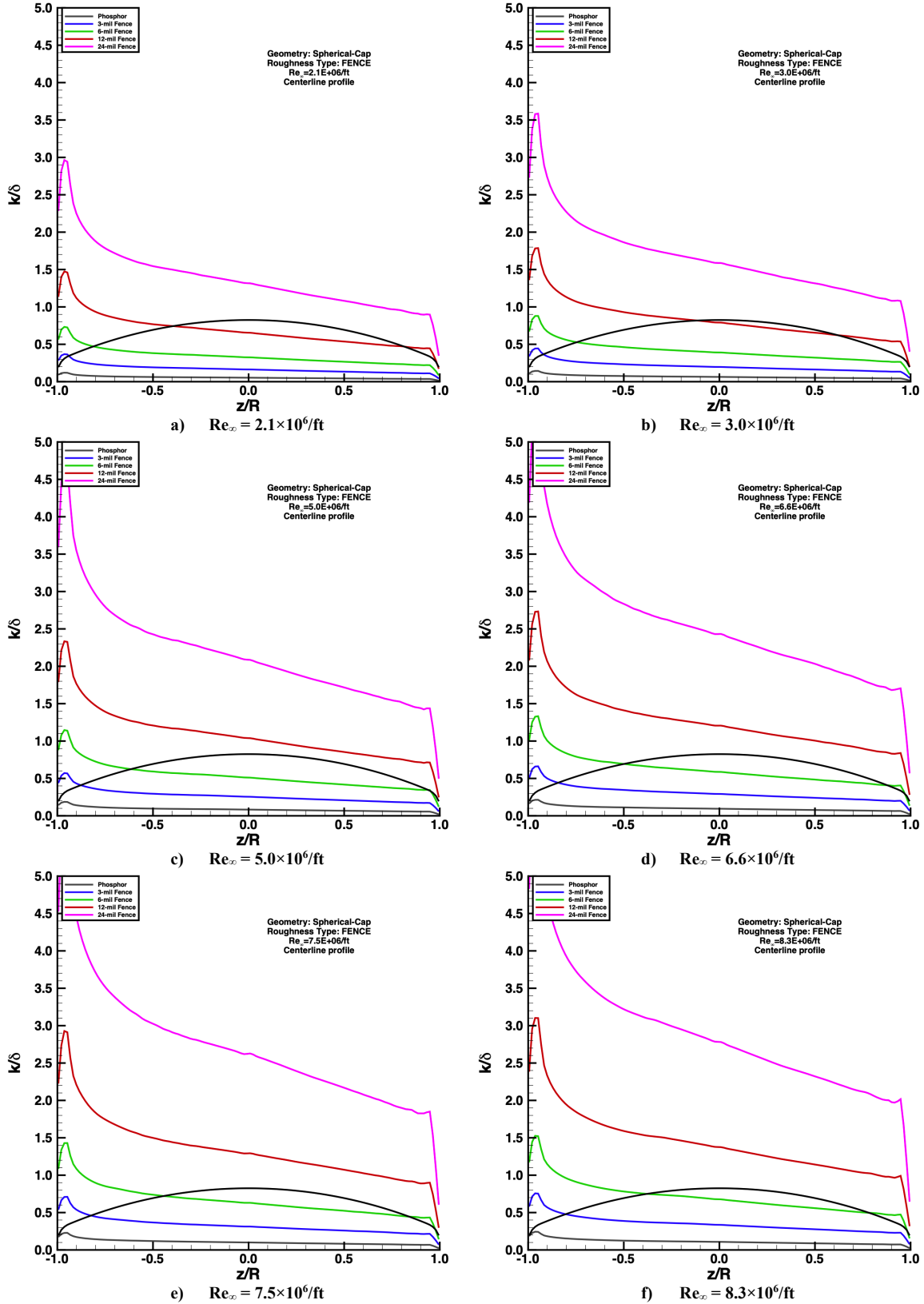


Figure 23. Centerline profiles of roughness effects on k/δ , spherical-cap geometry with fences.

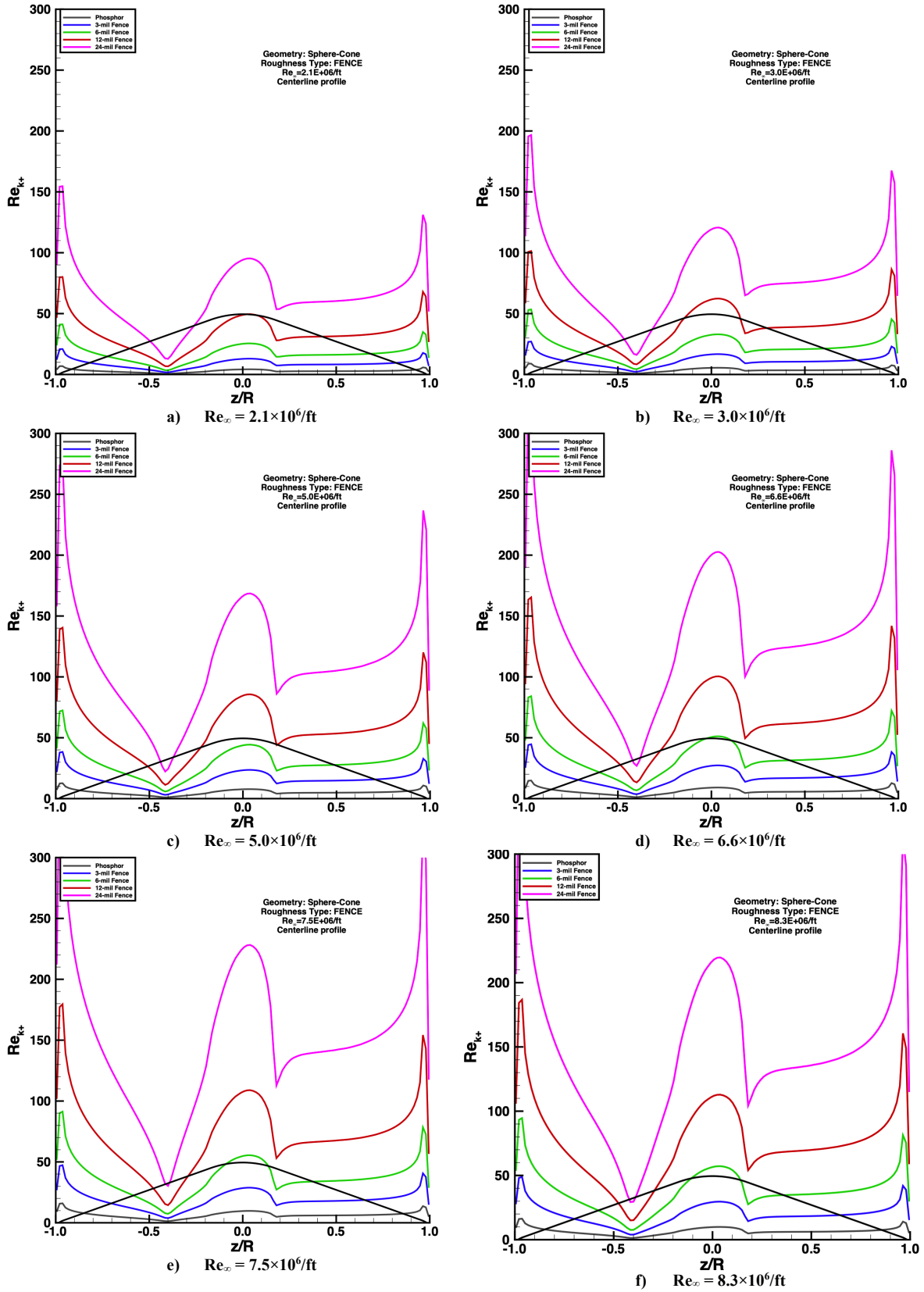


Figure 24. Centerline profiles of roughness effects on Re_{kt+} , sphere-cone geometry with fences.

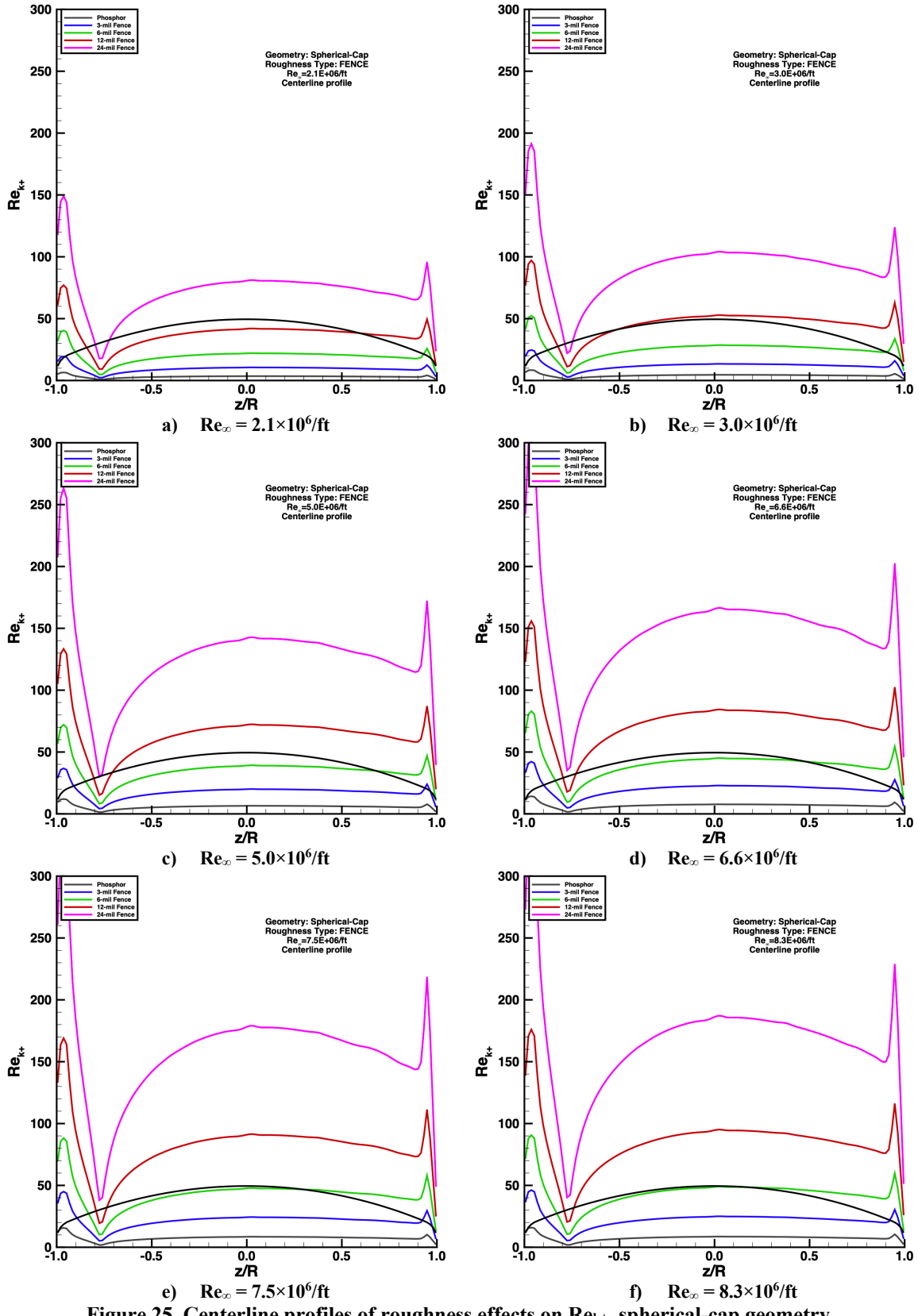


Figure 25. Centerline profiles of roughness effects on Re_{k+} , spherical-cap geometry.

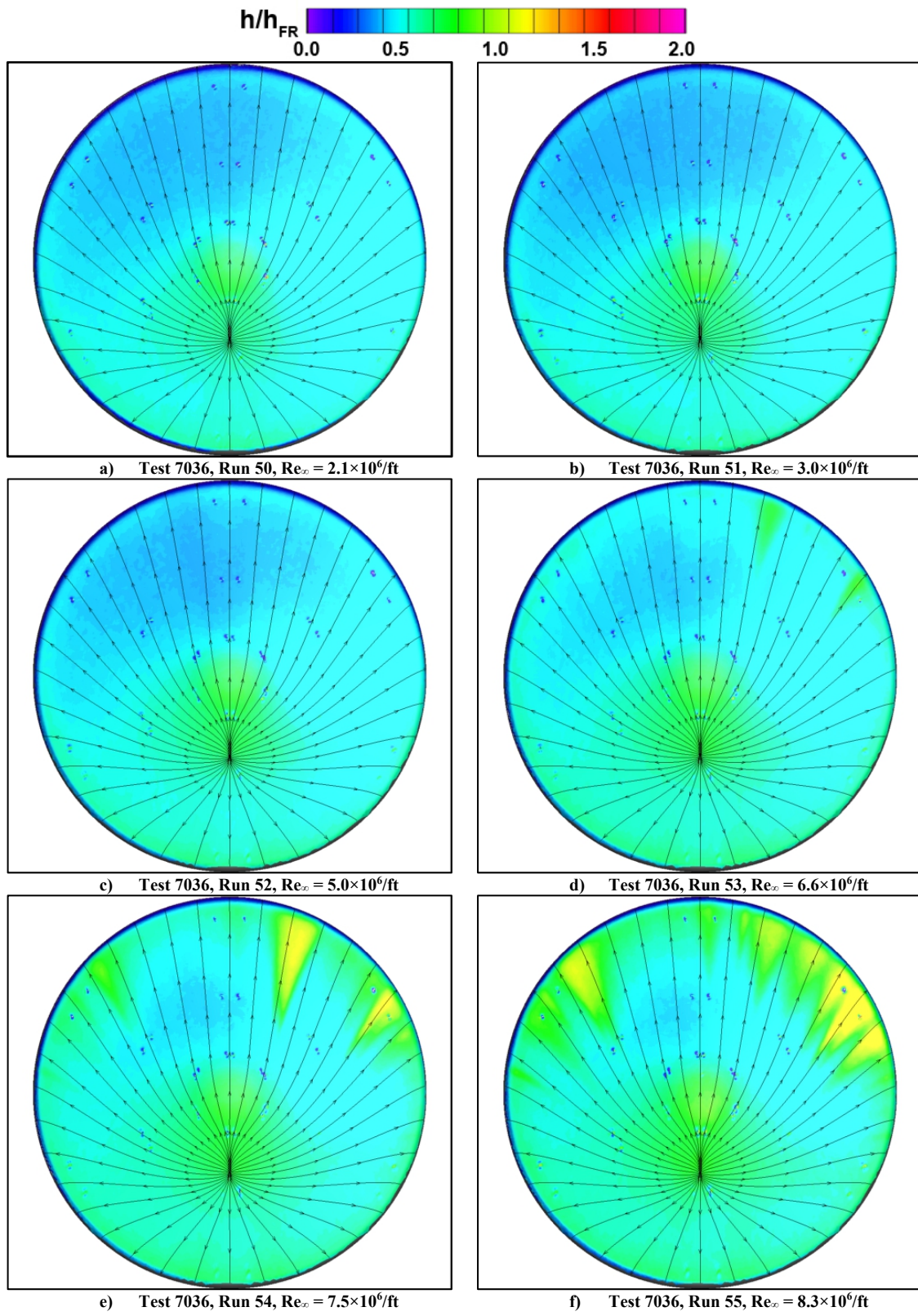


Figure 26. Reynolds Number effects, smooth sphere-cone model images.

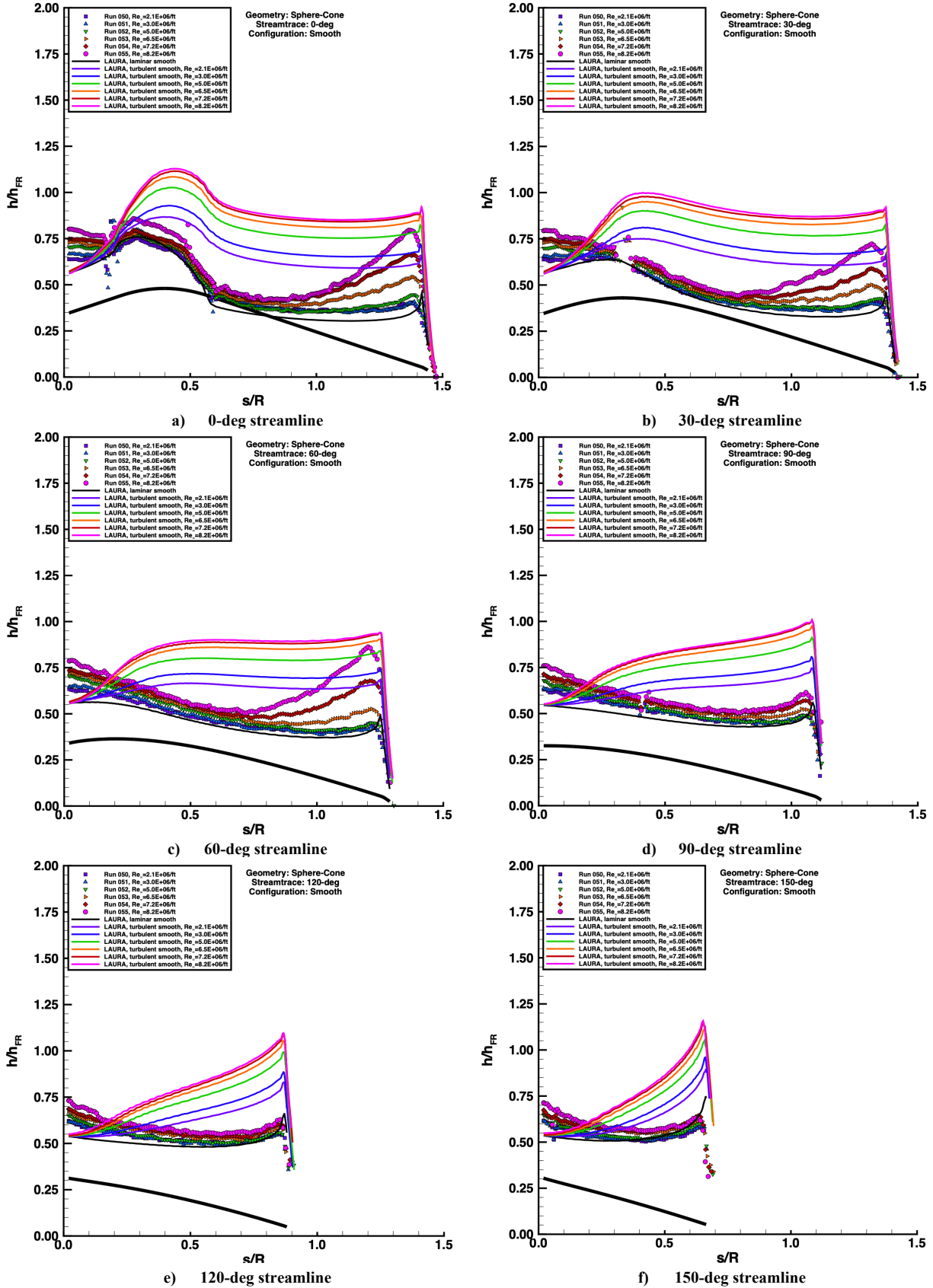


Figure 27. Reynolds number effects, smooth sphere-cone model plots.

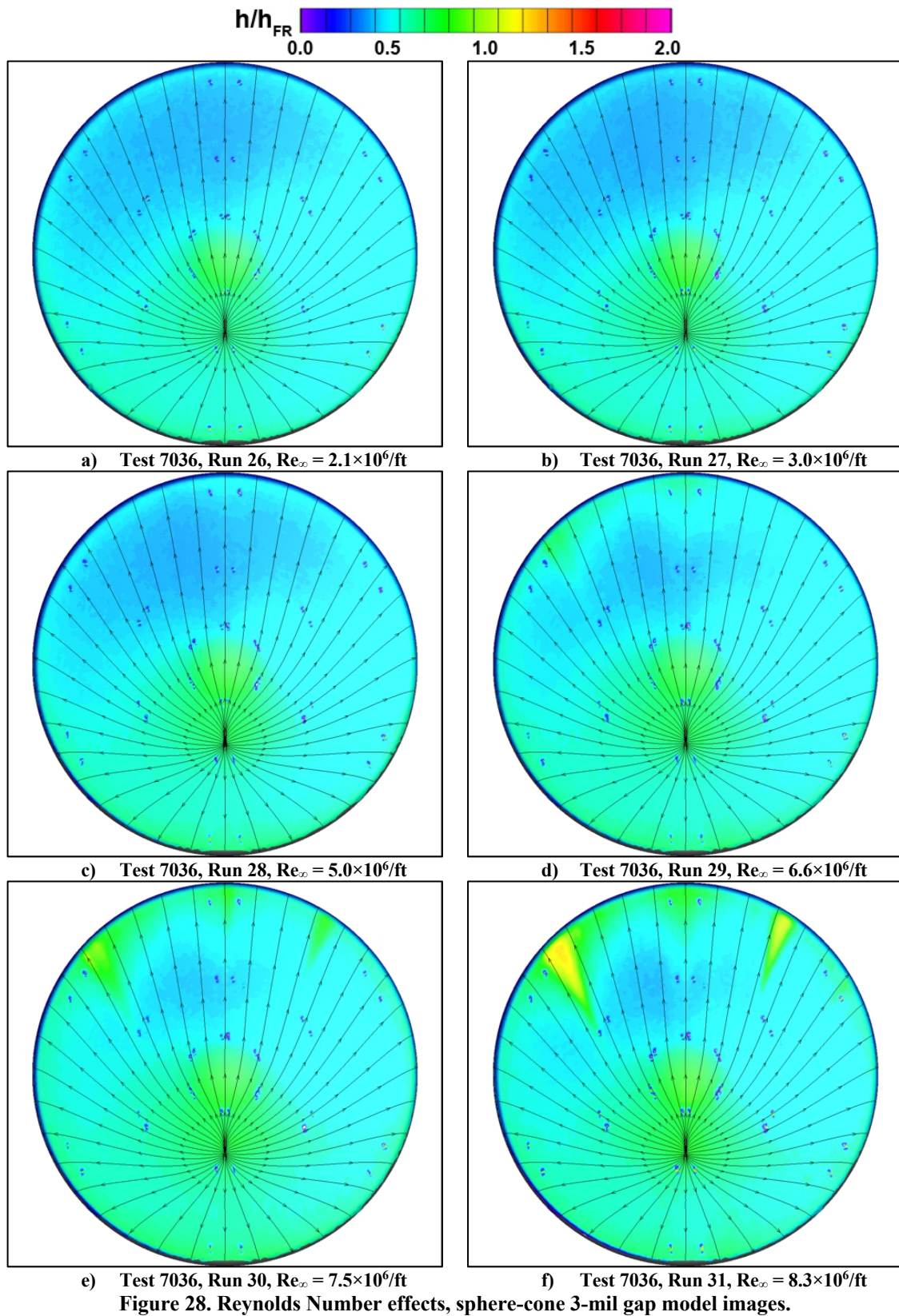


Figure 28. Reynolds Number effects, sphere-cone 3-mil gap model images.

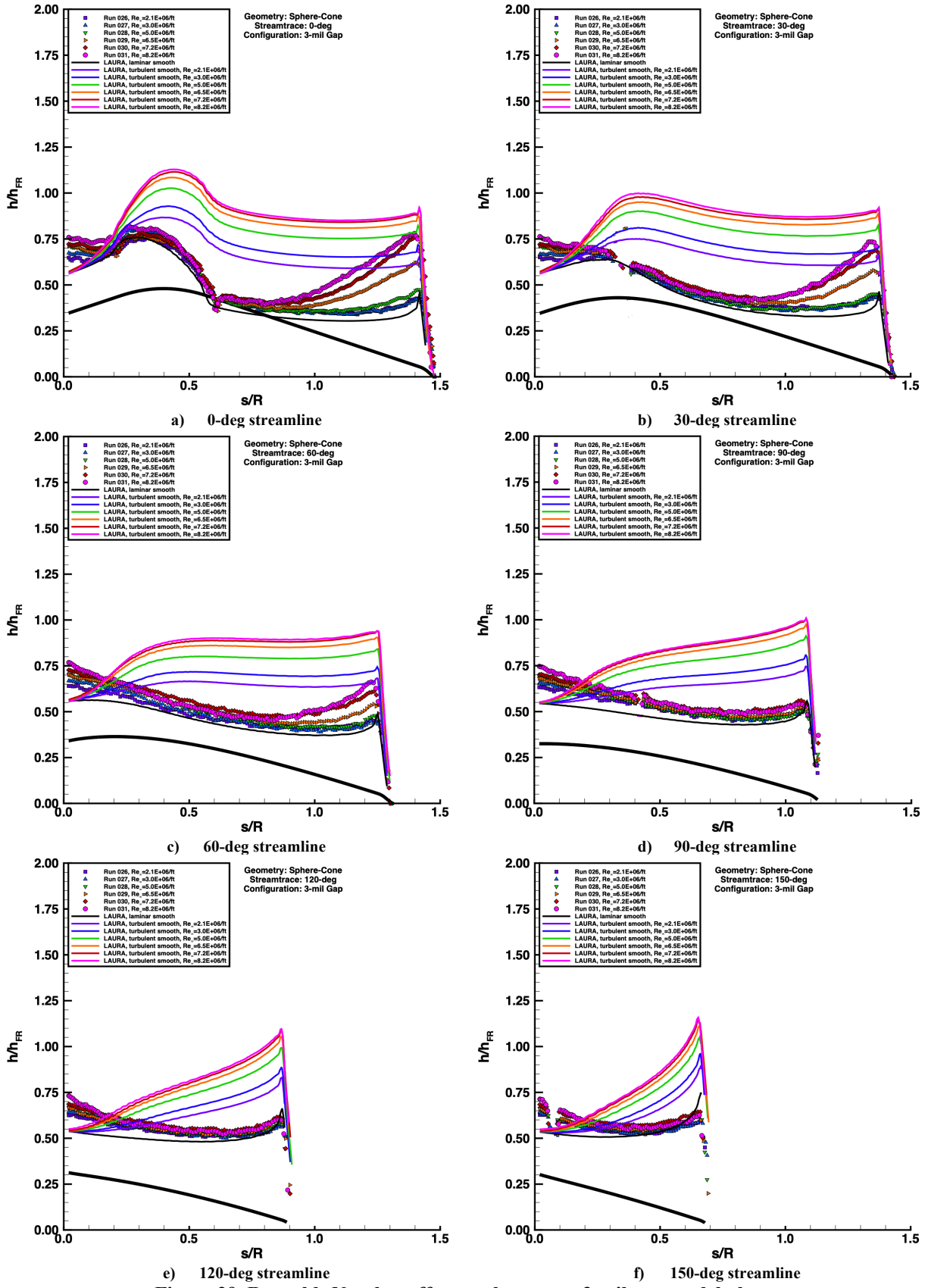


Figure 29. Reynolds Number effects, sphere-cone 3-mil gap model plots.

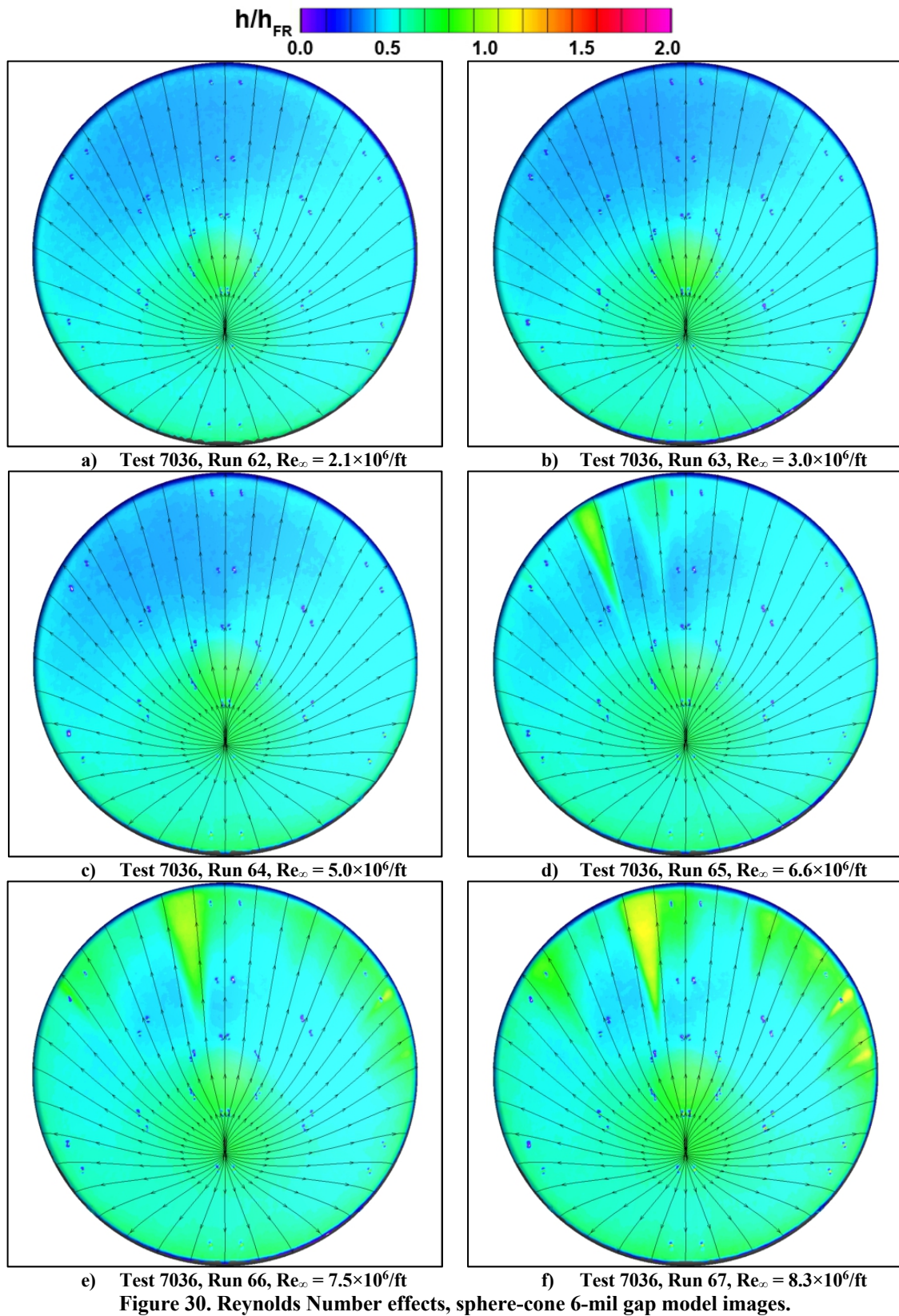


Figure 30. Reynolds Number effects, sphere-cone 6-mil gap model images.

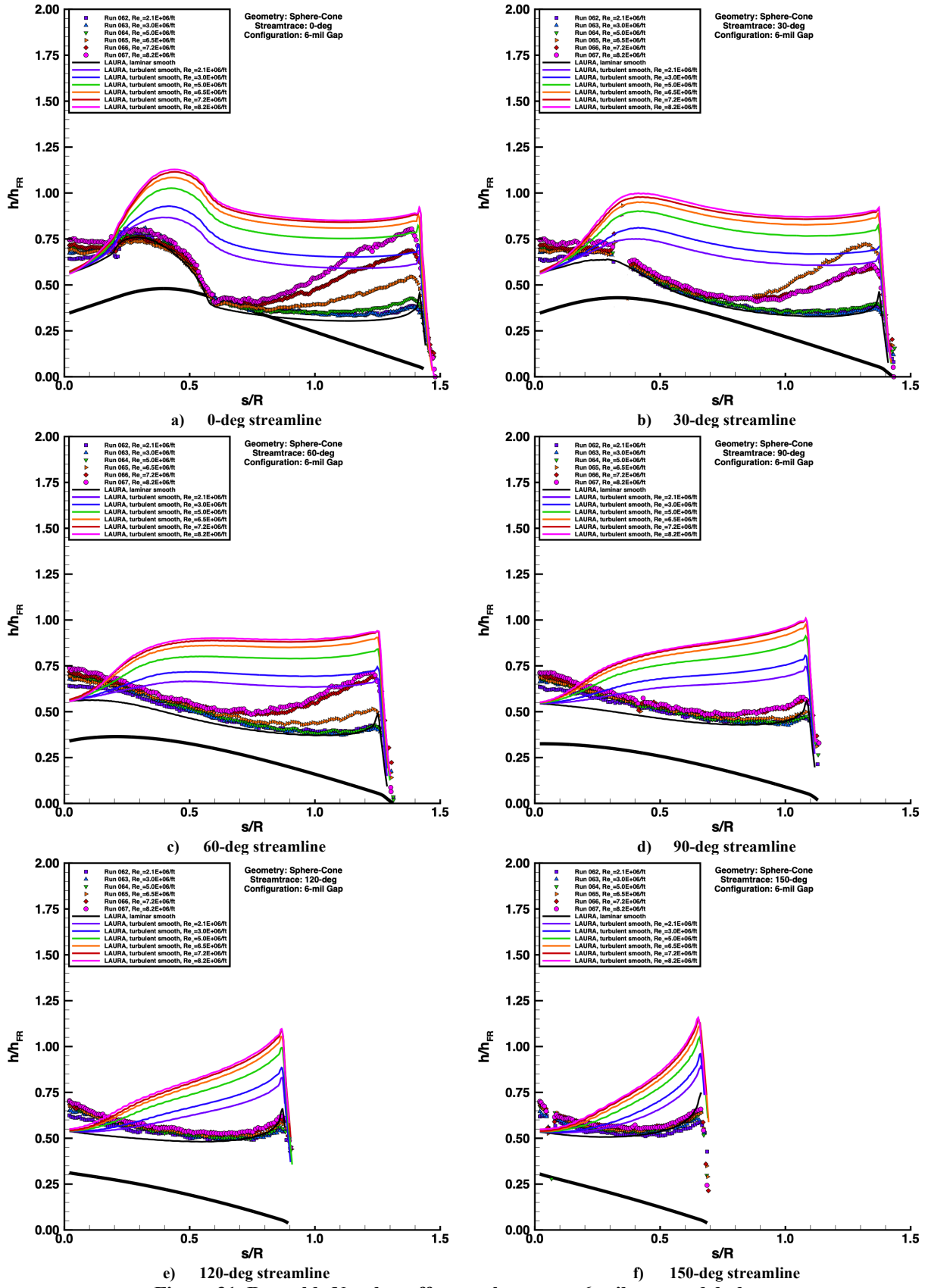


Figure 31. Reynolds Number effects, sphere-cone 6-mil gap model plots.

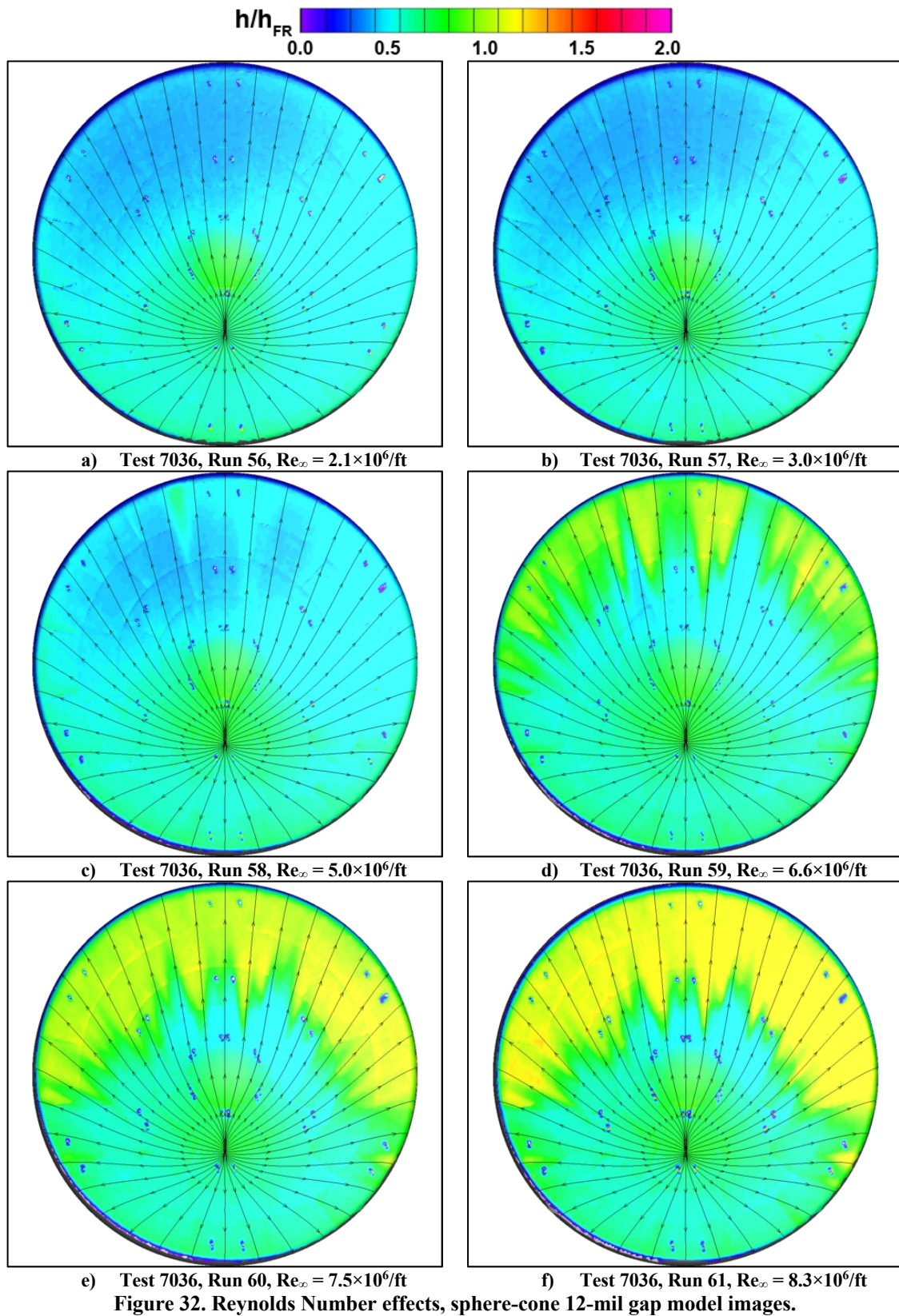


Figure 32. Reynolds Number effects, sphere-cone 12-mil gap model images.

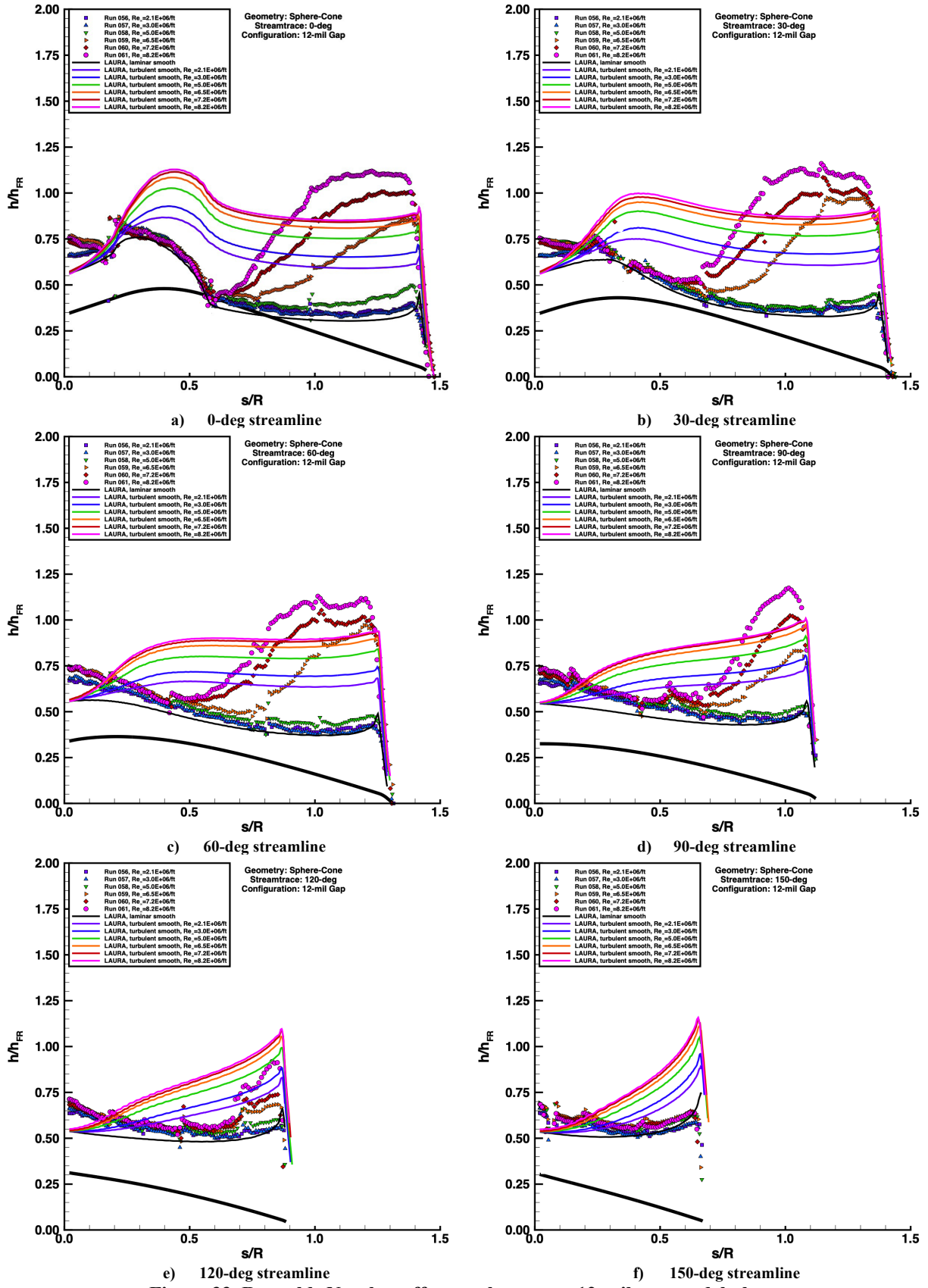


Figure 33. Reynolds Number effects, sphere-cone 12-mil gap model plots.

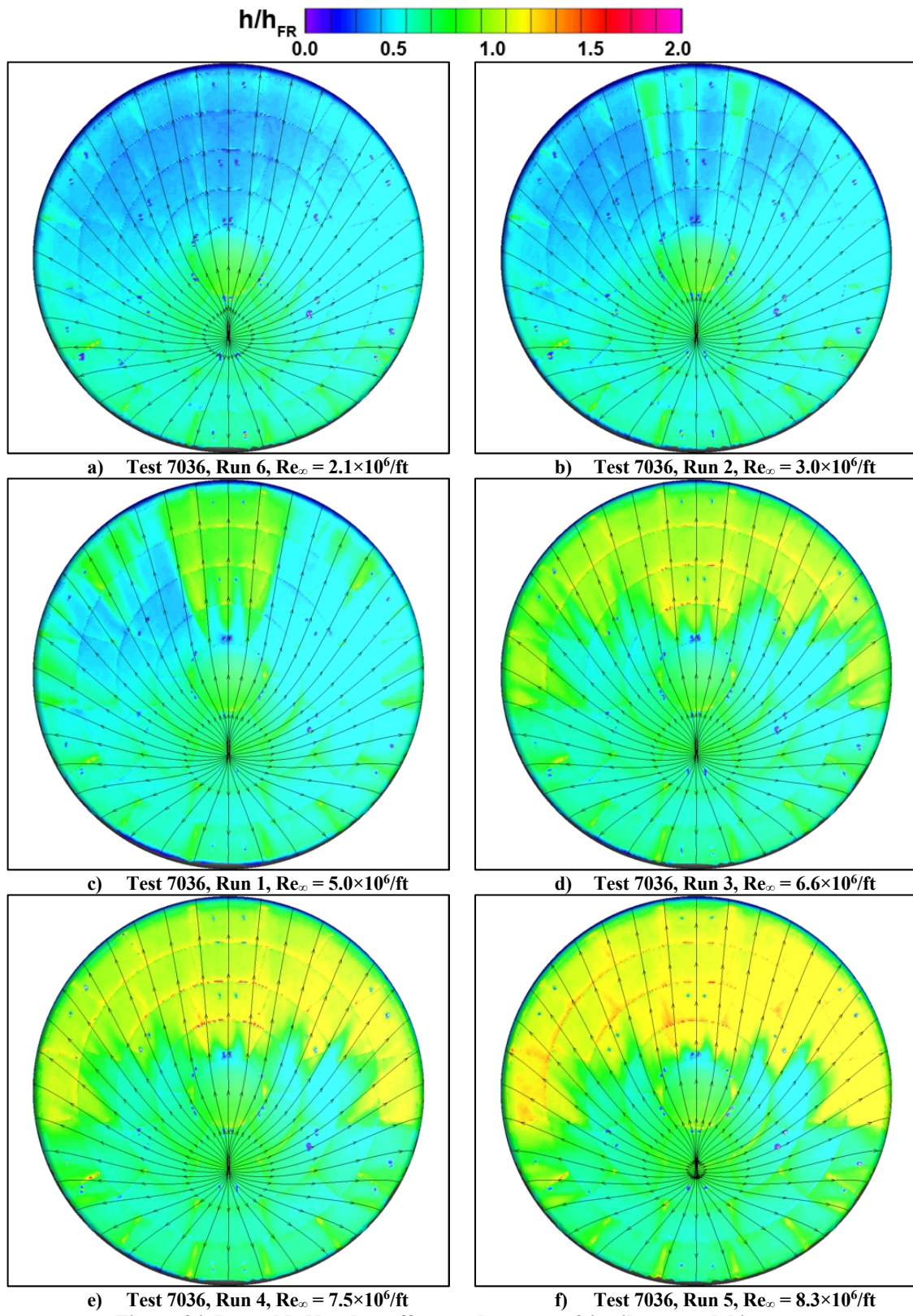
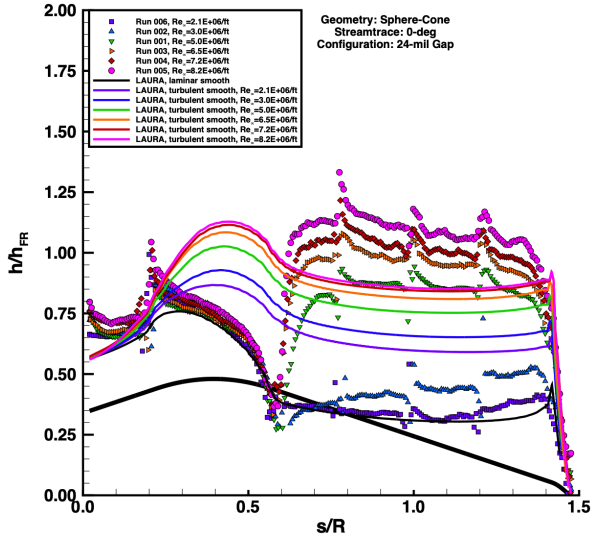
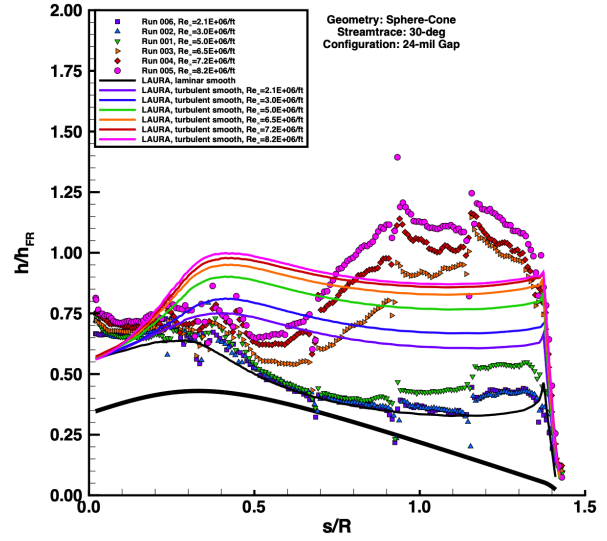


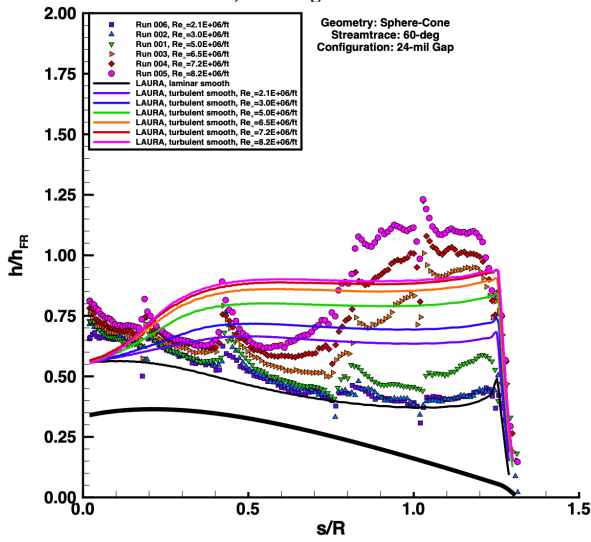
Figure 34. Reynolds Number effects, sphere-cone 24-mil gap model images.



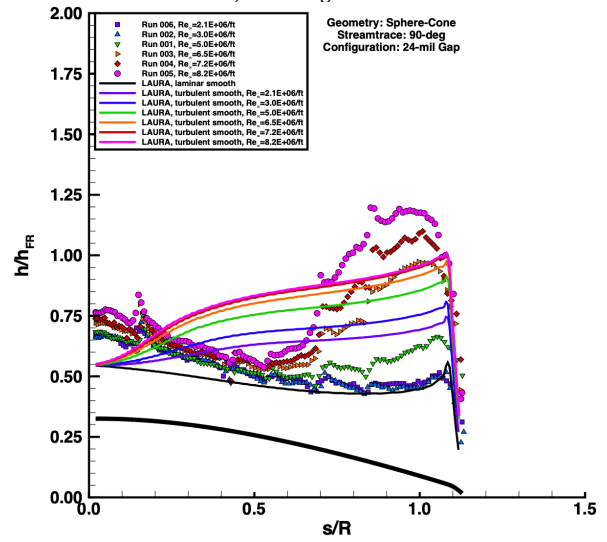
a) 0-deg streamline



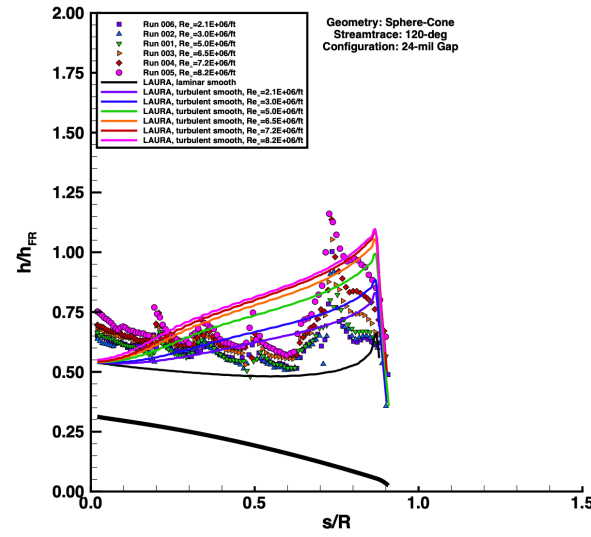
b) 30-deg streamline



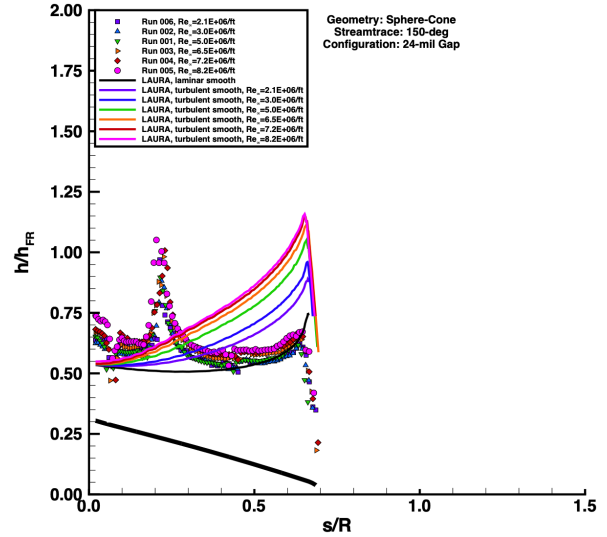
c) 60-deg streamline



d) 90-deg streamline



e) 120-deg streamline



f) 150-deg streamline

Figure 35. Reynolds Number effects, sphere-cone 24-mil gap model plots.

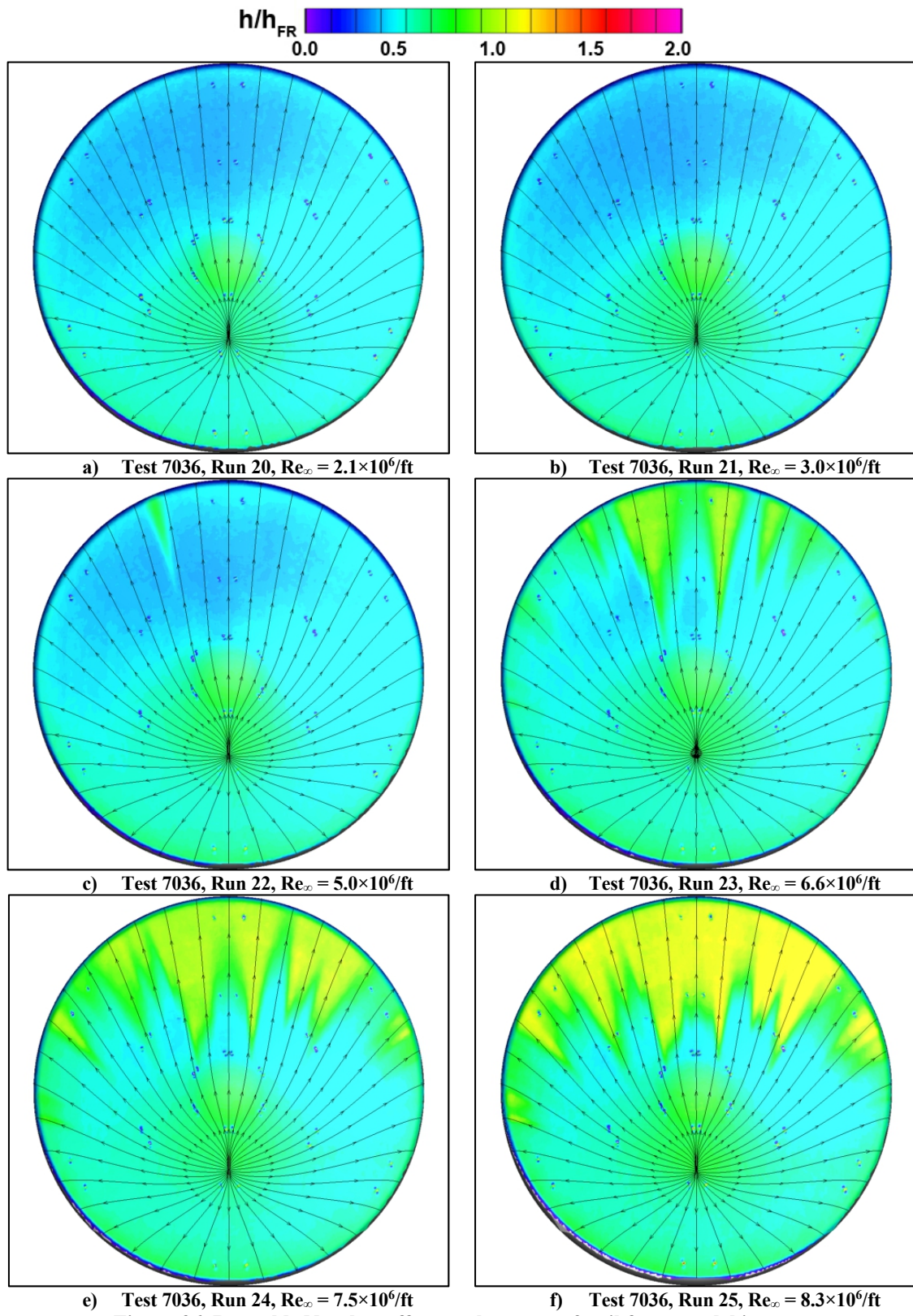
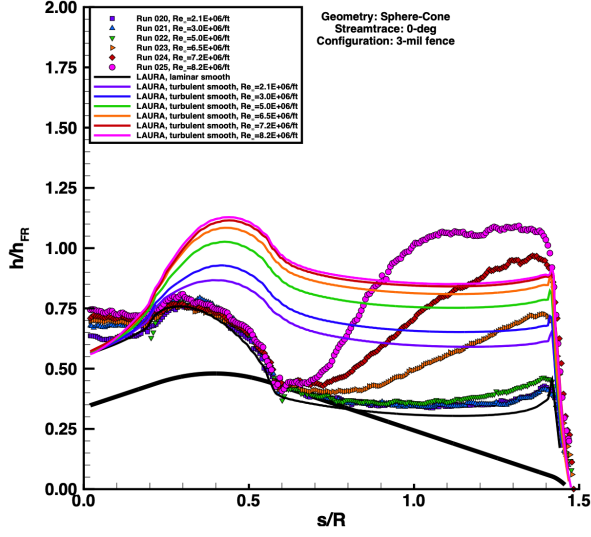
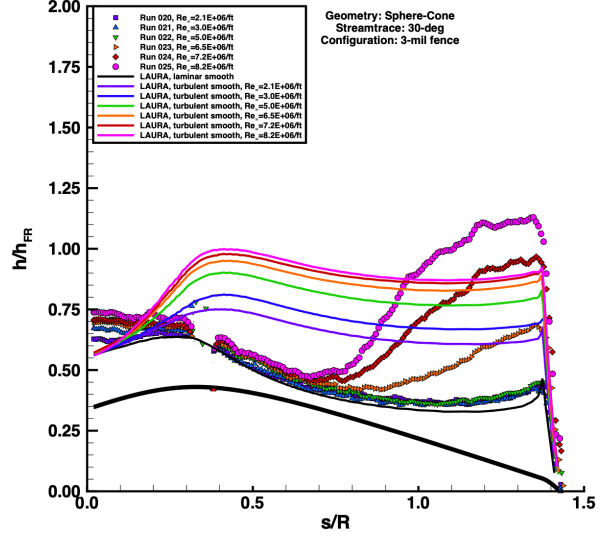


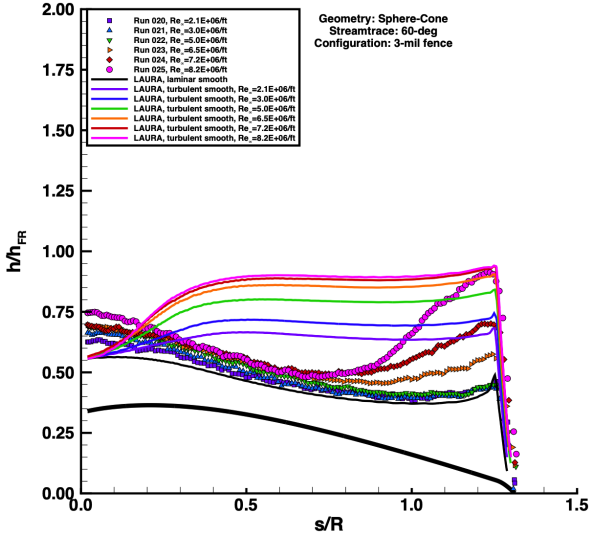
Figure 36. Reynolds Number effects, sphere-cone 3-mil fence model images.



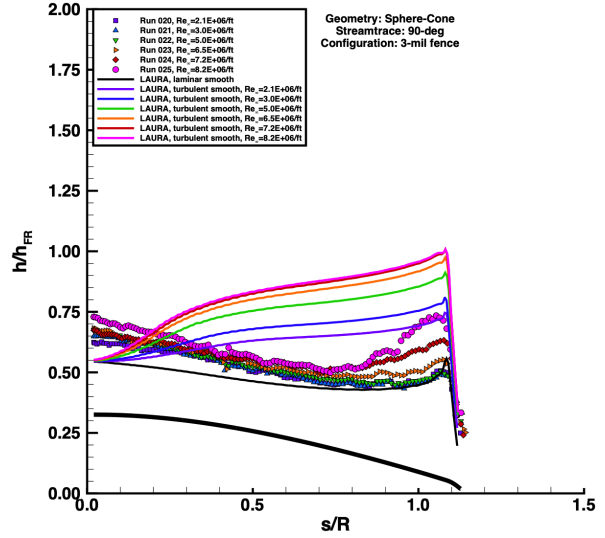
a) 0-deg streamline



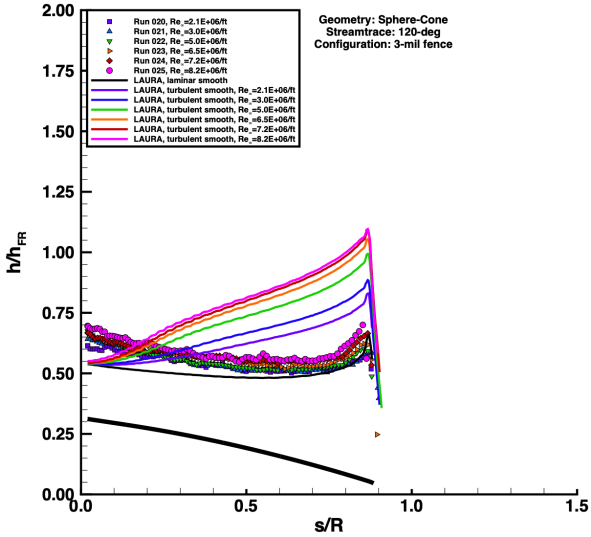
b) 30-deg streamline



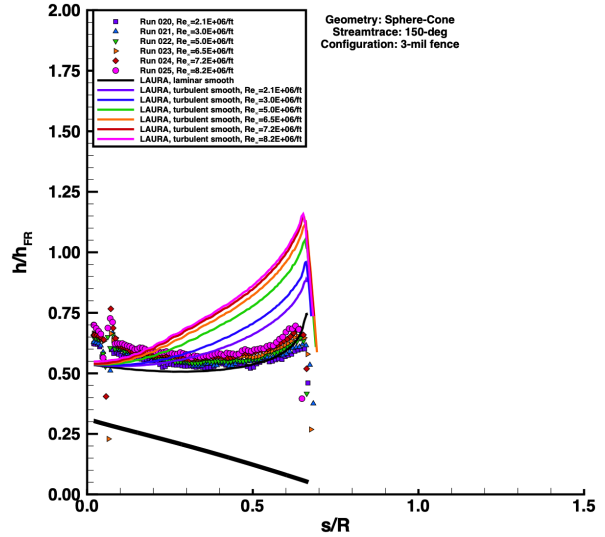
c) 60-deg streamline



d) 90-deg streamline



e) 120-deg streamline



f) 150-deg streamline

Figure 37. Reynolds Number effects, sphere-cone 3-mil fence model plots.

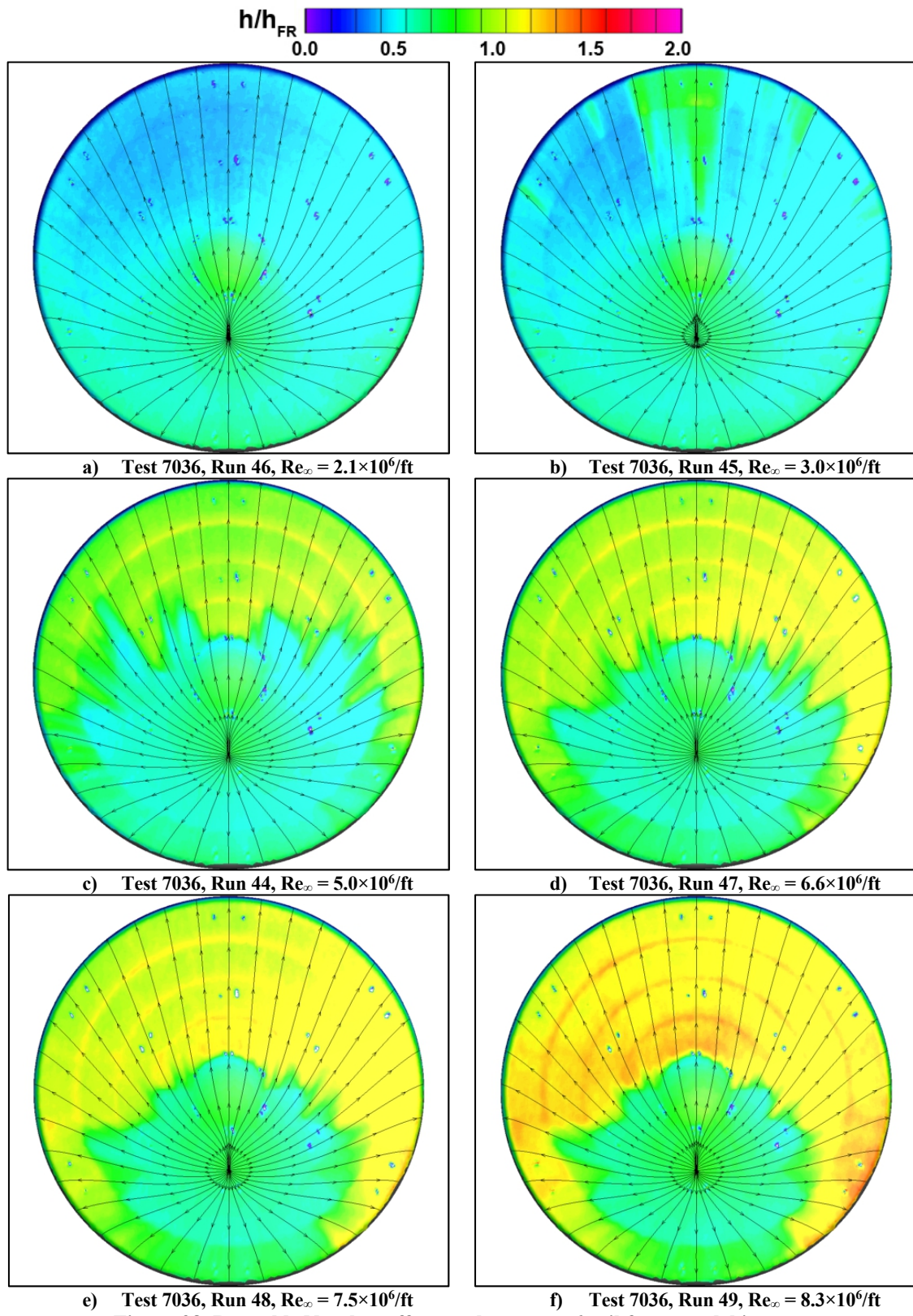


Figure 38. Reynolds Number effects, sphere-cone 6-mil fence model images.

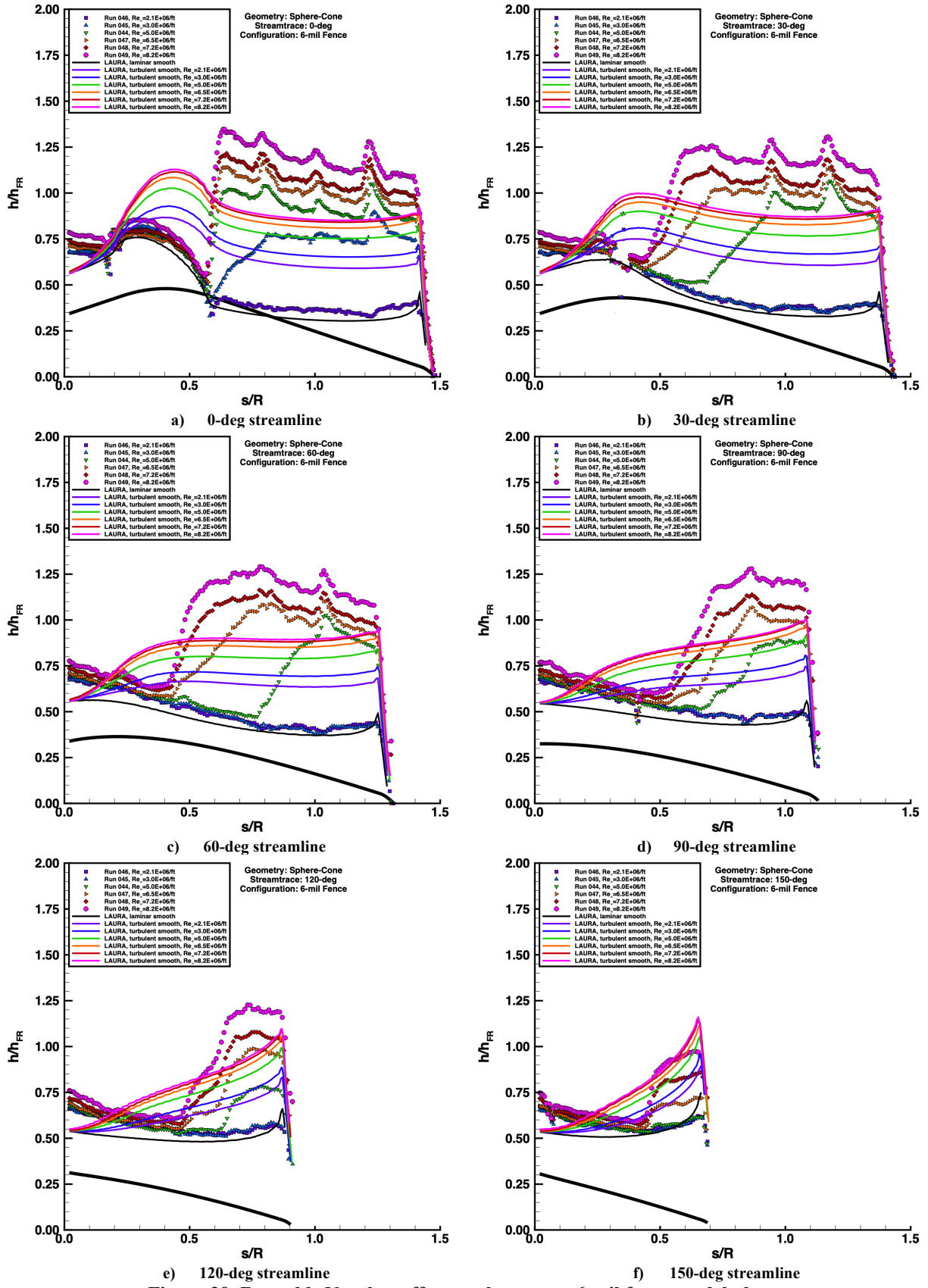


Figure 39. Reynolds Number effects, sphere-cone 6-mil fence model plots.

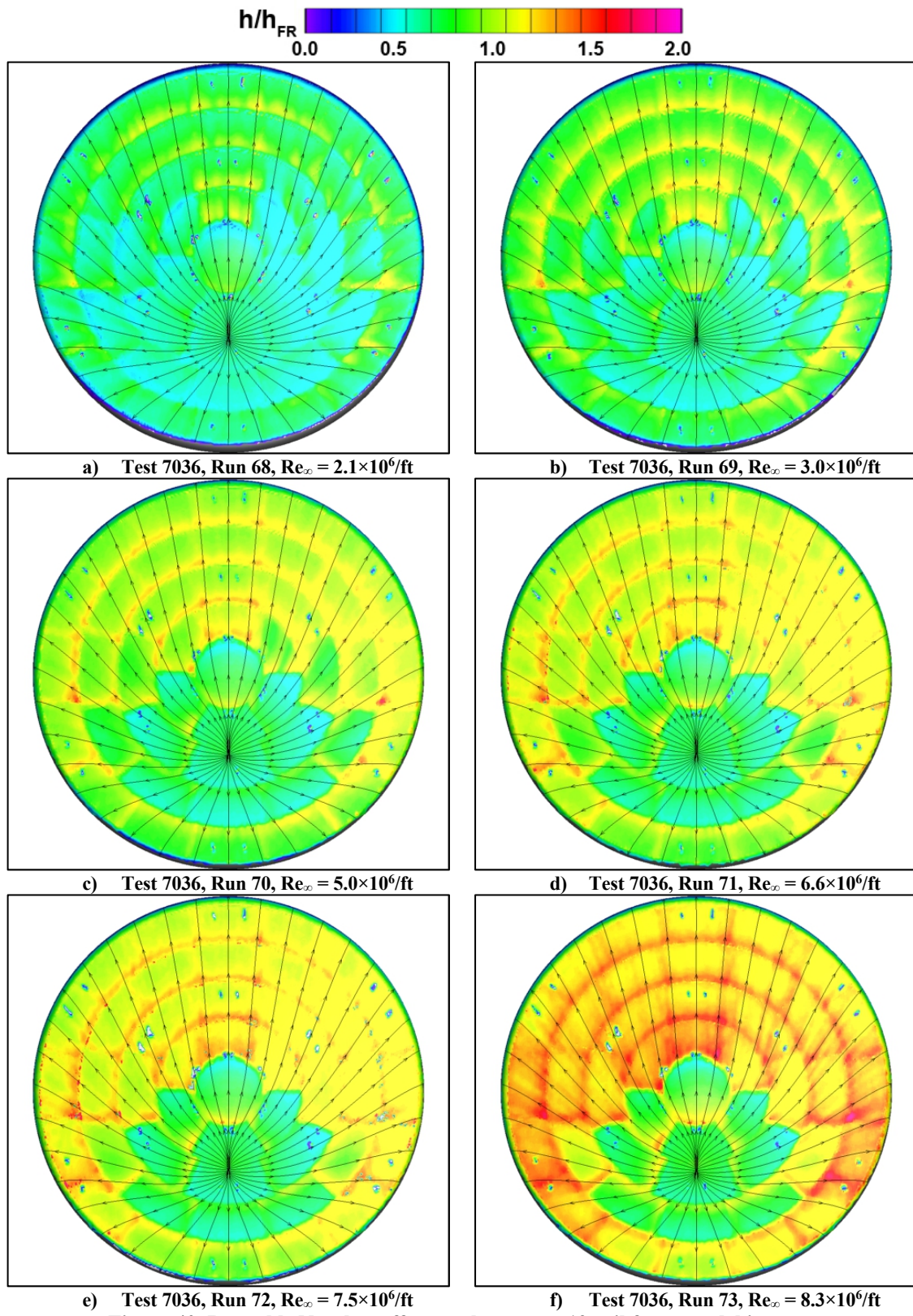


Figure 40. Reynolds Number effects, sphere-cone 12-mil fence model images.

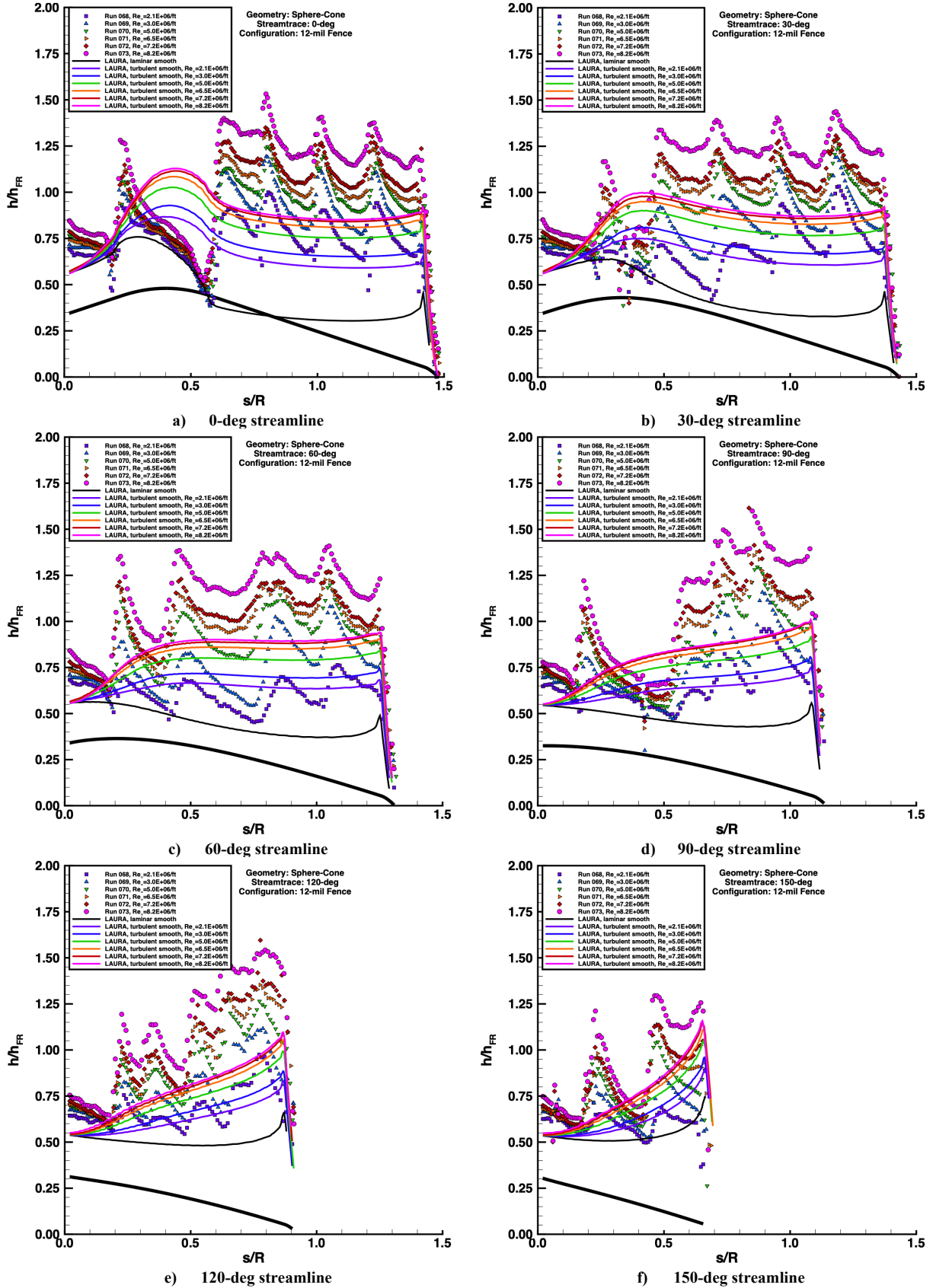


Figure 41. Reynolds Number effects, sphere-cone 12-mil fence model plots.

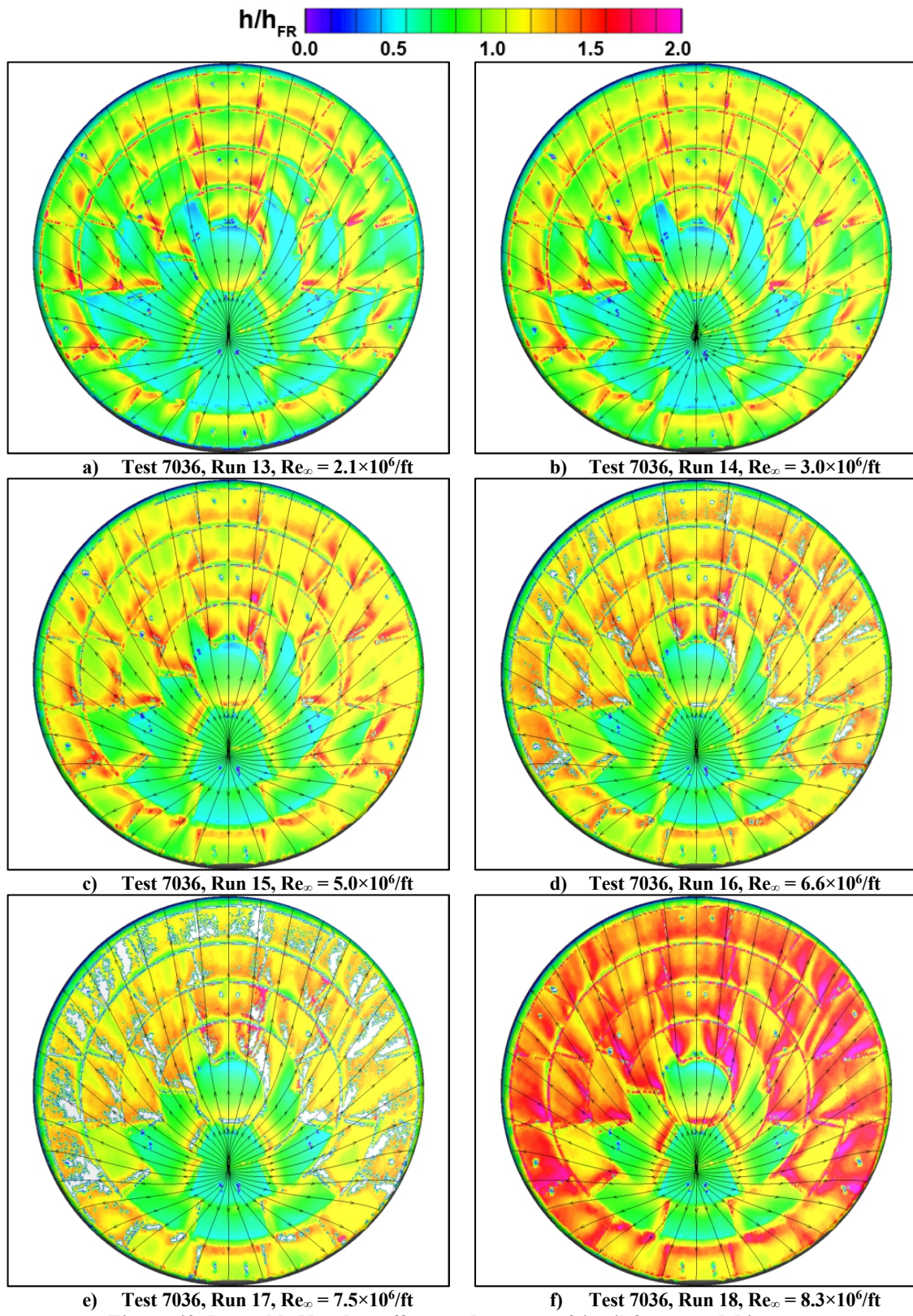


Figure 42. Reynolds Number effects, sphere-cone 24-mil fence model images.

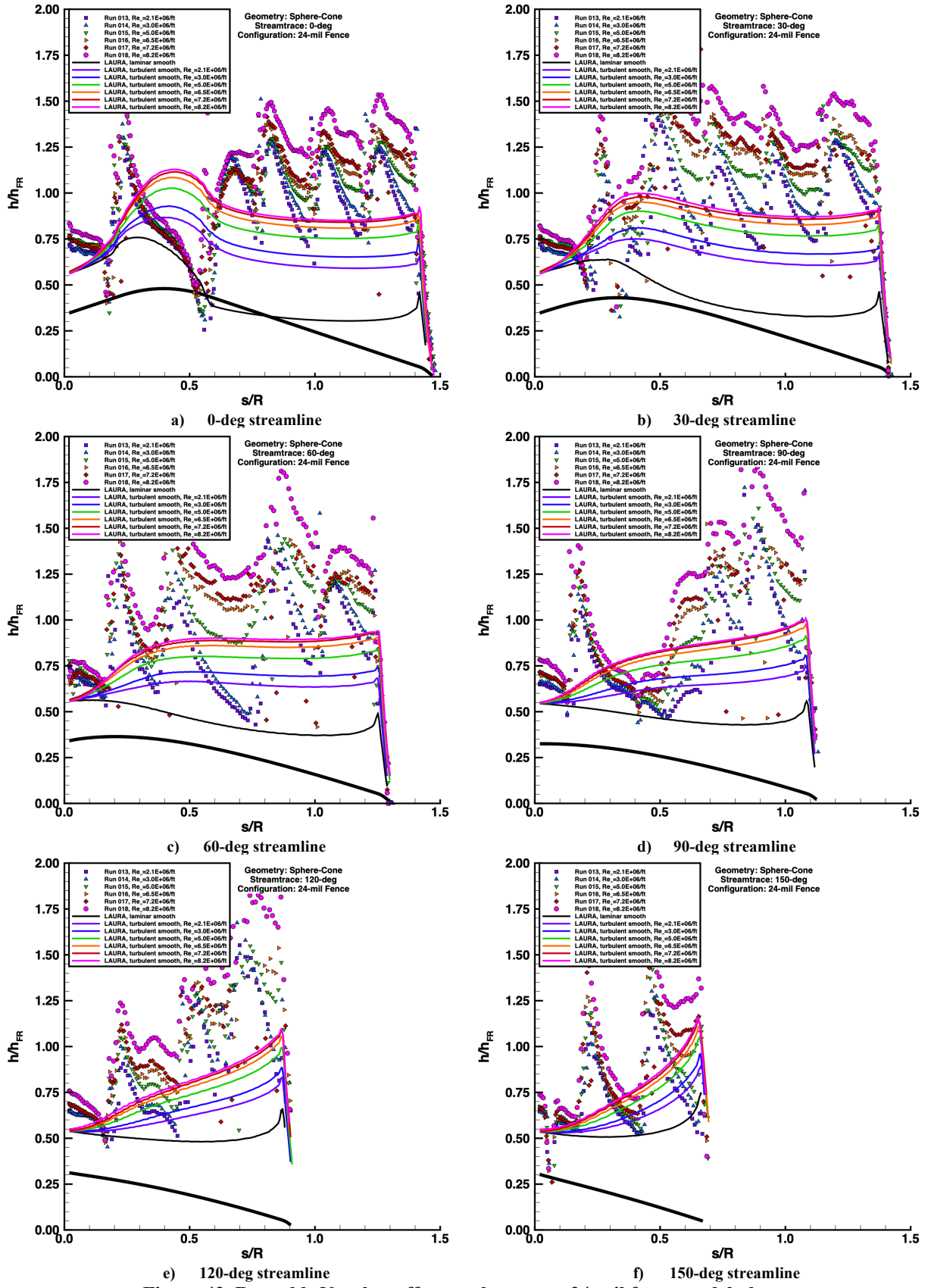


Figure 43. Reynolds Number effects, sphere-cone 24-mil fence model plots.

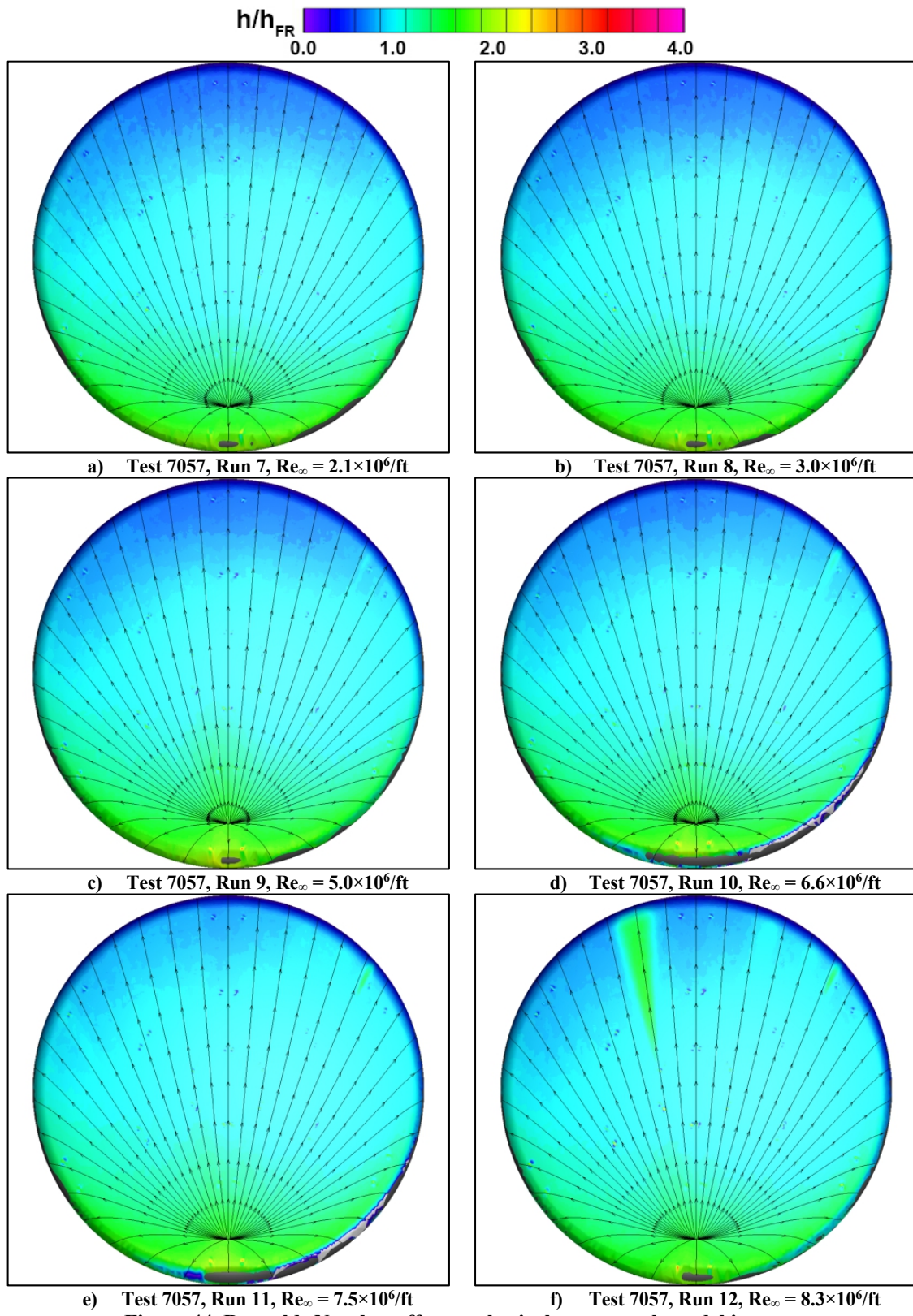
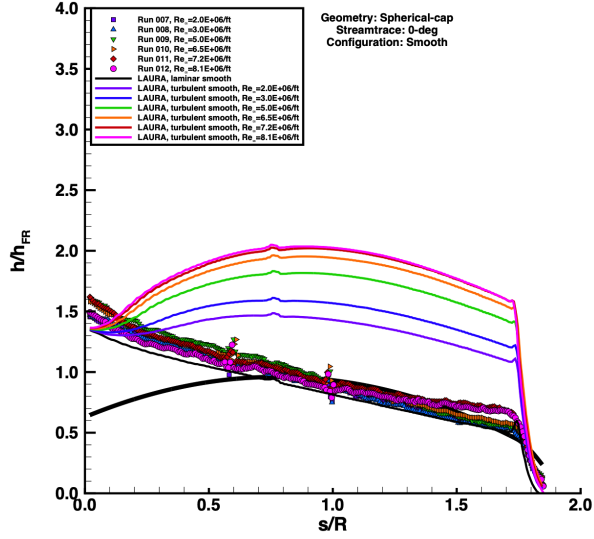
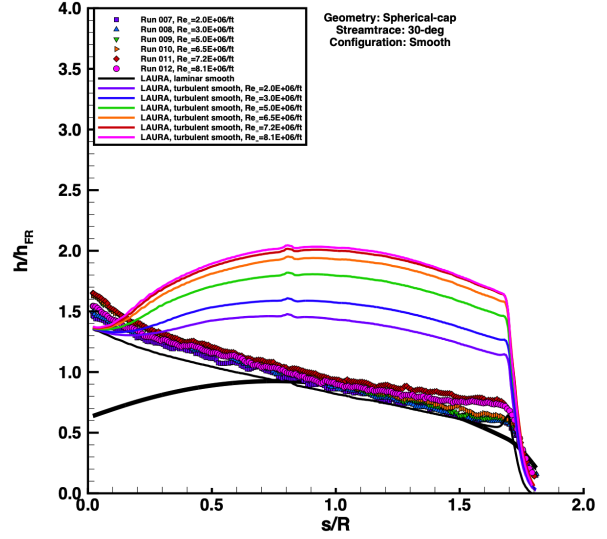


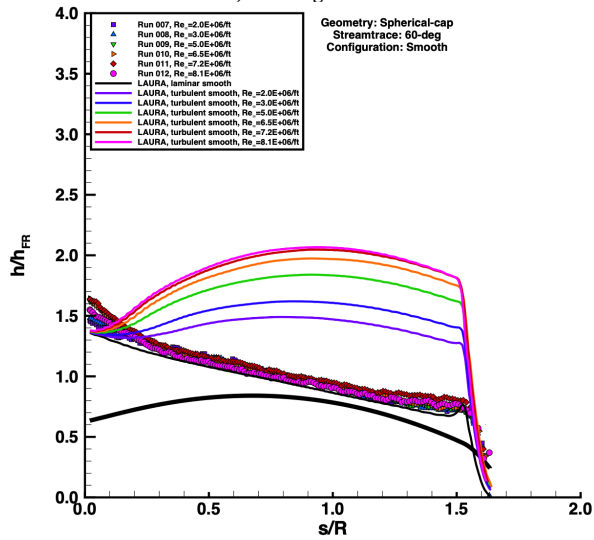
Figure 44. Reynolds Number effects, spherical-cap smooth model images.



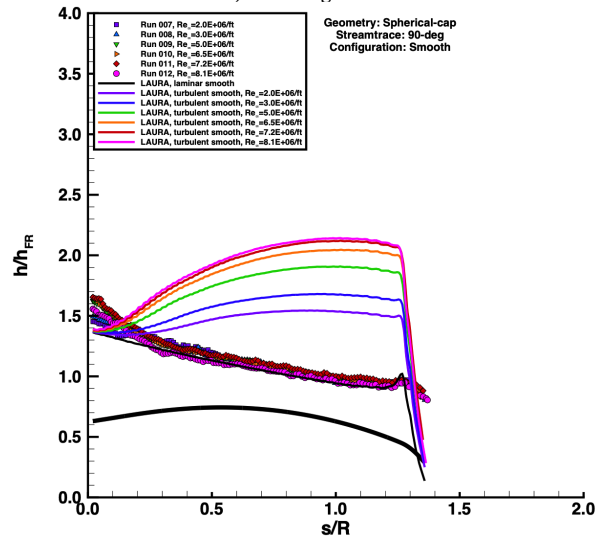
a) 0-deg streamline



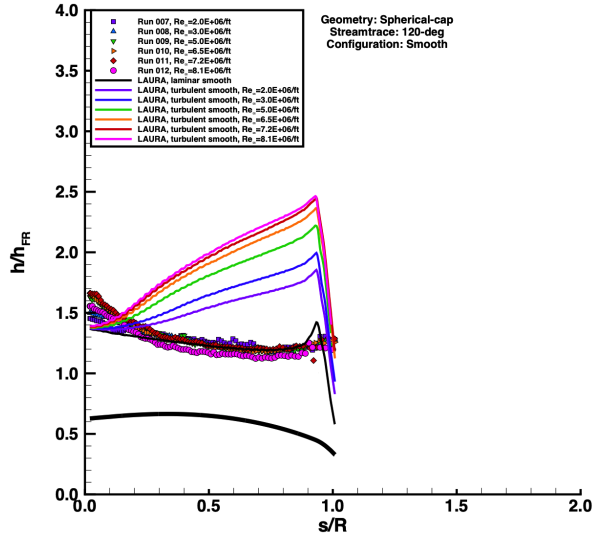
b) 30-deg streamline



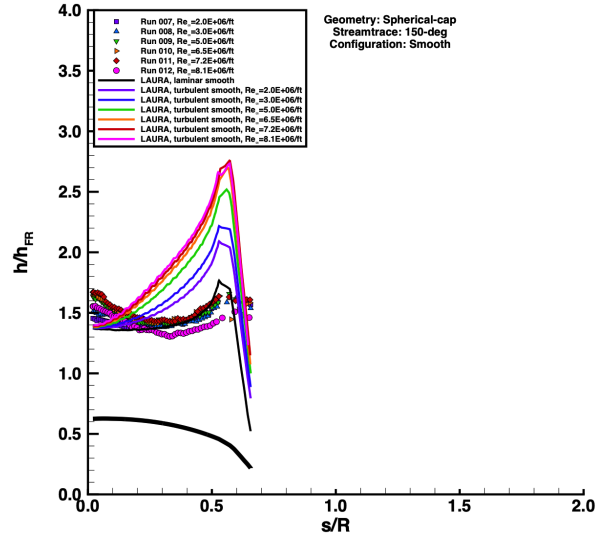
c) 60-deg streamline



d) 90-deg streamline



e) 120-deg streamline



f) 150-deg streamline

Figure 45. Reynolds Number effects, spherical-cap smooth model plots.

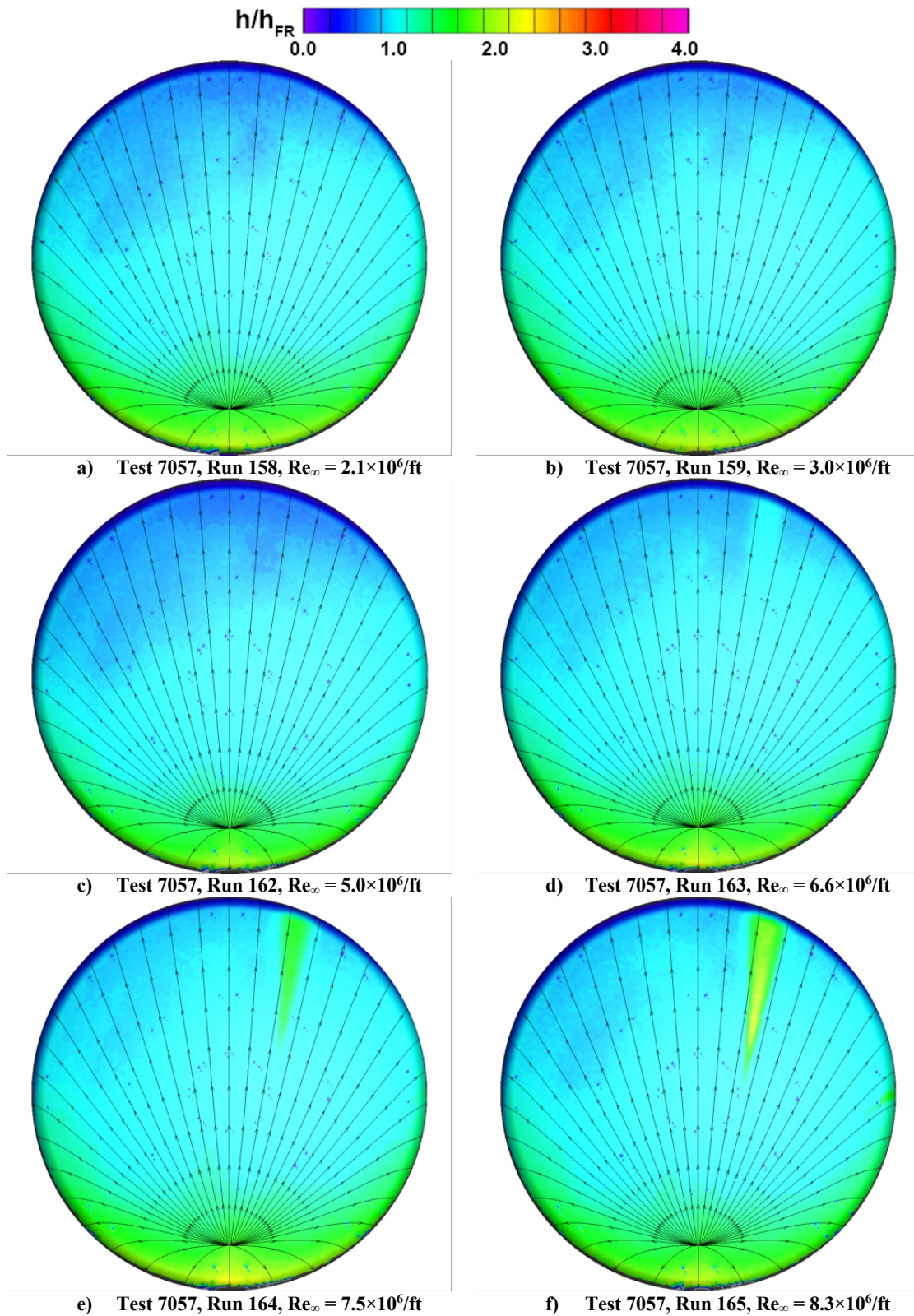
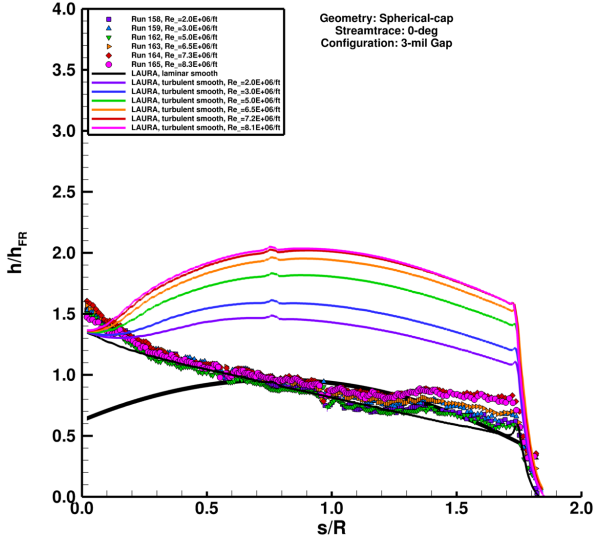
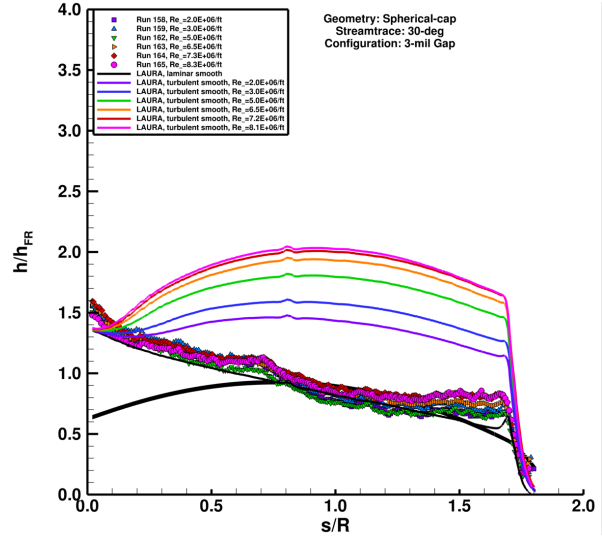


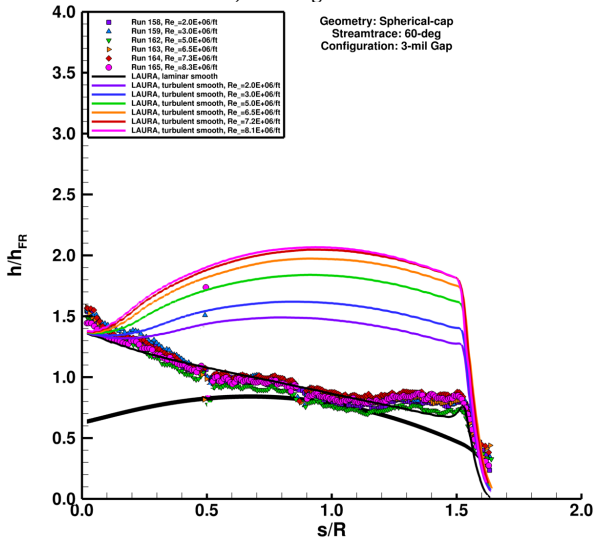
Figure 46. Reynolds Number effects, spherical-cap 3-mil gap model images.



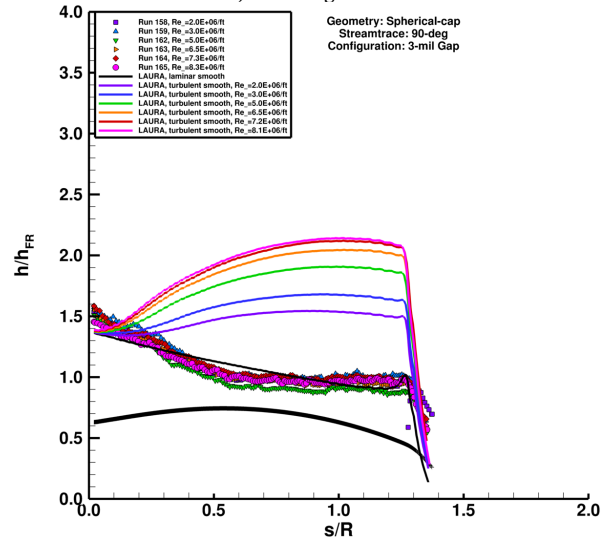
a) 0-deg streamline



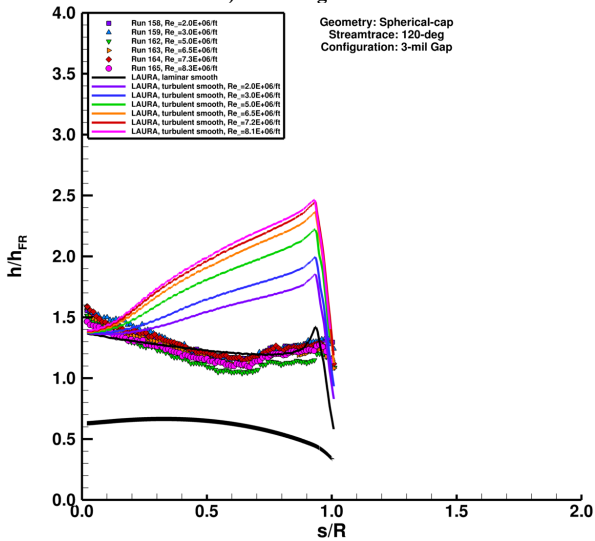
b) 30-deg streamline



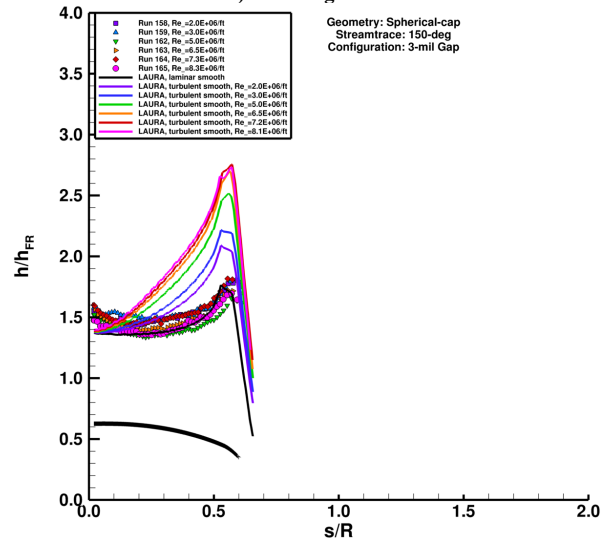
c) 60-deg streamline



d) 90-deg streamline



e) 120-deg streamline



f) 150-deg streamline

Figure 47. Reynolds Number effects, spherical-cap 3-mil gap model plots.

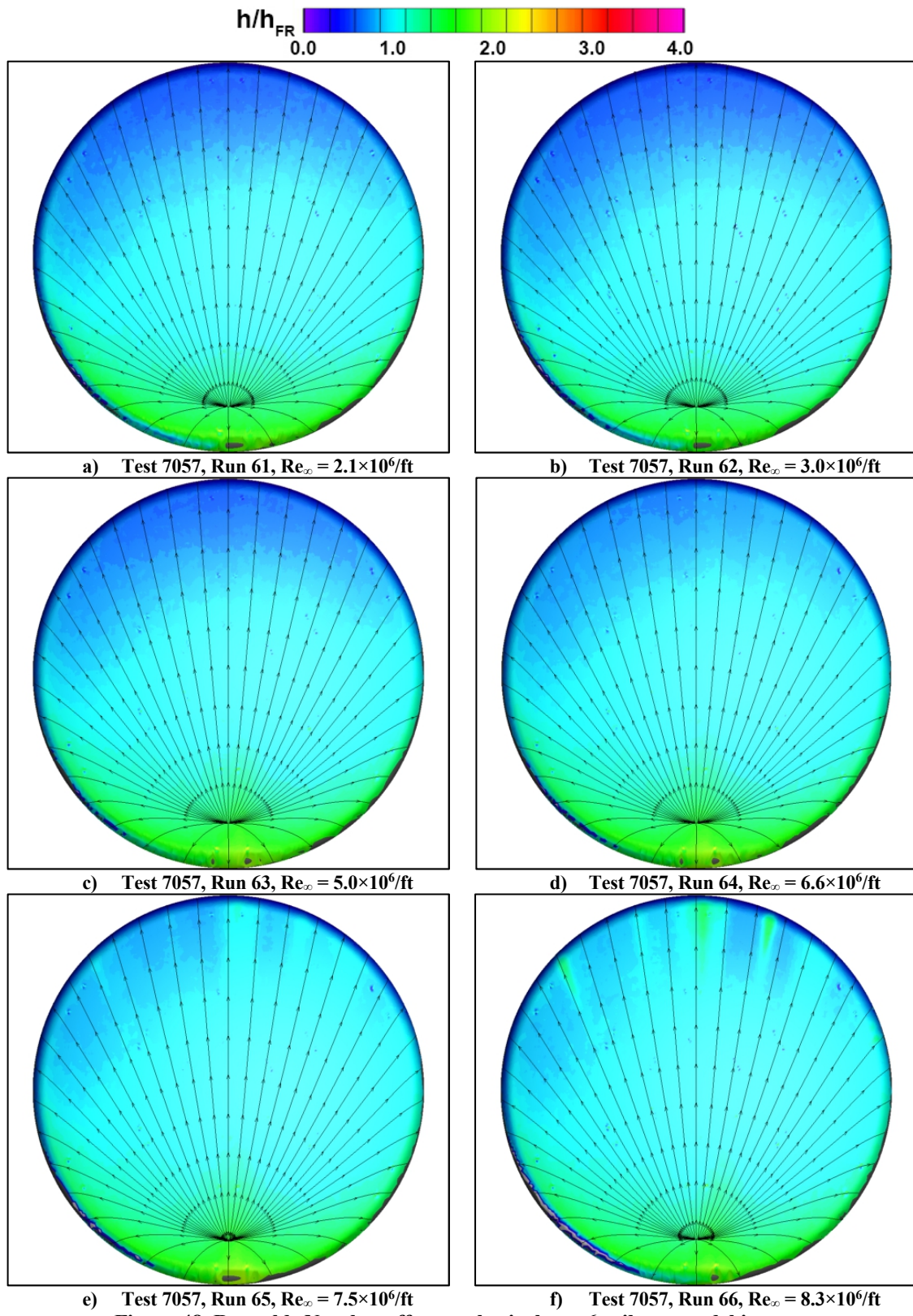


Figure 48. Reynolds Number effects, spherical-cap 6-mil gap model images.

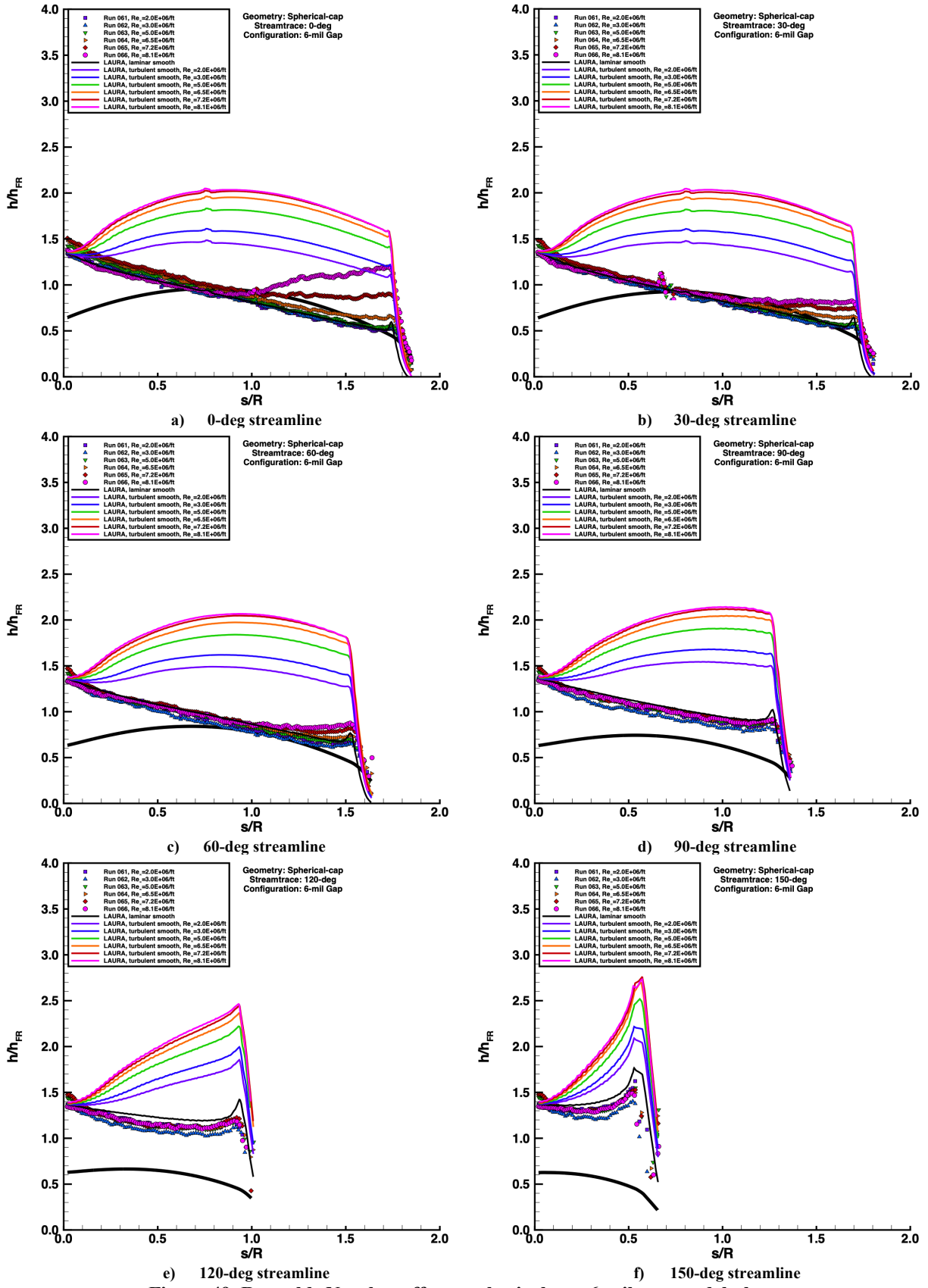


Figure 49. Reynolds Number effects, spherical-cap 6-mil gap model plots.

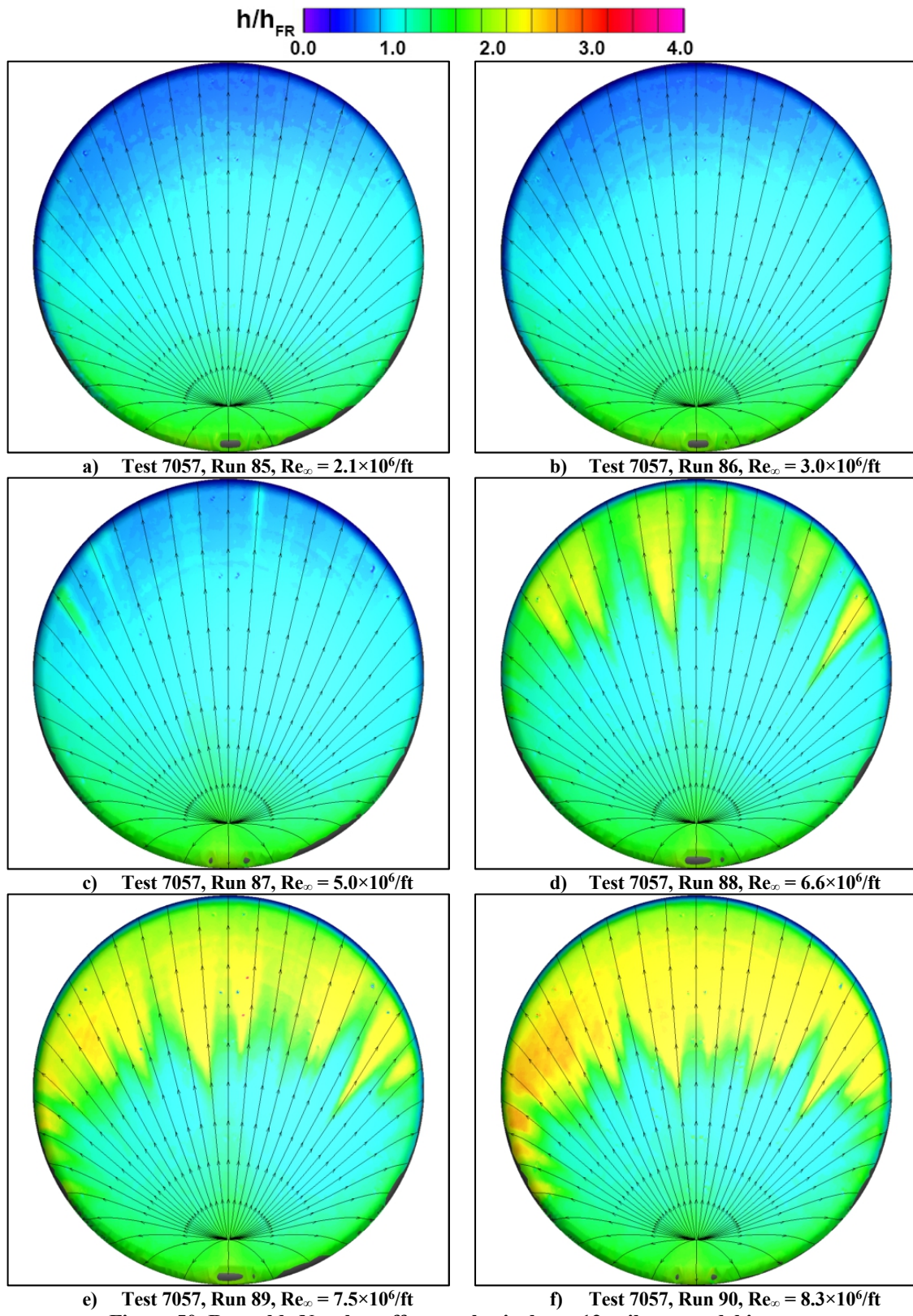
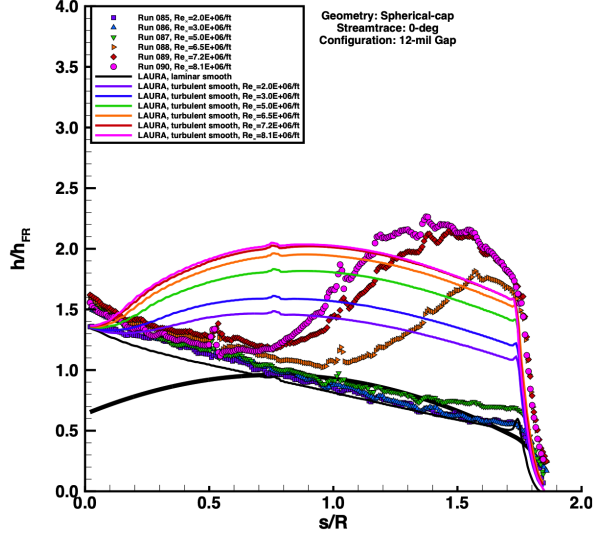
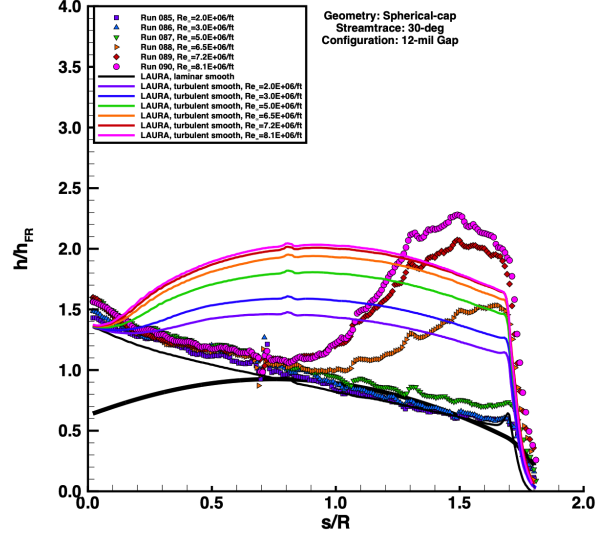


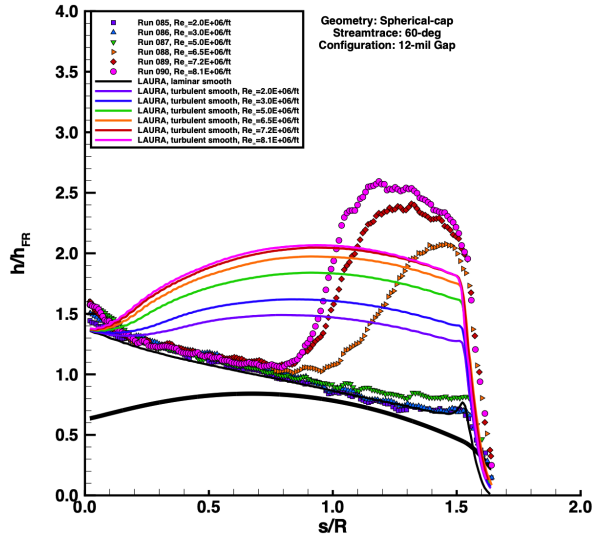
Figure 50. Reynolds Number effects, spherical-cap 12-mil gap model images.



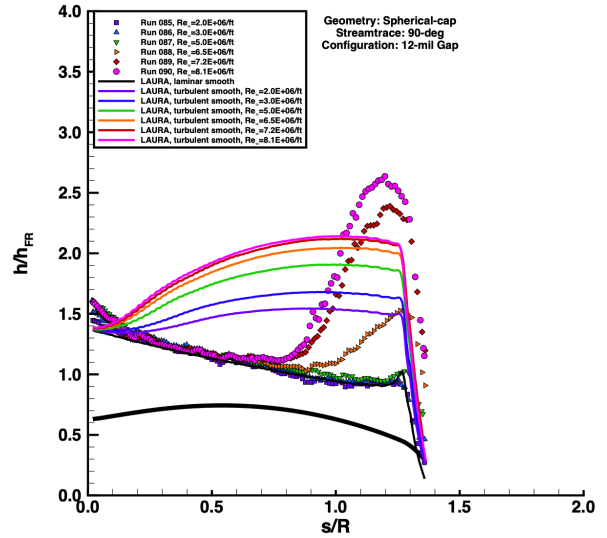
a) 0-deg streamline



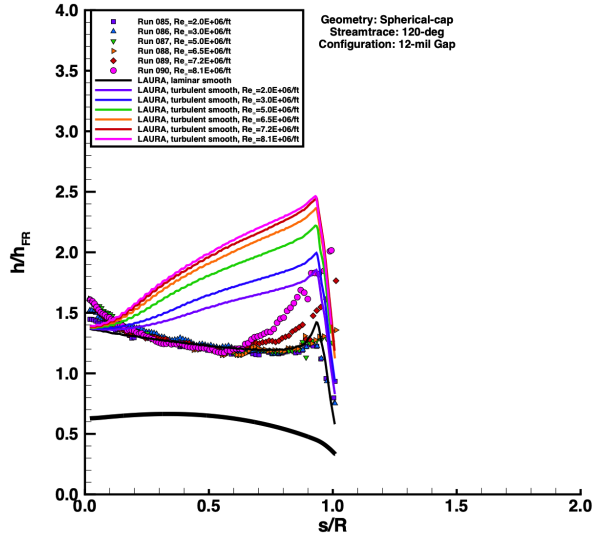
b) 30-deg streamline



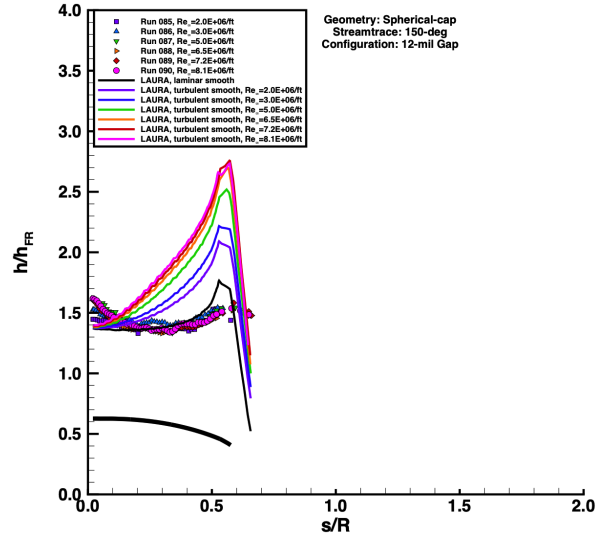
c) 60-deg streamline



d) 90-deg streamline

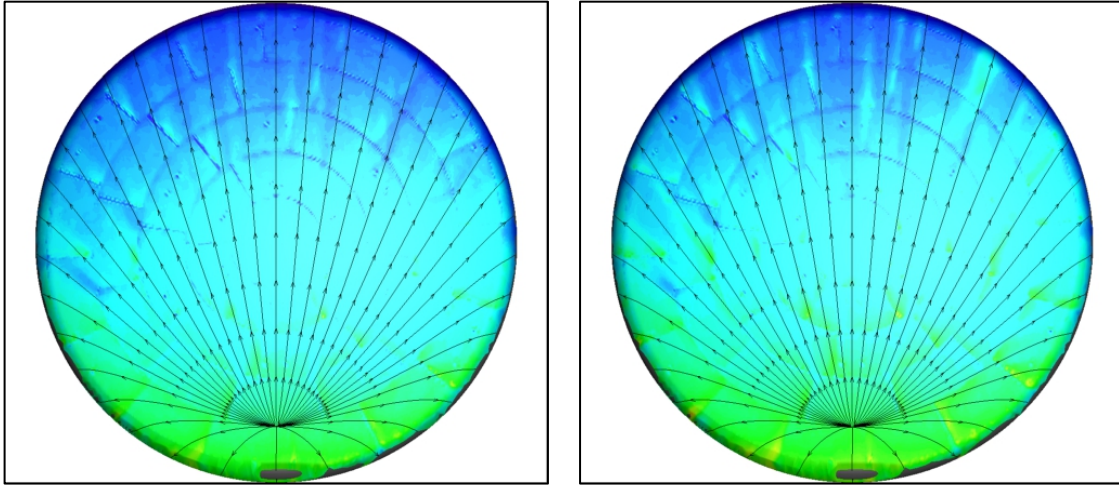
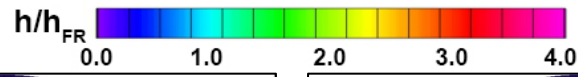


e) 120-deg streamline



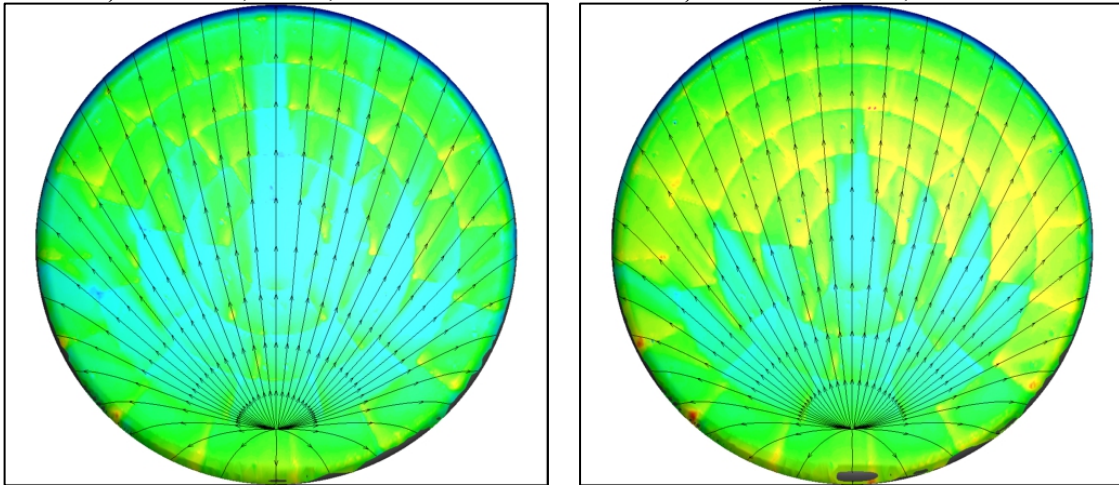
f) 150-deg streamline

Figure 51. Reynolds Number effects, spherical-cap 12-mil gap model plots.



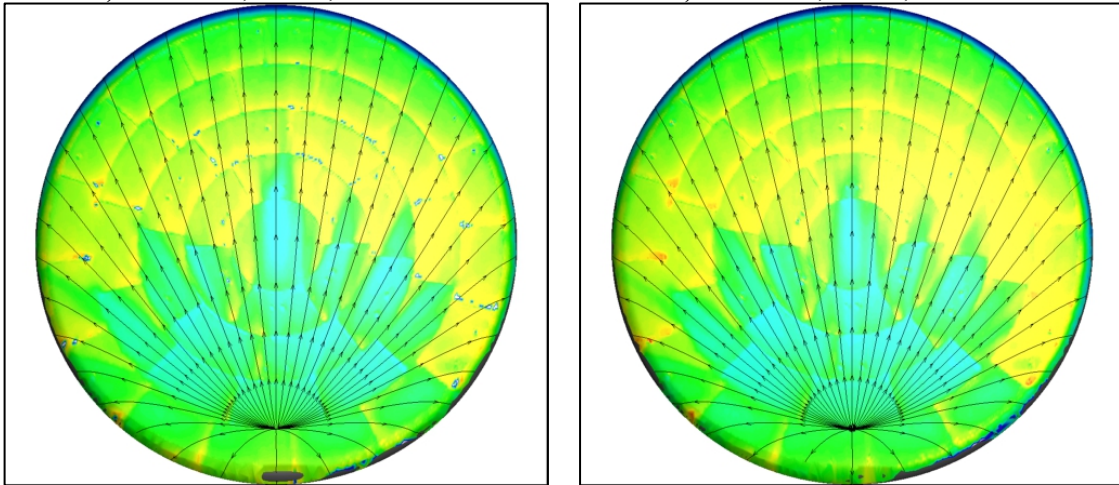
a) Test 7057, Run 91, $Re_\infty = 2.1 \times 10^6/\text{ft}$

b) Test 7057, Run 92, $Re_\infty = 3.0 \times 10^6/\text{ft}$



c) Test 7057, Run 93, $Re_\infty = 5.0 \times 10^6/\text{ft}$

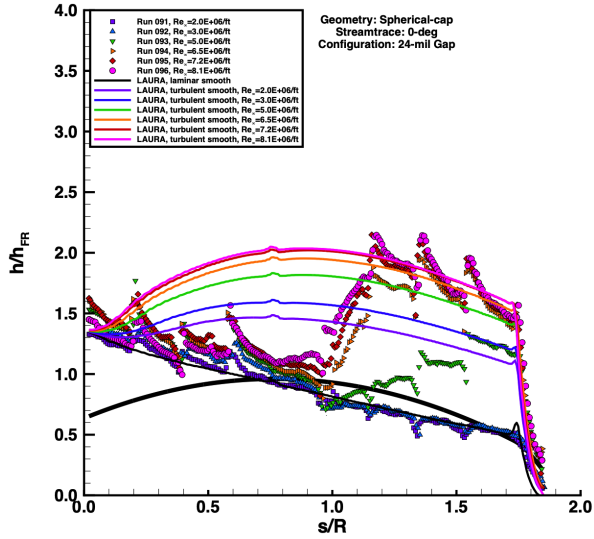
d) Test 7057, Run 94, $Re_\infty = 6.6 \times 10^6/\text{ft}$



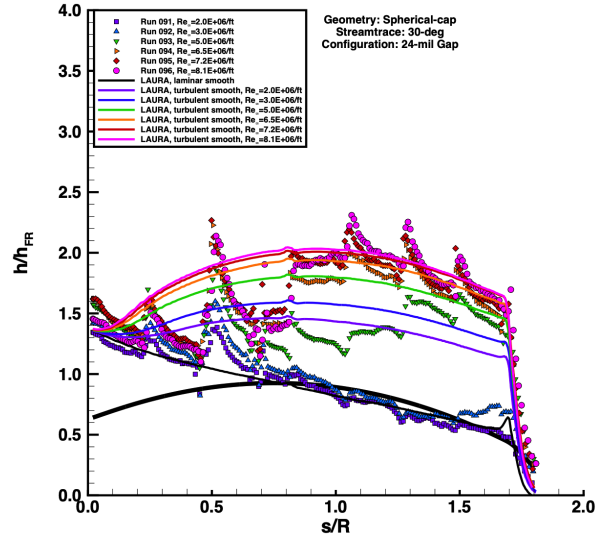
e) Test 7057, Run 95, $Re_\infty = 7.5 \times 10^6/\text{ft}$

f) Test 7057, Run 96, $Re_\infty = 8.3 \times 10^6/\text{ft}$

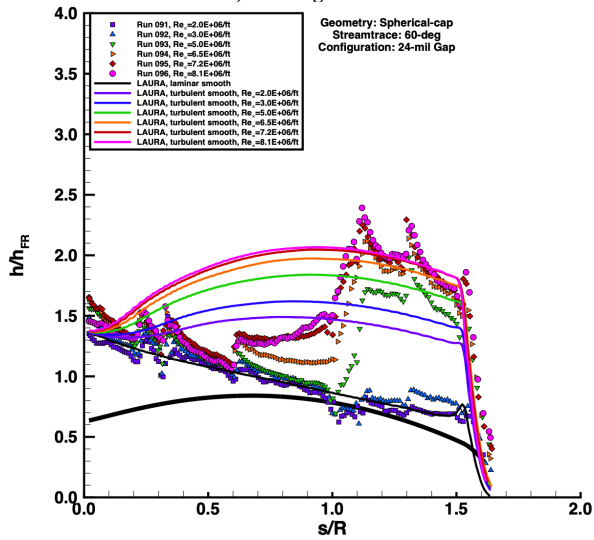
Figure 52. Reynolds Number effects, spherical-cap 24-mil gap model images.



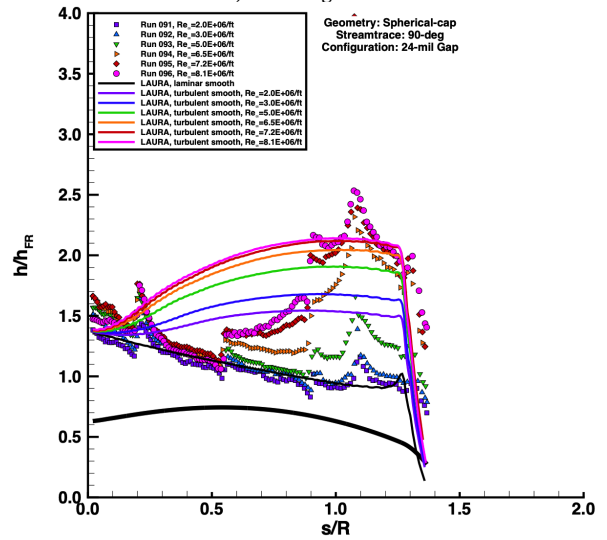
a) 0-deg streamline



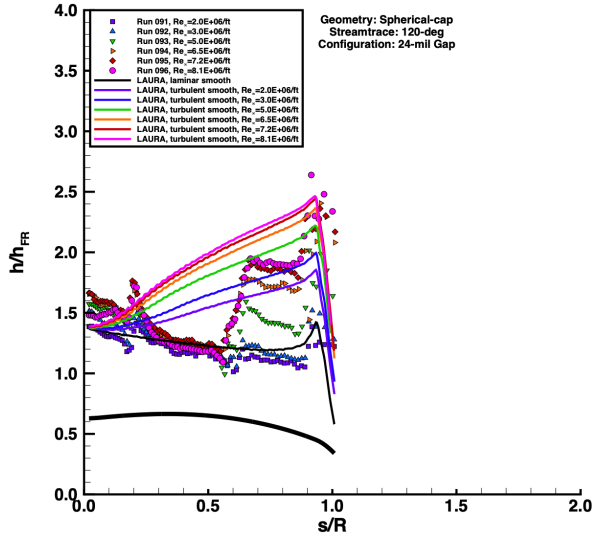
b) 30-deg streamline



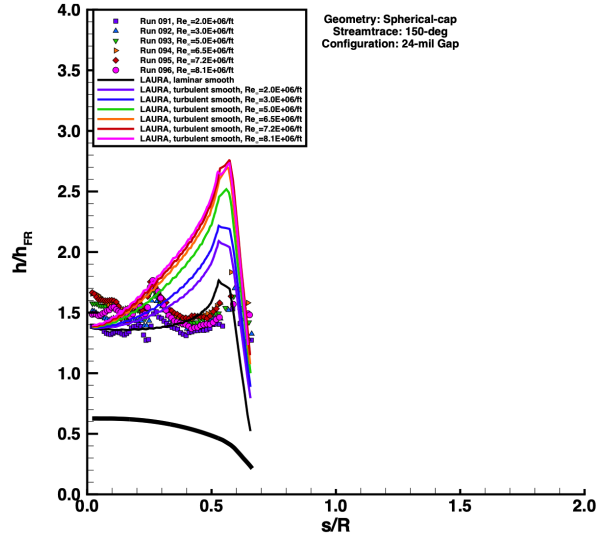
c) 60-deg streamline



d) 90-deg streamline



e) 120-deg streamline



f) 150-deg streamline

Figure 53. Reynolds Number effects, spherical-cap 24-mil gap model plots.

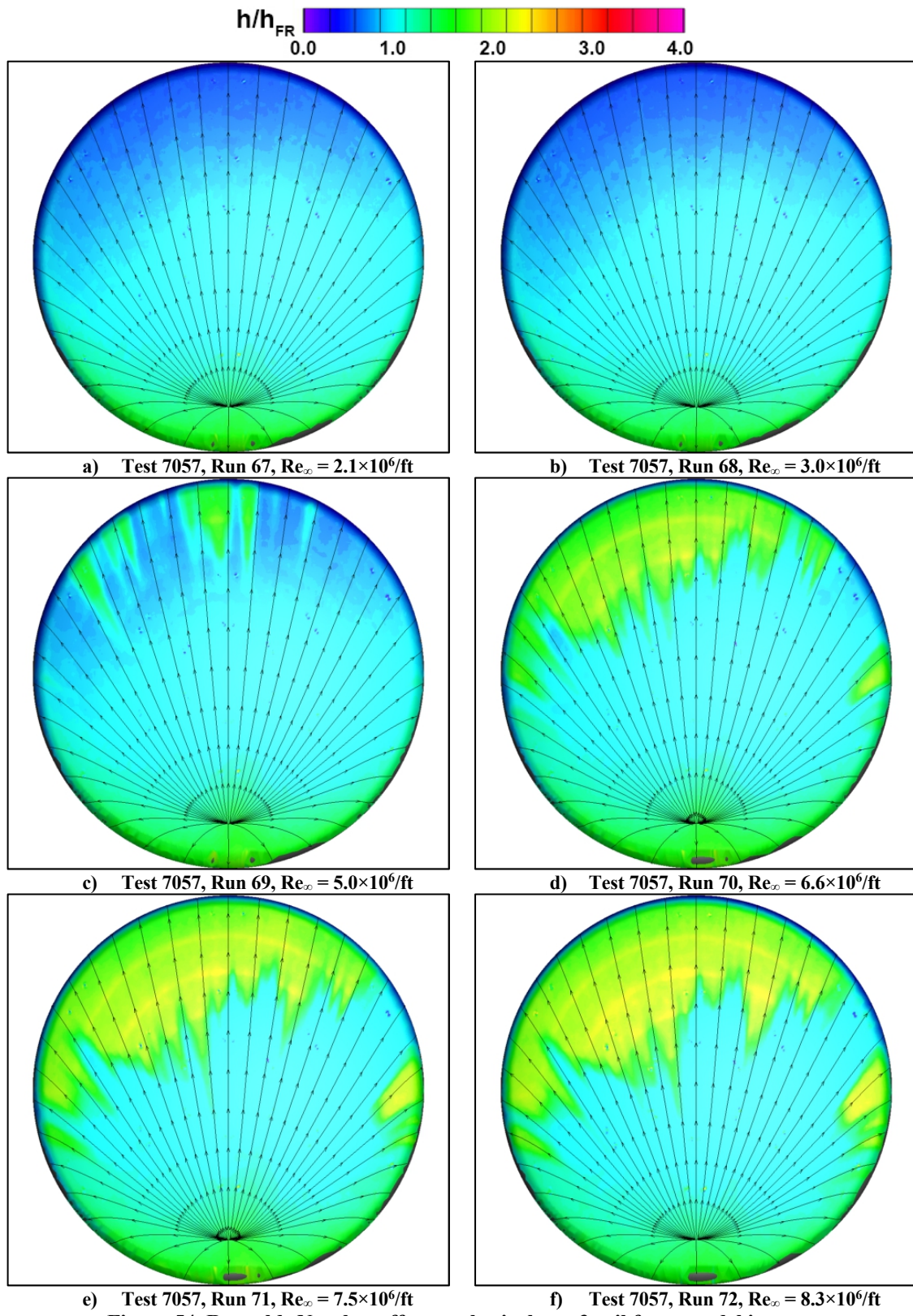
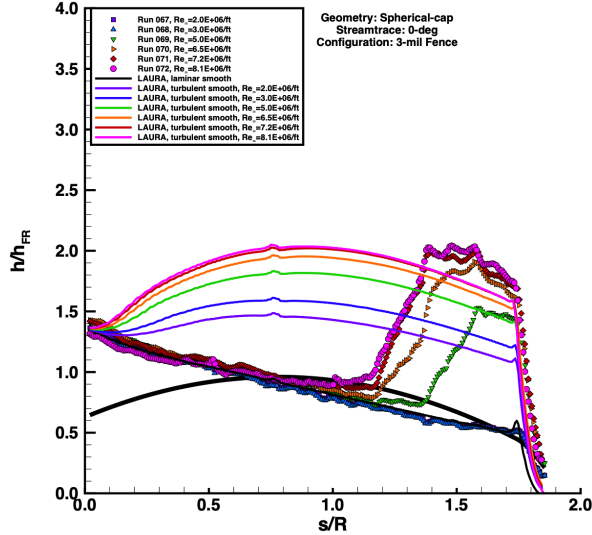
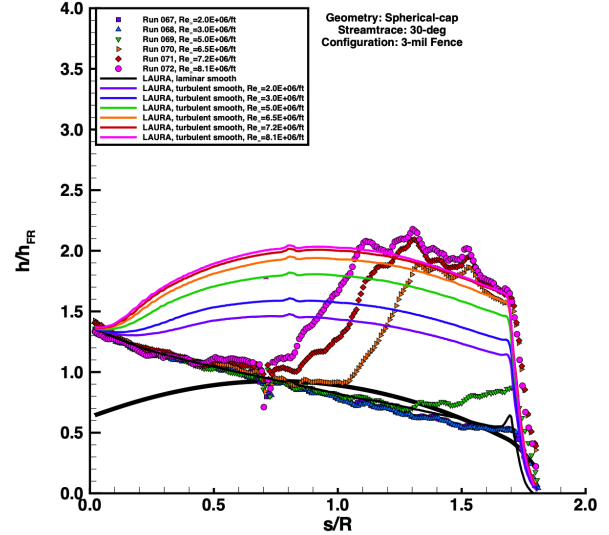


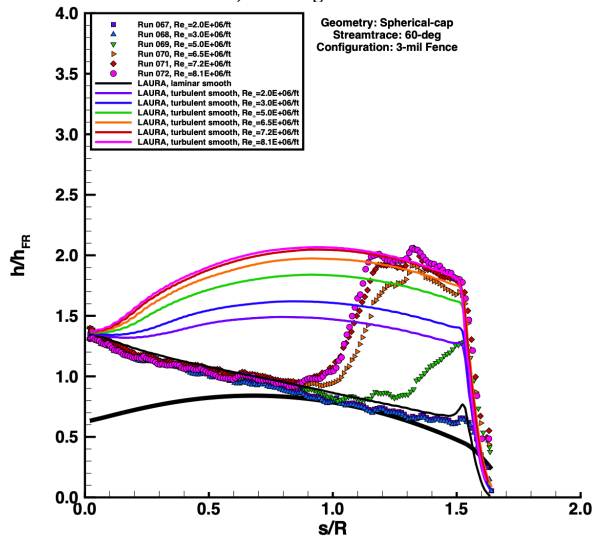
Figure 54. Reynolds Number effects, spherical-cap 3-mil fence model images.



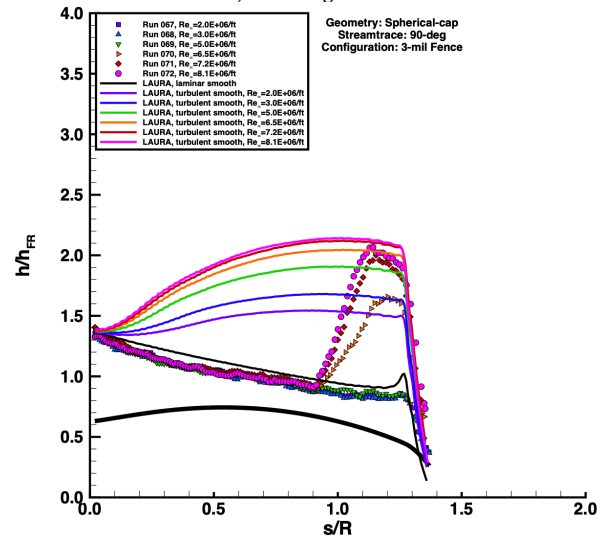
a) 0-deg streamline



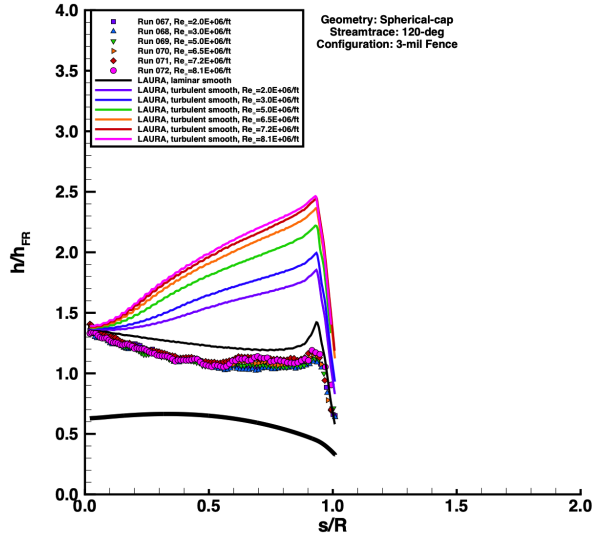
b) 30-deg streamline



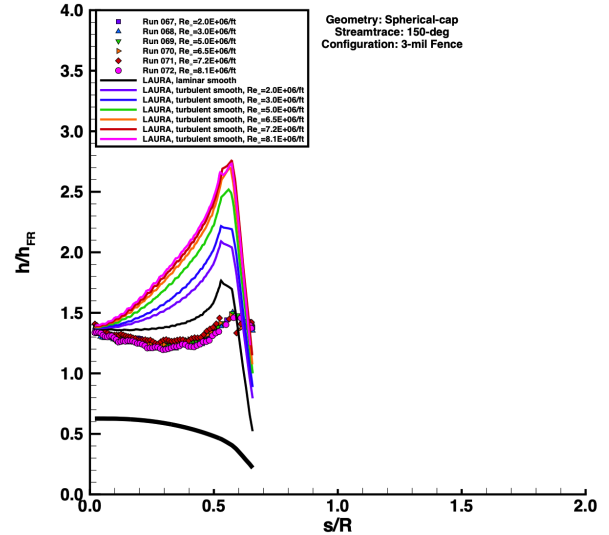
c) 60-deg streamline



d) 90-deg streamline

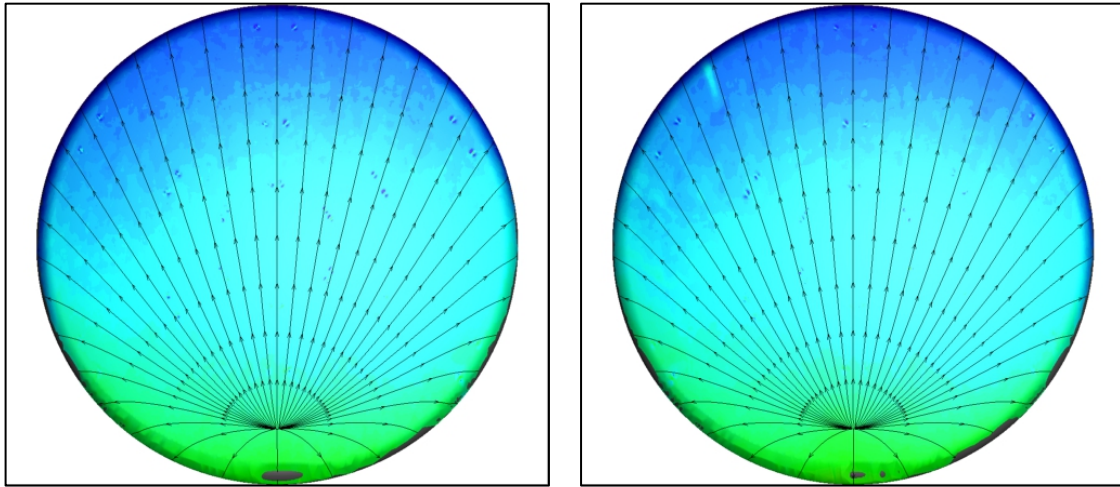
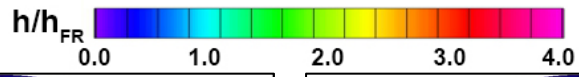


e) 120-deg streamline



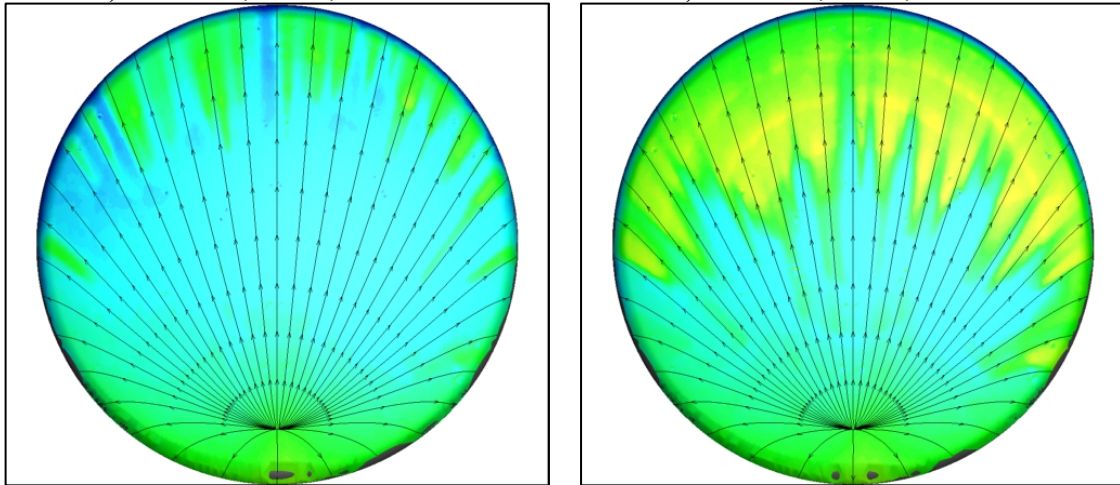
f) 150-deg streamline

Figure 55. Reynolds Number effects, spherical-cap 3-mil fence model plots.



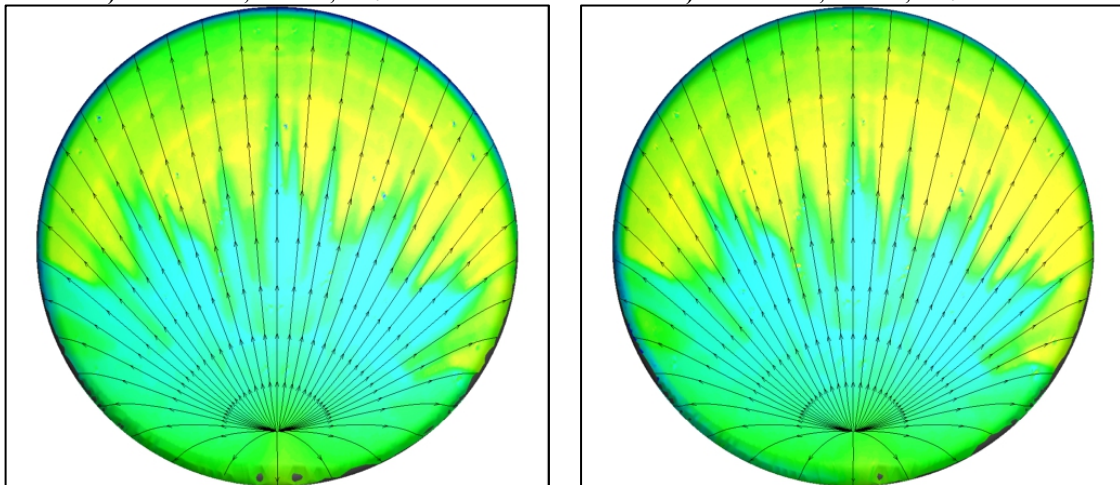
a) Test 7057, Run 73, $Re_\infty = 2.1 \times 10^6/\text{ft}$

b) Test 7057, Run 74, $Re_\infty = 3.0 \times 10^6/\text{ft}$



c) Test 7057, Run 75, $Re_\infty = 5.0 \times 10^6/\text{ft}$

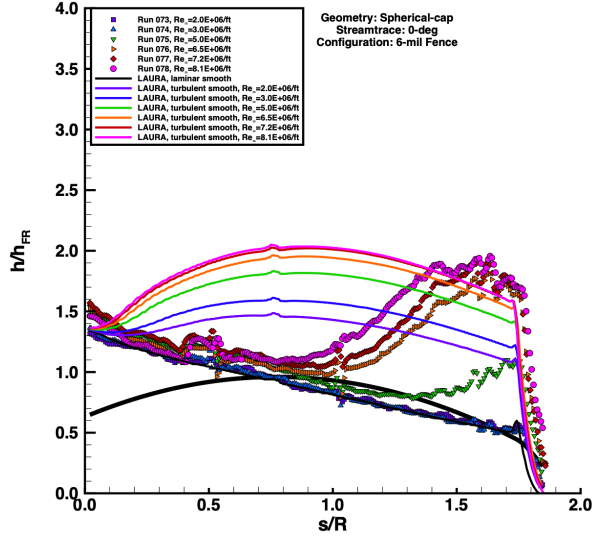
d) Test 7057, Run 76, $Re_\infty = 6.6 \times 10^6/\text{ft}$



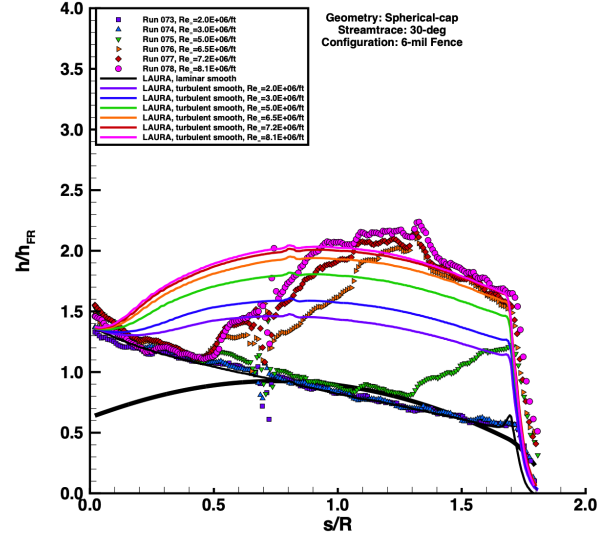
e) Test 7057, Run 77, $Re_\infty = 7.5 \times 10^6/\text{ft}$

f) Test 7057, Run 78, $Re_\infty = 8.3 \times 10^6/\text{ft}$

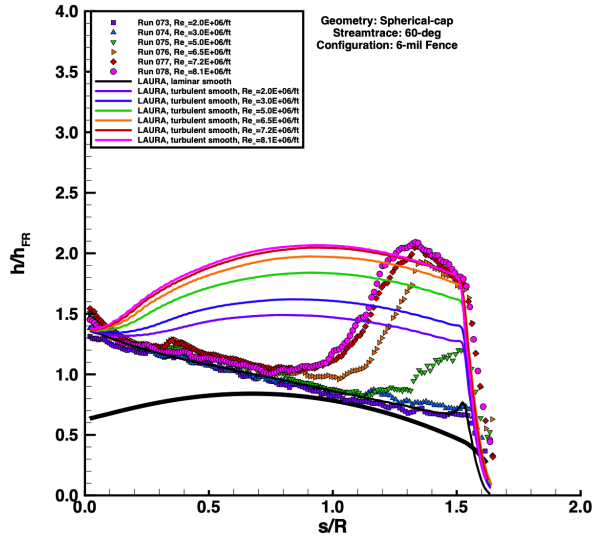
Figure 56. Reynolds Number effects, spherical-cap 6-mil fence model images.



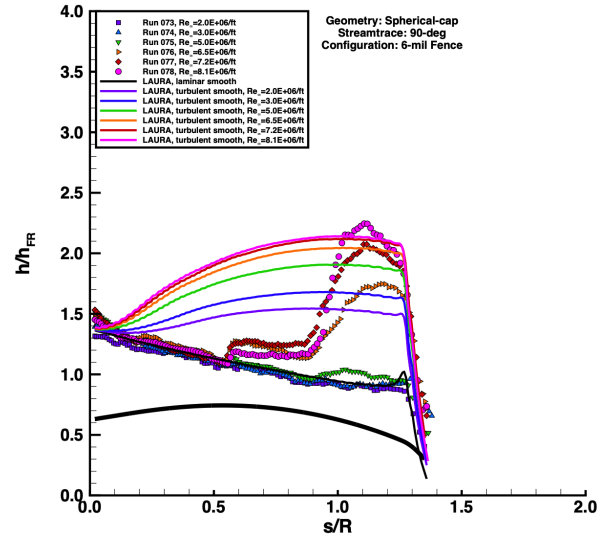
a) 0-deg streamline



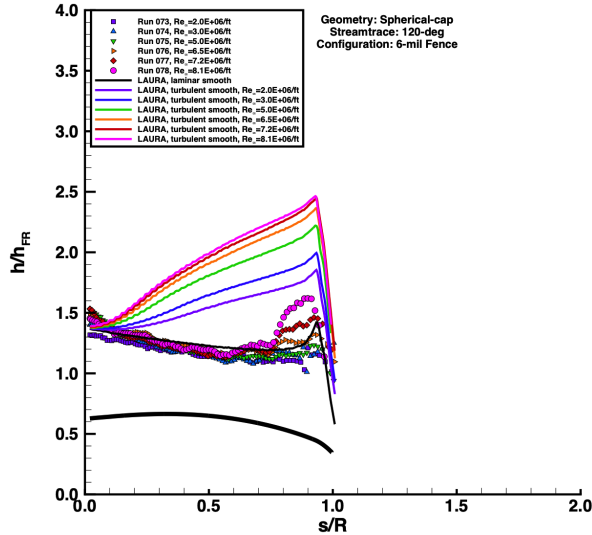
b) 30-deg streamline



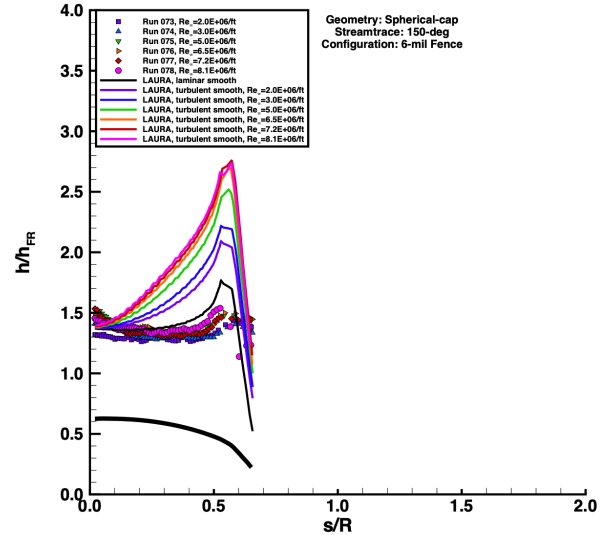
c) 60-deg streamline



d) 90-deg streamline



e) 120-deg streamline



f) 150-deg streamline

Figure 57. Reynolds Number effects, spherical-cap 6-mil fence model plots.

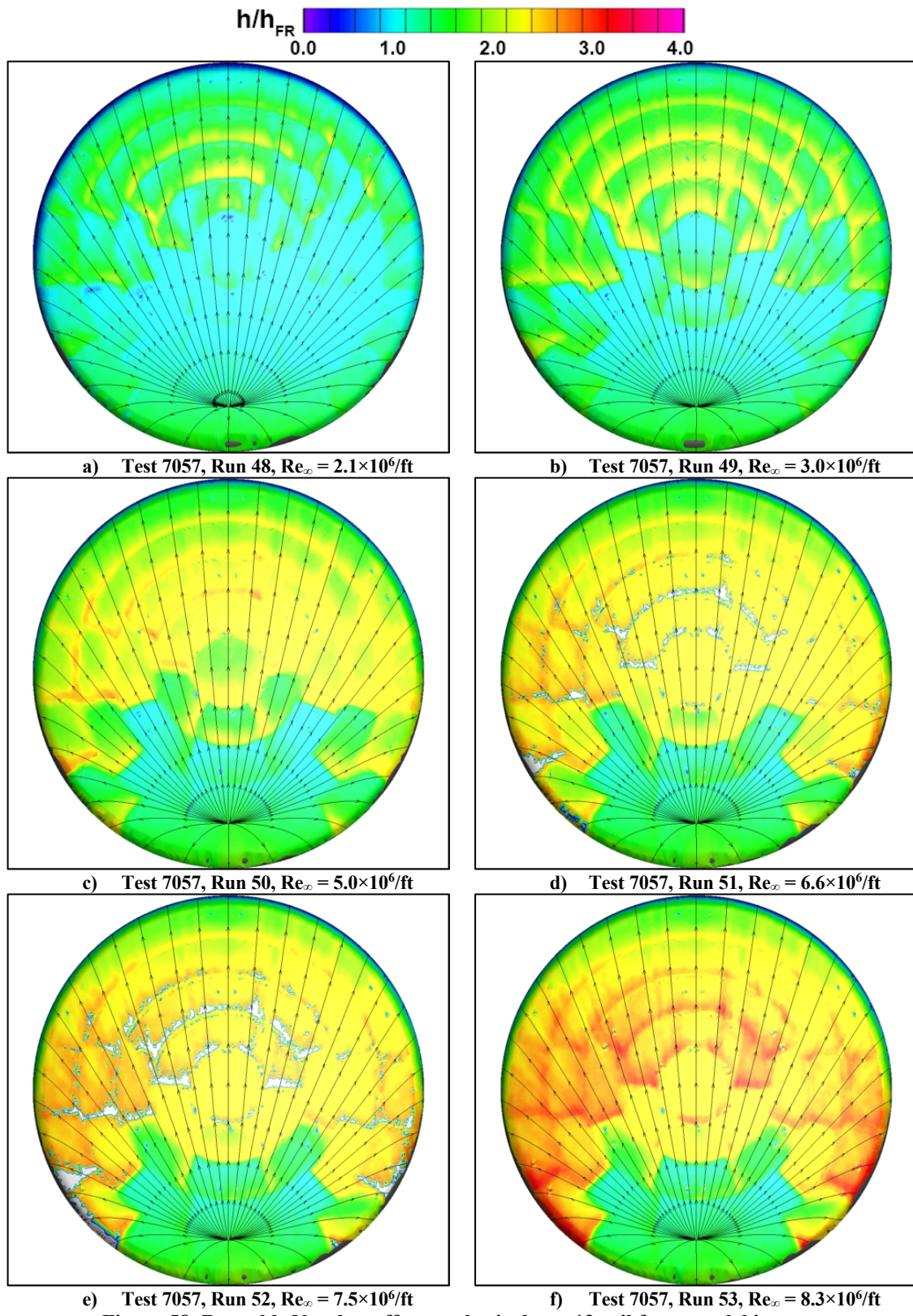
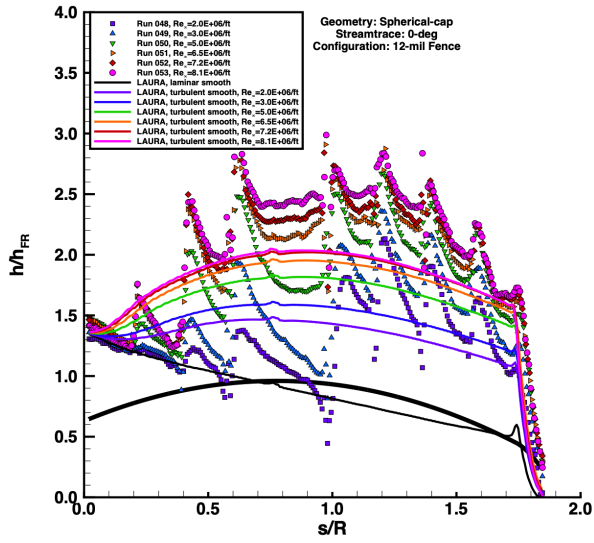
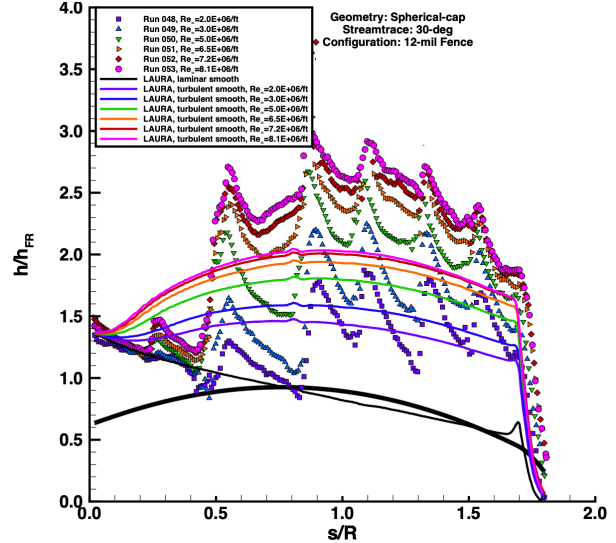


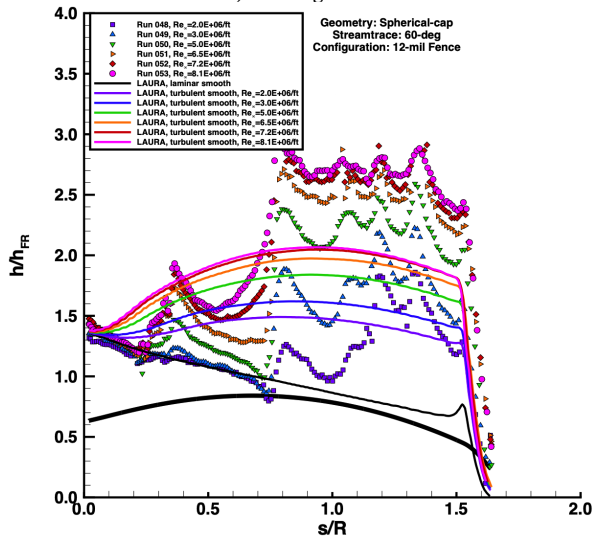
Figure 58. Reynolds Number effects, spherical-cap 12-mil fence model images.



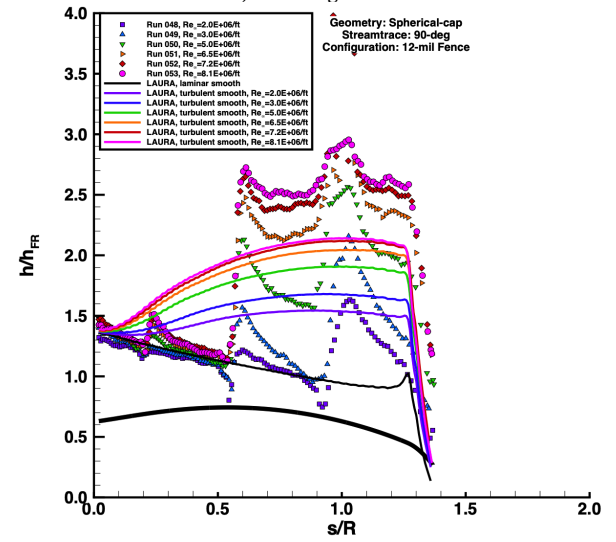
a) 0-deg streamline



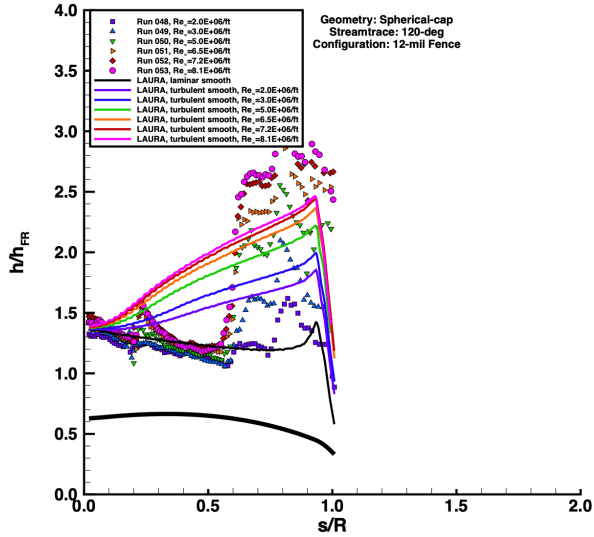
b) 30-deg streamline



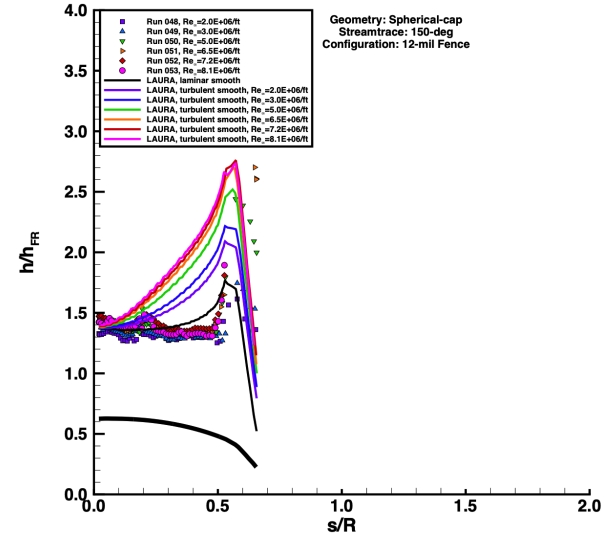
c) 60-deg streamline



d) 90-deg streamline

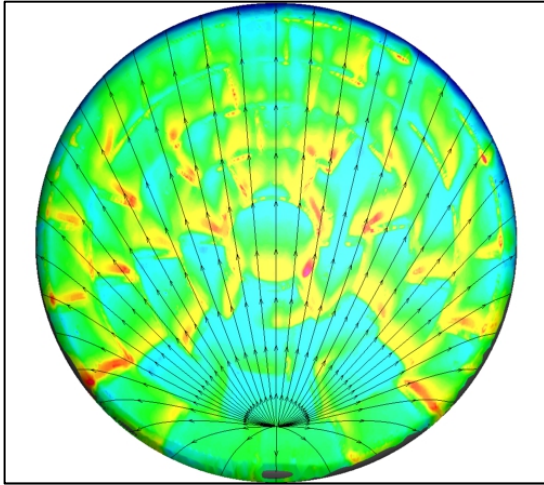
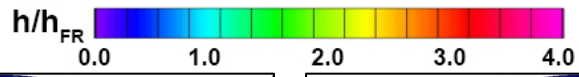


e) 120-deg streamline

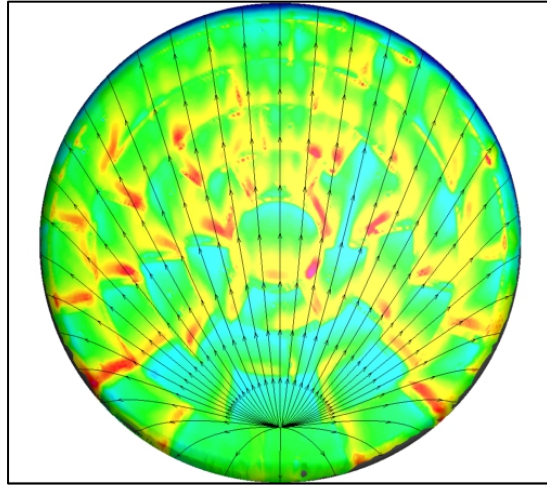


f) 150-deg streamline

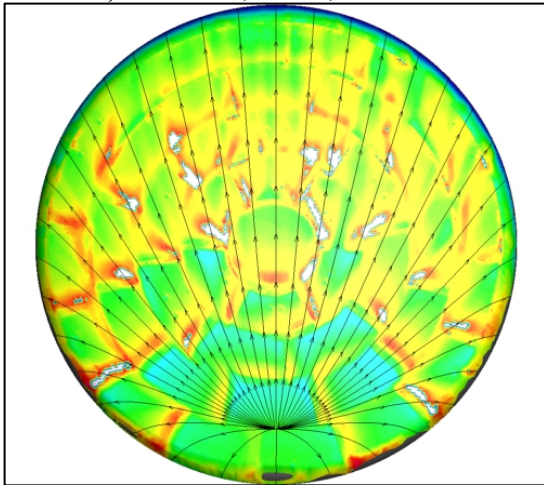
Figure 59. Reynolds Number effects, spherical-cap 12-mil fence model plots.



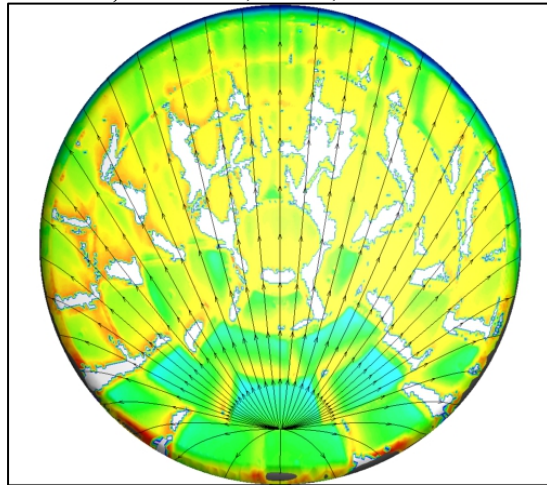
a) Test 7057, Run 97, $Re_\infty = 2.1 \times 10^6/ft$



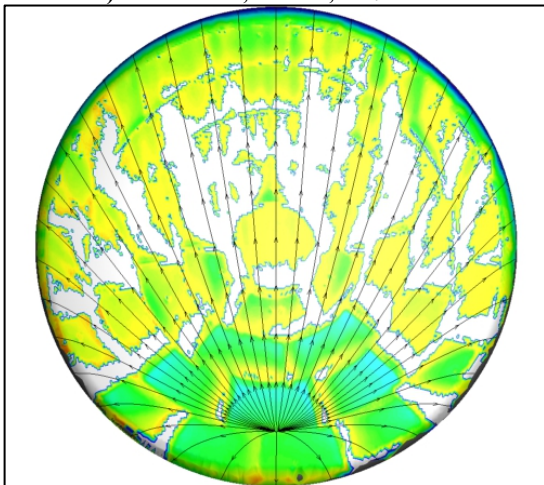
b) Test 7057, Run 98, $Re_\infty = 3.0 \times 10^6/ft$



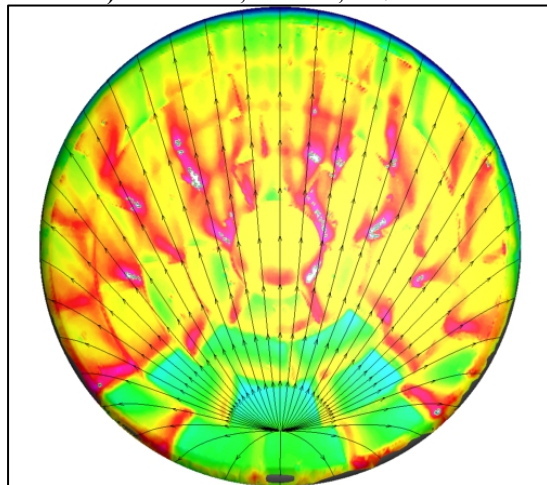
c) Test 7057, Run 99, $Re_\infty = 5.0 \times 10^6/ft$



d) Test 7057, Run 100, $Re_\infty = 6.6 \times 10^6/ft$

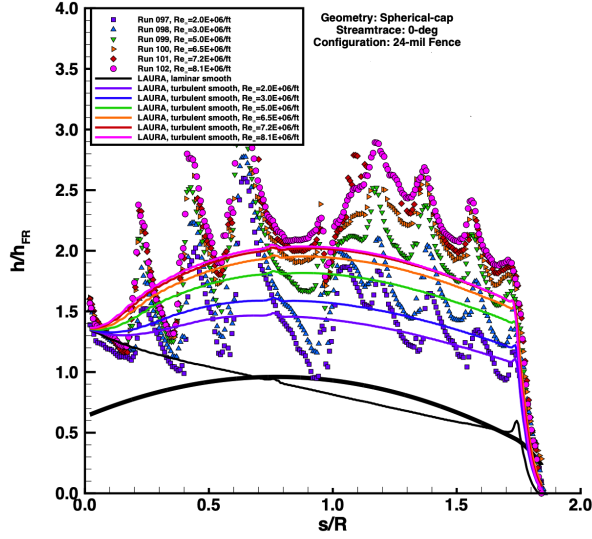


e) Test 7057, Run 101, $Re_\infty = 7.5 \times 10^6/ft$

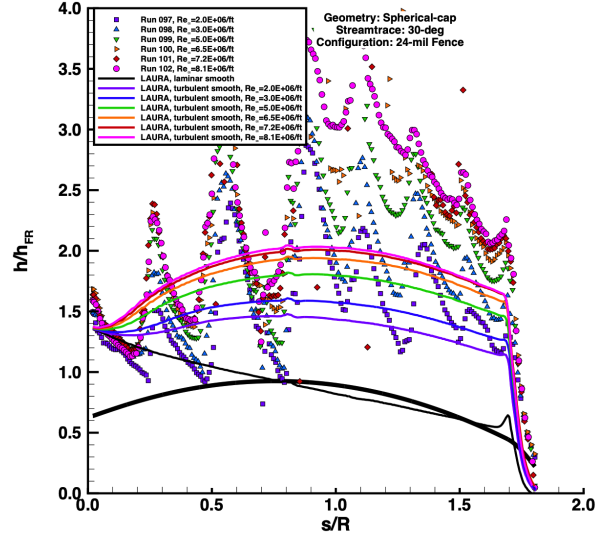


f) Test 7057, Run 102, $Re_\infty = 8.3 \times 10^6/ft$

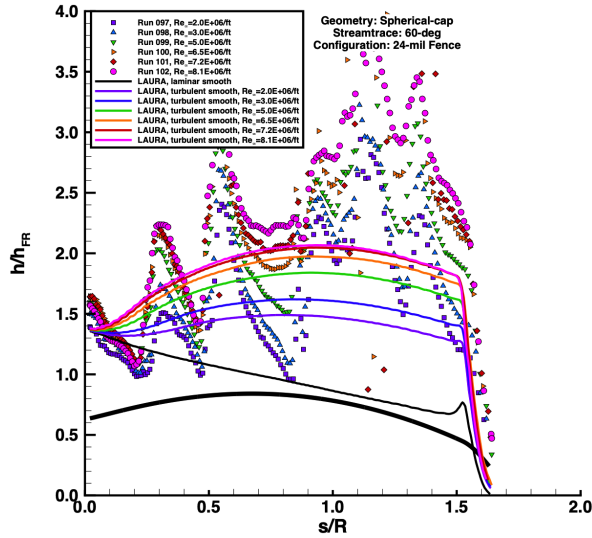
Figure 60. Reynolds Number effects, spherical-cap 24-mil fence model images.



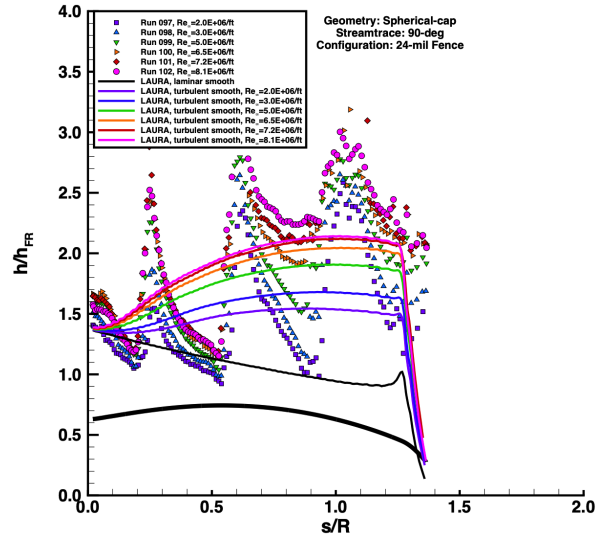
a) 0-deg streamline



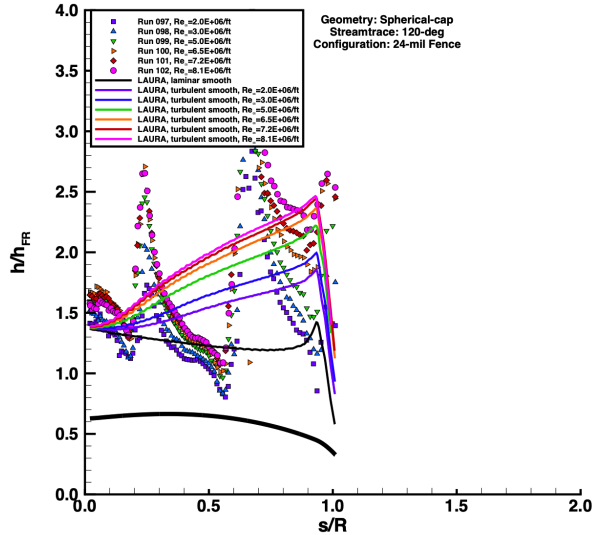
b) 30-deg streamline



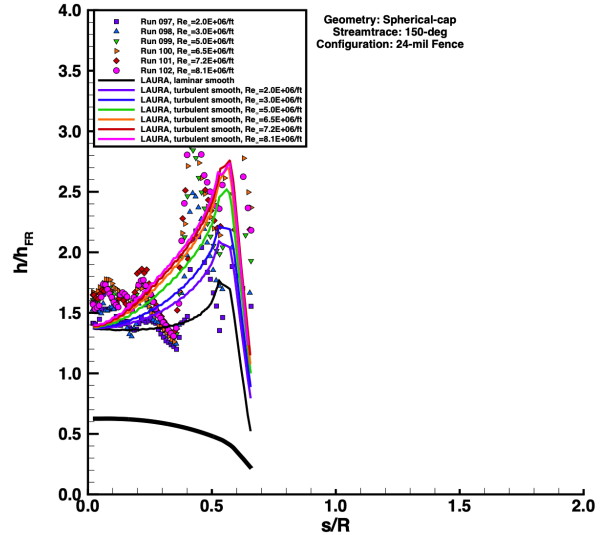
c) 60-deg streamline



d) 90-deg streamline



e) 120-deg streamline



f) 150-deg streamline

Figure 61. Reynolds Number effects, spherical-cap 24-mil fence model plots.

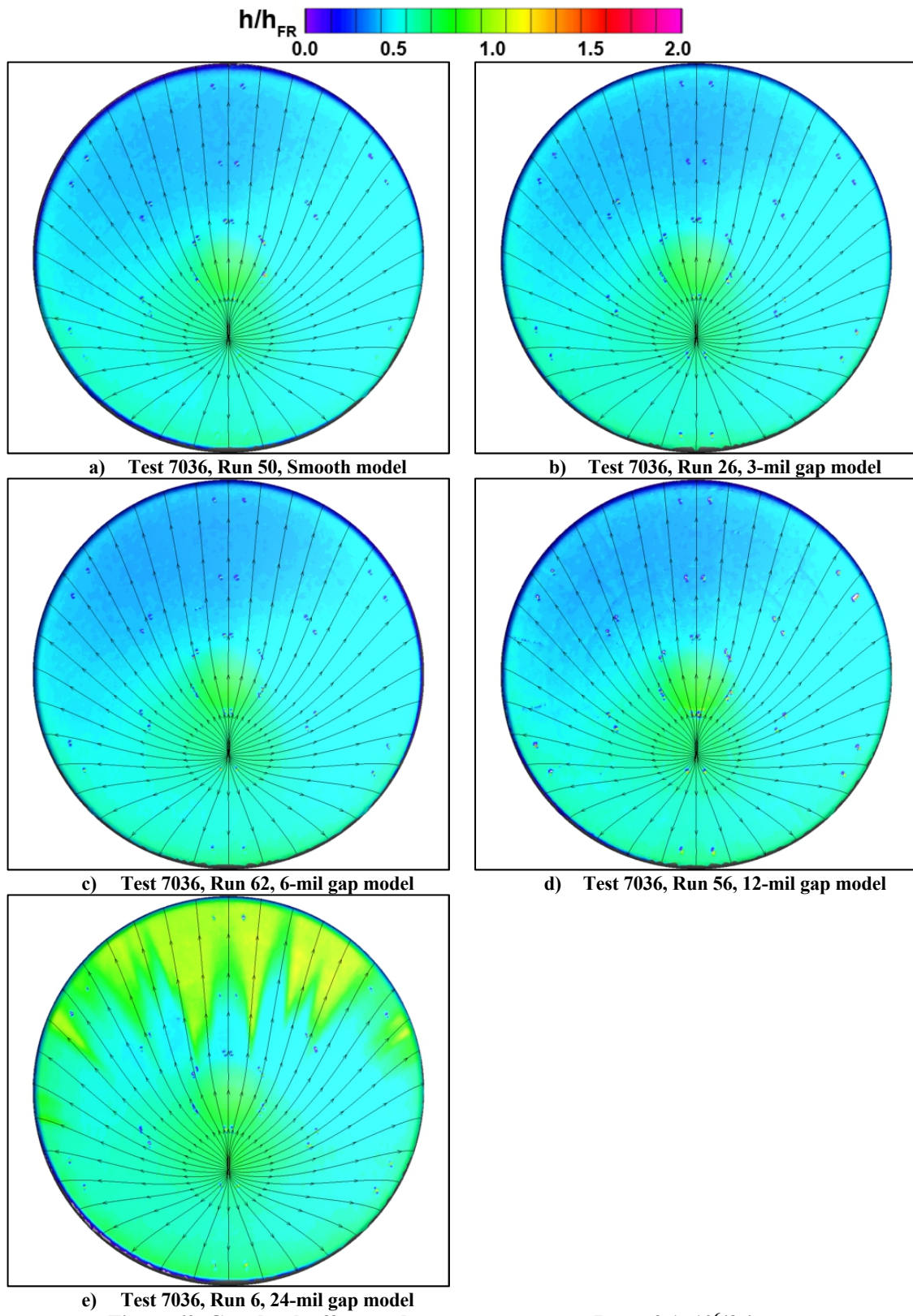


Figure 62. Gap depth effects, sphere-cone geometry, $Re_\infty = 2.1 \times 10^6$ /ft images.

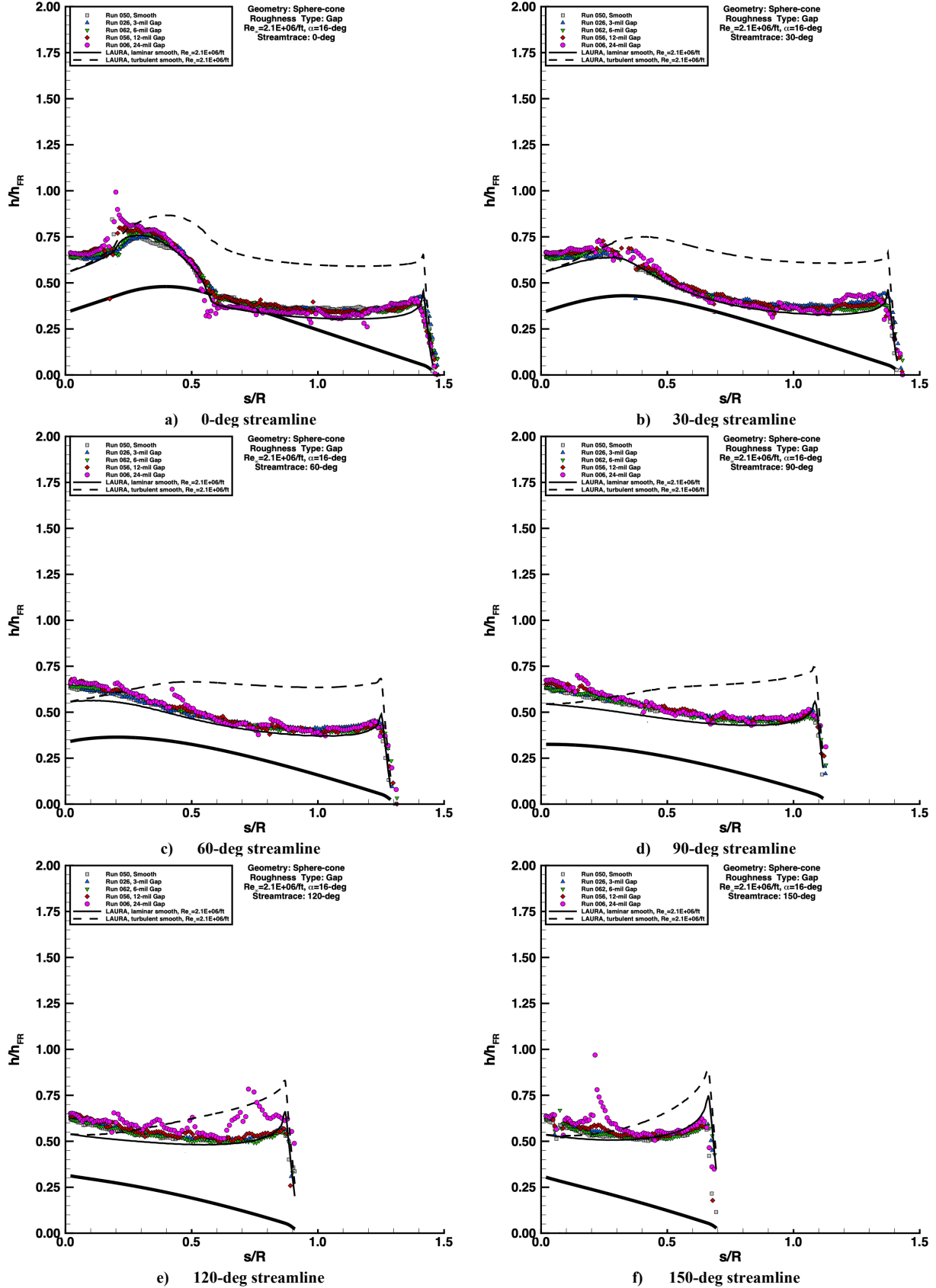


Figure 63. Gap depth effects, sphere-cone geometry, $Re_{\infty} = 2.1 \times 10^6/ft$ plots.

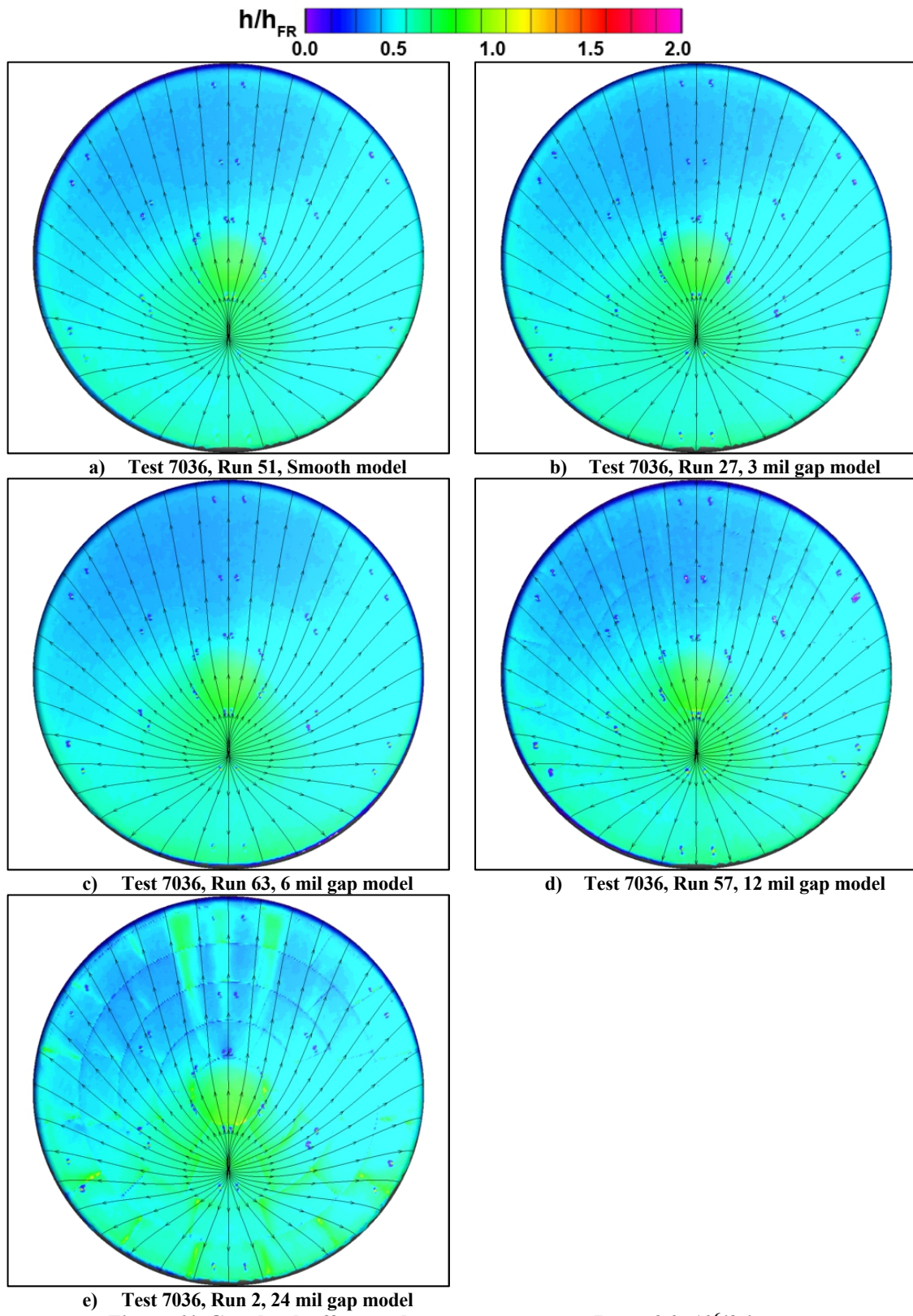


Figure 64. Gap depth effects, sphere-cone geometry, $Re_\infty = 3.0 \times 10^6$ /ft images.

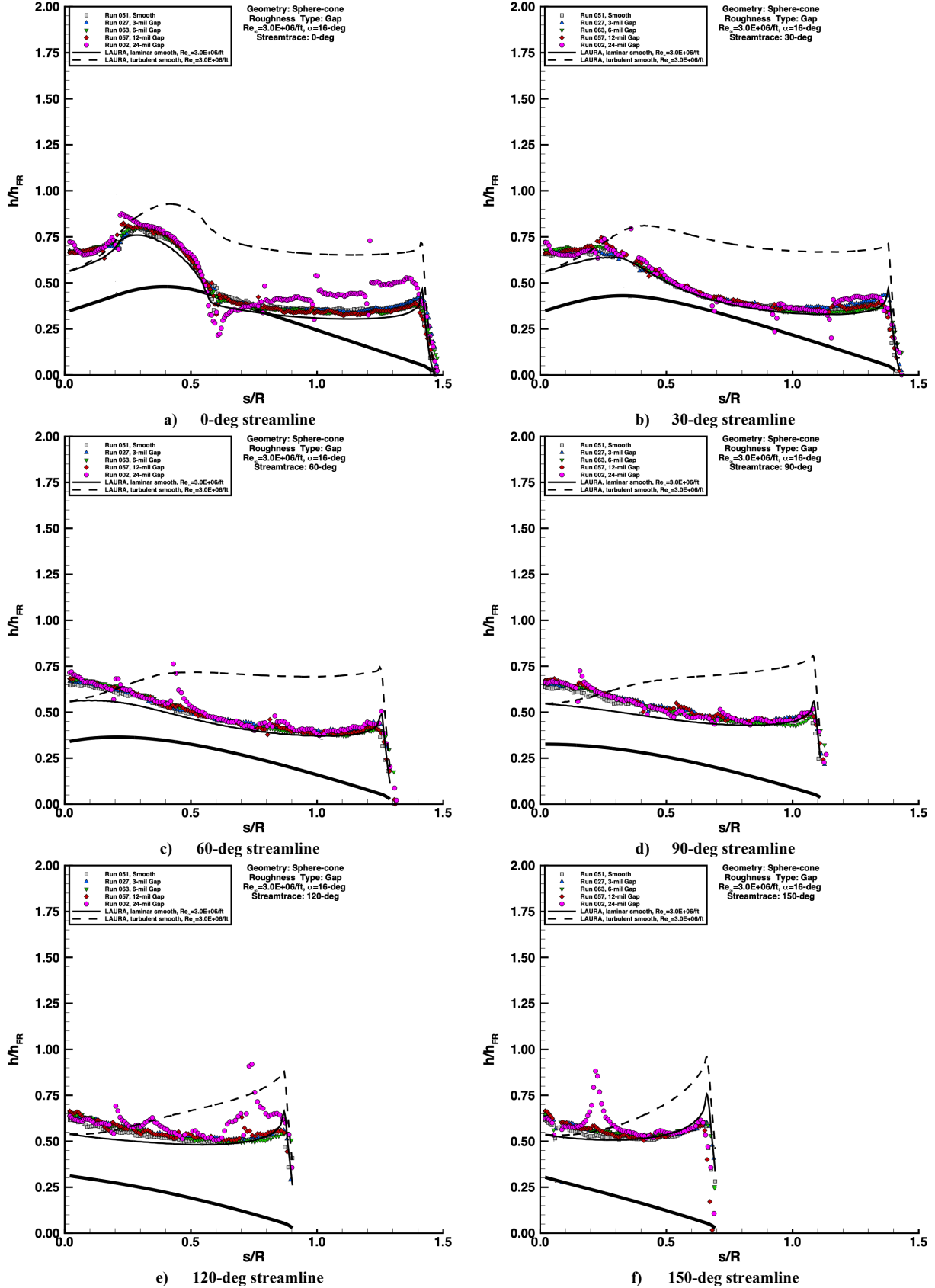


Figure 65. Gap depth effects, sphere-cone geometry, $Re_\infty = 3.0 \times 10^6/ft$ plots.

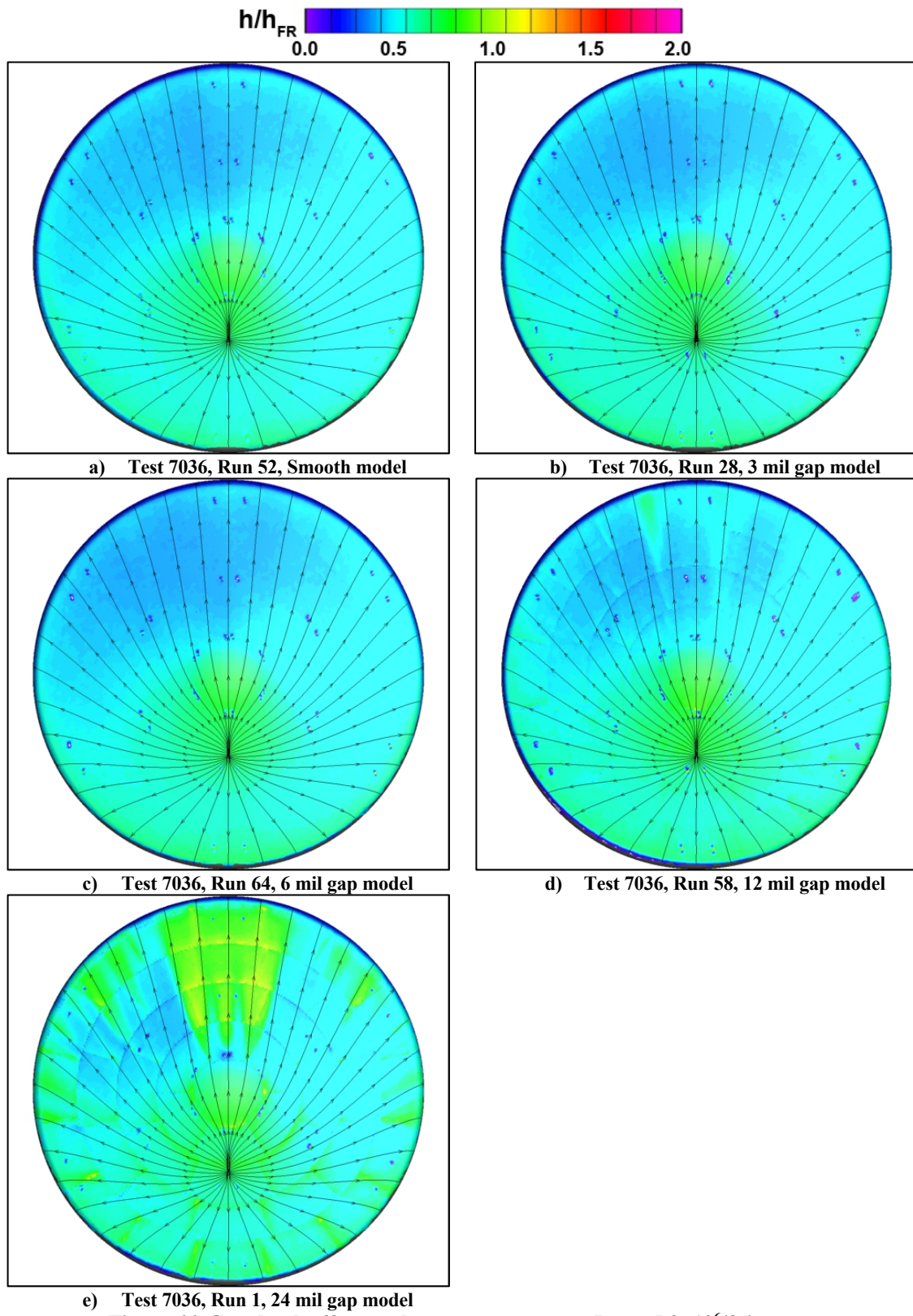


Figure 66. Gap depth effects, sphere-cone geometry, $Re_\infty = 5.0 \times 10^6$ /ft images.

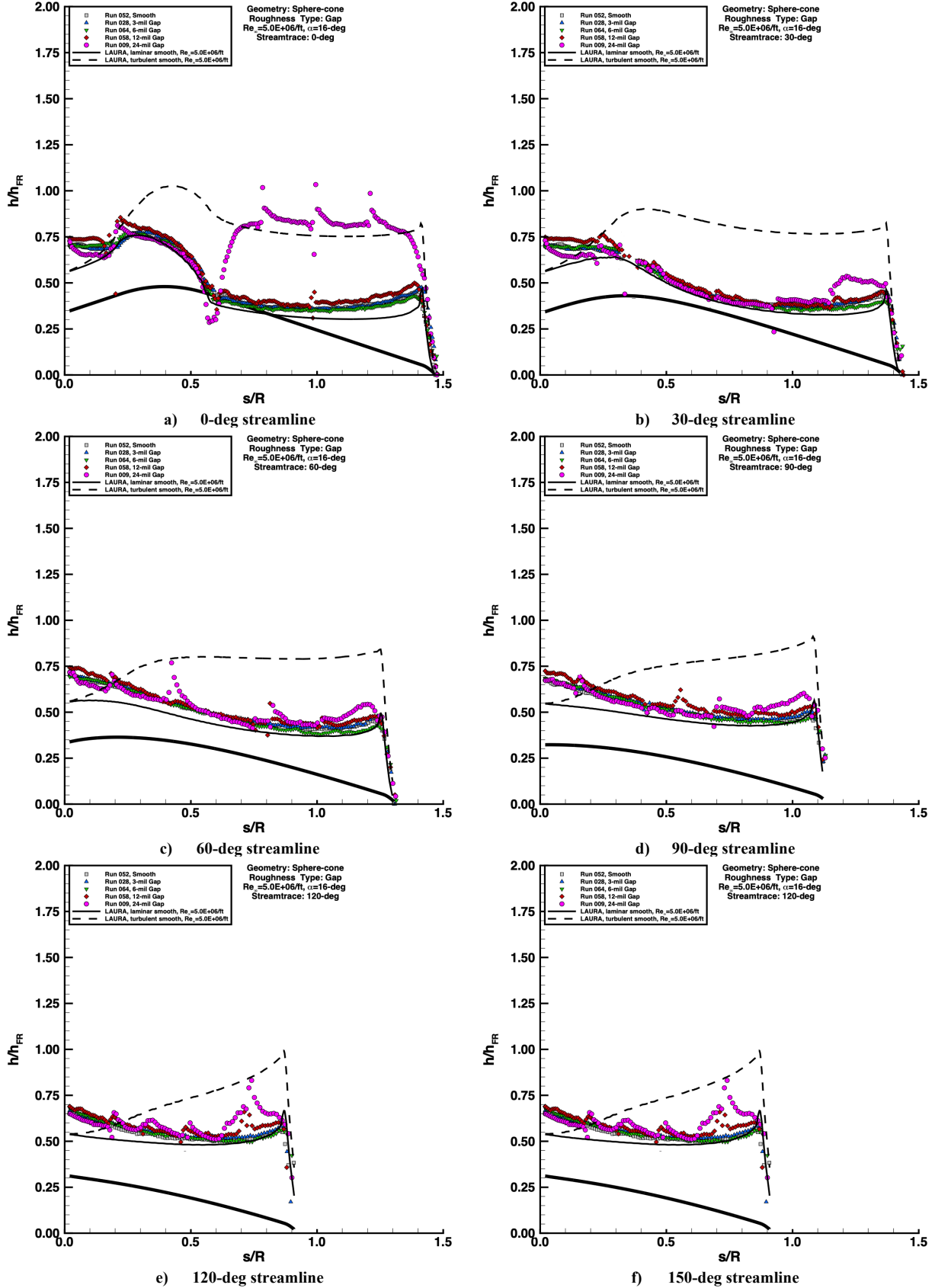


Figure 67. Gap depth effects, sphere-cone geometry, $Re_{\infty} = 5.0 \times 10^6/ft$ plots.

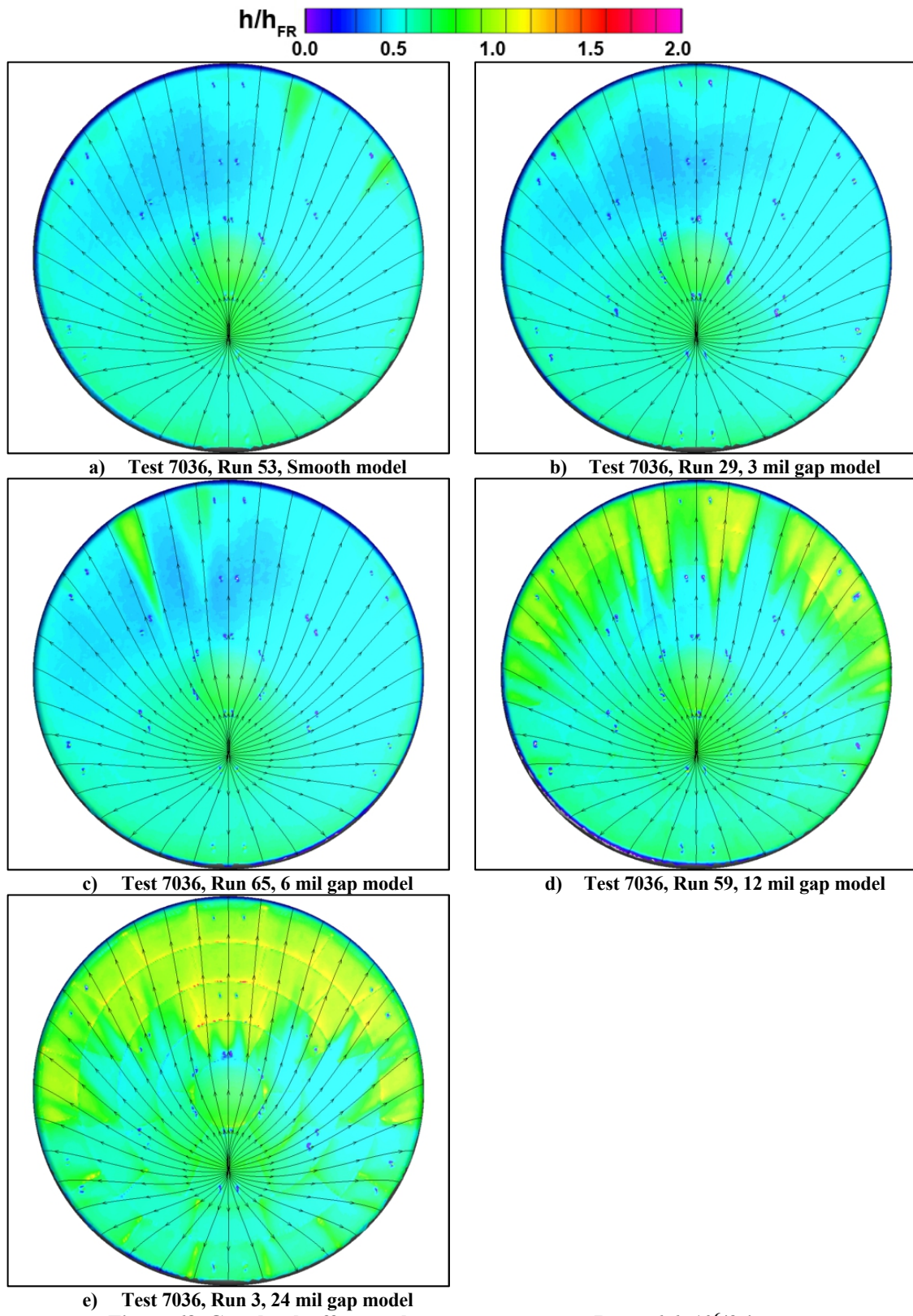


Figure 68. Gap depth effects, sphere-cone geometry, $Re_\infty = 6.6 \times 10^6$ /ft images.

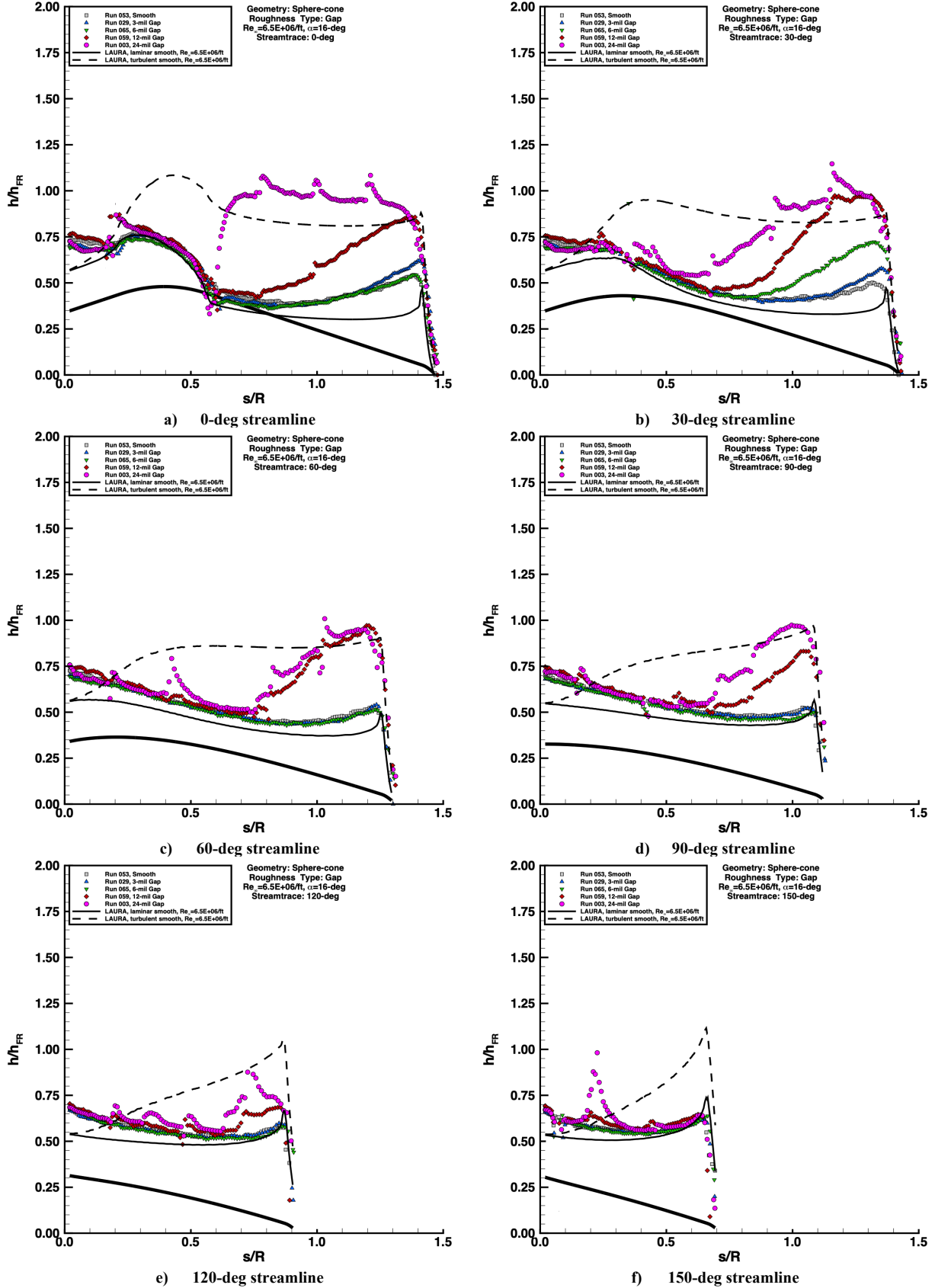


Figure 69. Gap depth effects, sphere-cone geometry, $Re_{\infty} = 6.6 \times 10^6/ft$ plots.

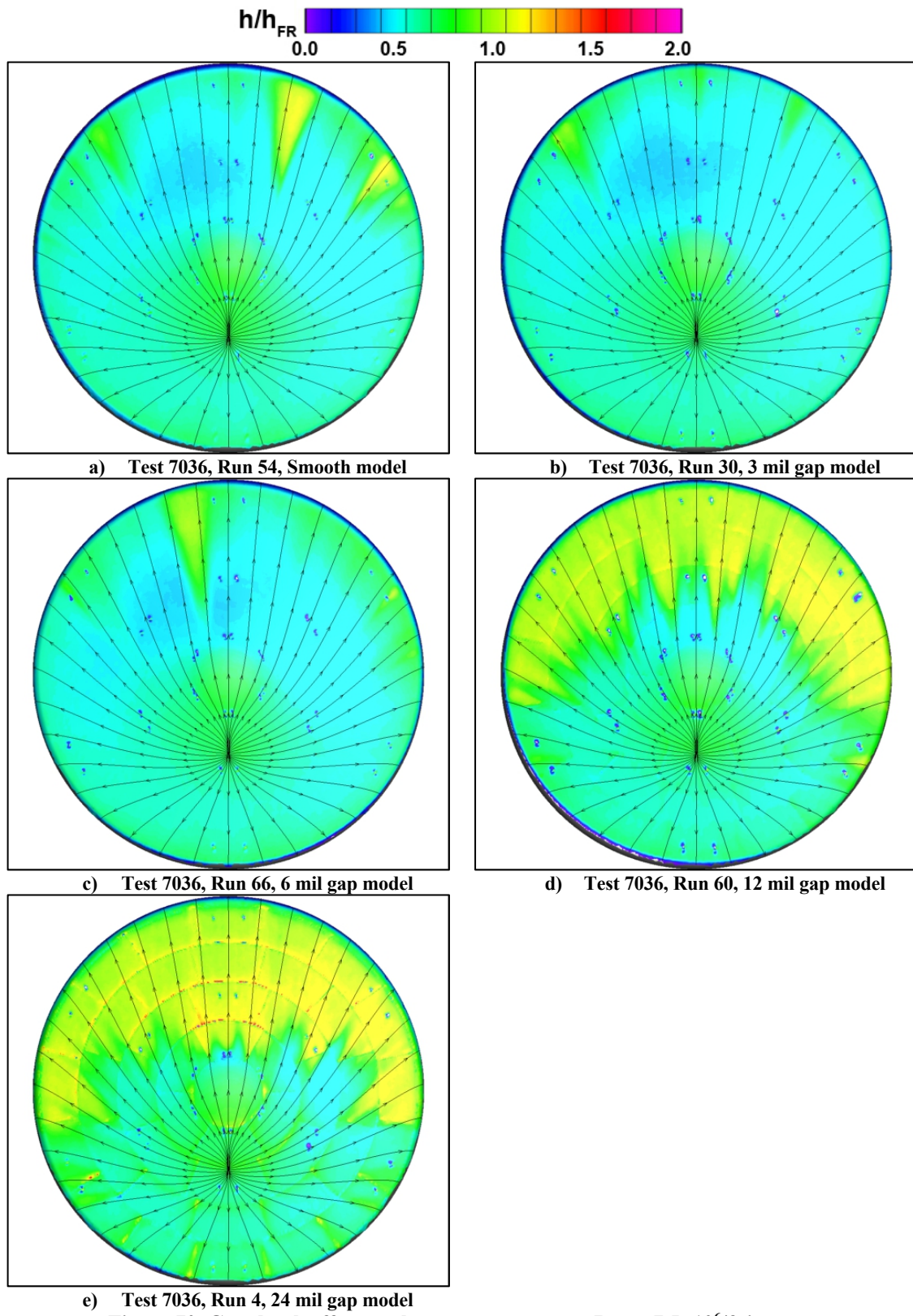


Figure 70. Gap depth effects, sphere-cone geometry, $Re_\infty = 7.5 \times 10^6$ /ft images.

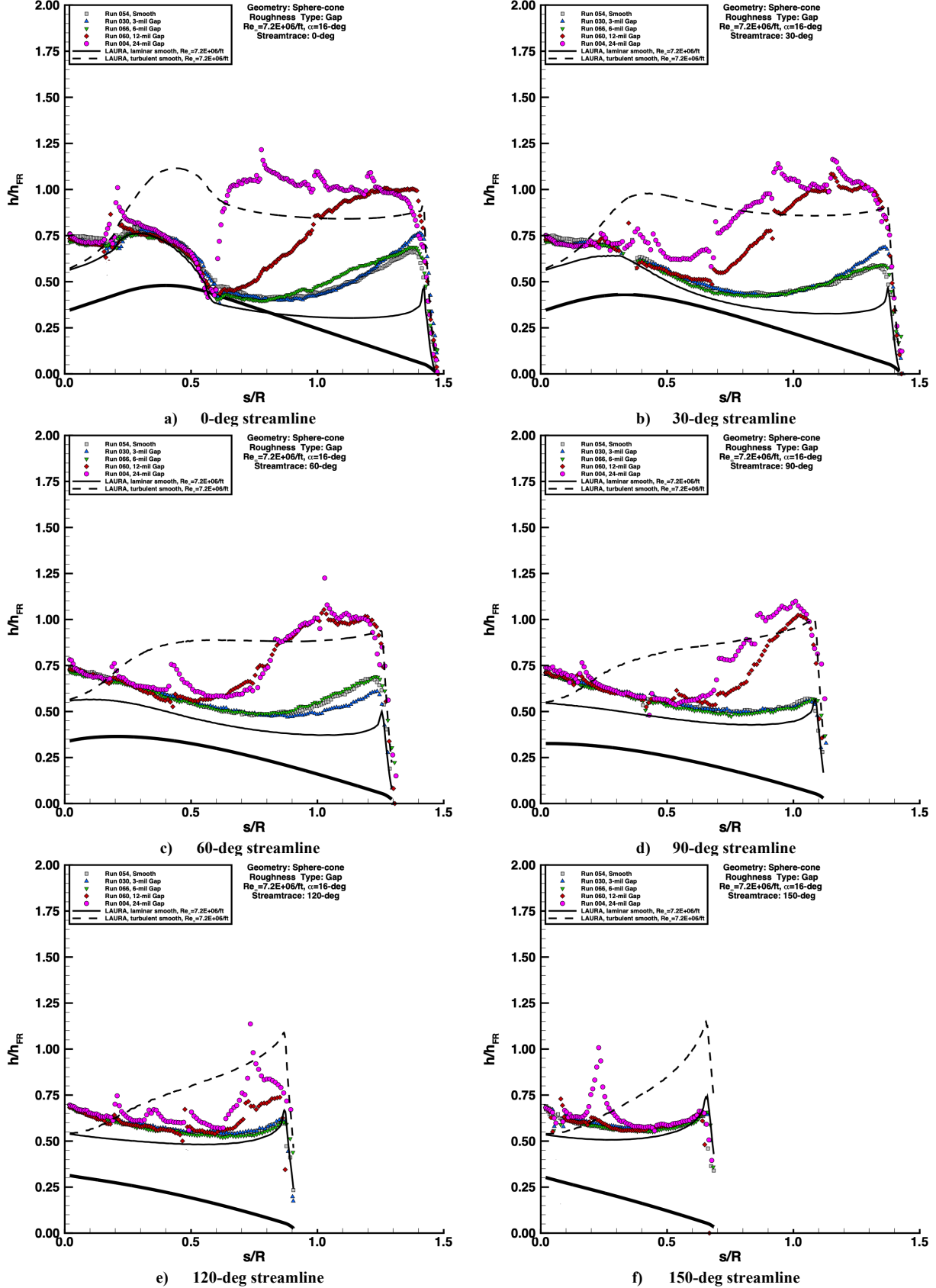


Figure 71. Gap depth effects, sphere-cone geometry, $Re_{\infty} = 7.5 \times 10^6/ft$ plots.

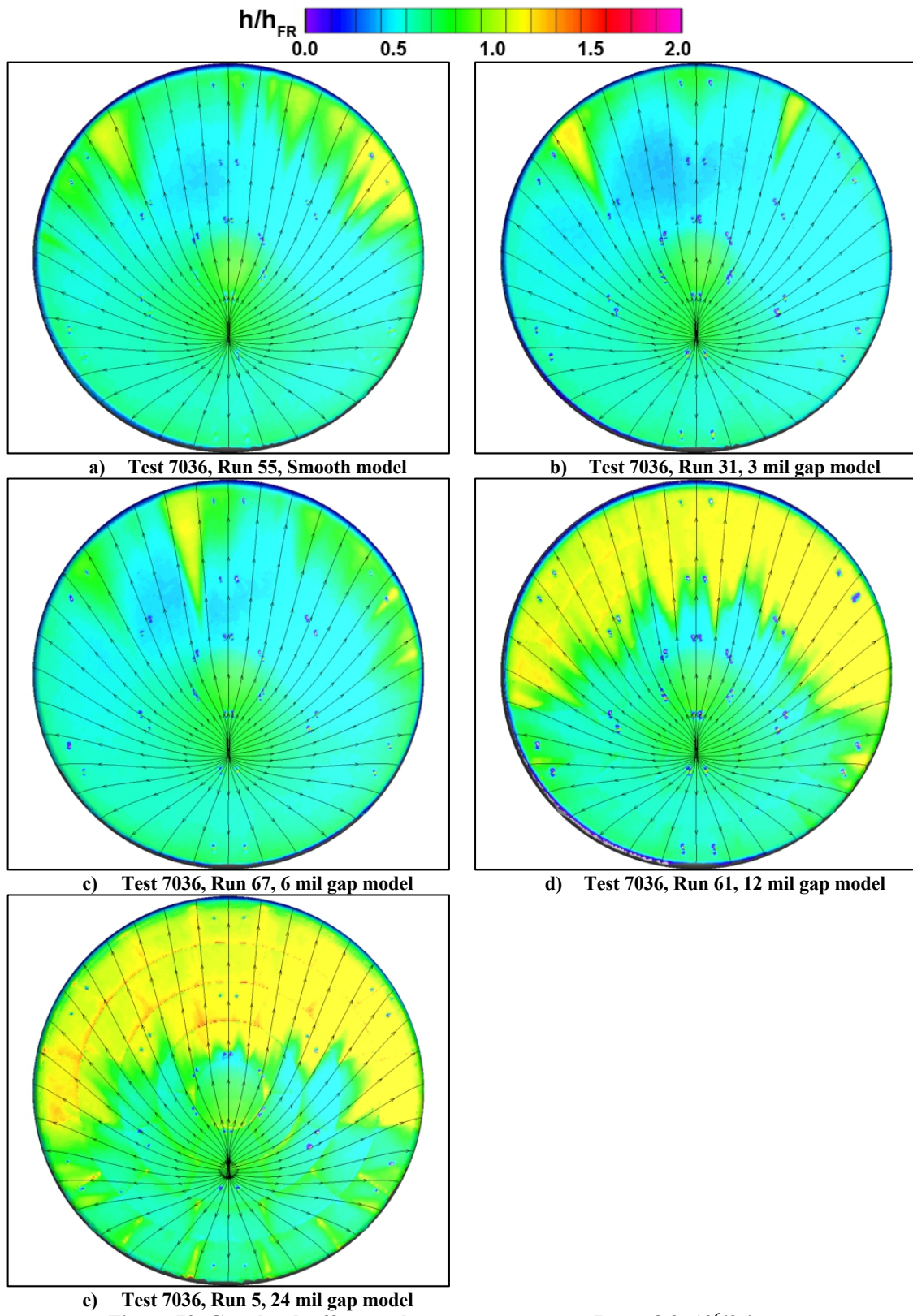


Figure 72. Gap depth effects, sphere-cone geometry, $Re_\infty = 8.3 \times 10^6$ /ft images.

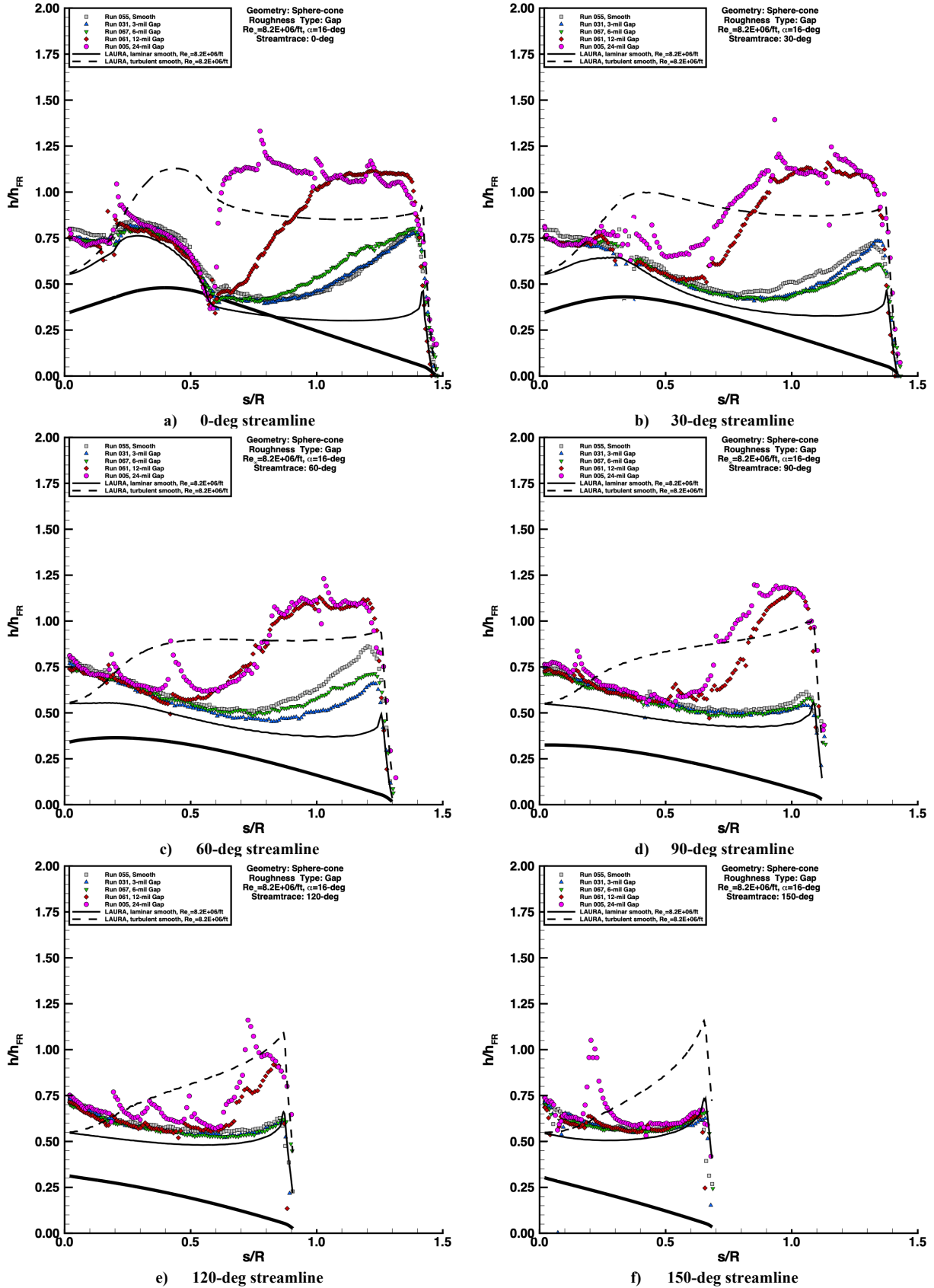


Figure 73. Gap depth effects, sphere-cone geometry, $Re_\infty = 8.3 \times 10^6 / ft$ images.

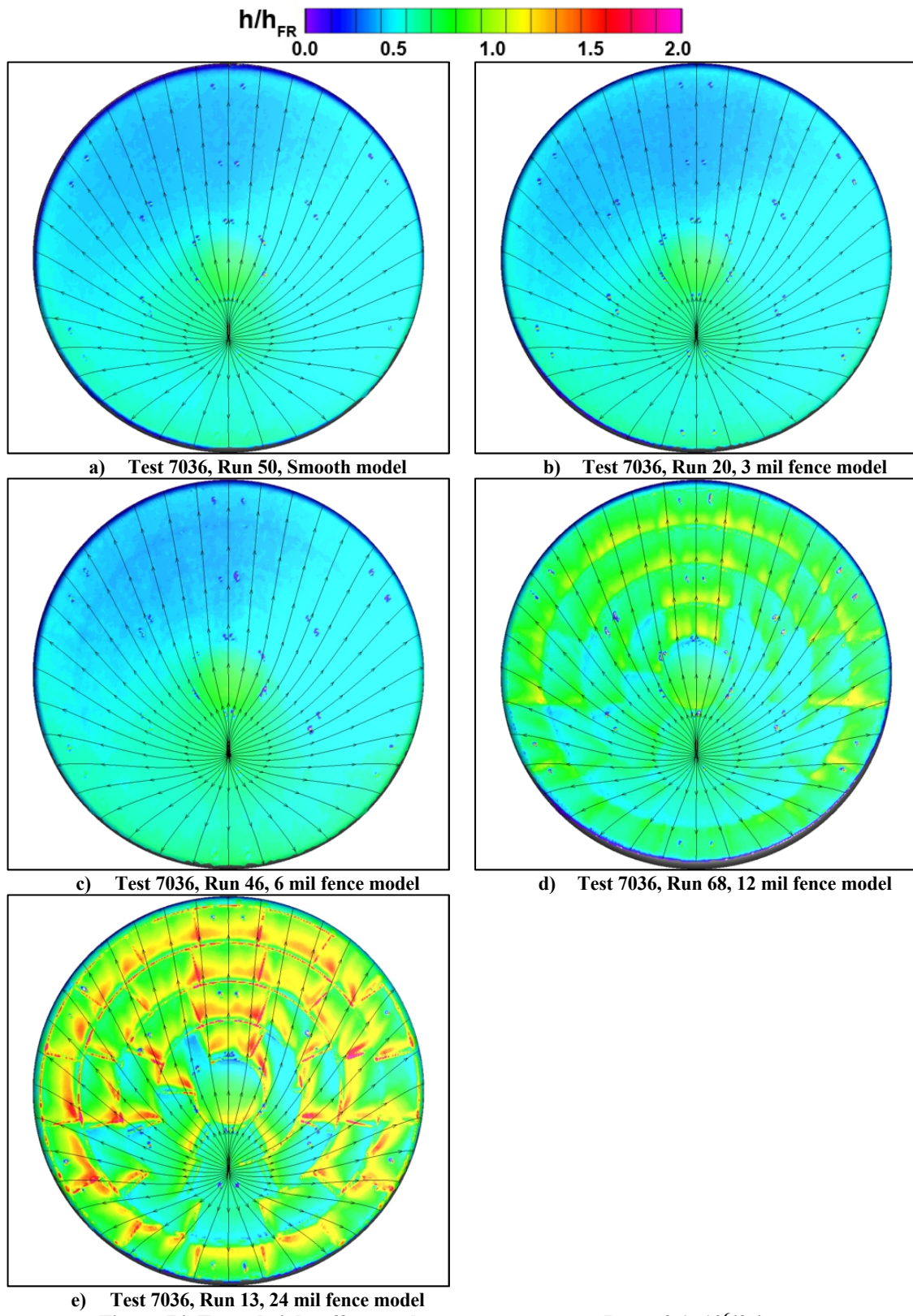


Figure 74. Fence height effects, sphere-cone geometry, $Re_\infty = 2.1 \times 10^6$ /ft images.

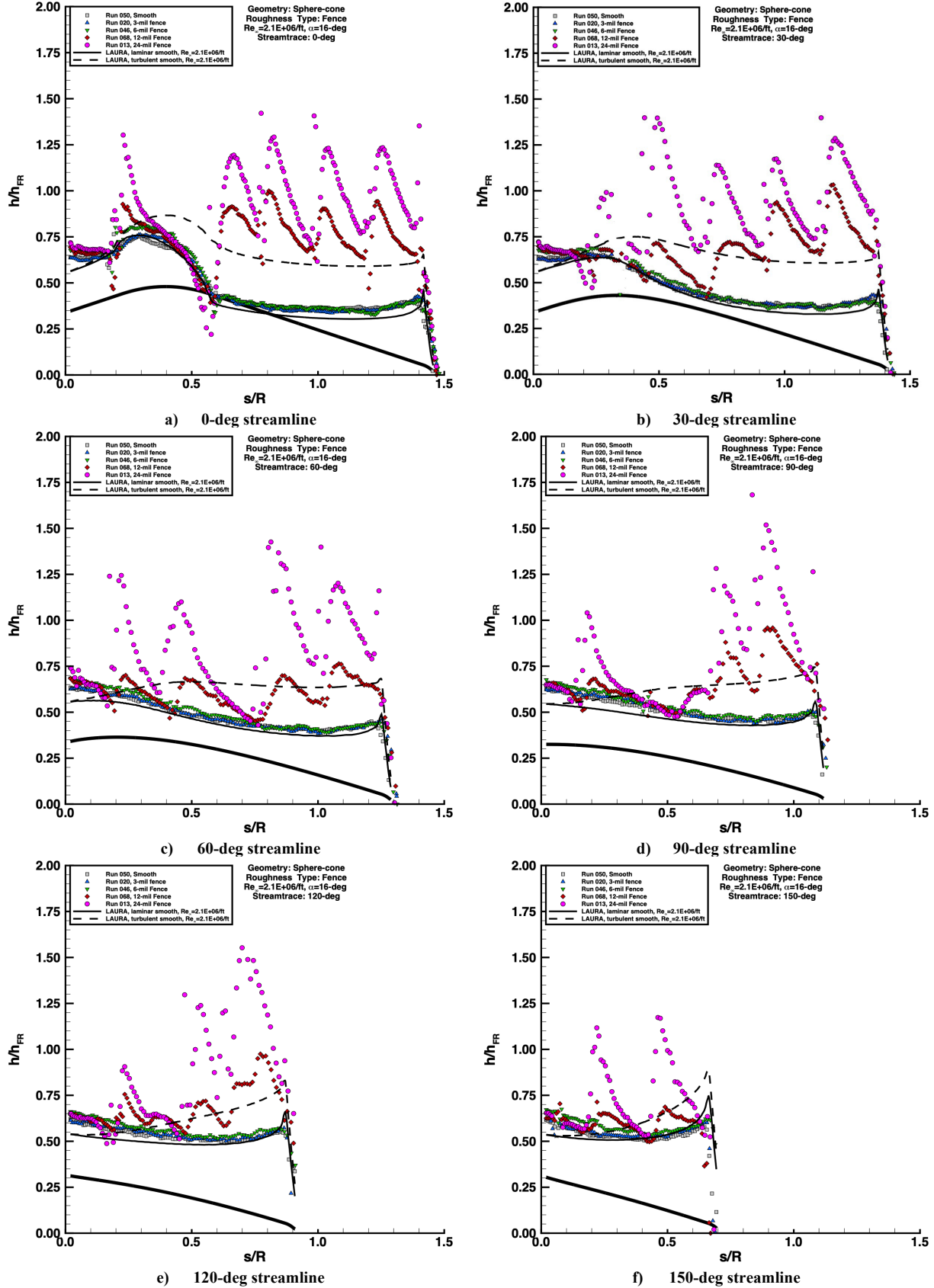


Figure 75. Fence height effects, sphere-cone geometry, $Re_\infty = 2.1 \times 10^6/ft$ images.

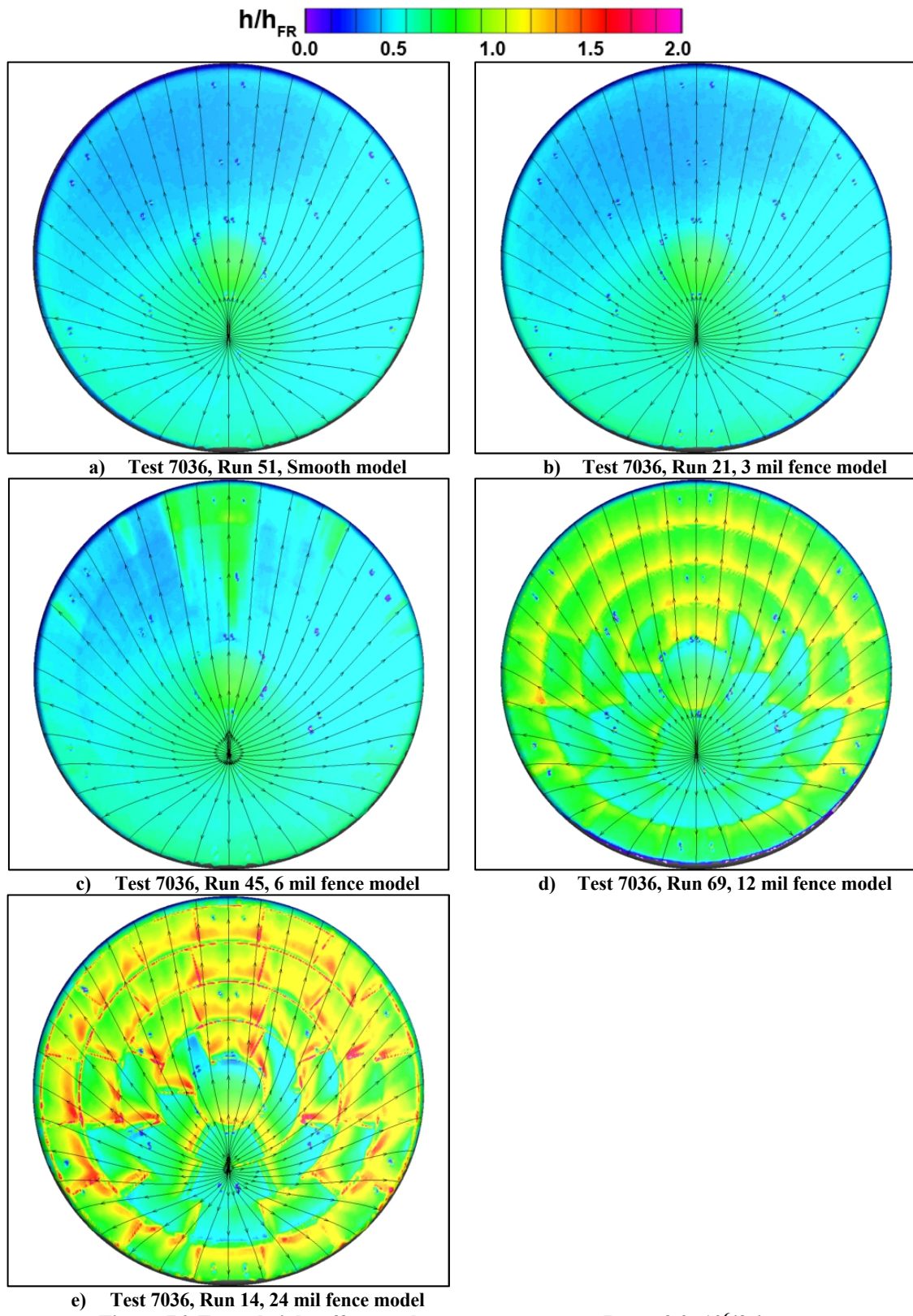


Figure 76. Fence height effects, sphere-cone geometry, $Re_\infty = 3.0 \times 10^6$ /ft images.

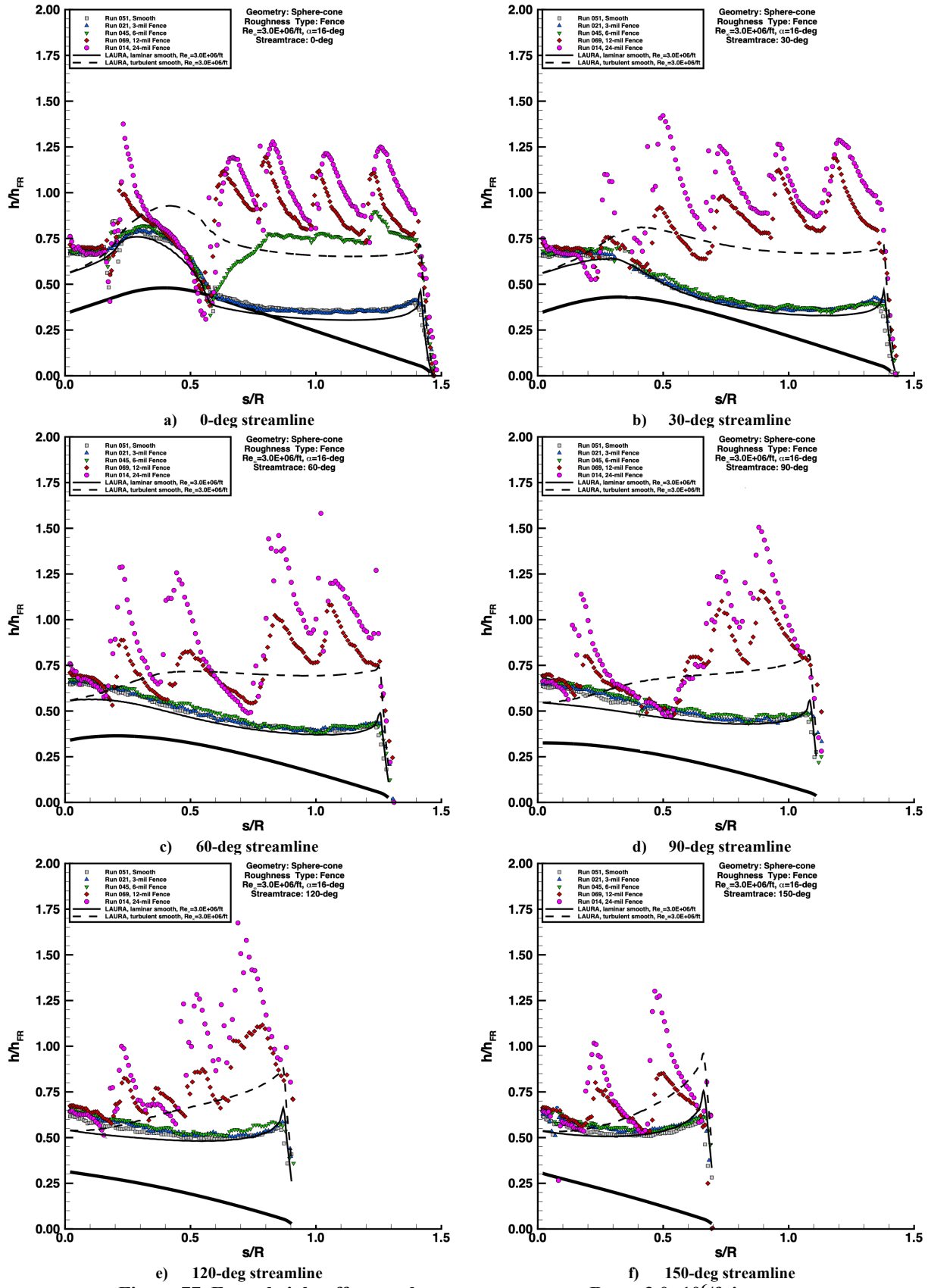


Figure 77. Fence height effects, sphere-cone geometry, $Re_\infty = 3.0 \times 10^6/ft$ images.

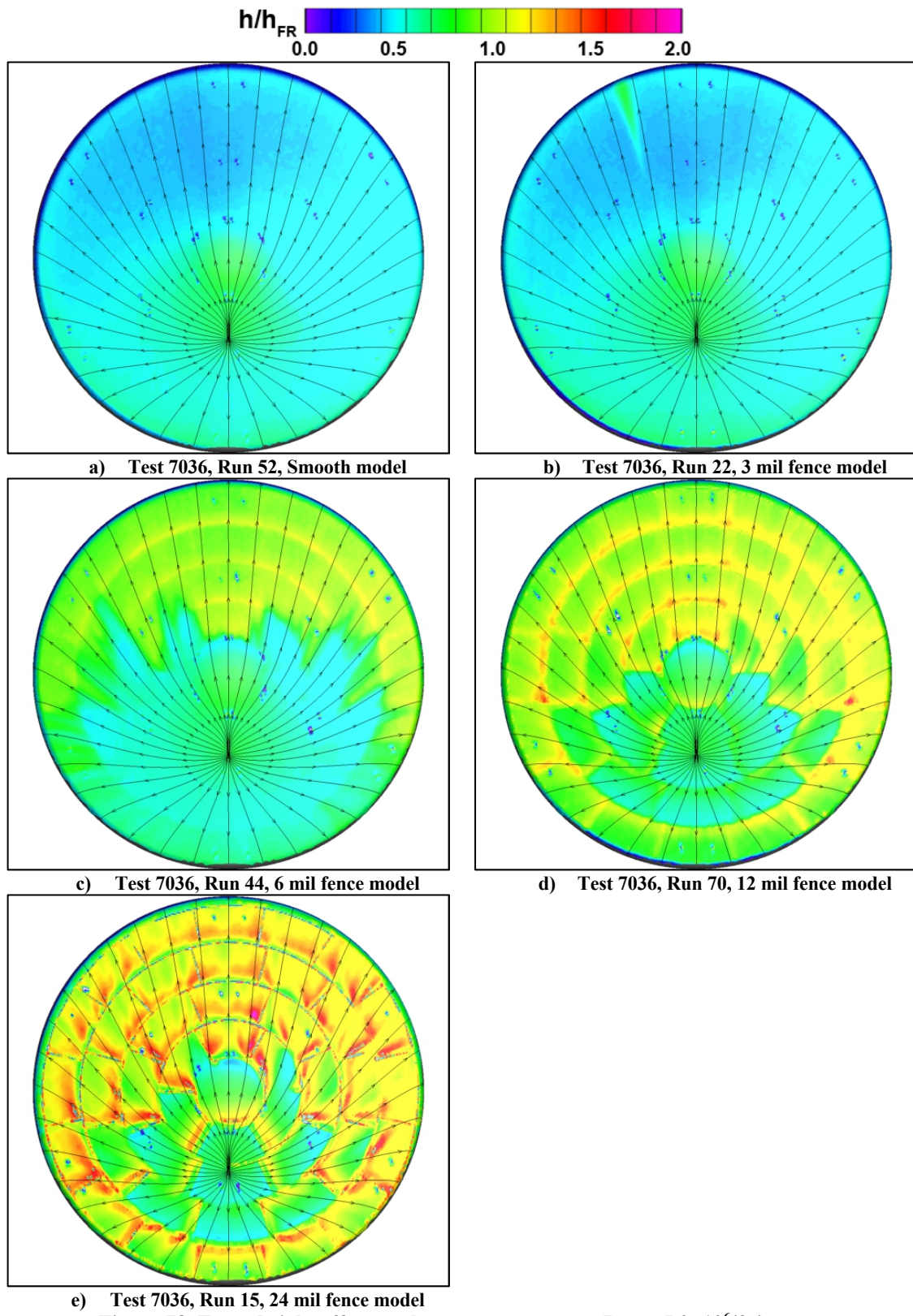


Figure 78. Fence height effects, sphere-cone geometry, $Re_\infty = 5.0 \times 10^6$ /ft images.

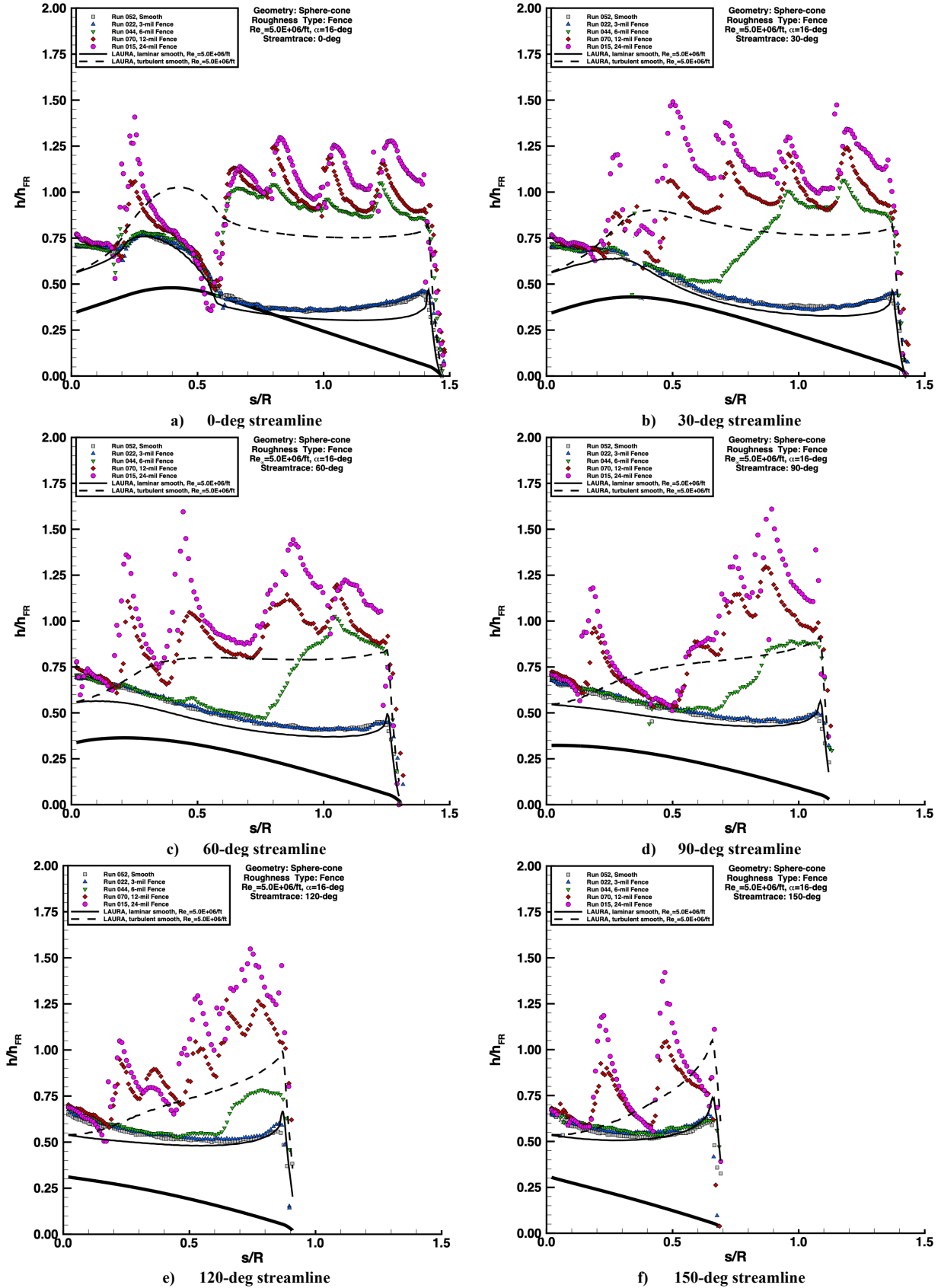


Figure 79. Fence height effects, sphere-cone geometry, $Re_\infty = 5.0 \times 10^6 / ft$ images.

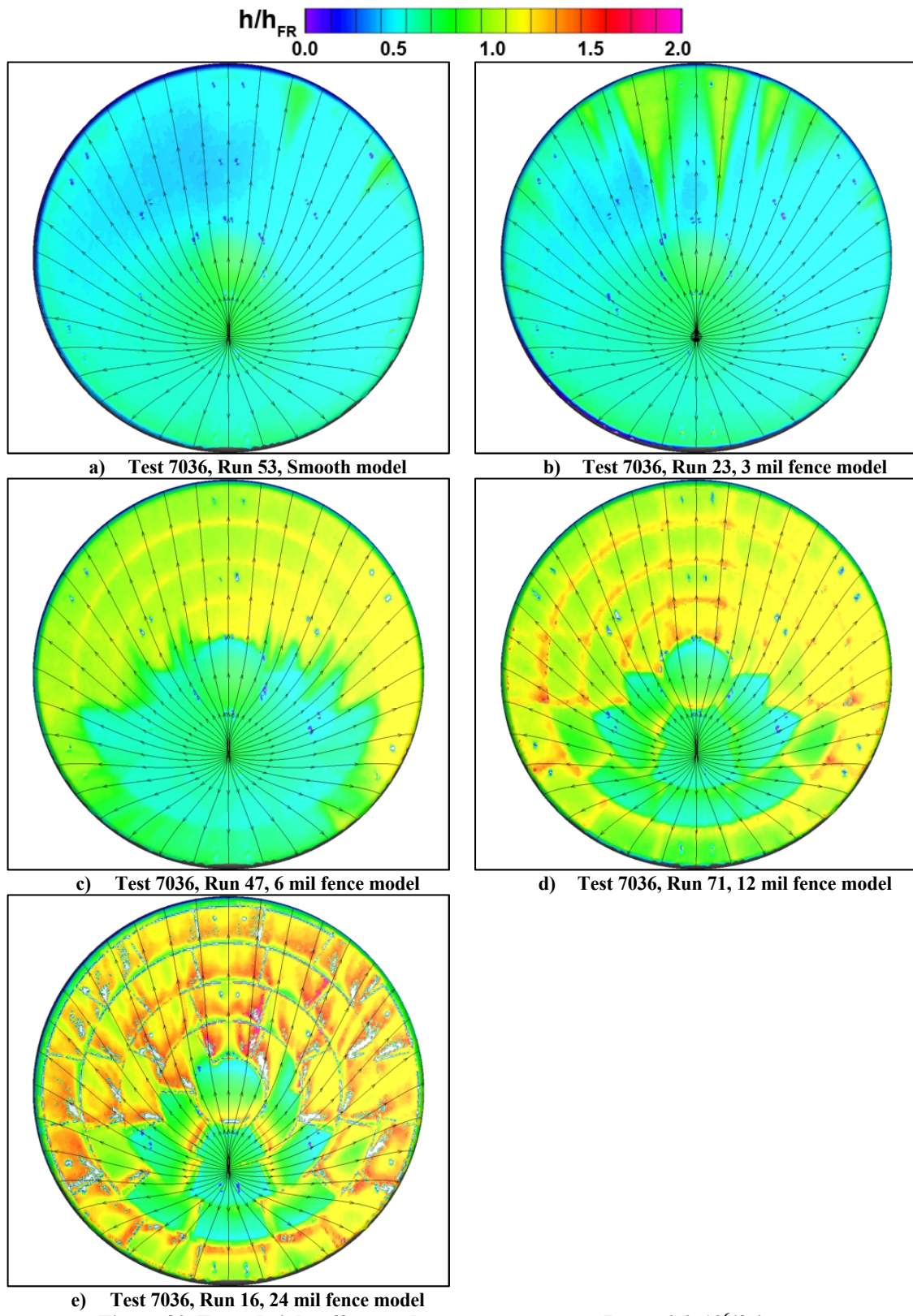


Figure 80. Fence height effects, sphere-cone geometry, $Re_\infty = 6.6 \times 10^6/ft$ images.

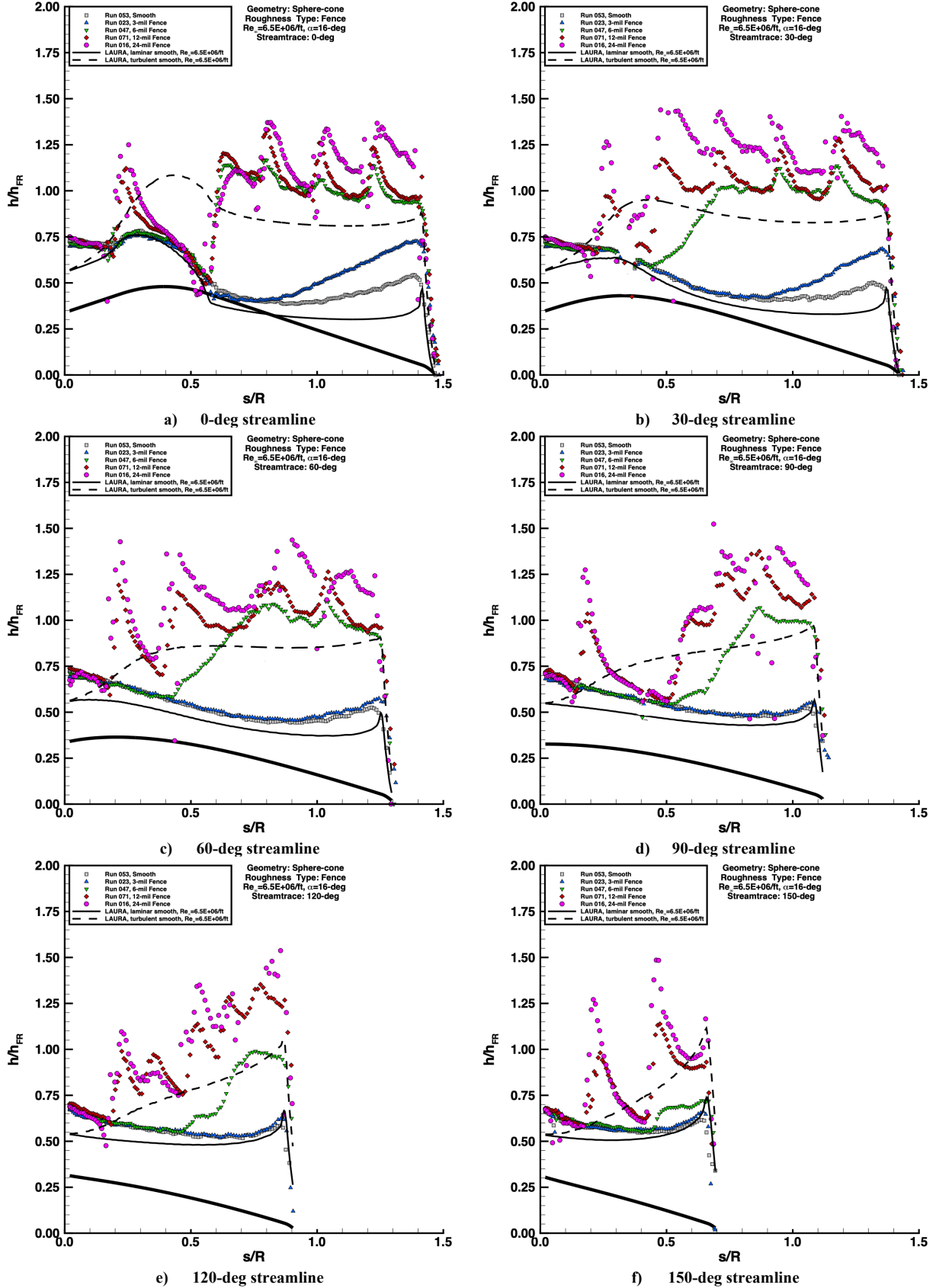


Figure 81. Fence height effects, sphere-cone geometry, $Re_{\infty} = 6.6 \times 10^6/ft$ images.

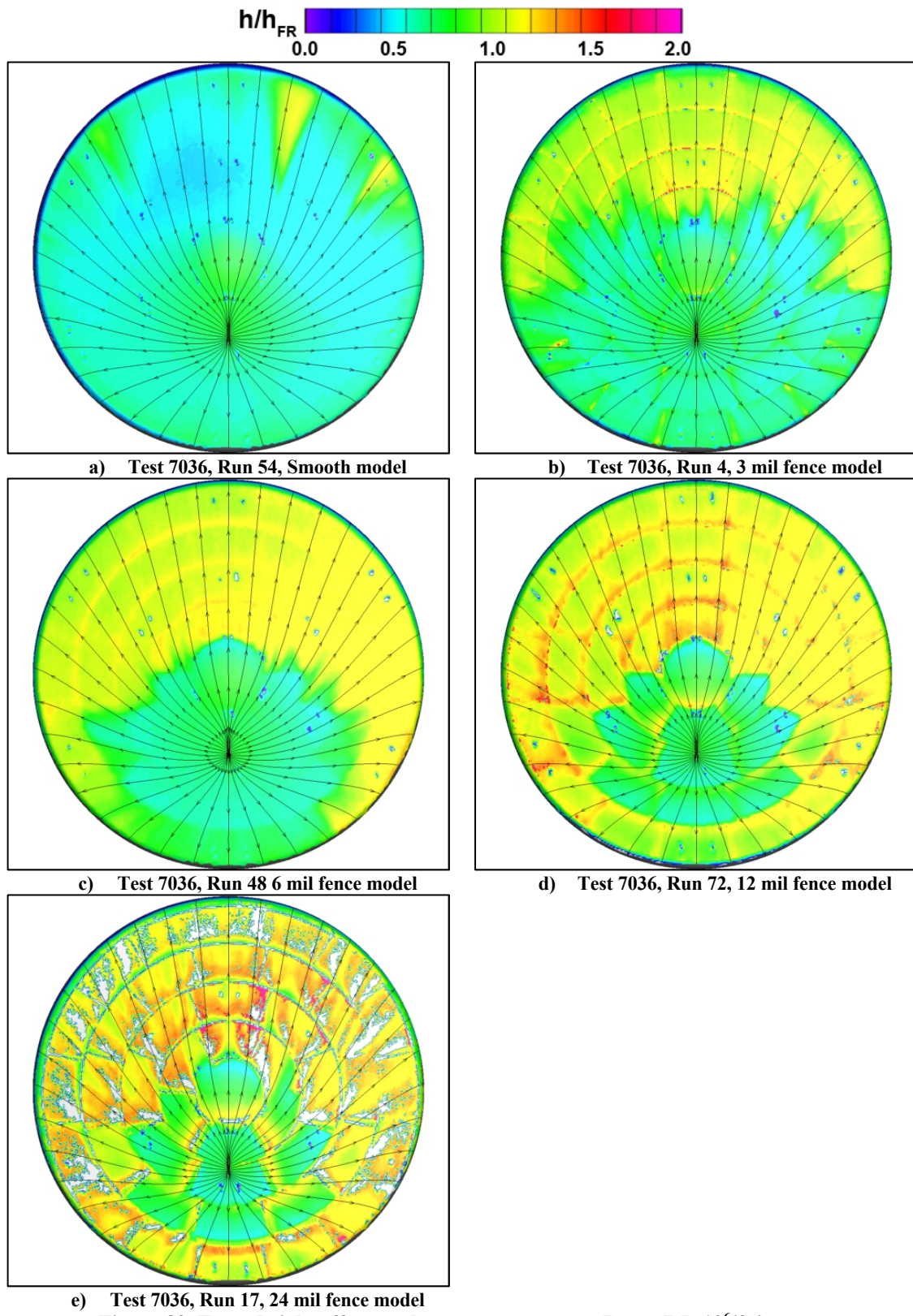


Figure 82. Fence height effects, sphere-cone geometry, $Re_\infty = 7.5 \times 10^6$ /ft images.

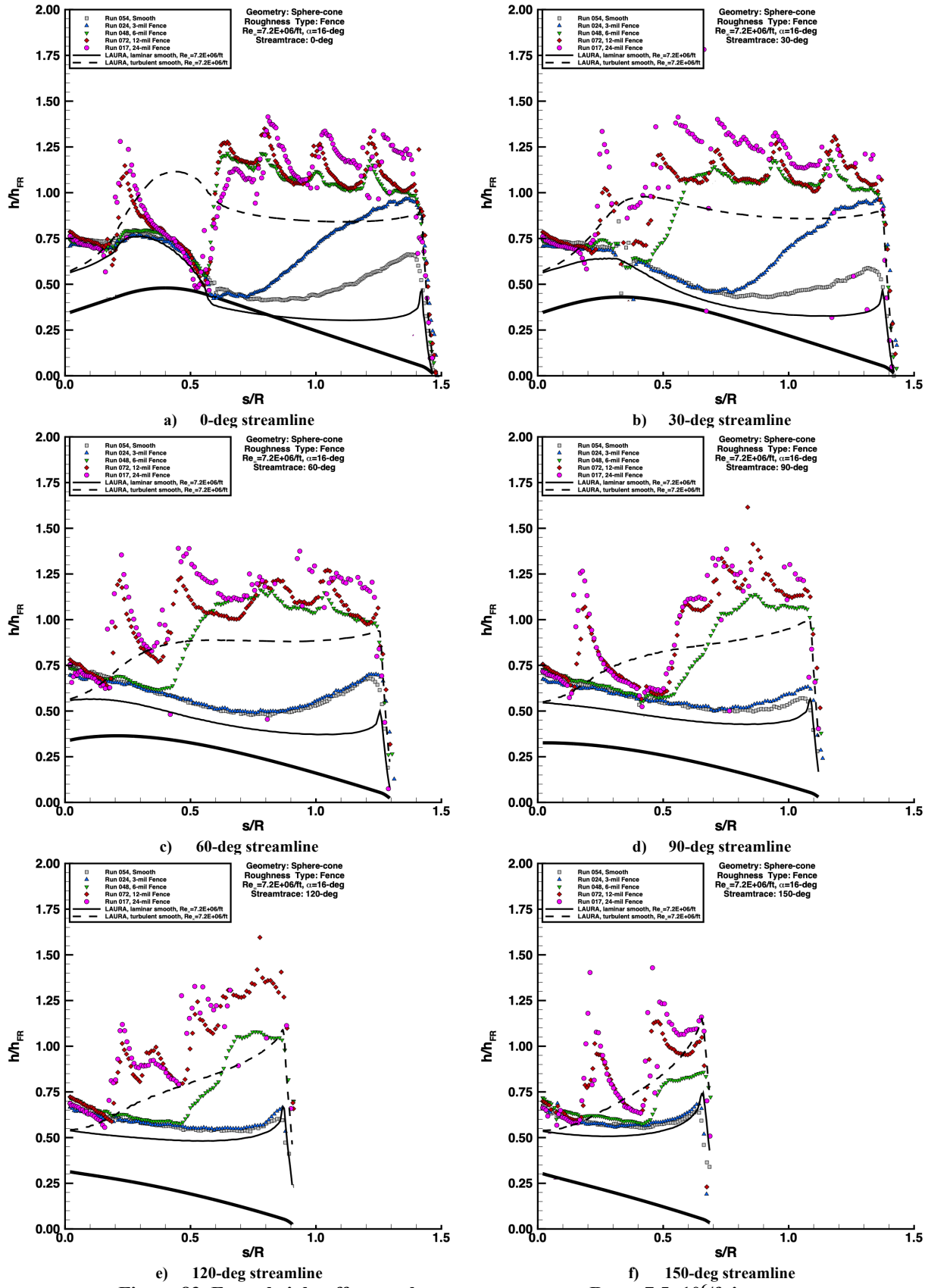


Figure 83. Fence height effects, sphere-cone geometry, $Re_{\infty} = 7.5 \times 10^6/ft$ images.

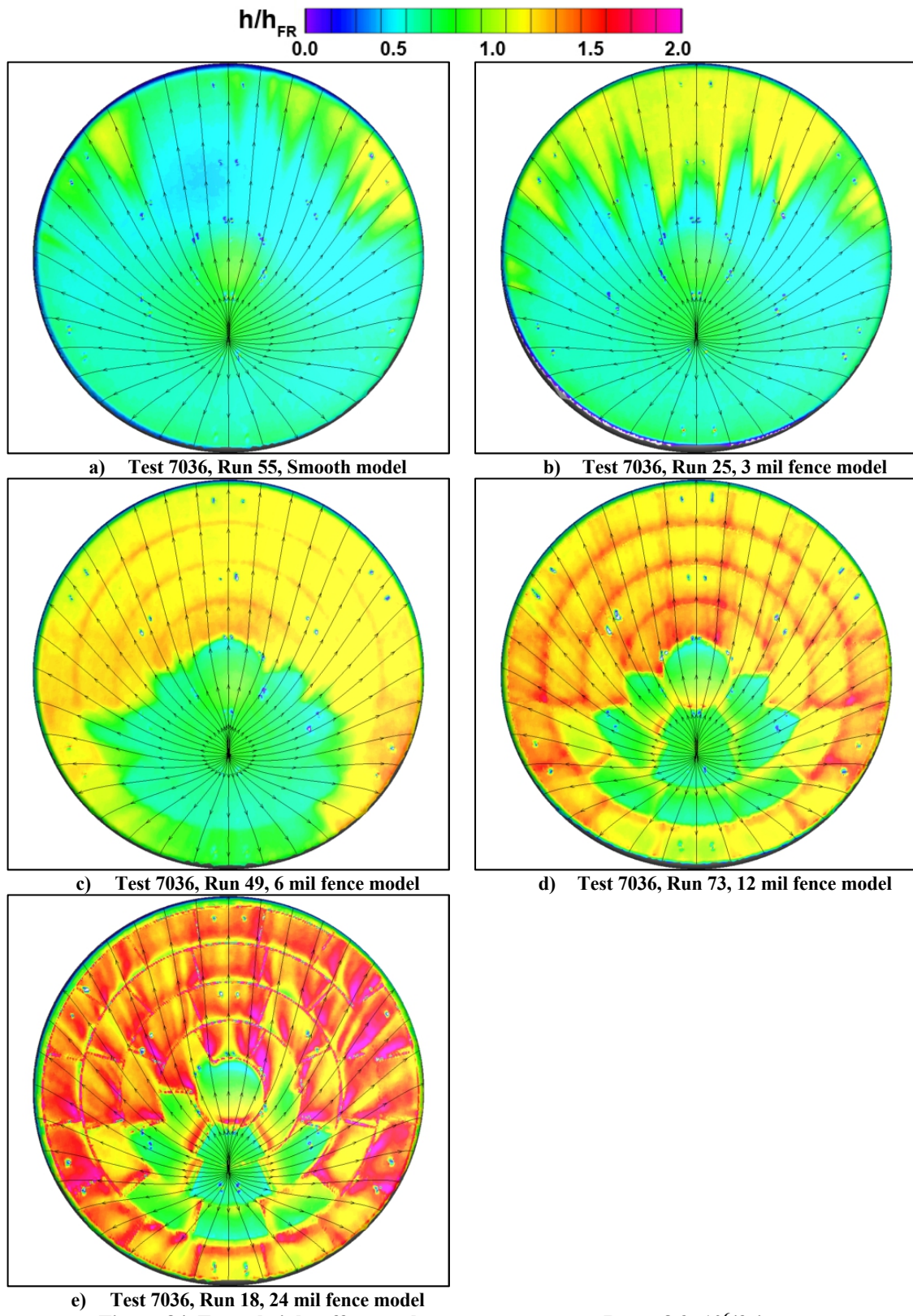


Figure 84. Fence height effects, sphere-cone geometry, $Re_\infty = 8.3 \times 10^6/ft$ images.

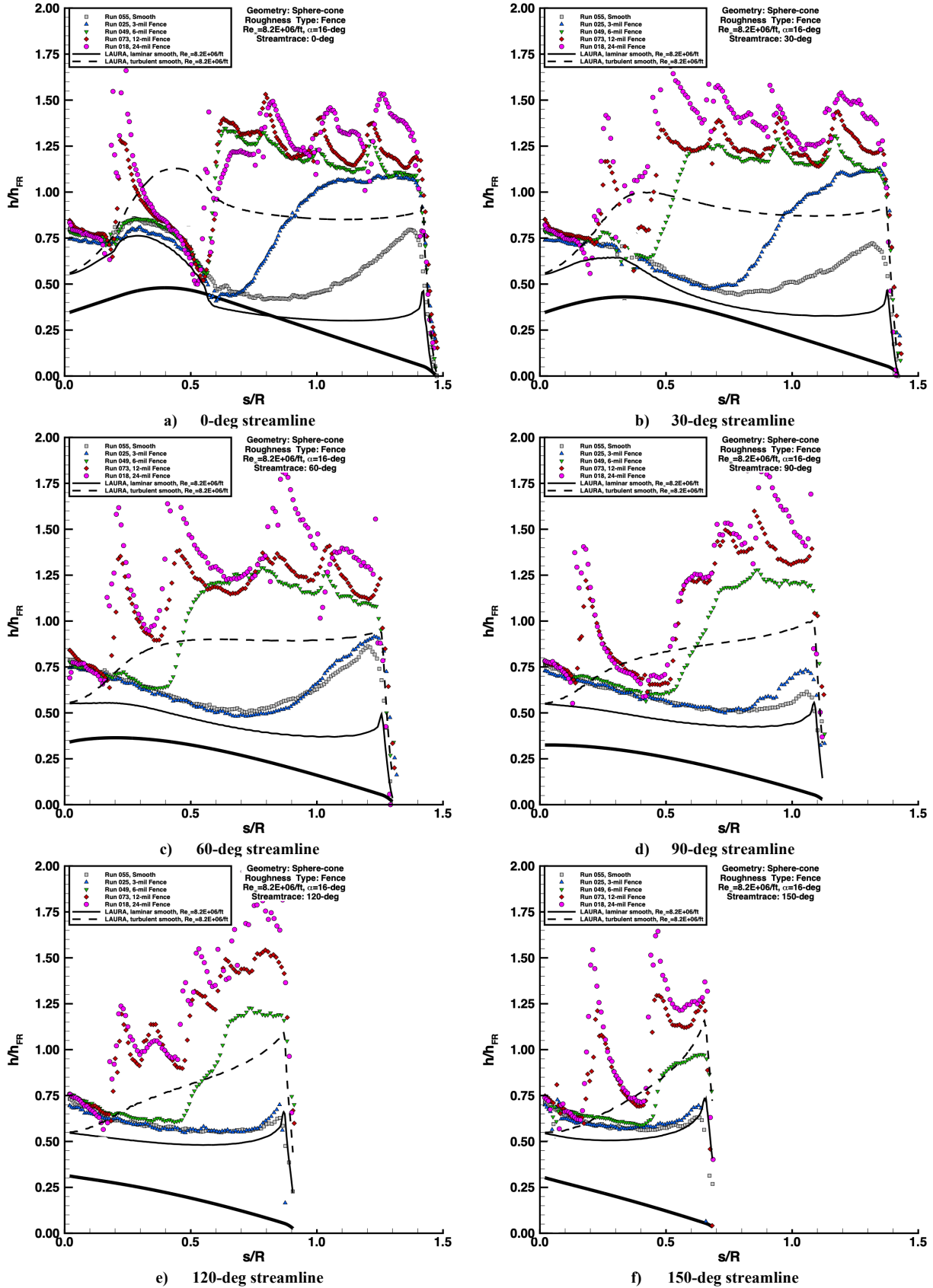


Figure 85. Fence height effects, sphere-cone geometry, $Re_{\infty} = 8.3 \times 10^6/ft$ images.

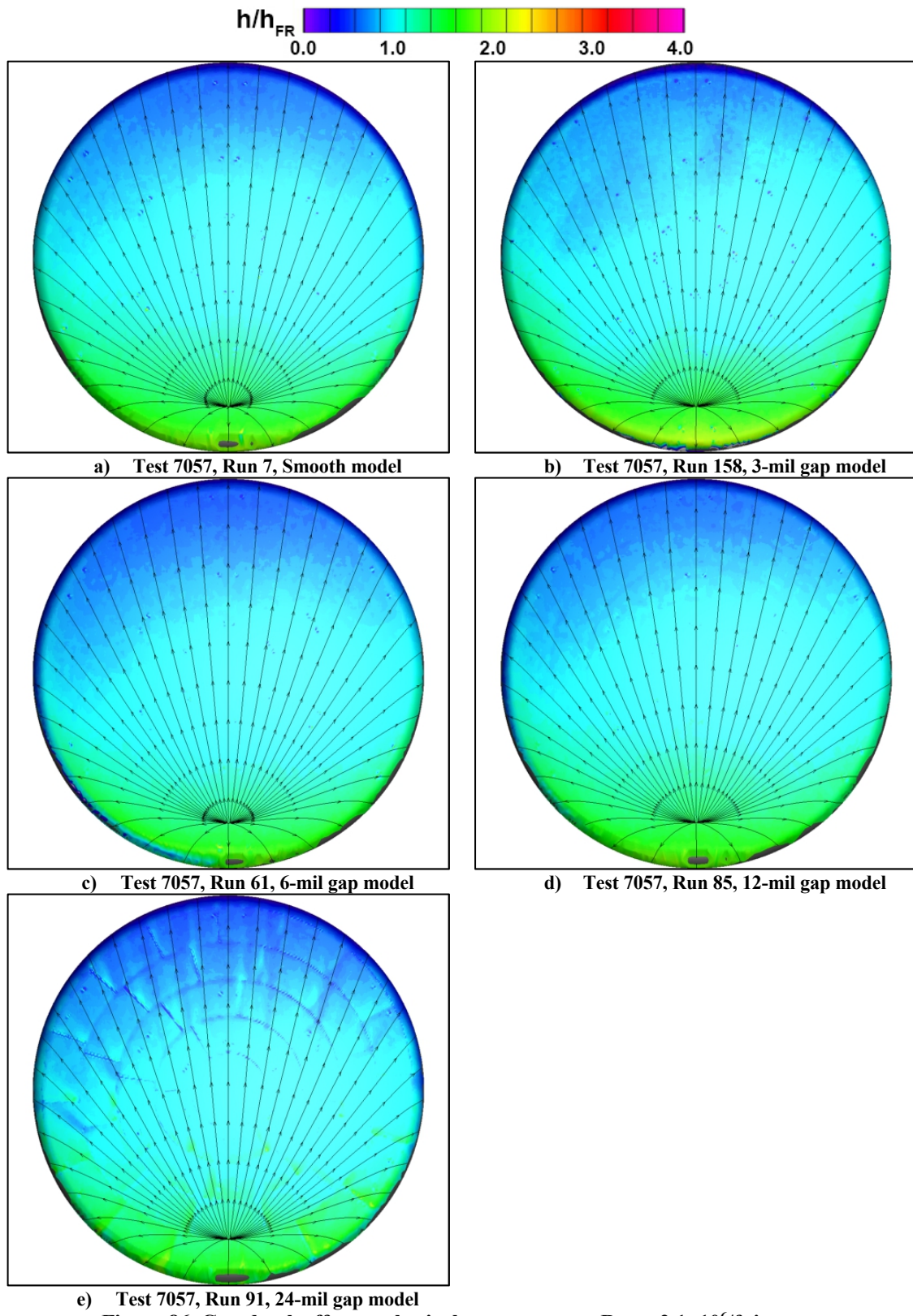


Figure 86. Gap depth effects, spherical-cap geometry, $Re_\infty = 2.1 \times 10^6/ft$ images.

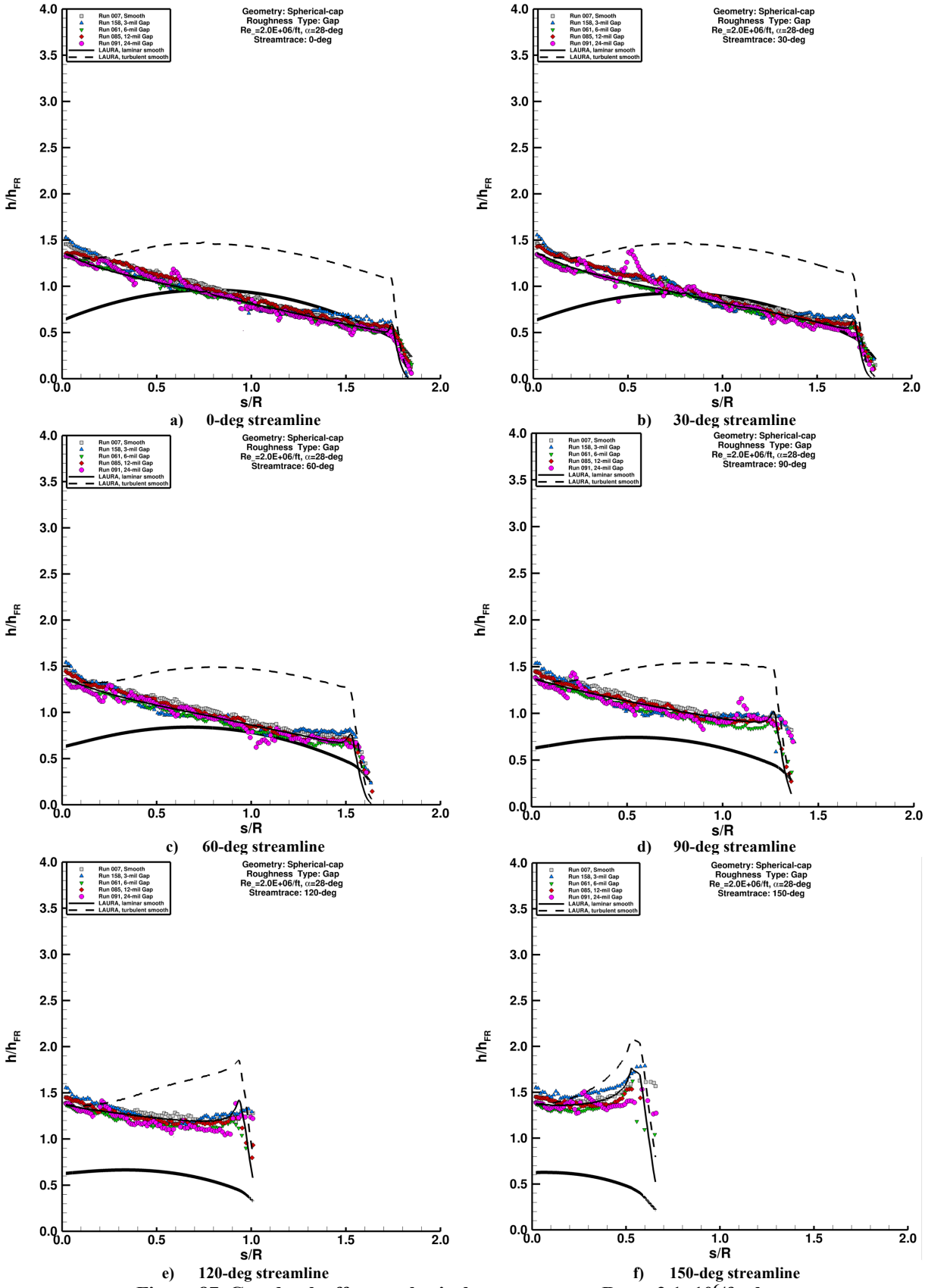


Figure 87. Gap depth effects, spherical-cap geometry, $Re_{\infty} = 2.1 \times 10^6/ft$ plots.

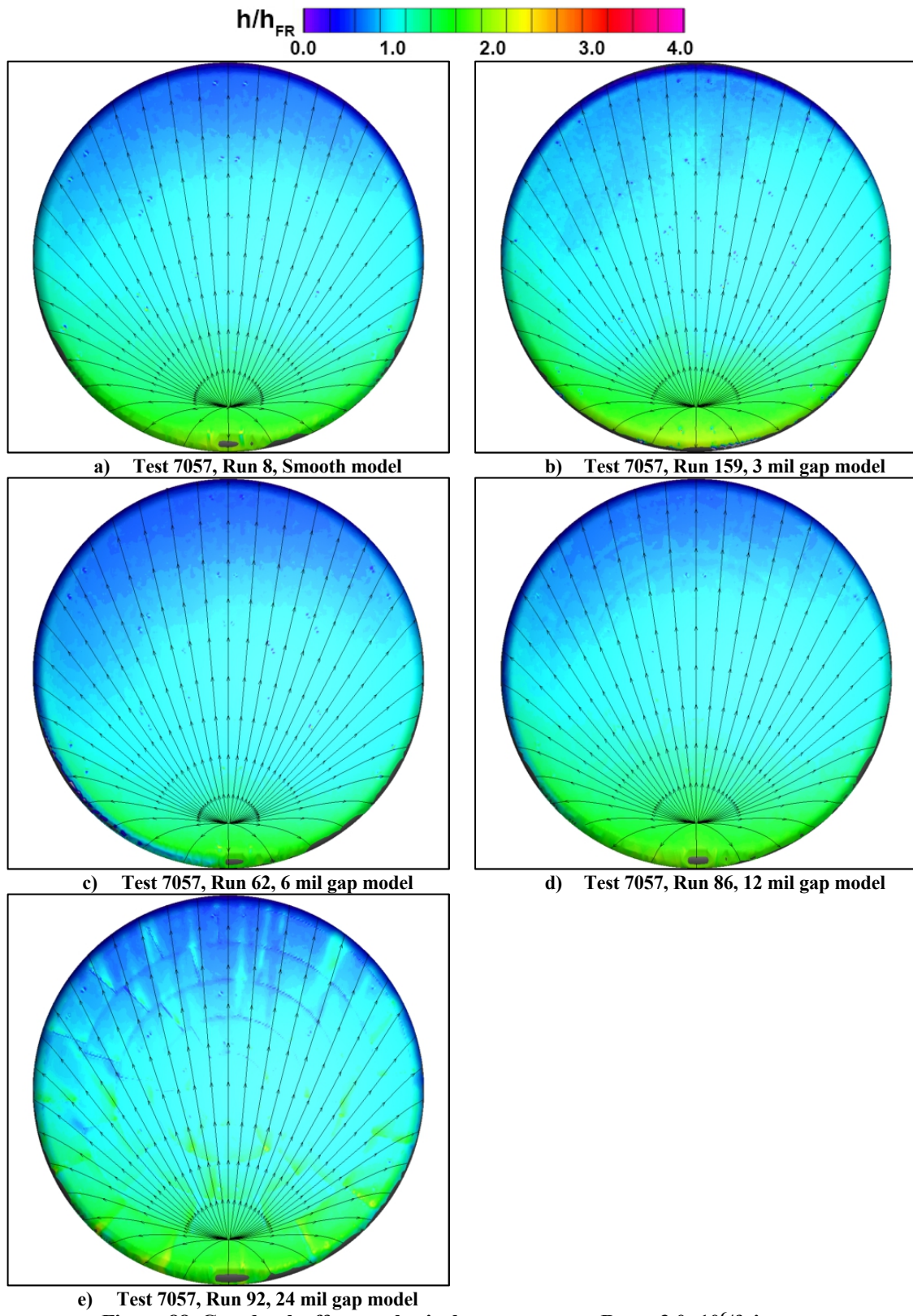


Figure 88. Gap depth effects, spherical-cap geometry, $Re_\infty = 3.0 \times 10^6$ /ft images.

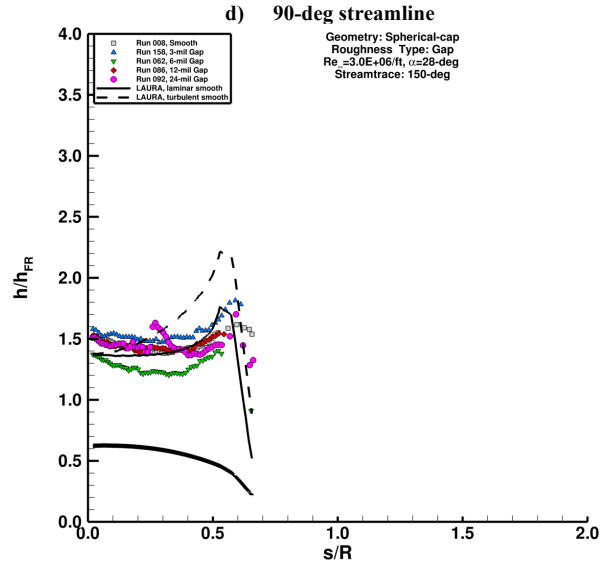
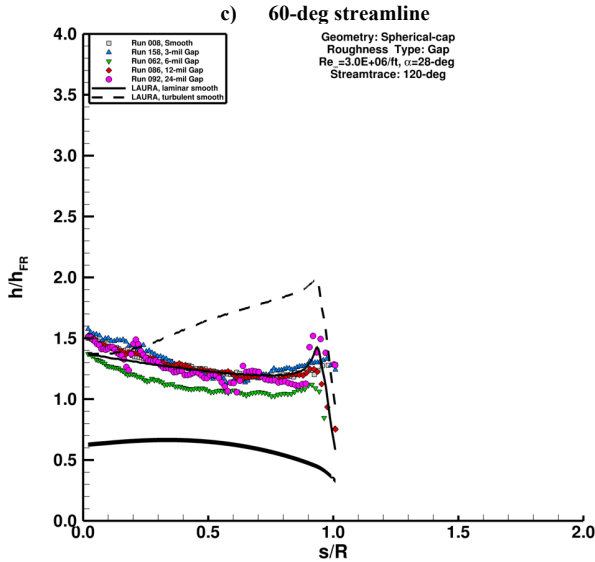
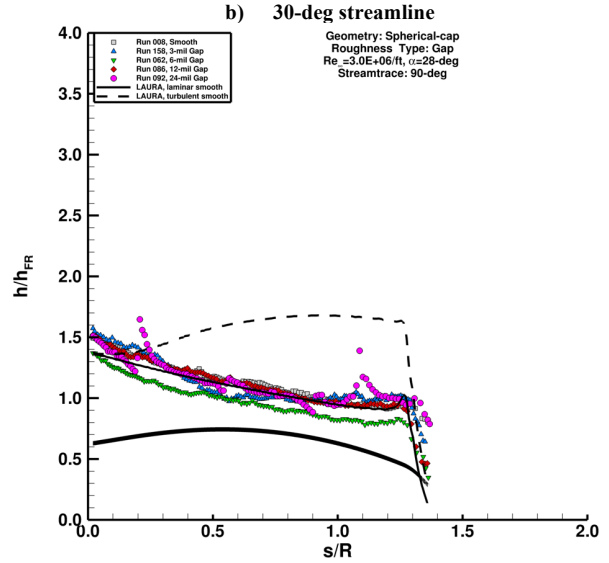
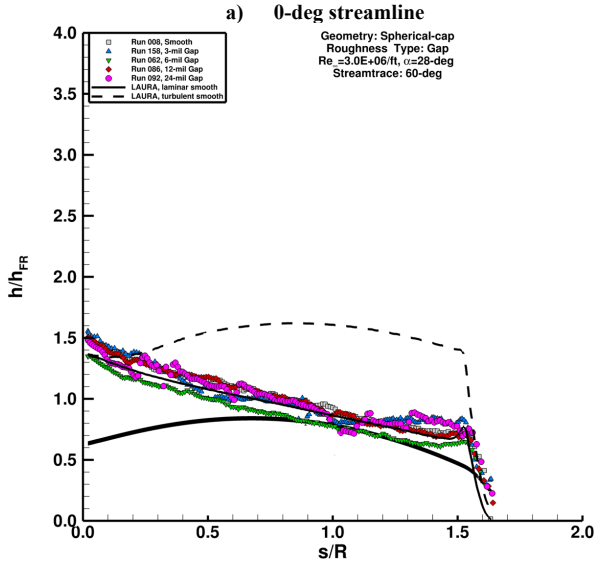
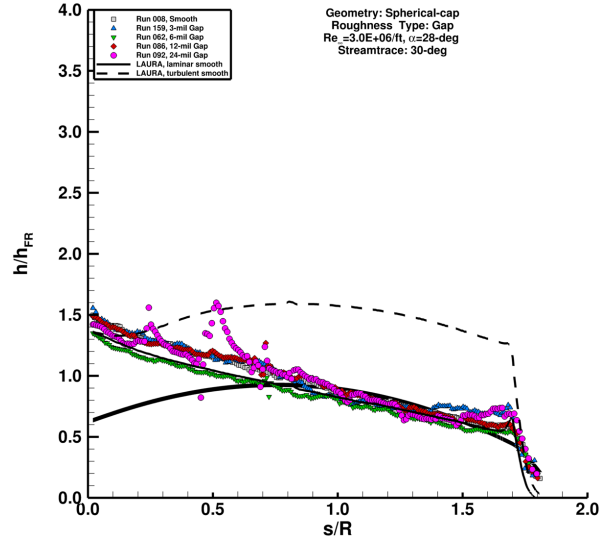
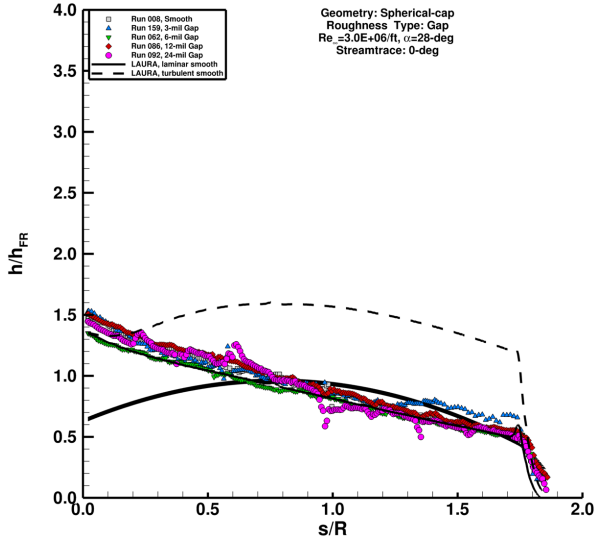


Figure 89. Gap depth effects, spherical-cap geometry, $Re_{\infty} = 3.0 \times 10^6/ft$ plots.

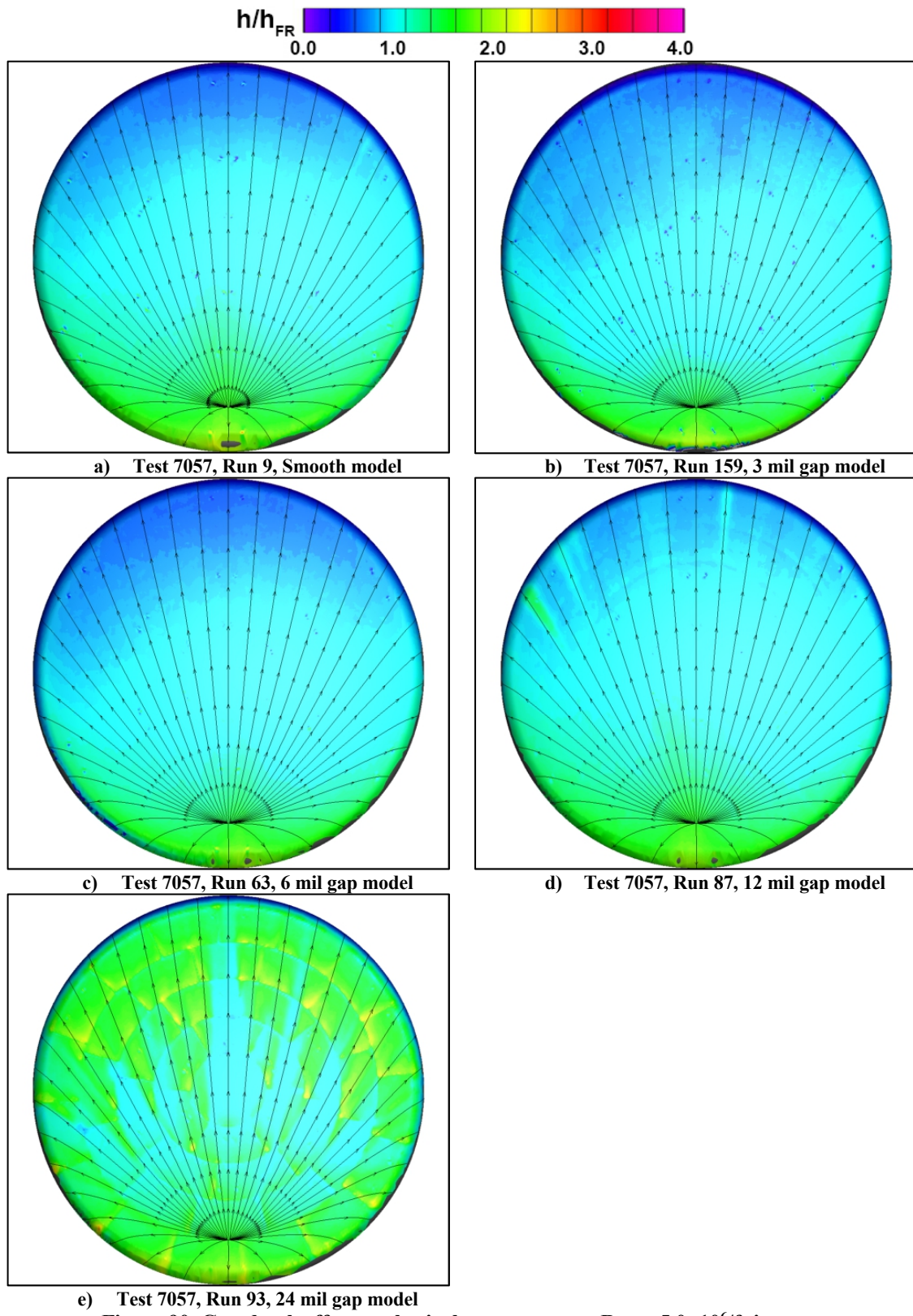


Figure 90. Gap depth effects, spherical-cap geometry, $Re_\infty = 5.0 \times 10^6$ /ft images.

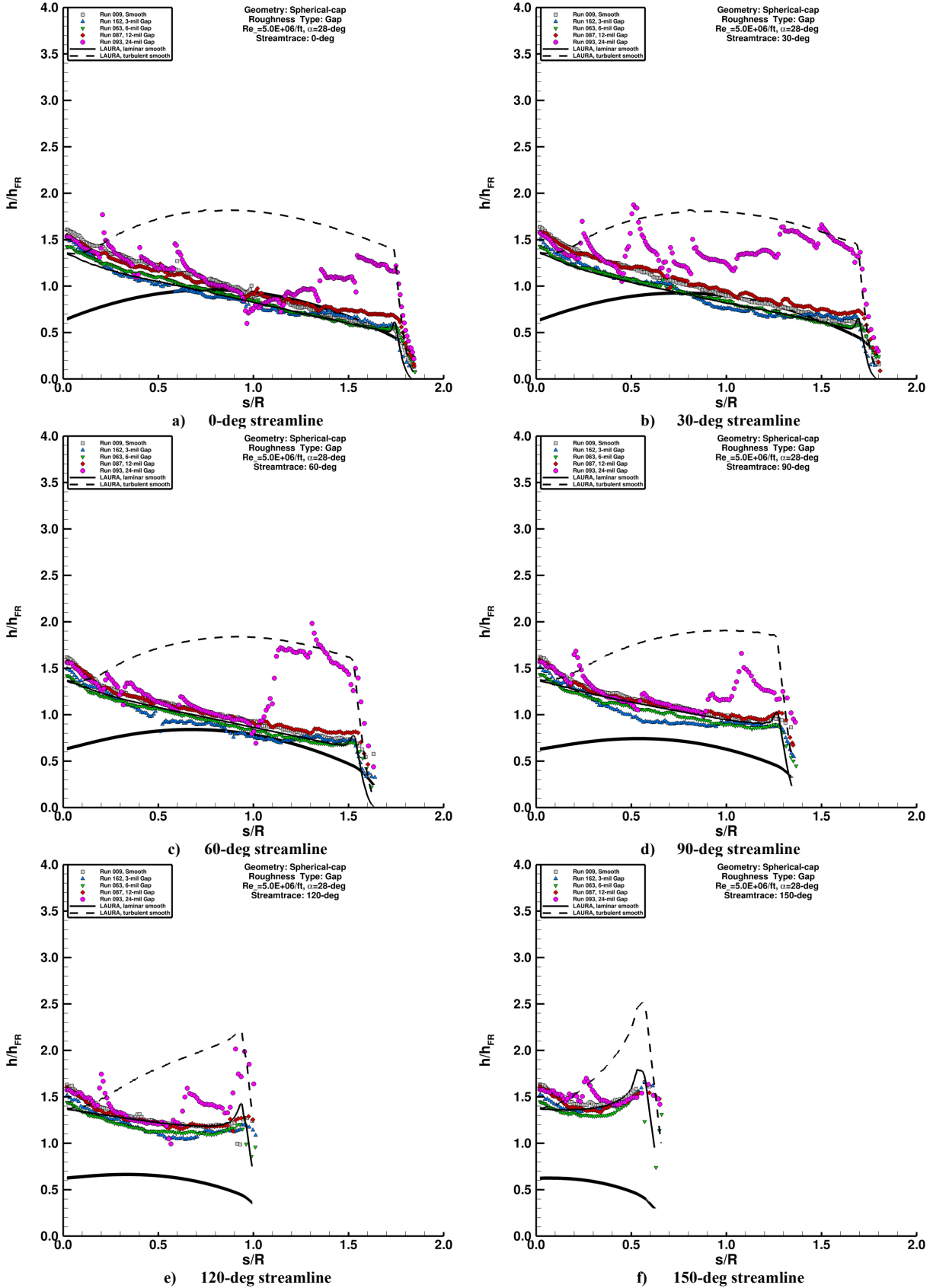


Figure 91. Gap depth effects, spherical-cap geometry, $Re_{\infty} = 5.0 \times 10^6/ft$ plots.

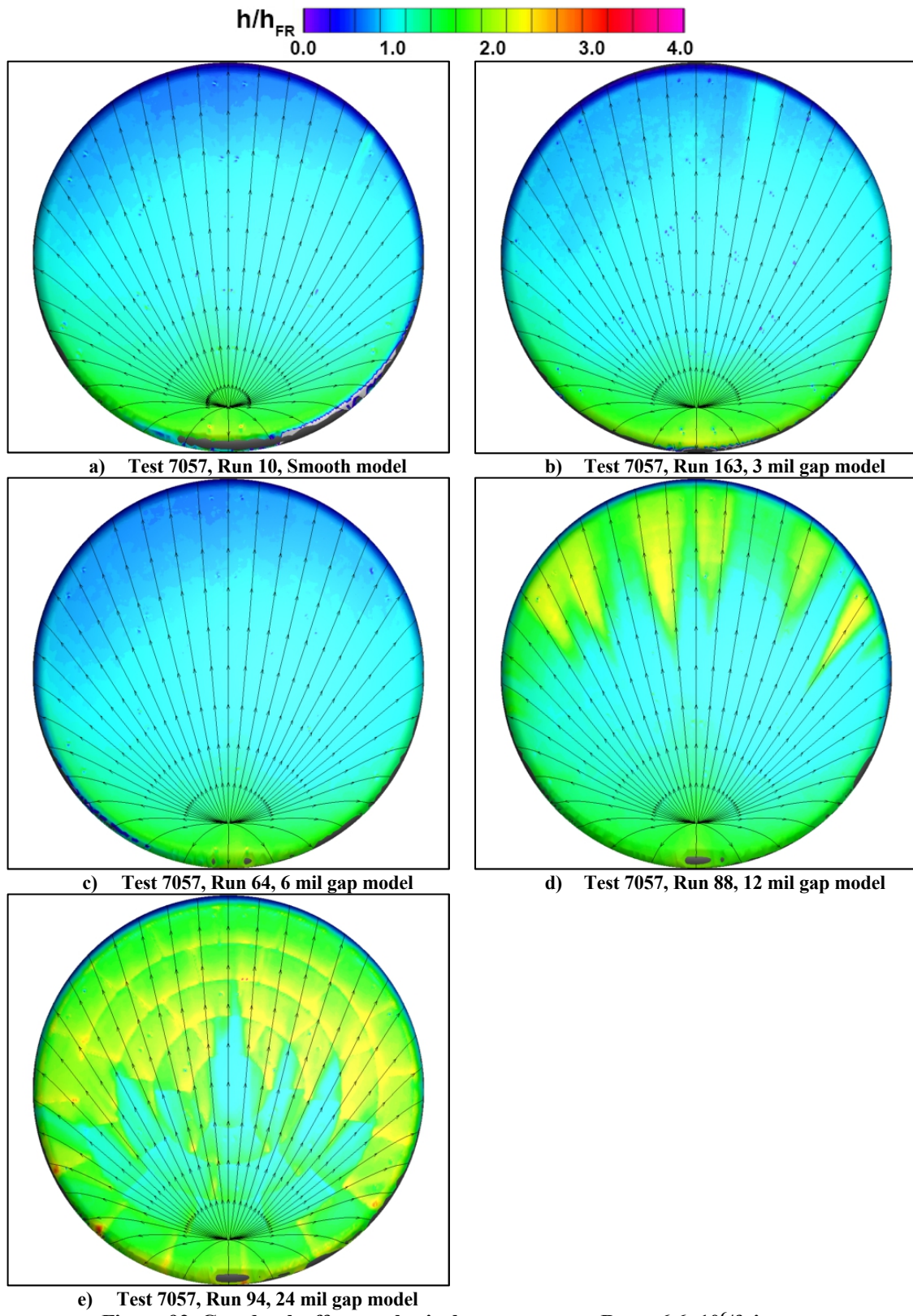


Figure 92. Gap depth effects, spherical-cap geometry, $Re_\infty = 6.6 \times 10^6$ /ft images.

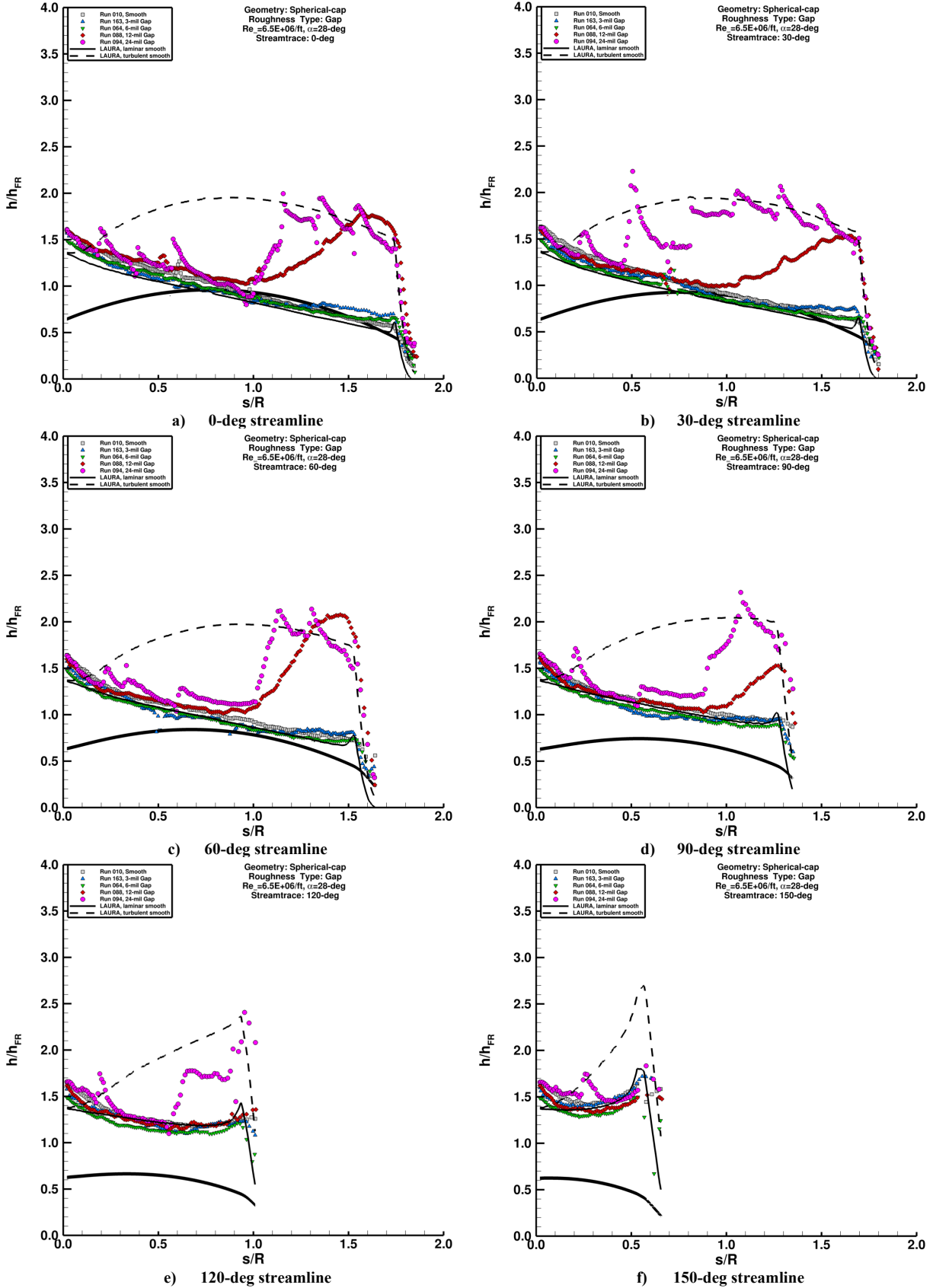


Figure 93. Gap depth effects, spherical-cap geometry, $Re_{\infty} = 6.6 \times 10^6/ft$ plots.

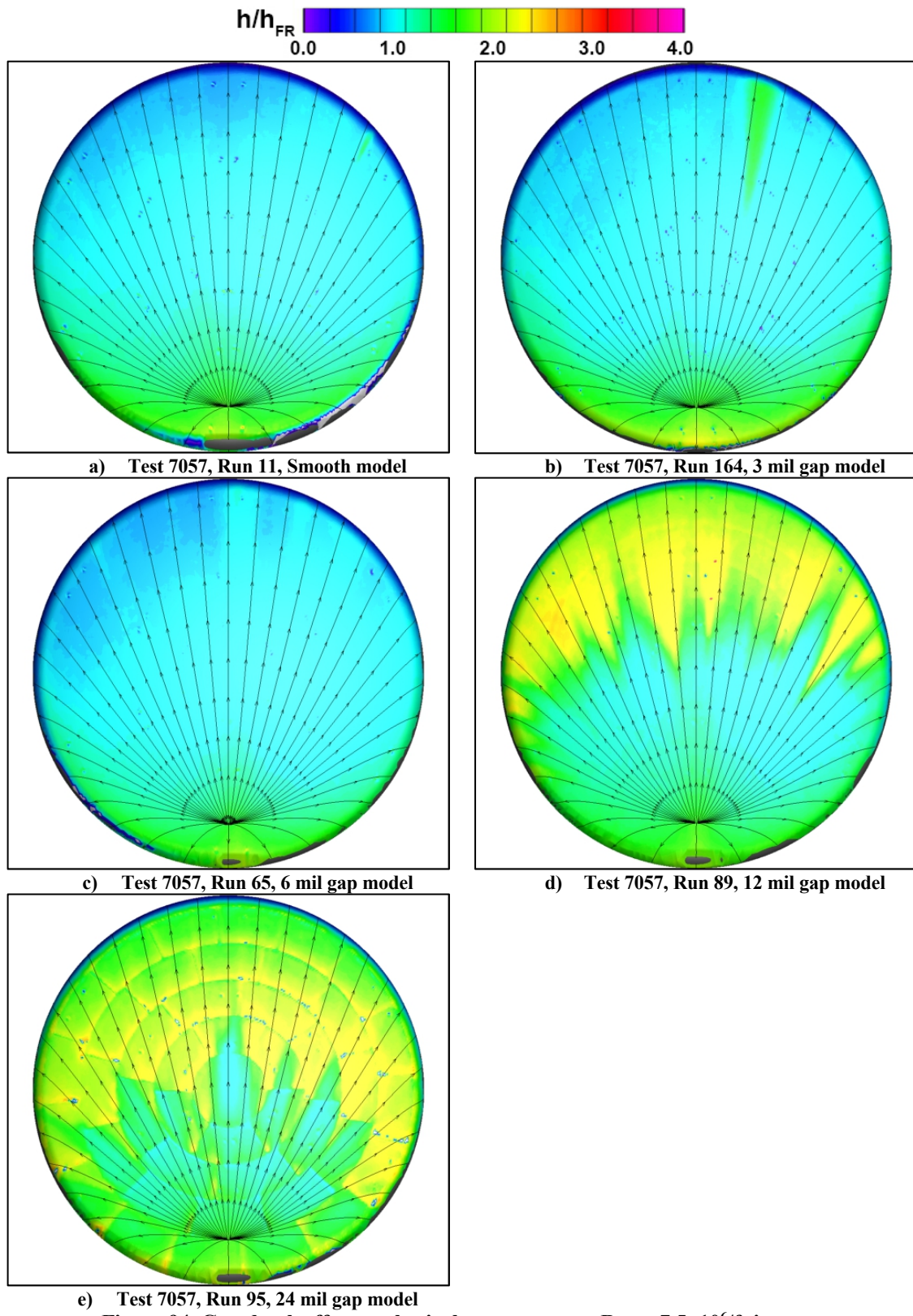


Figure 94. Gap depth effects, spherical-cap geometry, $Re_\infty = 7.5 \times 10^6/ft$ images.

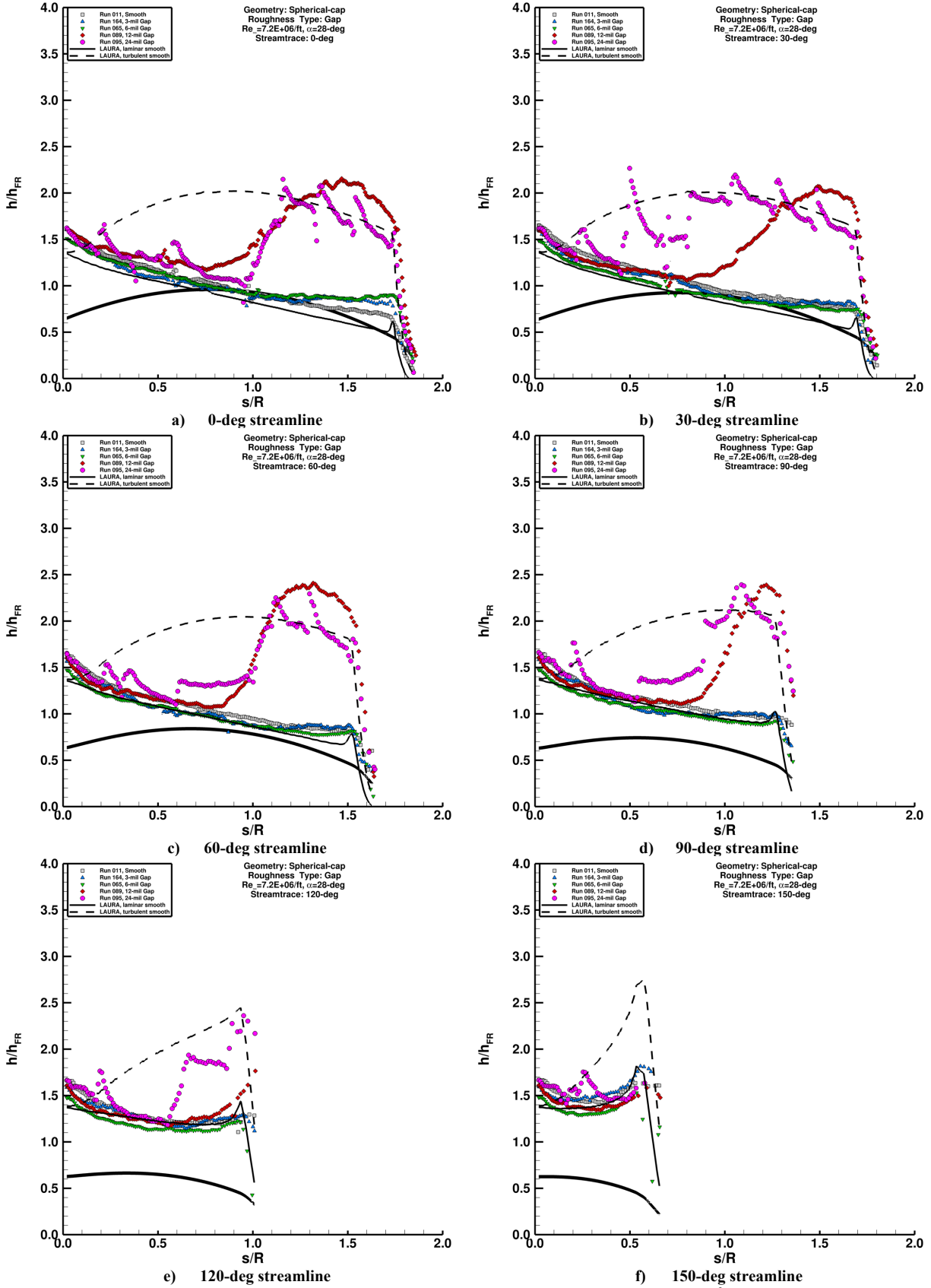


Figure 95. Gap depth effects, spherical-cap geometry, $Re_{\infty} = 7.5 \times 10^6/ft$ plots.

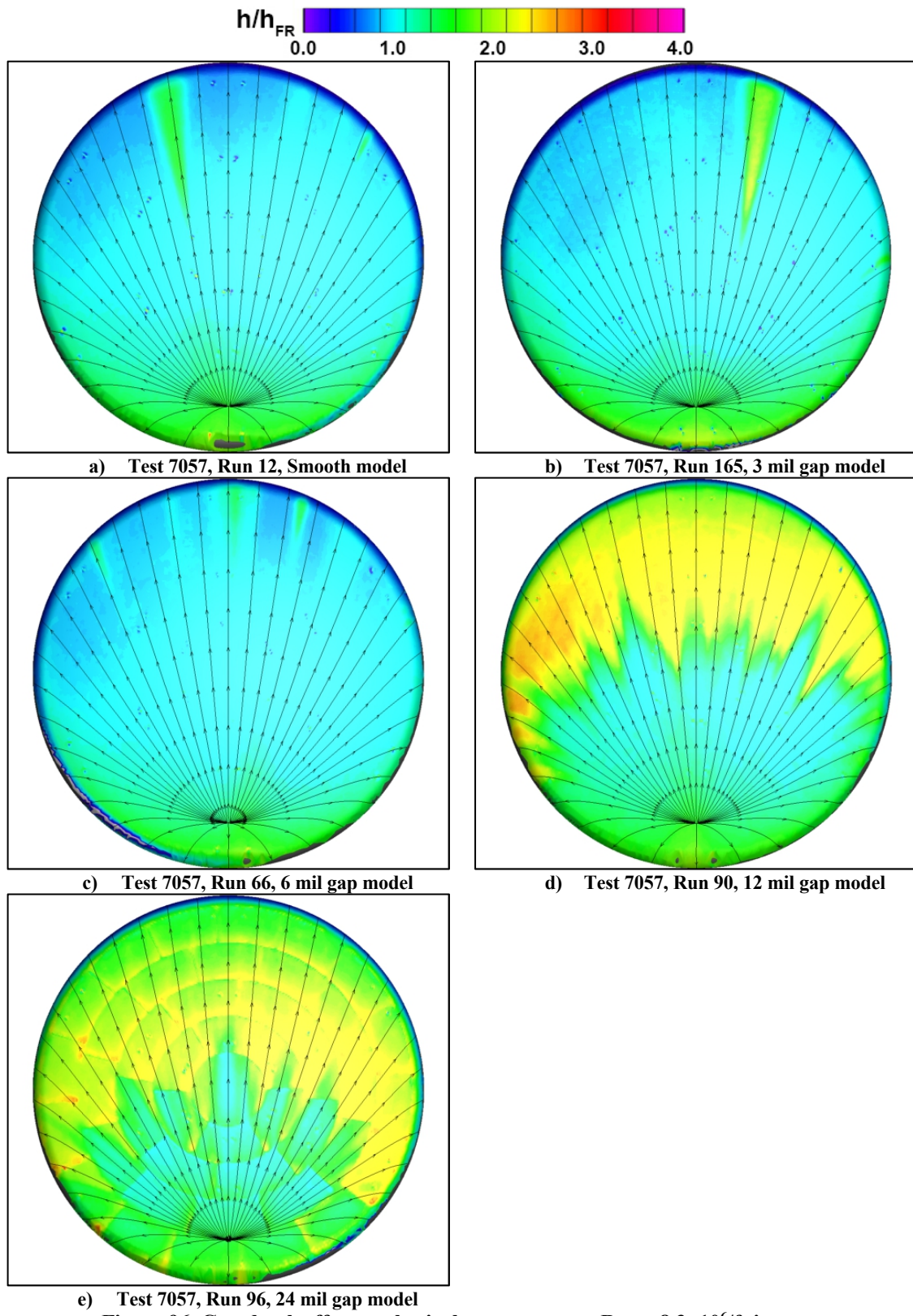


Figure 96. Gap depth effects, spherical-cap geometry, $Re_\infty = 8.3 \times 10^6$ /ft images.

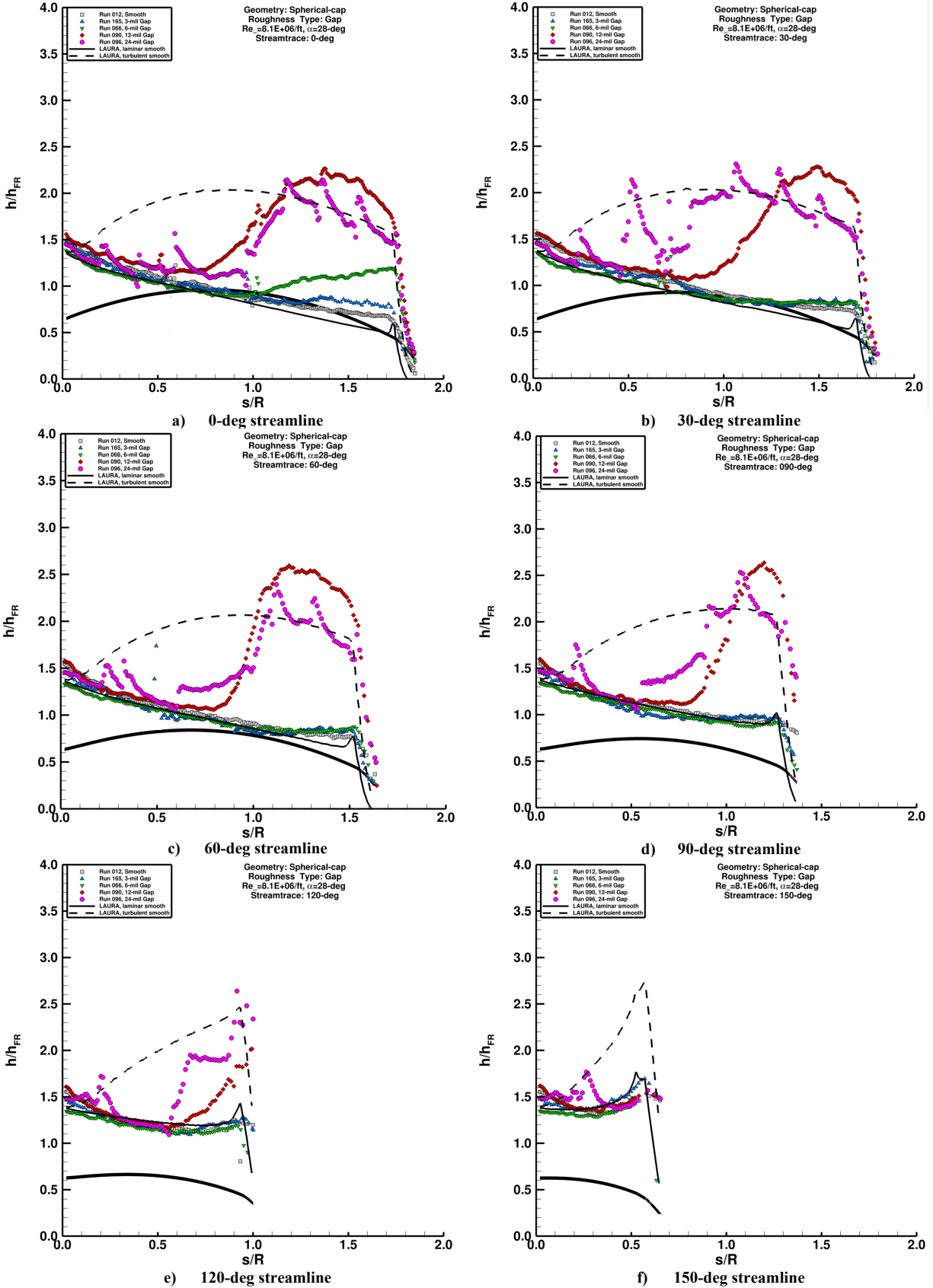


Figure 97. Gap depth effects, spherical-cap geometry, $Re_{\infty} = 8.3 \times 10^6/ft$ images.

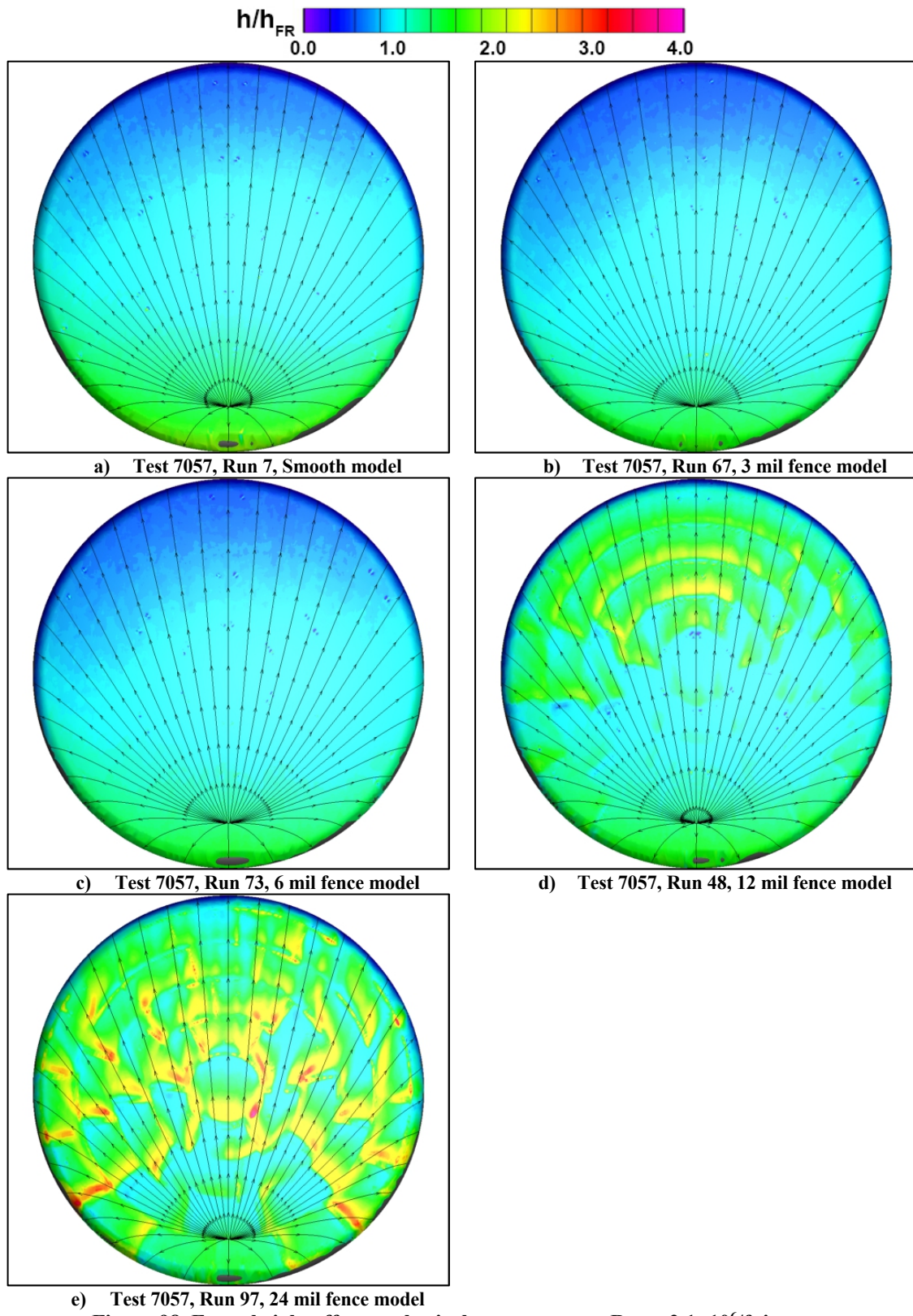


Figure 98. Fence height effects, spherical-cap geometry, $Re_\infty = 2.1 \times 10^6/ft$ images.

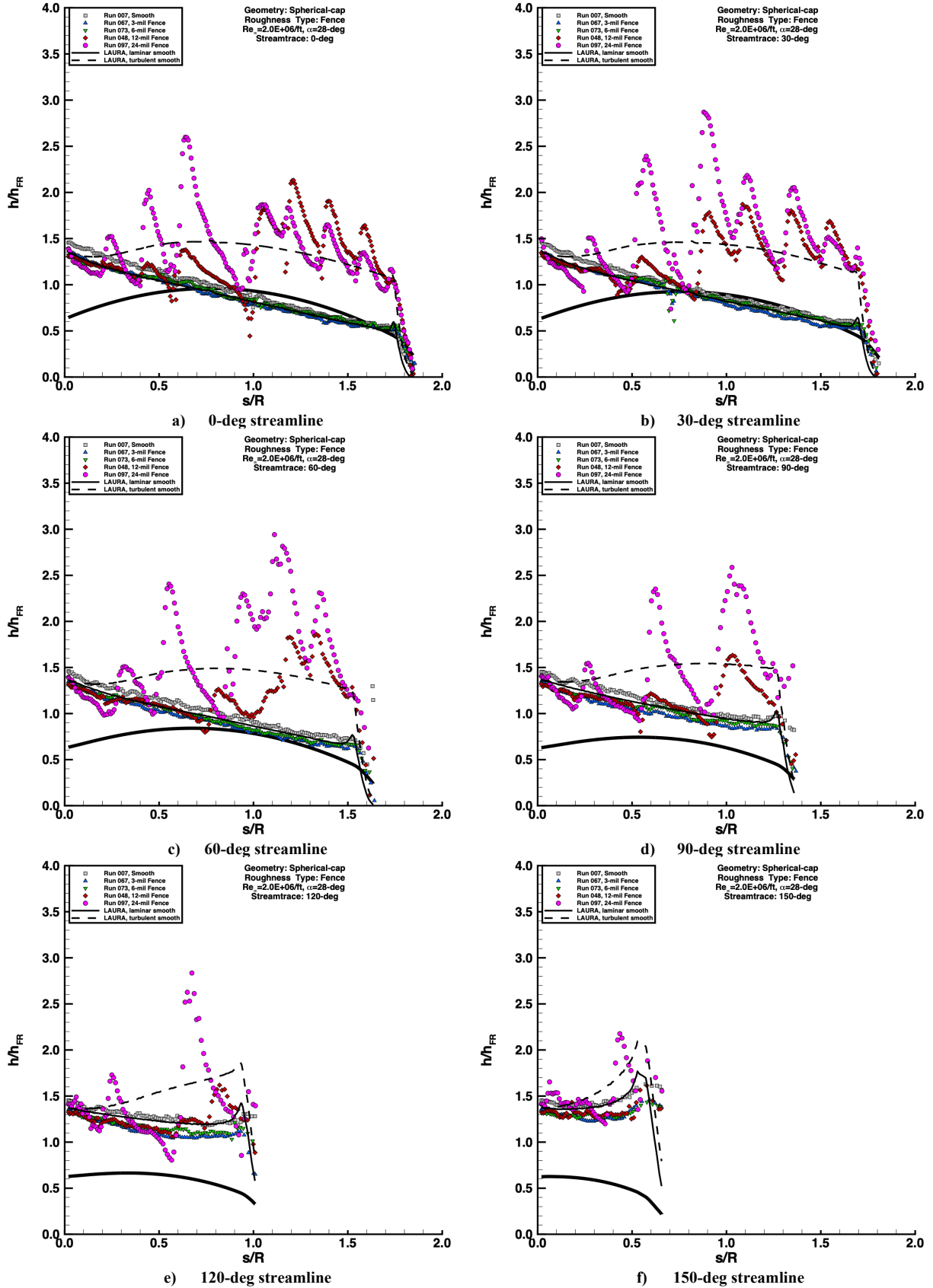


Figure 99. Fence height effects, spherical-cap geometry, $Re_{\infty} = 2.1 \times 10^6/ft$ images.

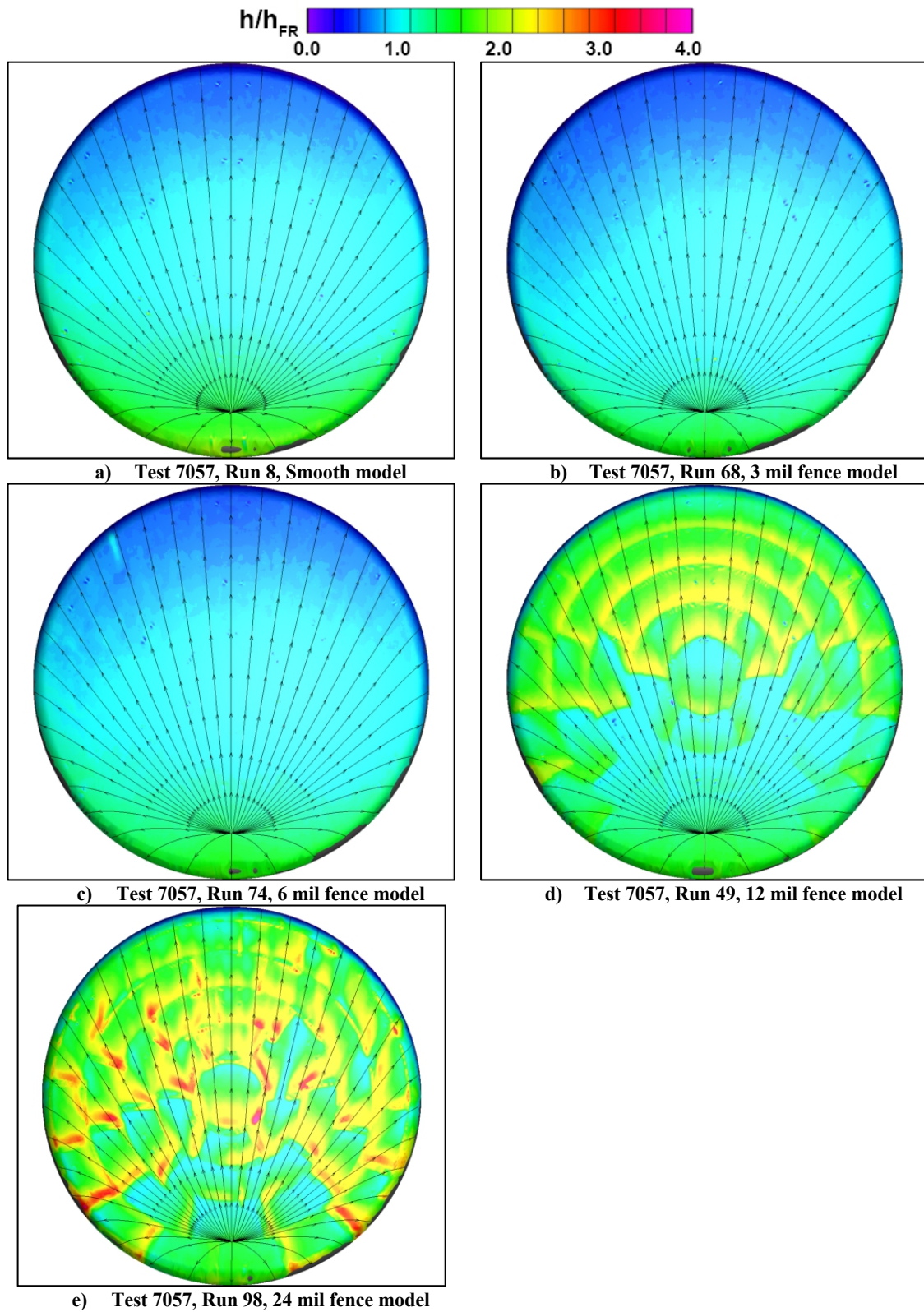


Figure 100. Fence height effects, spherical-cap geometry, $Re_\infty = 3.0 \times 10^6/ft$ images.

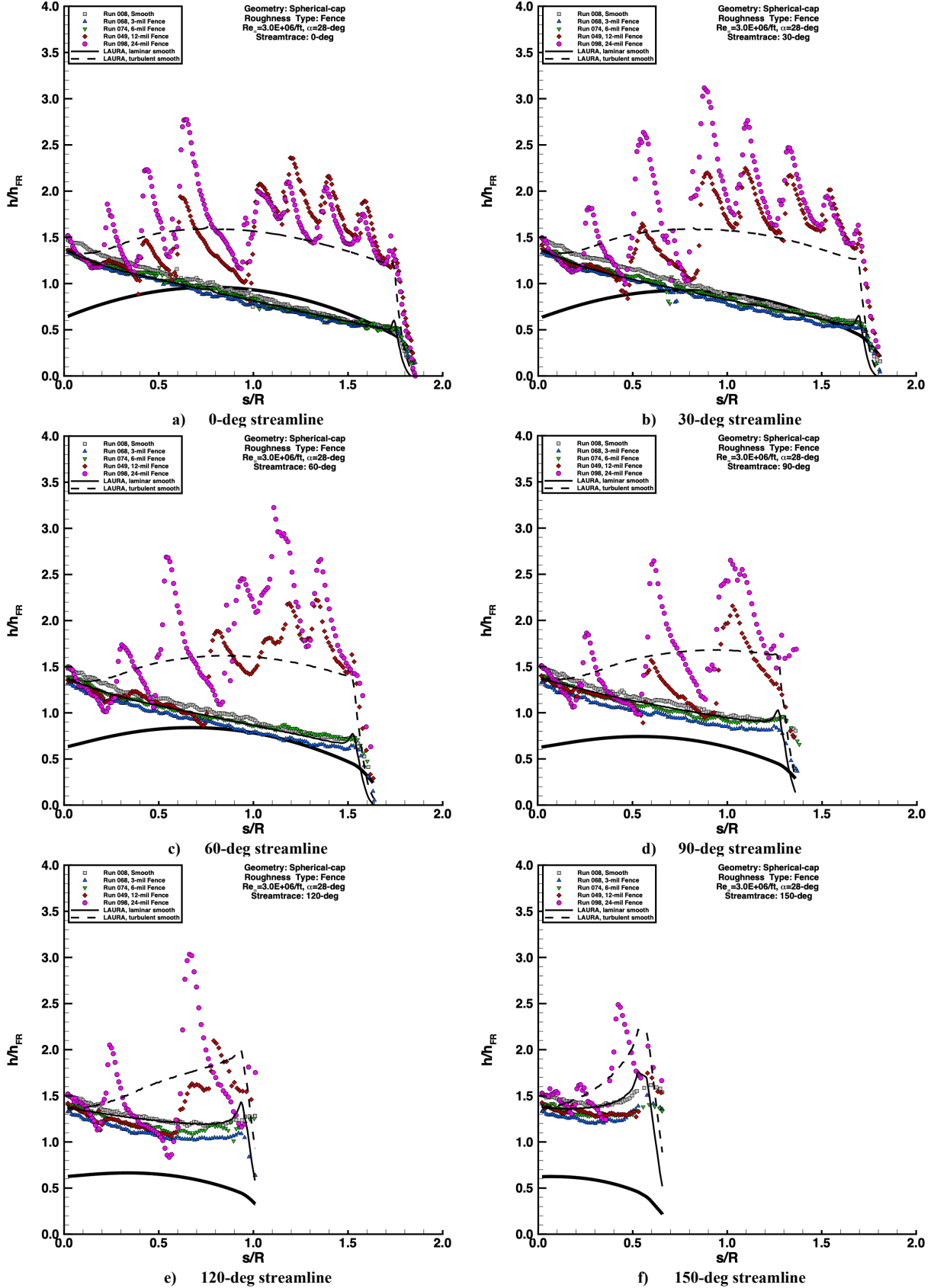


Figure 101. Fence height effects, spherical-cap geometry, $Re_{\infty} = 3.0 \times 10^6 / ft$ images.

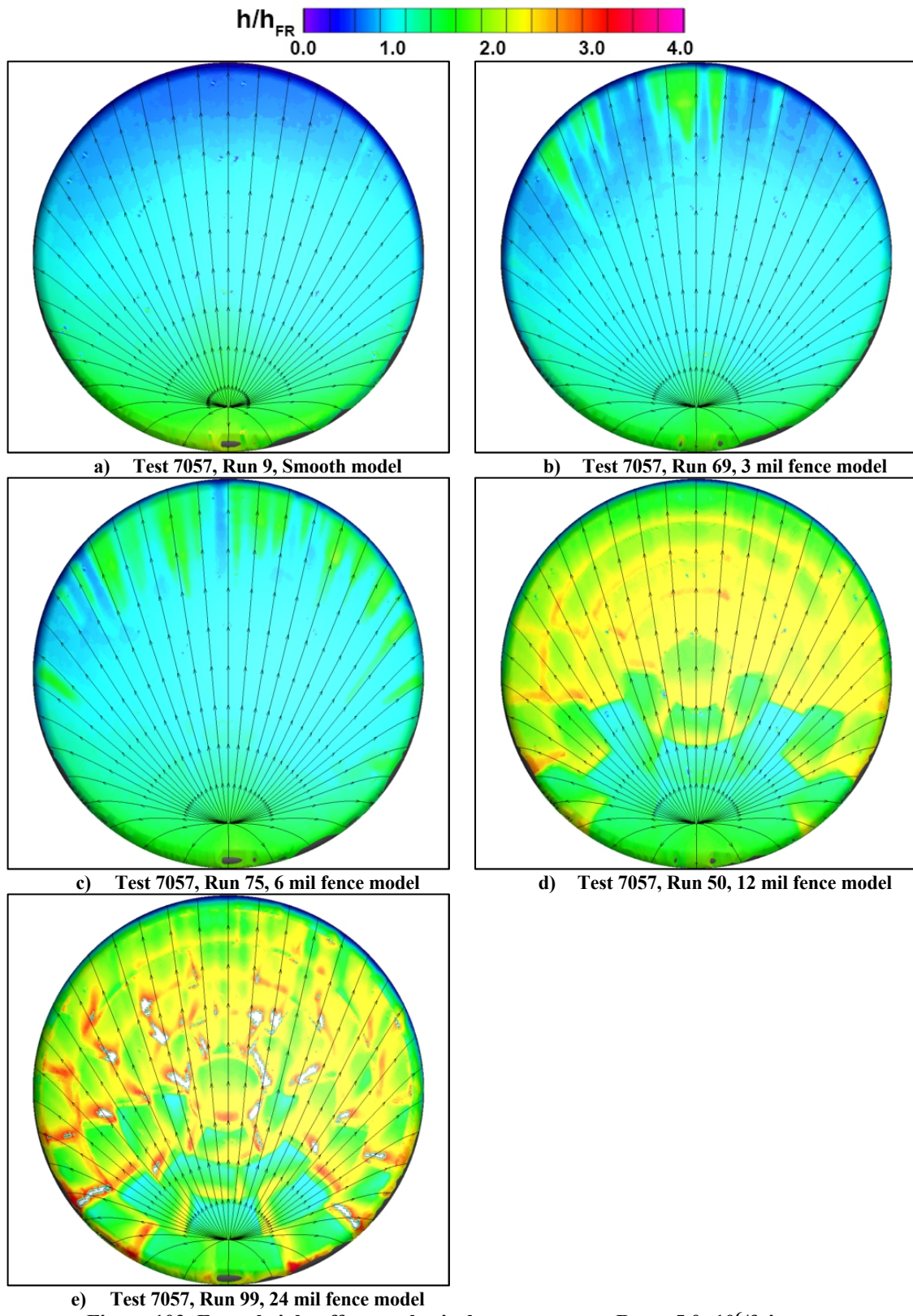


Figure 102. Fence height effects, spherical-cap geometry, $Re_\infty = 5.0 \times 10^6$ /ft images.

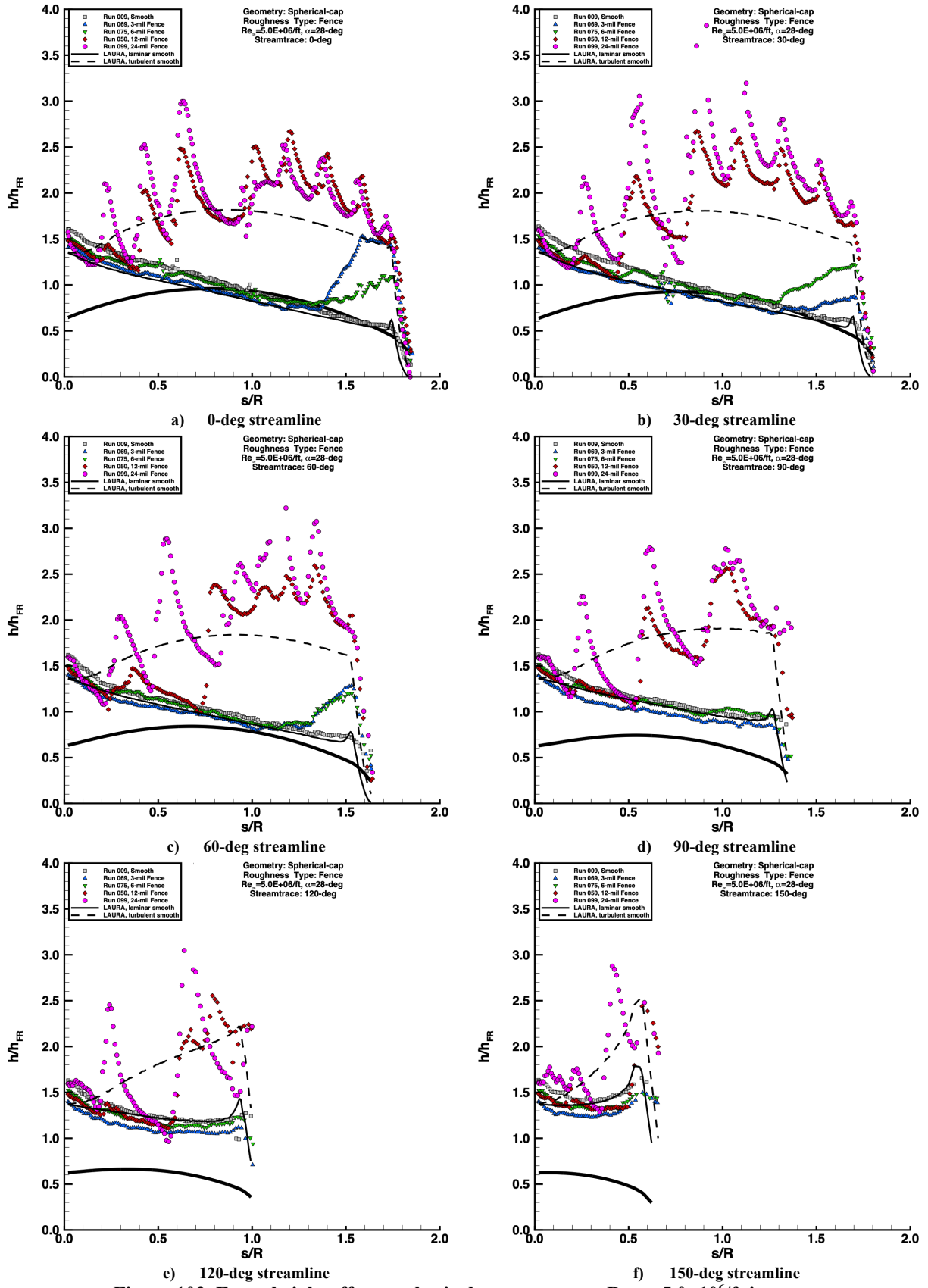


Figure 103. Fence height effects, spherical-cap geometry, $Re_{\infty} = 5.0 \times 10^6/ft$ images.

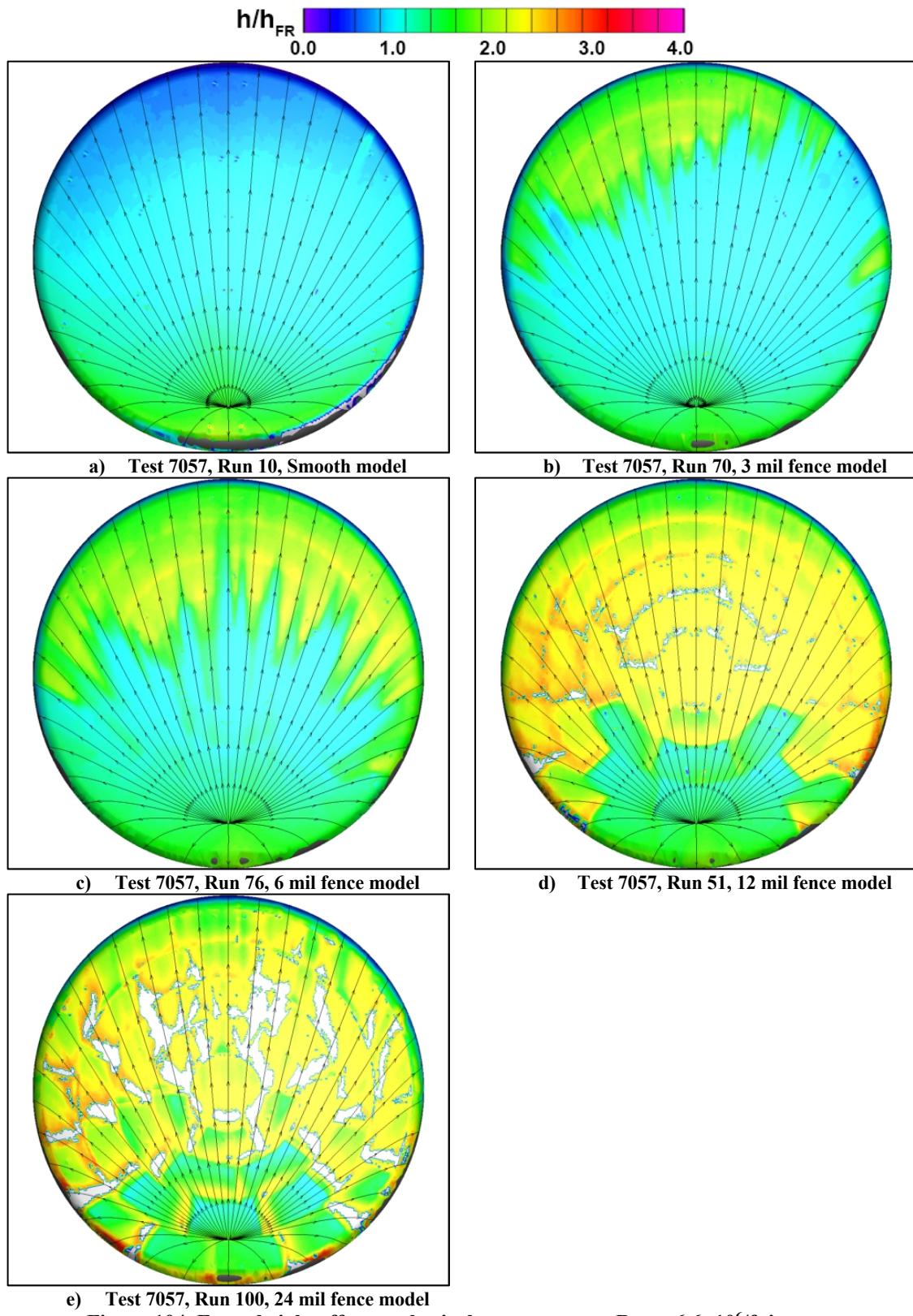


Figure 104. Fence height effects, spherical-cap geometry, $Re_\infty = 6.6 \times 10^6$ /ft images.

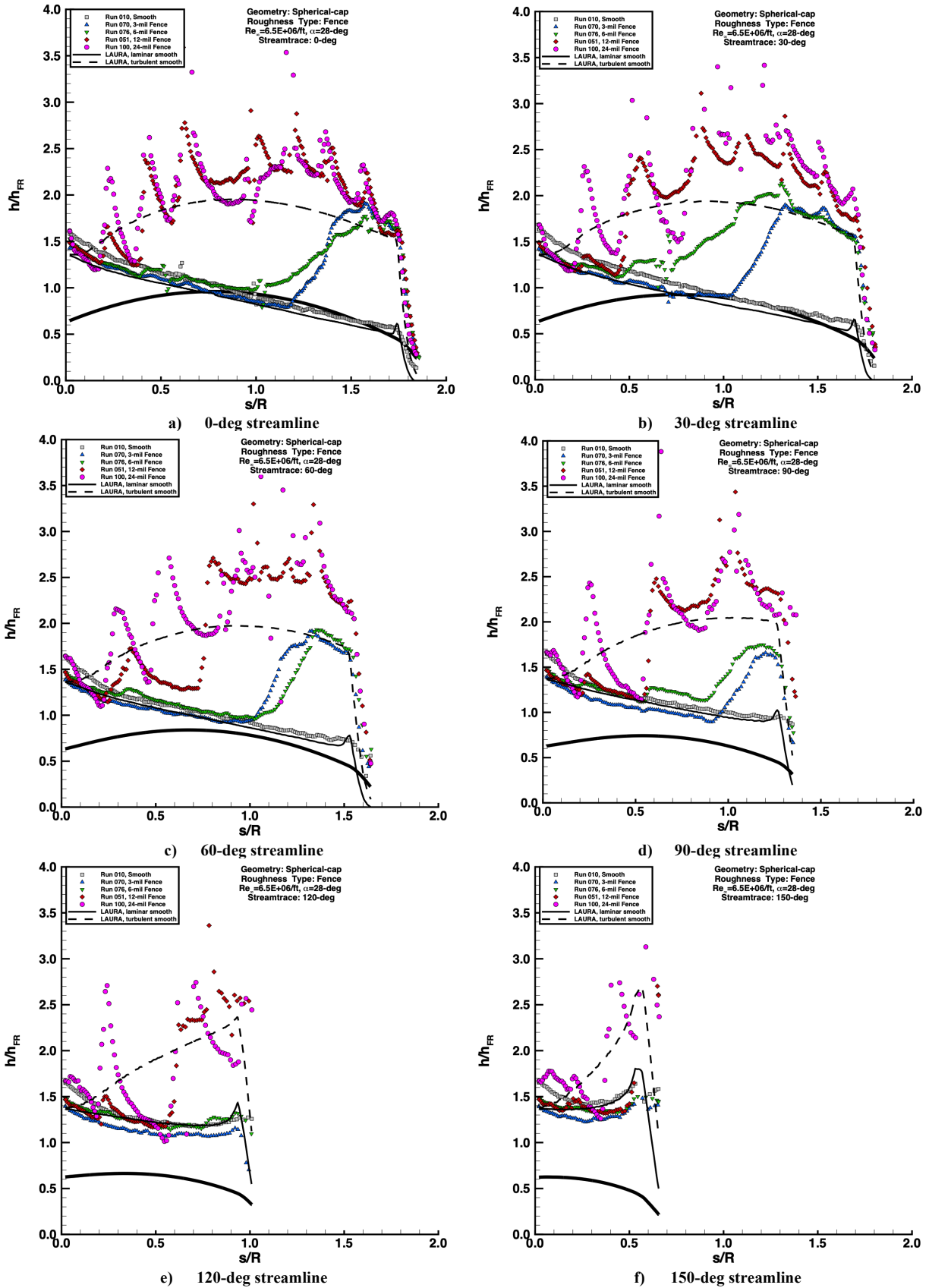


Figure 105. Fence height effects, spherical-cap geometry, $Re_{\infty} = 6.6 \times 10^6/ft$ images.

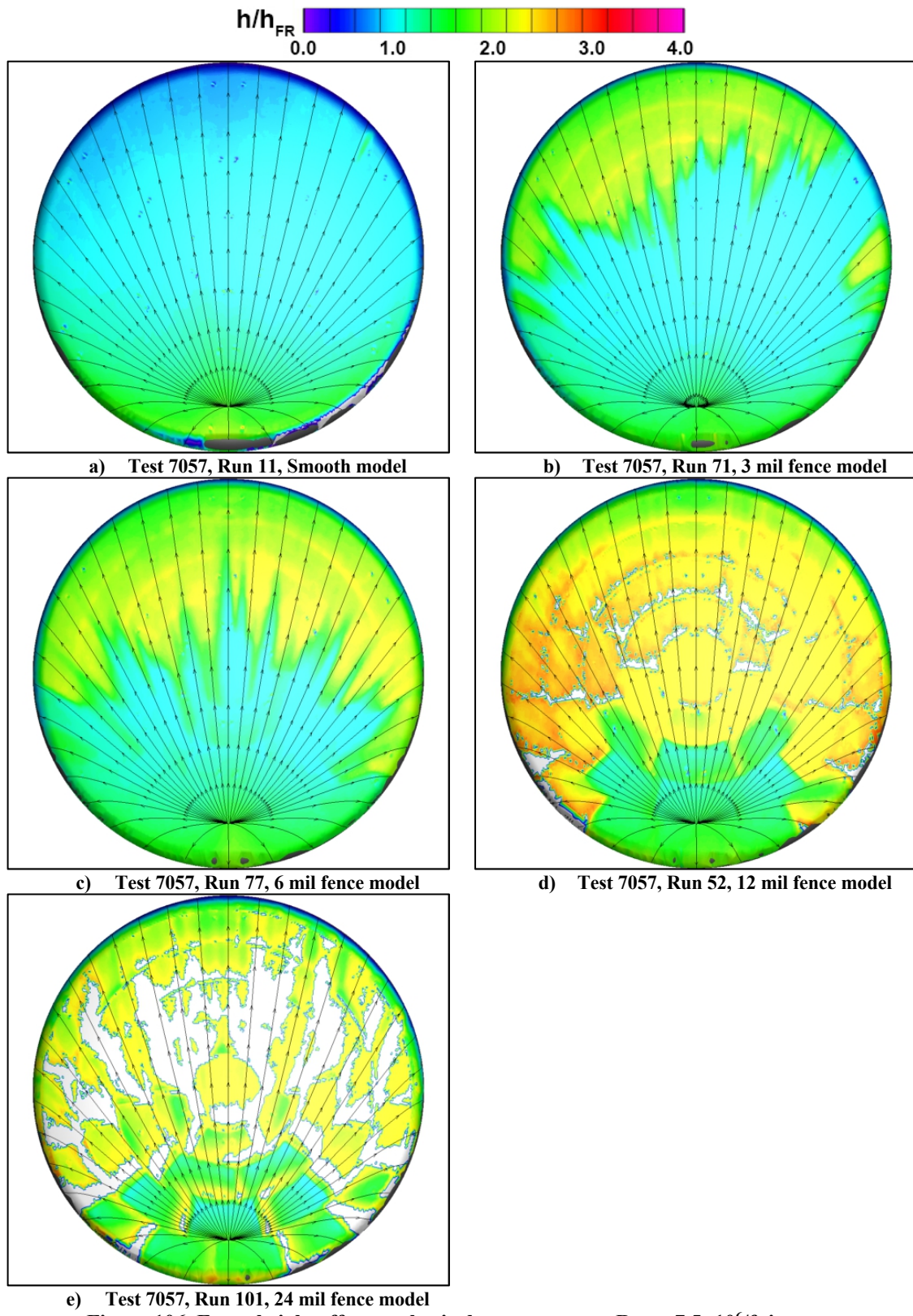


Figure 106. Fence height effects, spherical-cap geometry, $Re_\infty = 7.5 \times 10^6/ft$ images.

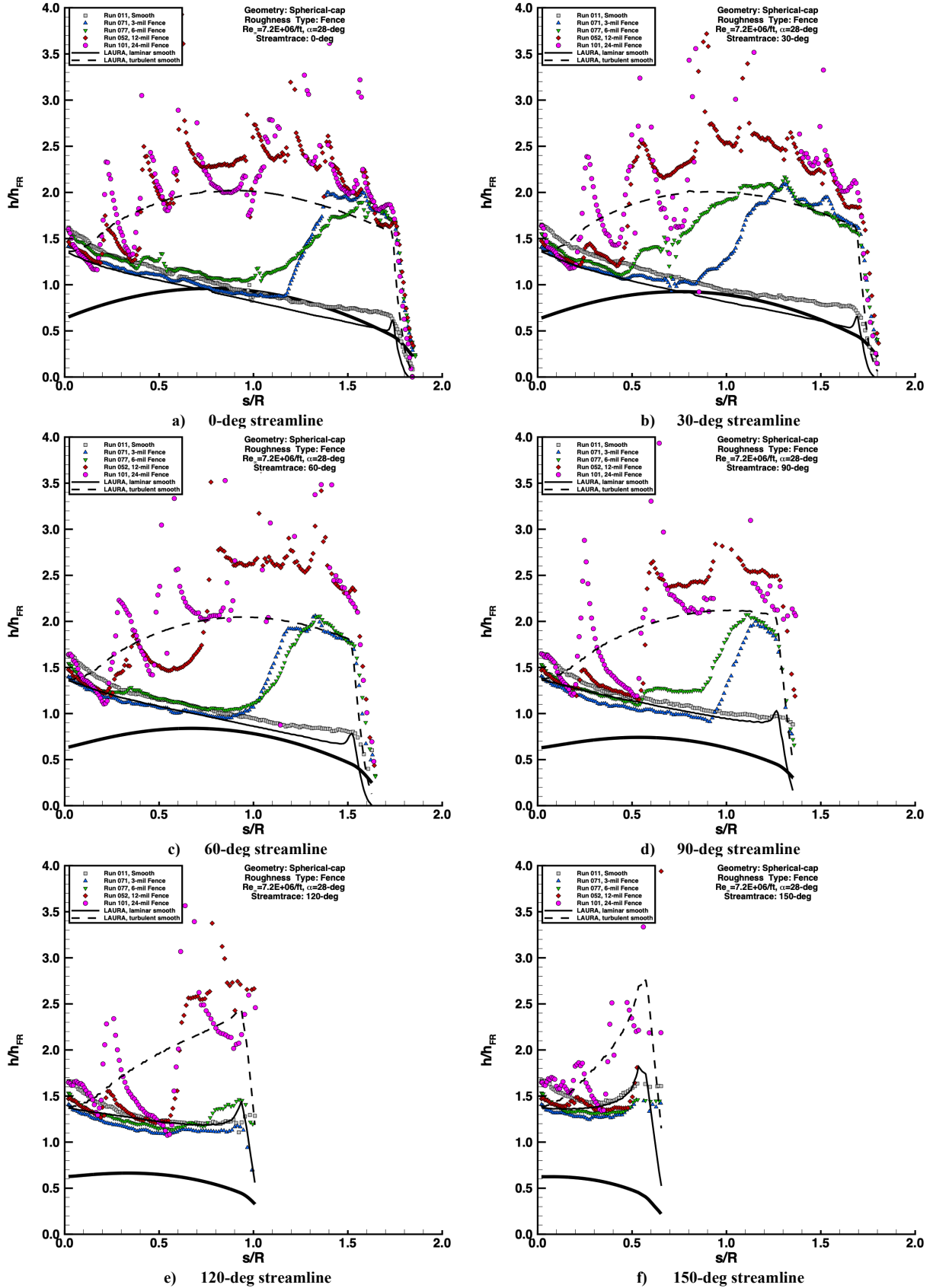


Figure 107. Fence height effects, spherical-cap geometry, $Re_{\infty} = 7.5 \times 10^6/ft$ images.

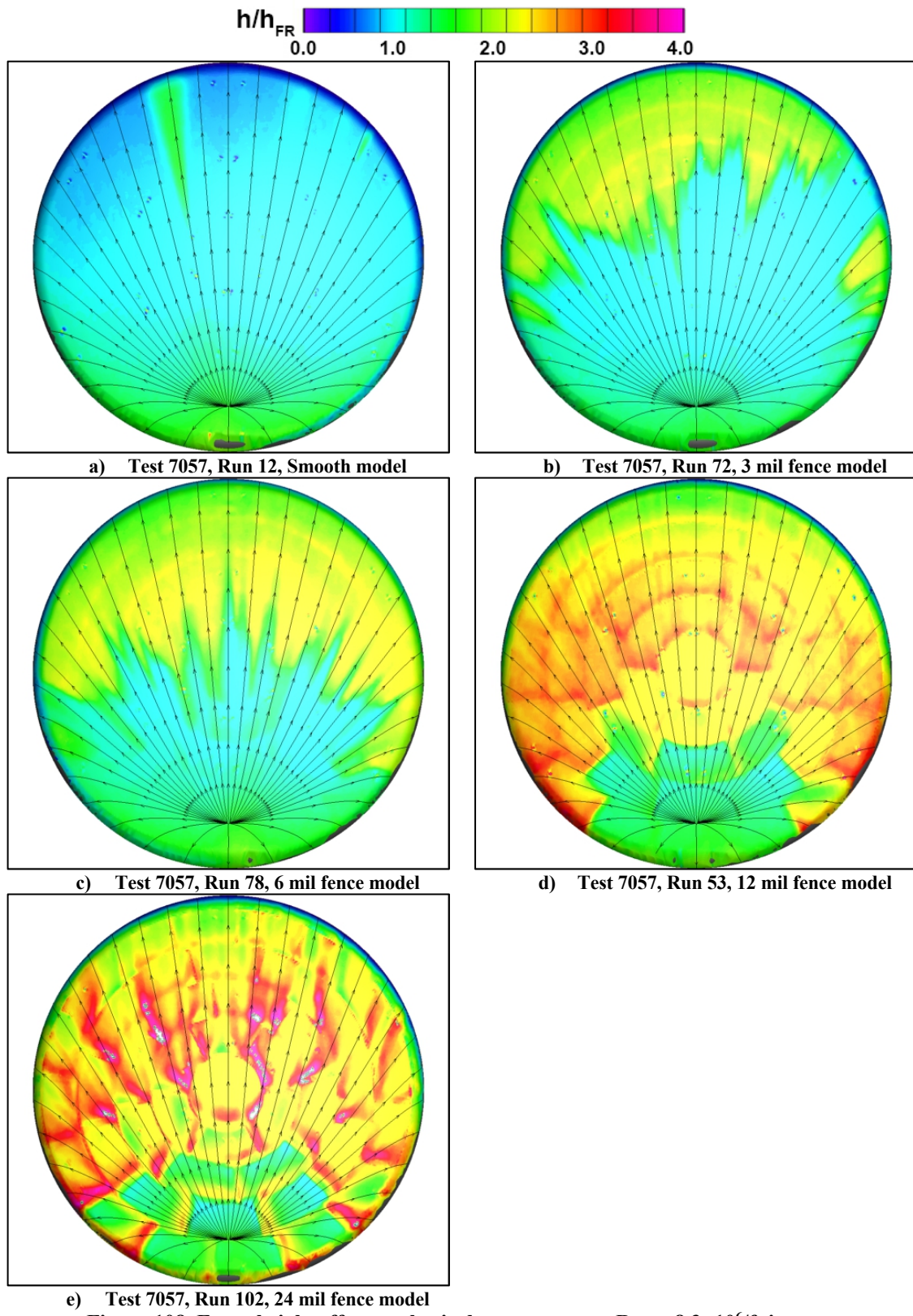


Figure 108. Fence height effects, spherical-cap geometry, $Re_\infty = 8.3 \times 10^6$ /ft images.

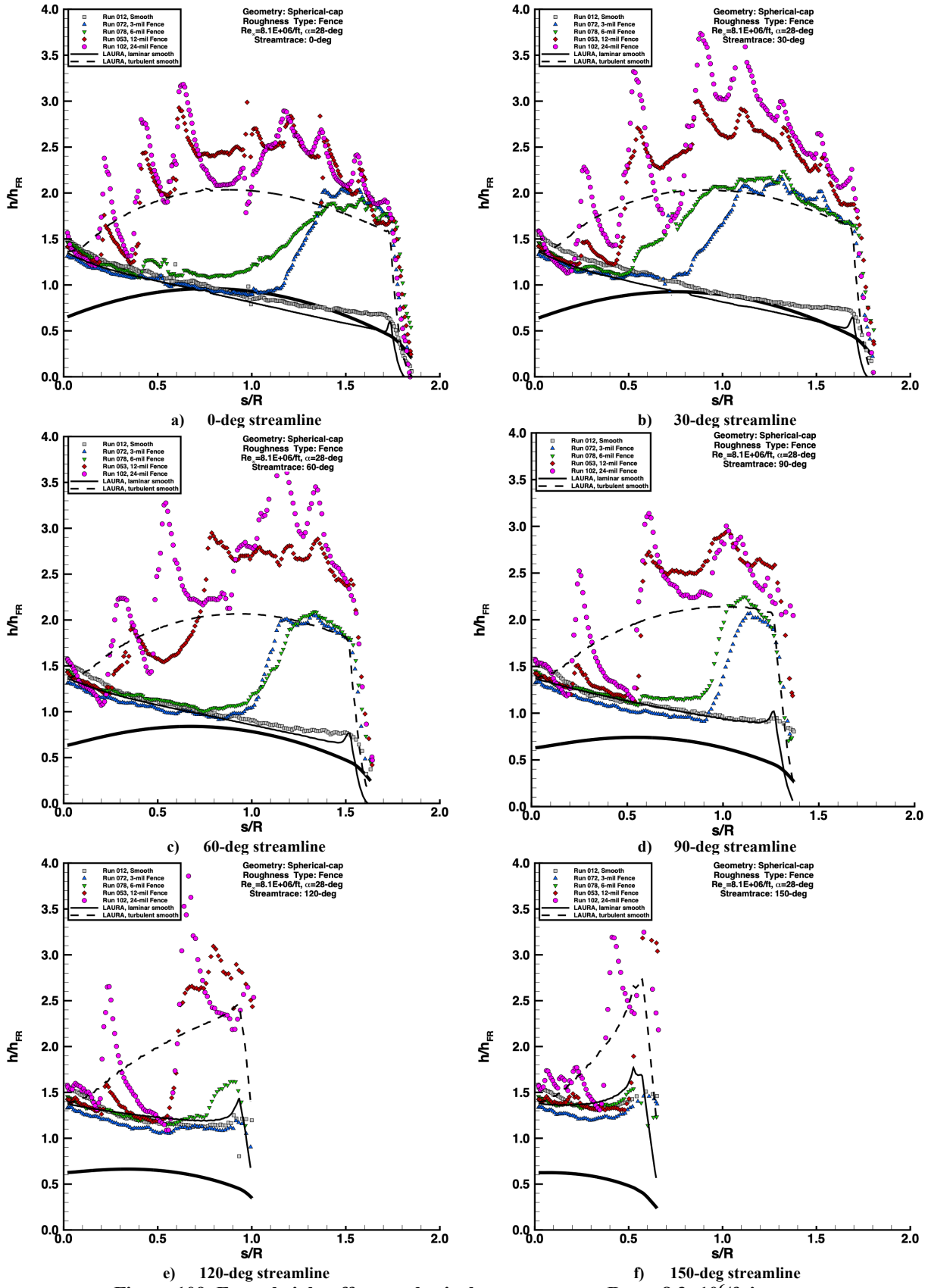


Figure 109. Fence height effects, spherical-cap geometry, $Re_{\infty} = 8.3 \times 10^6/ft$ images.

Appendix A. Sphere-cone Geometry Global Heating Images

Global heating images for the sphere-cone geometry from Test 7036 in the LAL 20-Inch Mach 6 Air Tunnel are presented in this Appendix. Smooth wall data are shown in Figure 110 to Figure 115, gap model data are shown in Figure 116 to Figure 139, and fence model data are presented in Figure 140 to Figure 163. In these images, boundary-layer edge streamlines determined from laminar, smooth-surface LAURA simulations have been superimposed to illustrate the nature of the flow field.

At higher Reynolds numbers and/or larger fence heights, white patches on the images indicate areas where the measured surface temperatures exceed the calibrated range of the phosphor thermography (approximately 460 K) and no valid data were obtained.

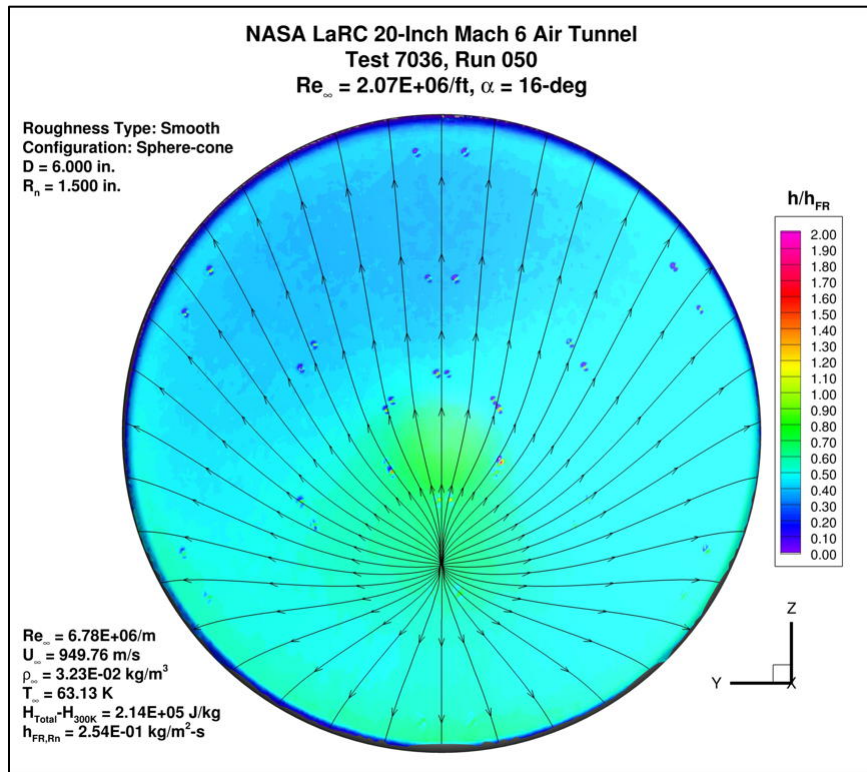


Figure 110. Test 7036, Run 50, $Re_{\infty} = 2.1 \times 10^6/ft$, sphere-cone, smooth OML.

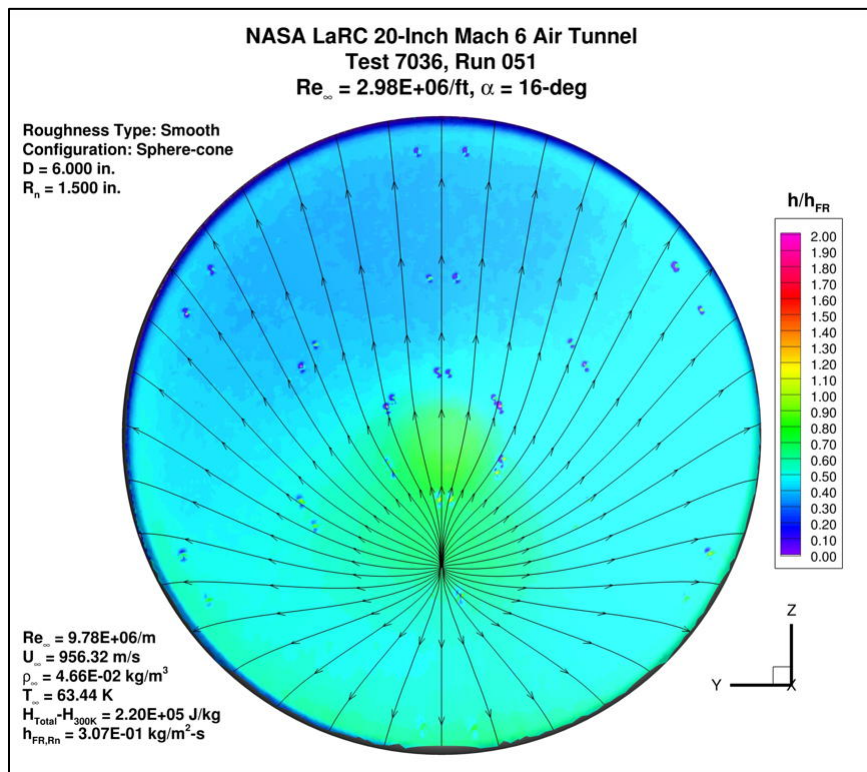


Figure 111. Test 7036, Run 51, $Re_{\infty} = 3.0 \times 10^6/ft$, sphere-cone, smooth OML.

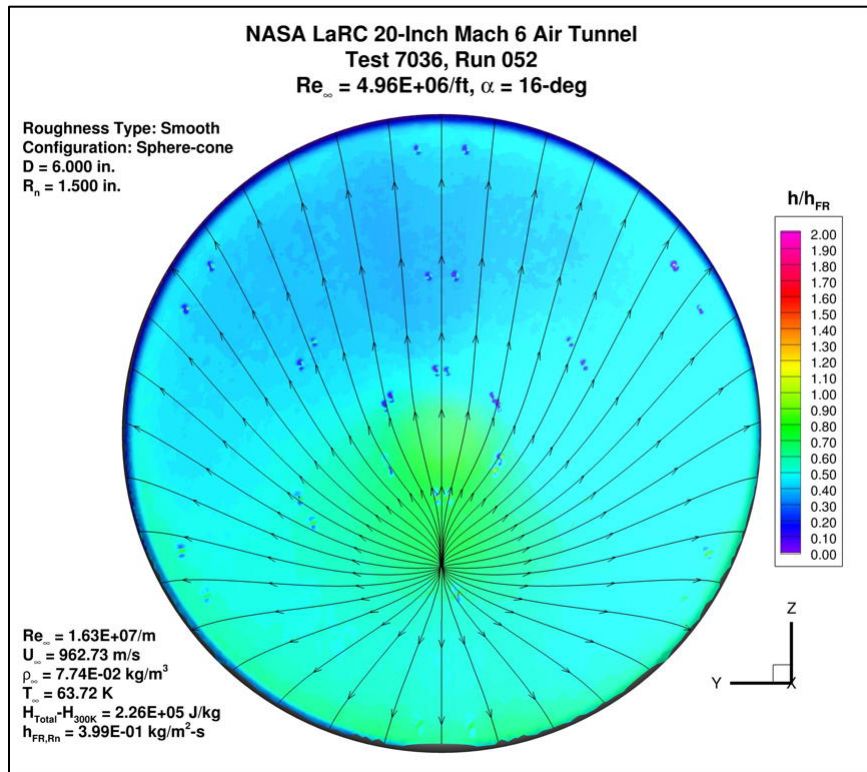


Figure 112. Test 7036, Run 52, $Re_{\infty} = 5.0 \times 10^6/ft$, sphere-cone, smooth OML.

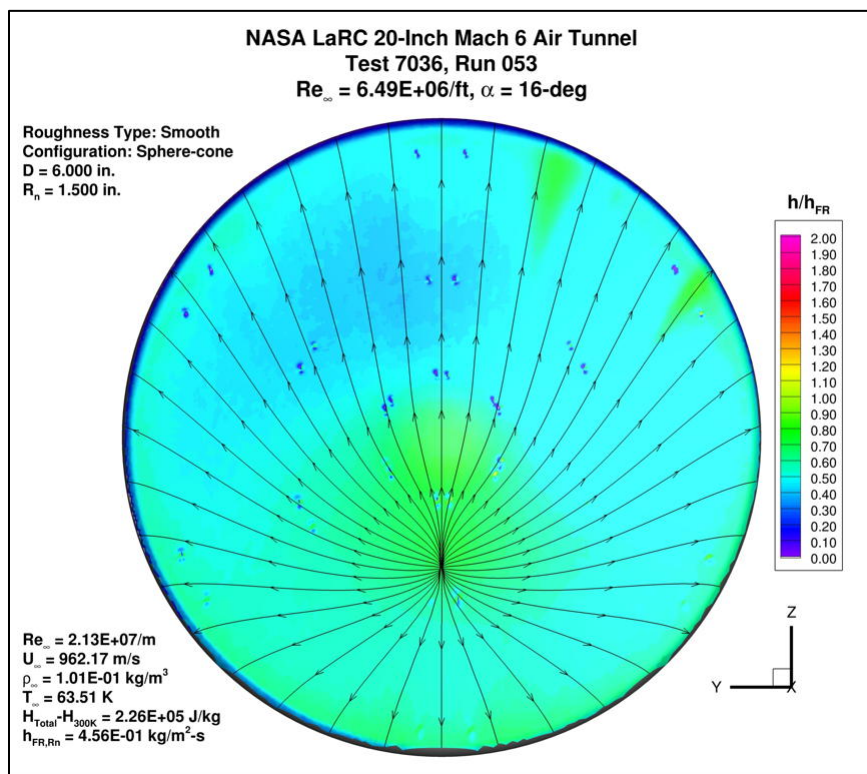


Figure 113. Test 7036, Run 53, $Re_{\infty} = 6.6 \times 10^6/ft$, sphere-cone, smooth OML.

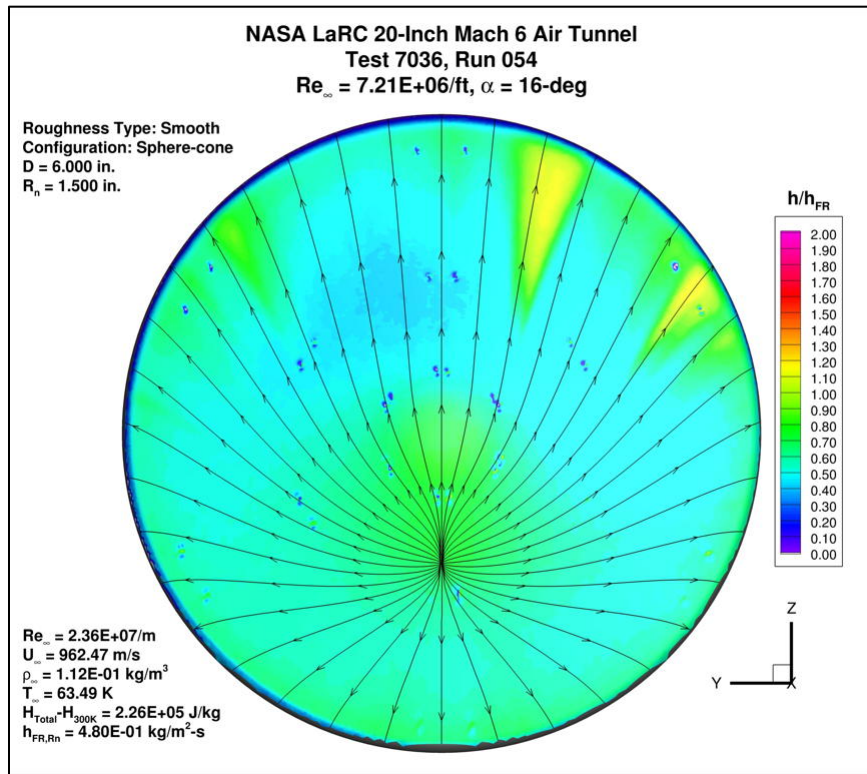


Figure 114. Test 7036, Run 54, $Re_{\infty} = 7.5 \times 10^6/ft$, sphere-cone, smooth OML.

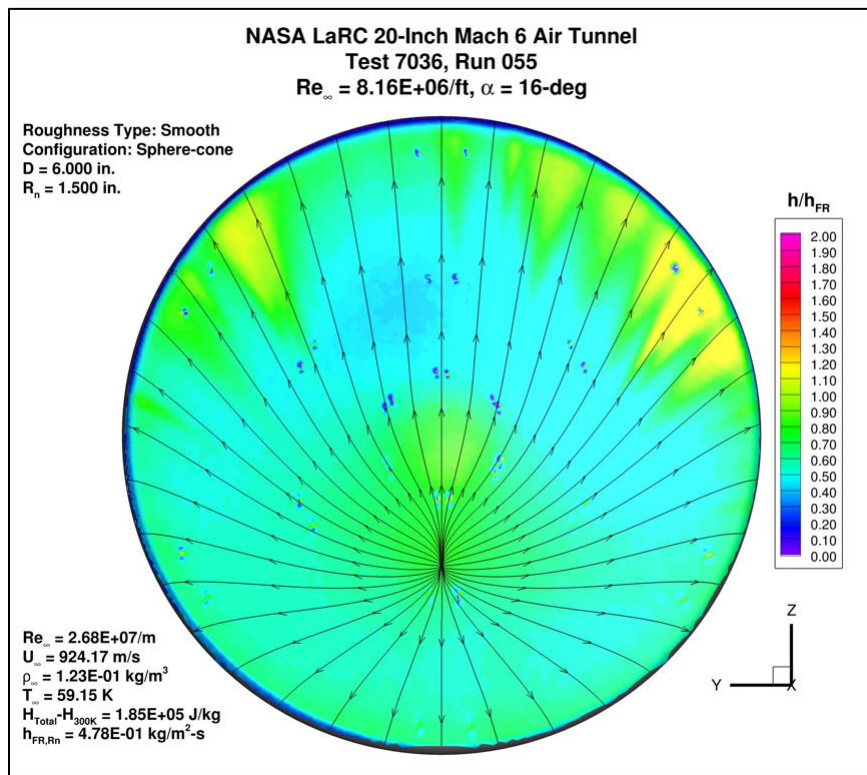


Figure 115. Test 7036, Run 55, $Re_{\infty} = 8.3 \times 10^6/ft$, sphere-cone, smooth OML.

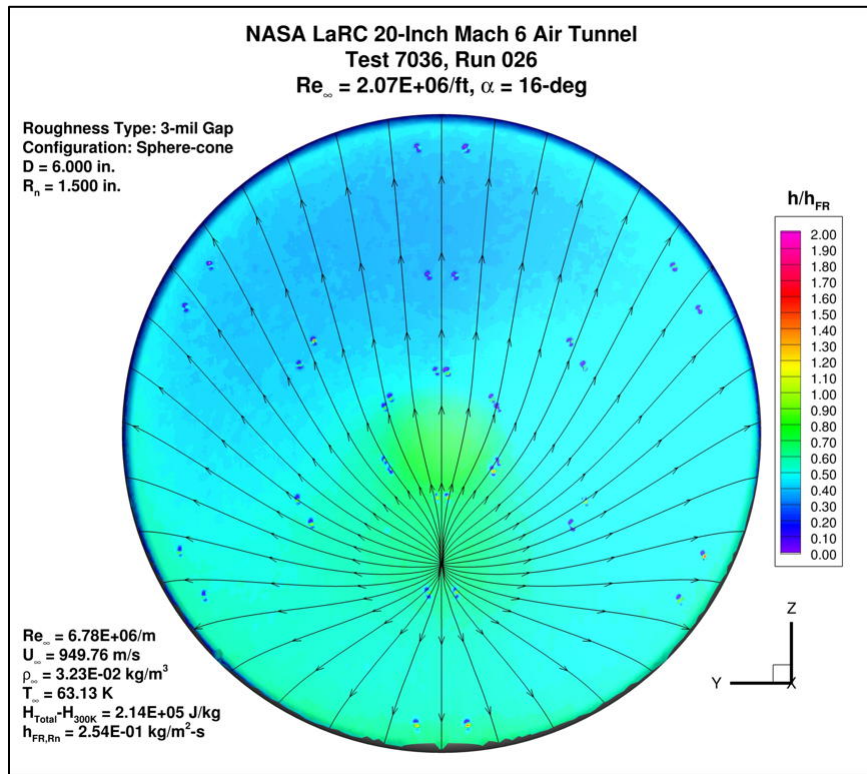


Figure 116. Test 7036, Run 26, $Re_\infty = 2.1 \times 10^6/\text{ft}$, sphere-cone 3 mil gap.

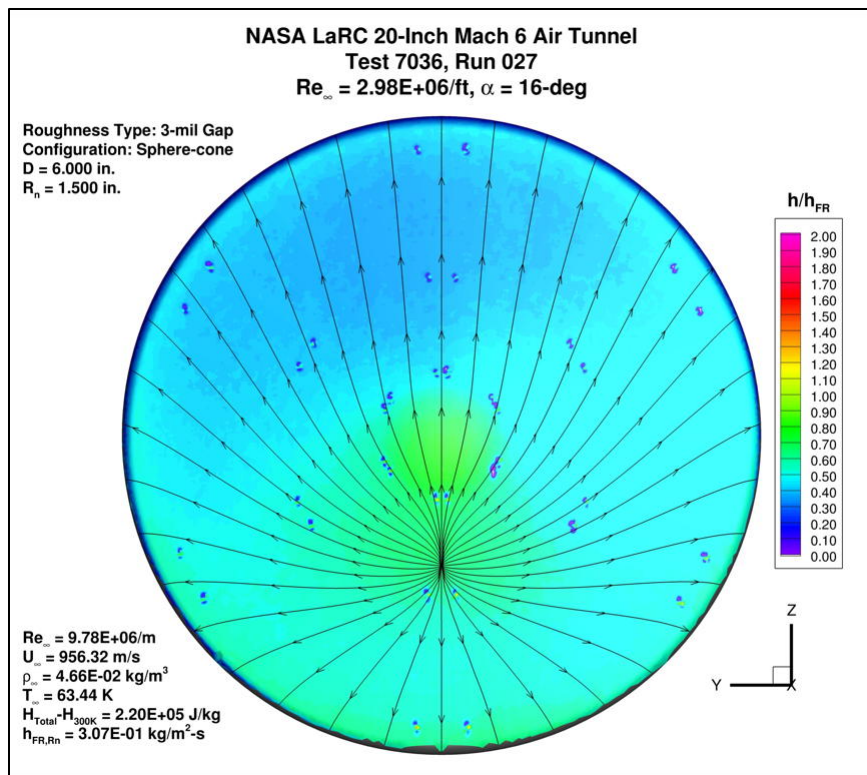


Figure 117. Test 7036, Run 27, $Re_\infty = 3.0 \times 10^6/\text{ft}$, sphere-cone 3 mil gap.

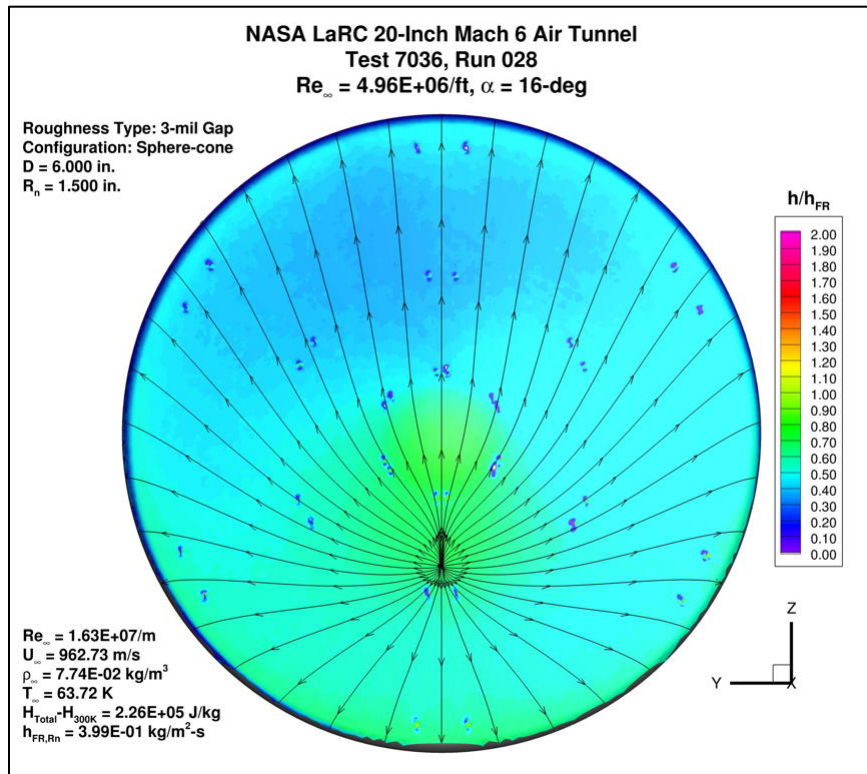


Figure 118. Test 7036, Run 28, $Re_\infty = 5.0 \times 10^6/\text{ft}$, sphere-cone 3 mil gap.

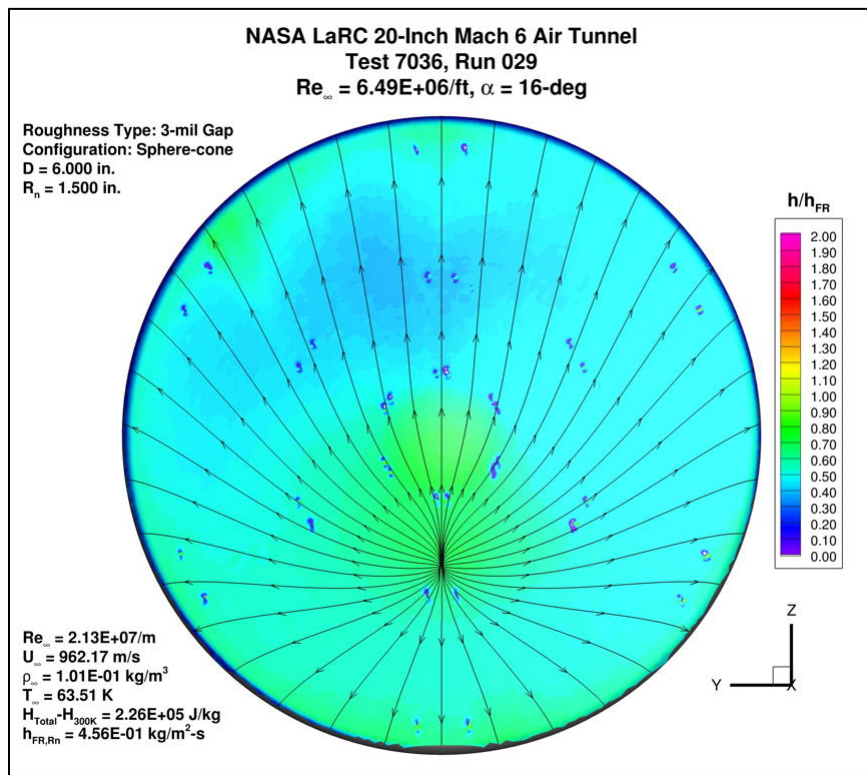


Figure 119. Test 7036, Run 29, $Re_\infty = 6.6 \times 10^6/\text{ft}$, sphere-cone 3 mil gap.

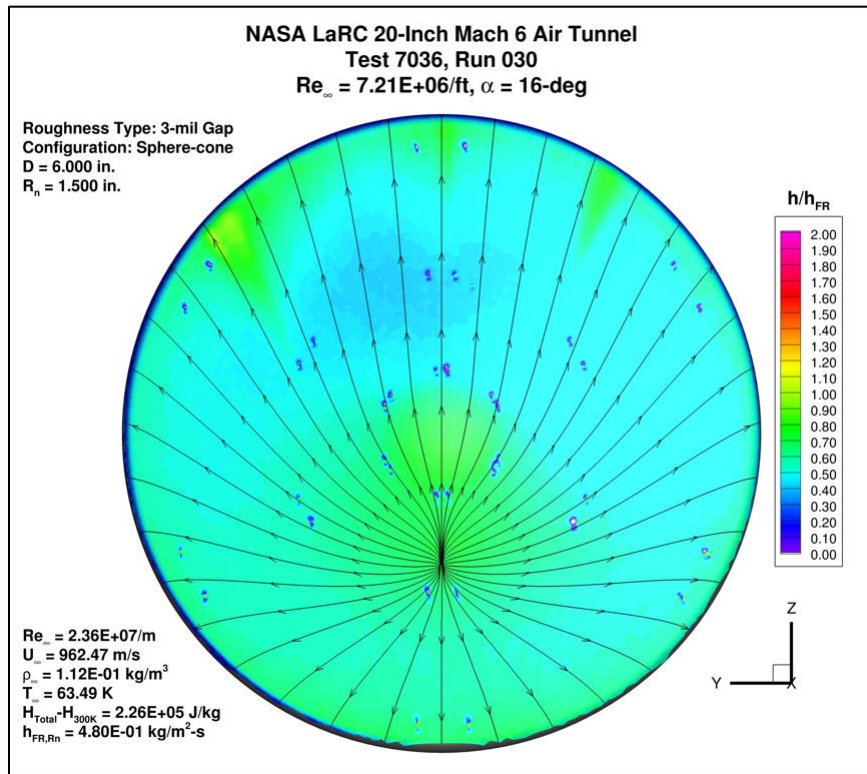


Figure 120. Test 7036, Run 30, $Re_\infty = 7.5 \times 10^6/ft$, sphere-cone 3 mil gap.

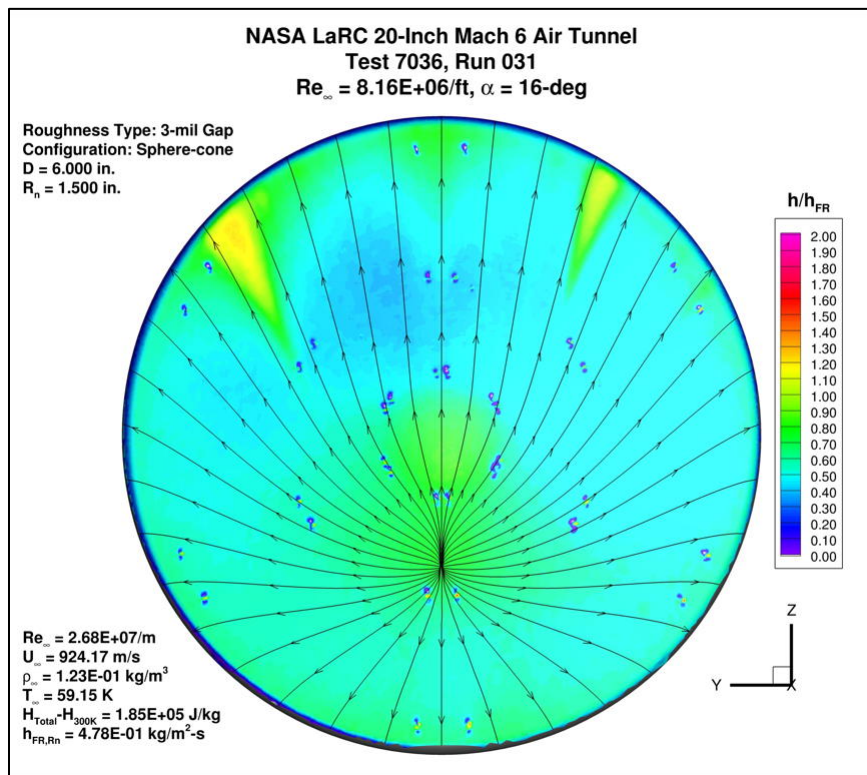


Figure 121. Test 7036, Run 31, $Re_\infty = 8.3 \times 10^6/ft$, sphere-cone 3 mil gap.

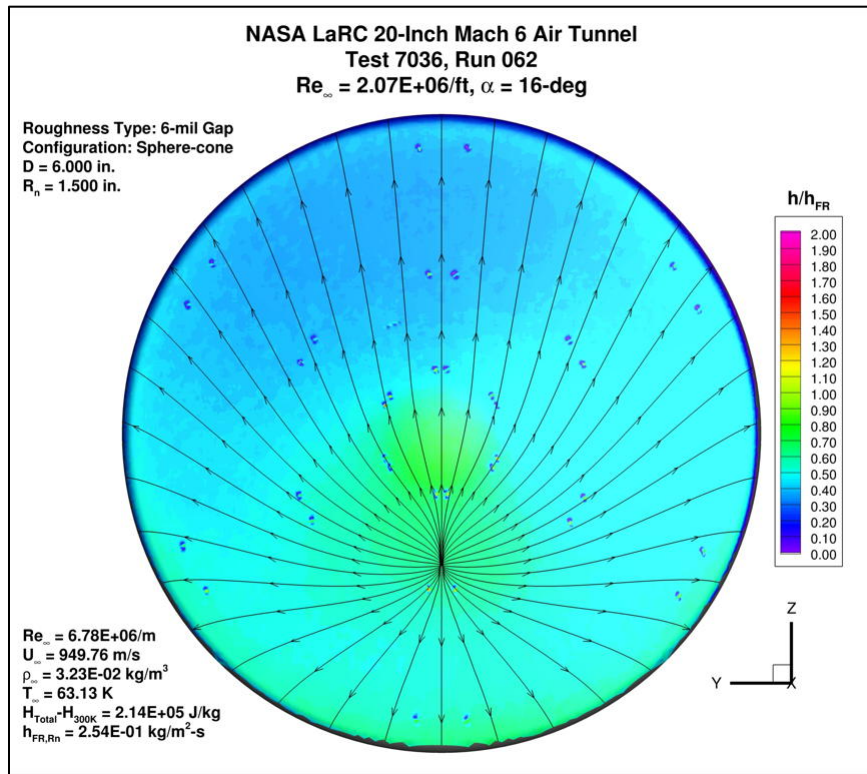


Figure 122. Test 7036, Run 62, $Re_\infty = 2.1 \times 10^6/\text{ft}$, sphere-cone 6 mil gap.

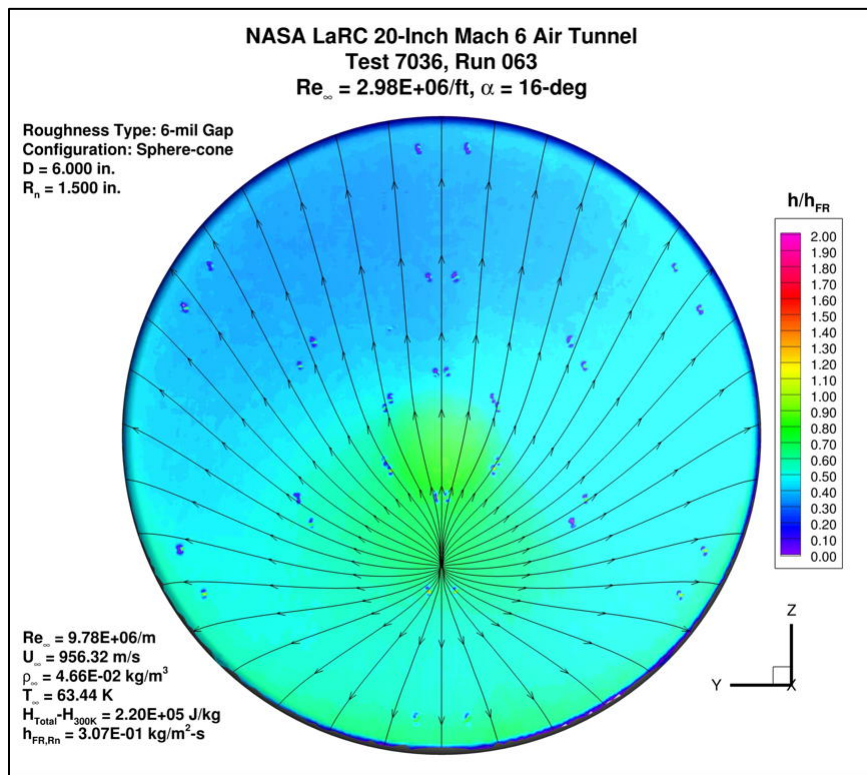


Figure 123. Test 7036, Run 63, $Re_\infty = 3.0 \times 10^6/\text{ft}$, sphere-cone 6 mil gap.

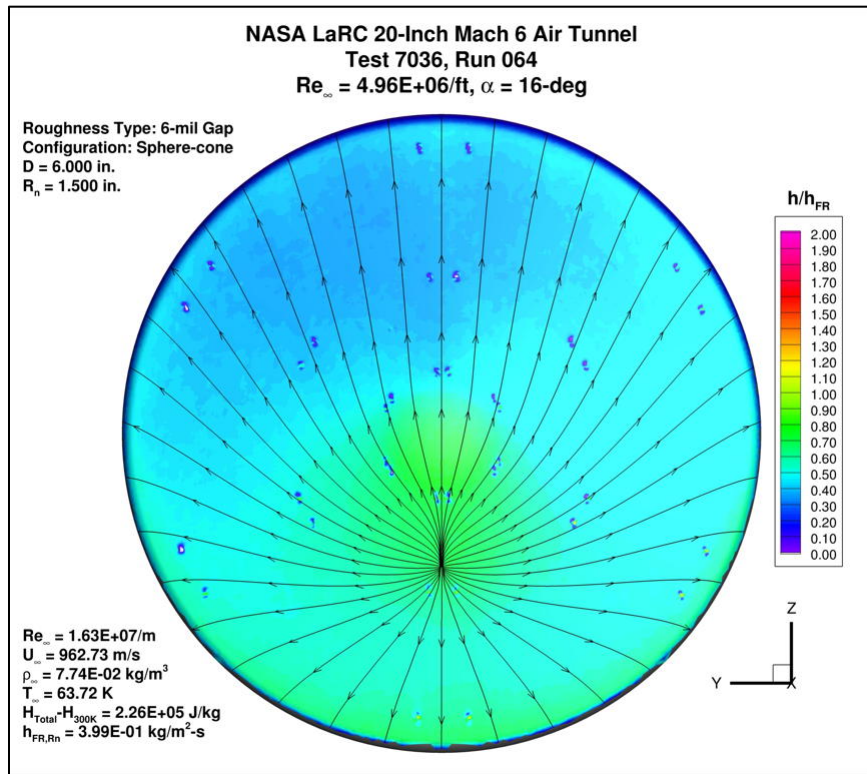


Figure 124. Test 7036, Run 64, $Re_\infty = 5.0 \times 10^6/\text{ft}$, sphere-cone 6 mil gap.

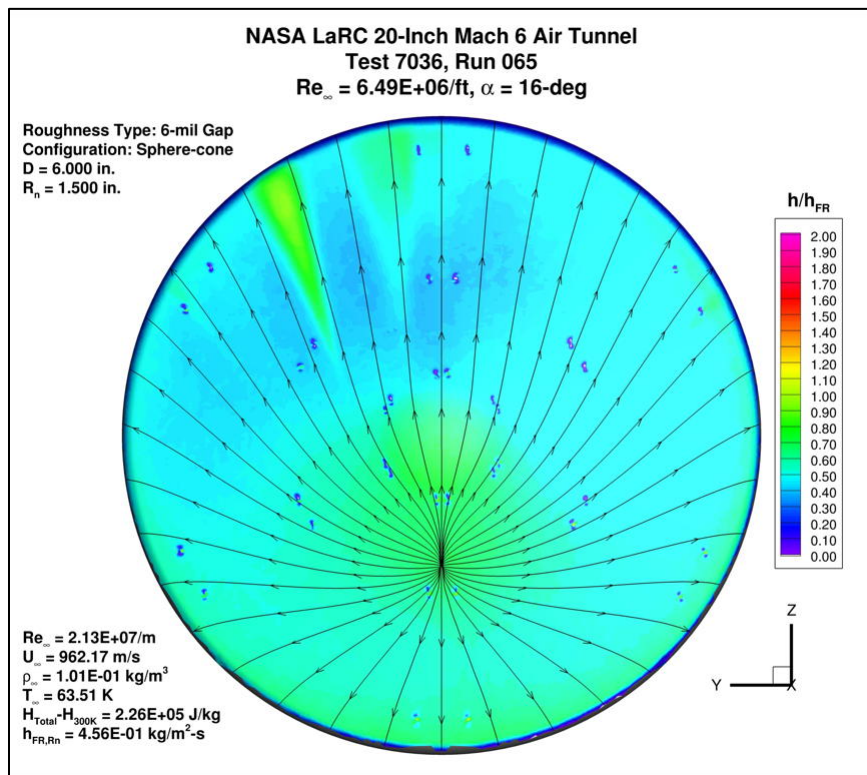


Figure 125. Test 7036, Run 65, $Re_\infty = 6.6 \times 10^6/\text{ft}$, sphere-cone 6 mil gap.

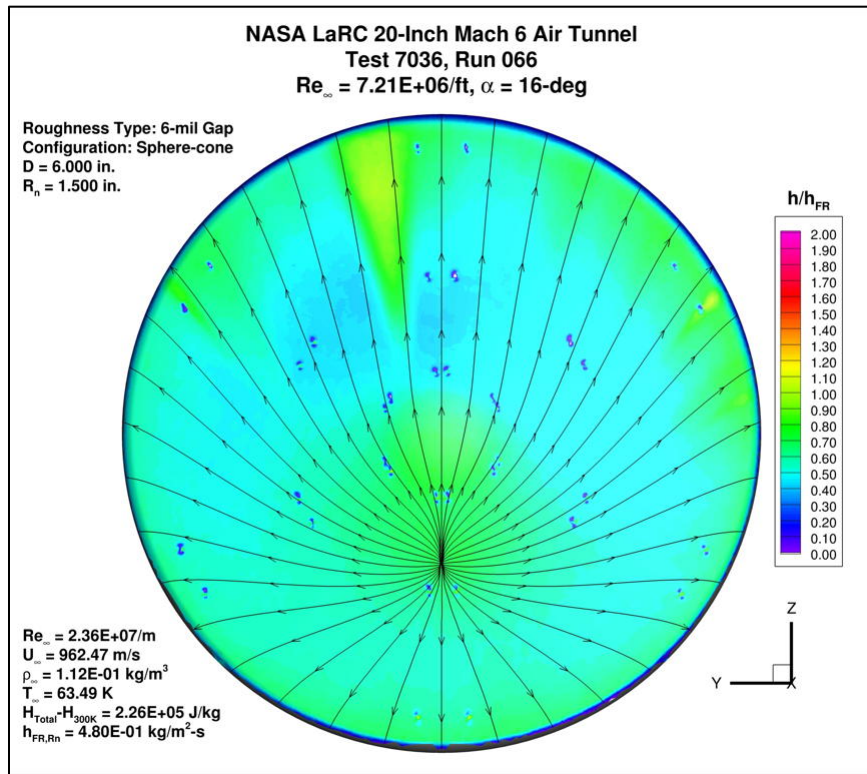


Figure 126. Test 7036, Run 66, $Re_\infty = 7.5 \times 10^6/ft$, sphere-cone 6 mil gap.

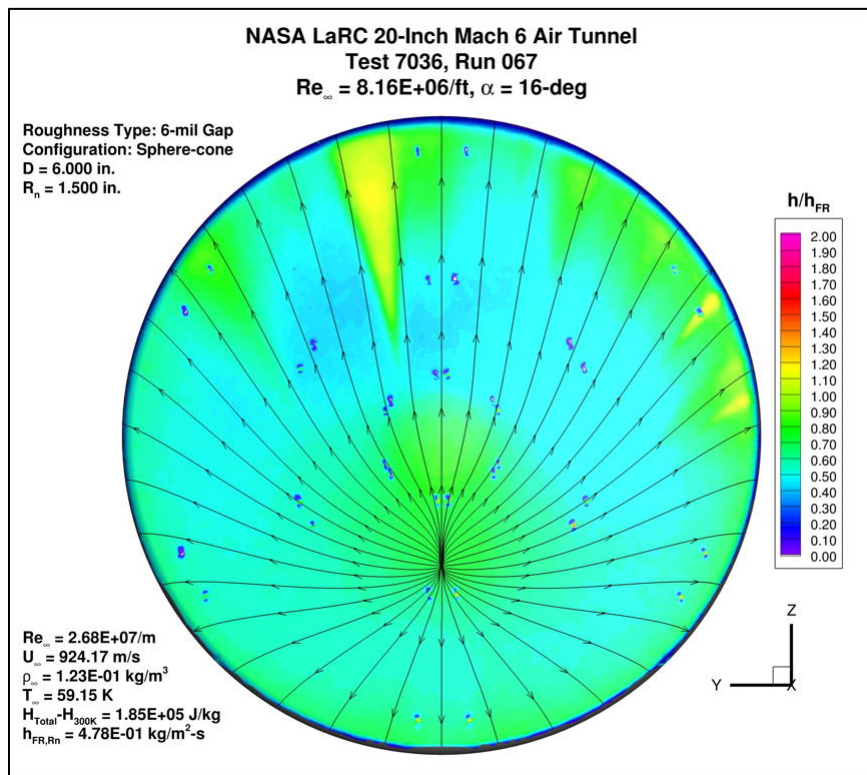


Figure 127. Test 7036, Run 67, $Re_\infty = 8.3 \times 10^6/ft$, sphere-cone 6 mil gap.

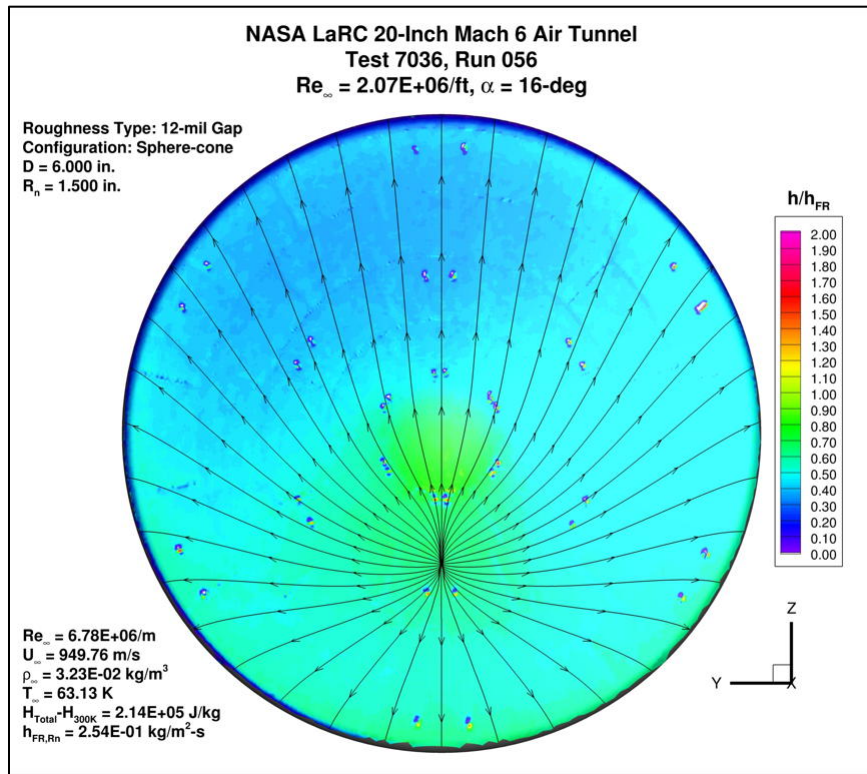


Figure 128. Test 7036, Run 56, $Re_{\infty} = 2.1 \times 10^6/ft$, sphere-cone 12 mil gap.

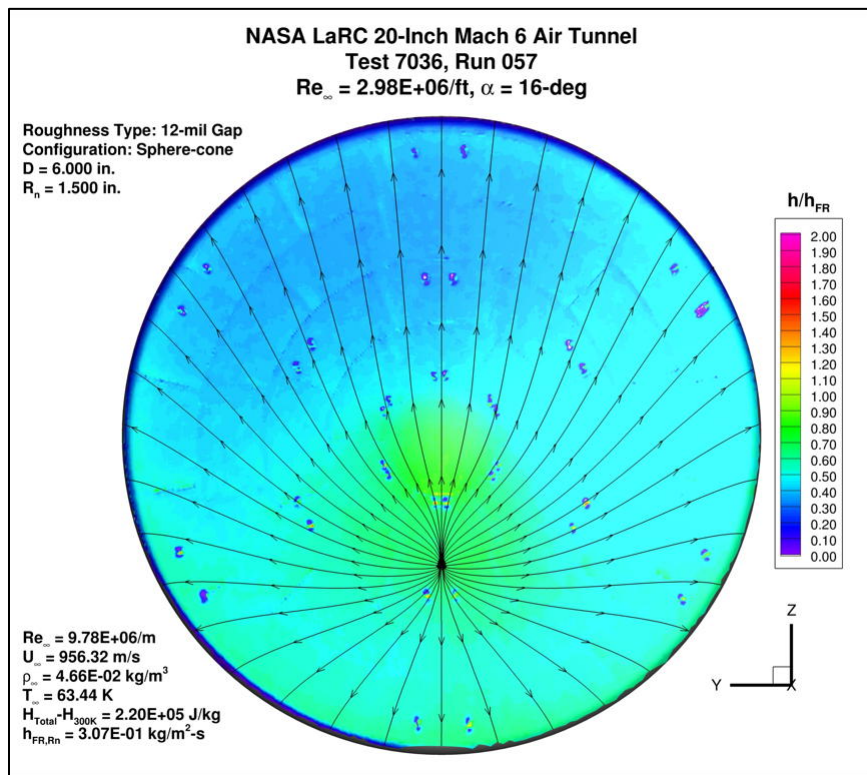


Figure 129. Test 7036, Run 57, $Re_{\infty} = 3.0 \times 10^6/ft$, sphere-cone 12 mil gap.

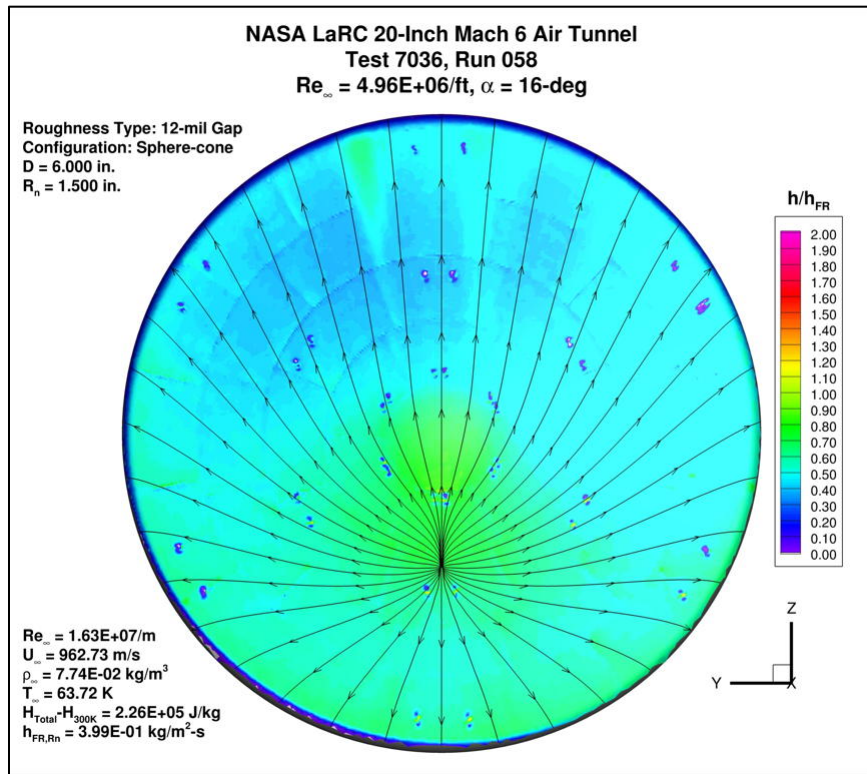


Figure 130. Test 7036, Run 58, $Re_{\infty} = 5.0 \times 10^6/ft$, sphere-cone 12 mil gap.

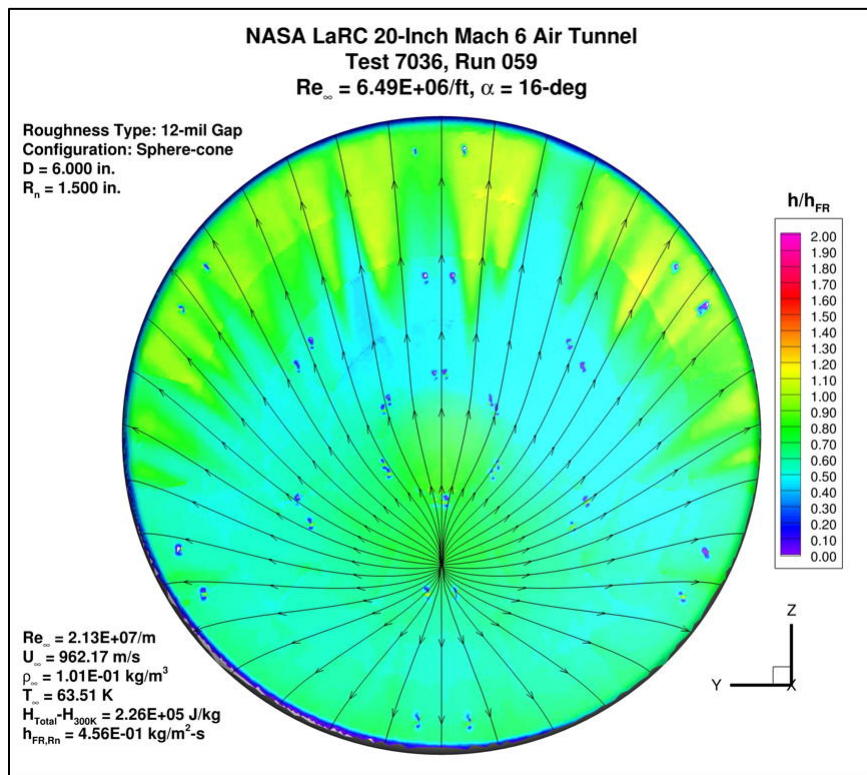


Figure 131. Test 7036, Run 59, $Re_{\infty} = 6.6 \times 10^6/ft$, sphere-cone 12 mil gap.

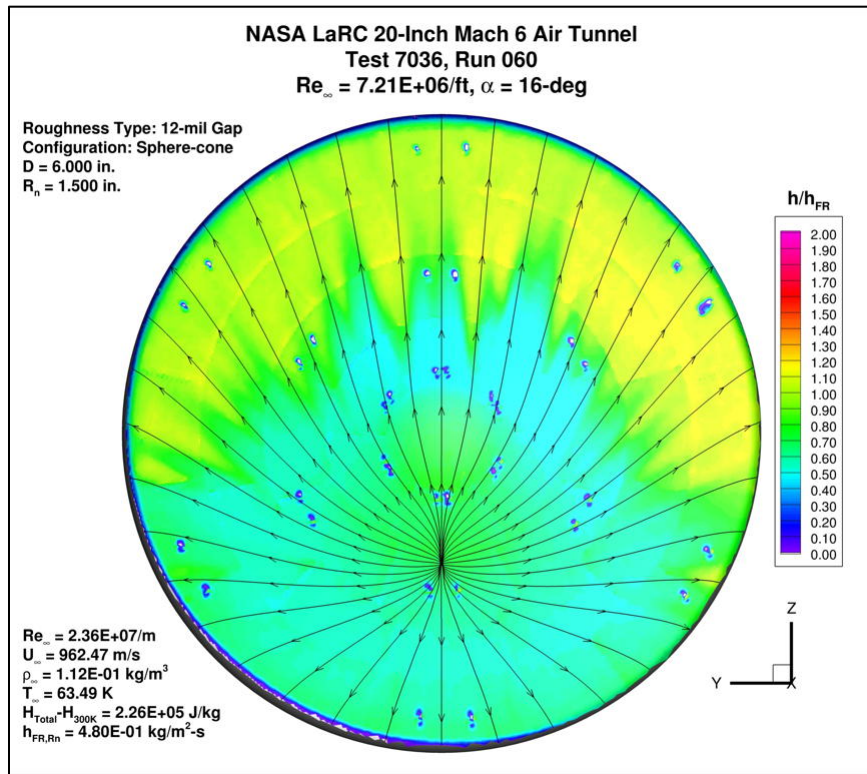


Figure 132. Test 7036, Run 60, $Re_\infty = 7.5 \times 10^6/ft$, sphere-cone 12 mil gap.

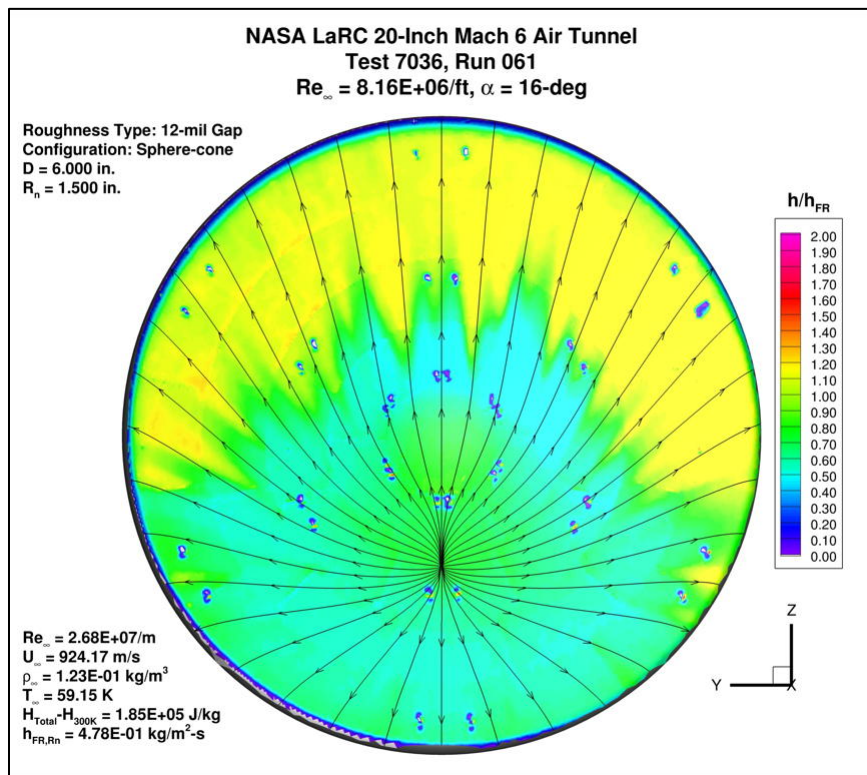


Figure 133. Test 7036, Run 61, $Re_\infty = 8.3 \times 10^6/ft$, sphere-cone 12 mil gap.

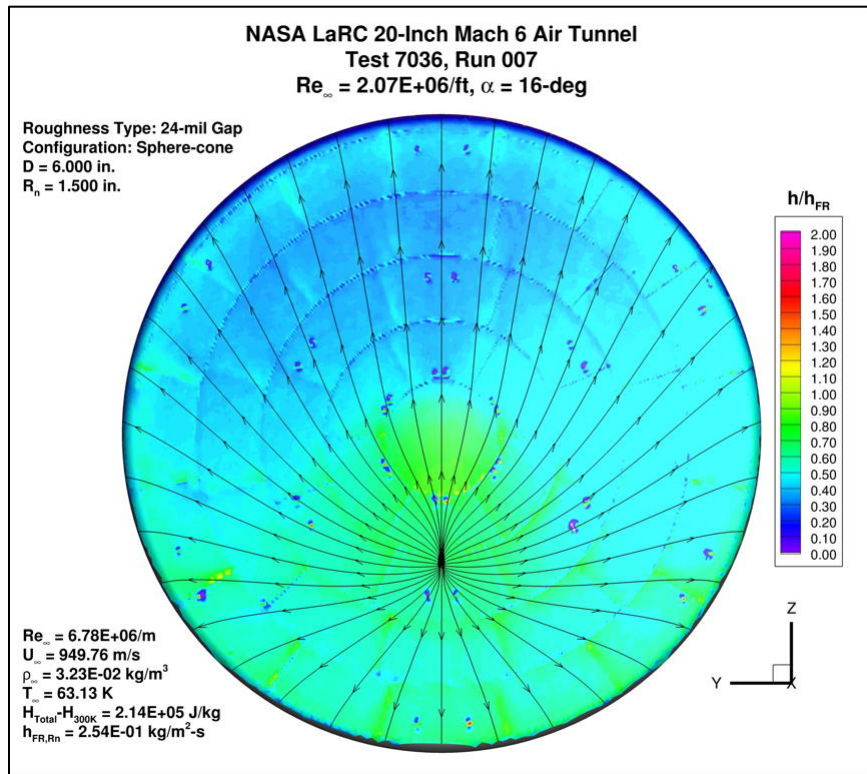


Figure 134. Test 7036, Run 7, $Re_\infty = 2.1 \times 10^6/\text{ft}$, sphere-cone 24 mil gap.

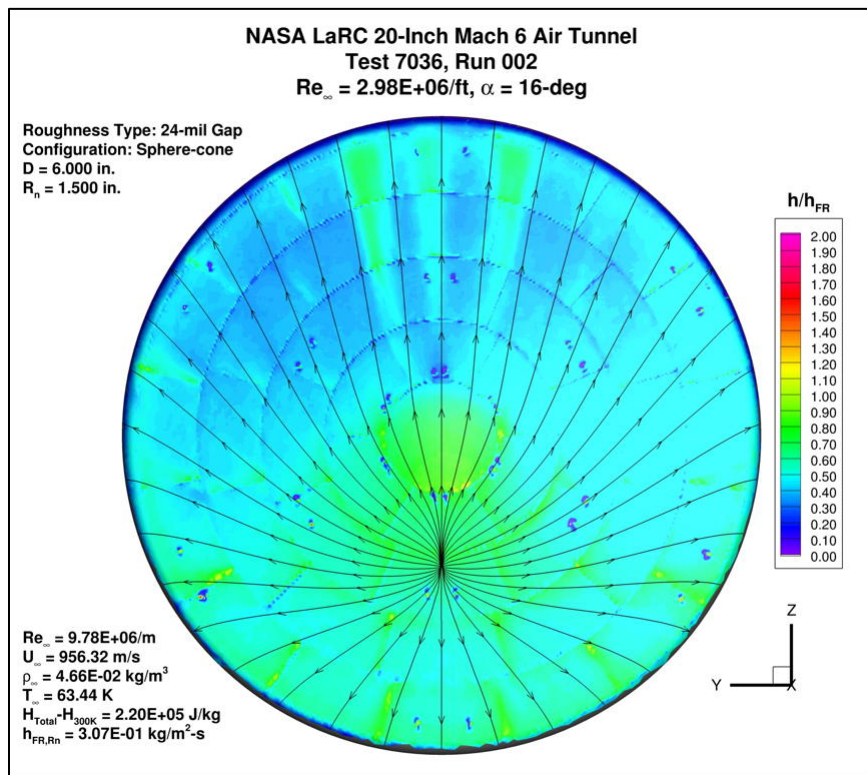


Figure 135. Test 7036, Run 2, $Re_\infty = 3.0 \times 10^6/\text{ft}$, sphere-cone 24 mil gap.

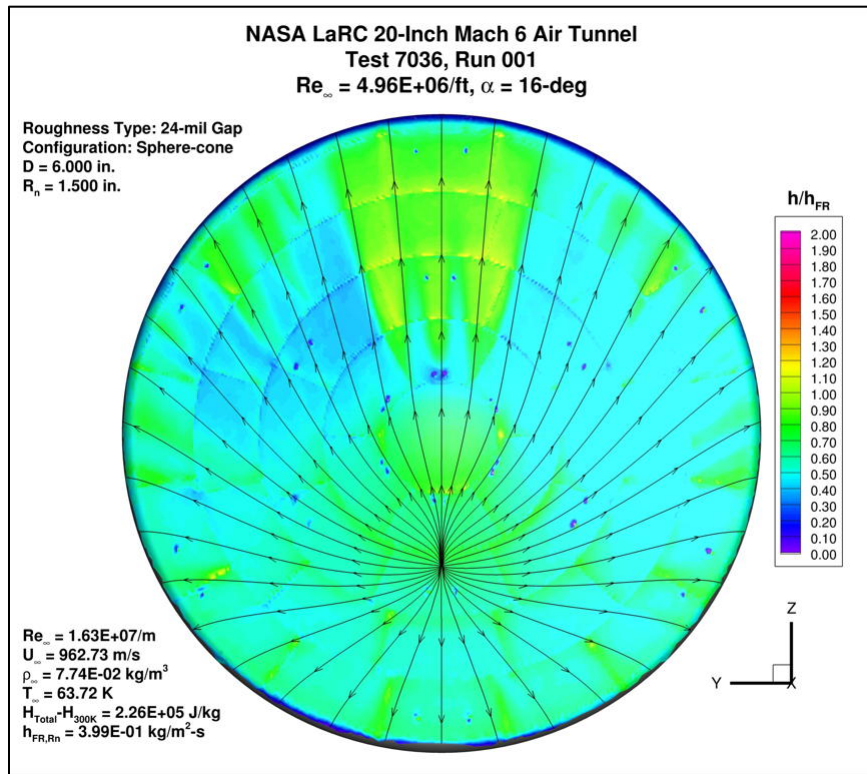


Figure 136. Test 7036, Run 1, $Re_\infty = 5.0 \times 10^6/\text{ft}$, sphere-cone 24 mil gap.

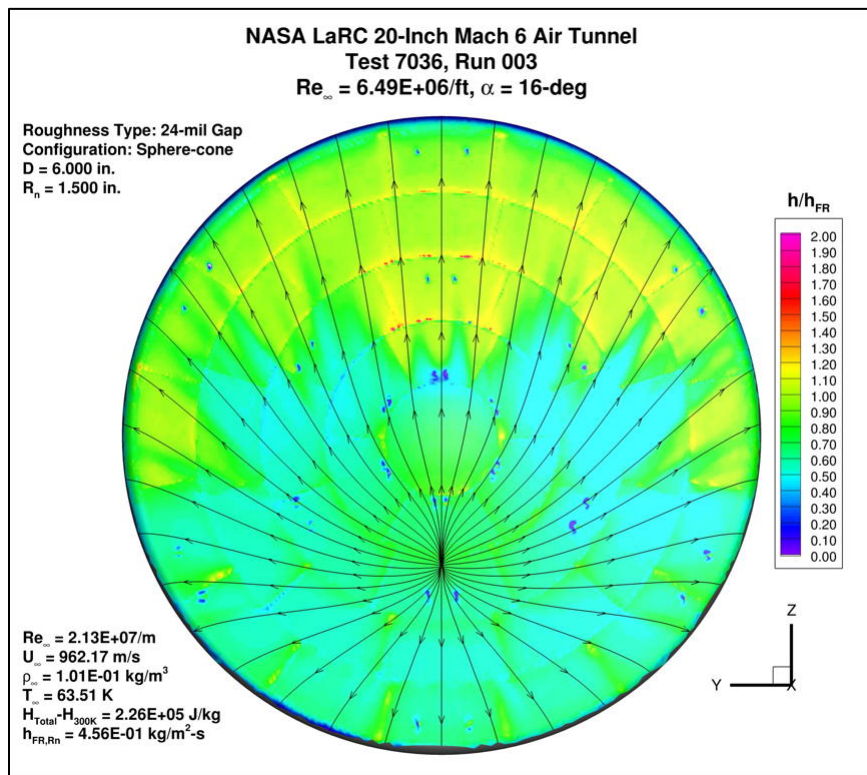


Figure 137. Test 7036, Run 3, $Re_\infty = 6.6 \times 10^6/\text{ft}$, sphere-cone 24 mil gap.

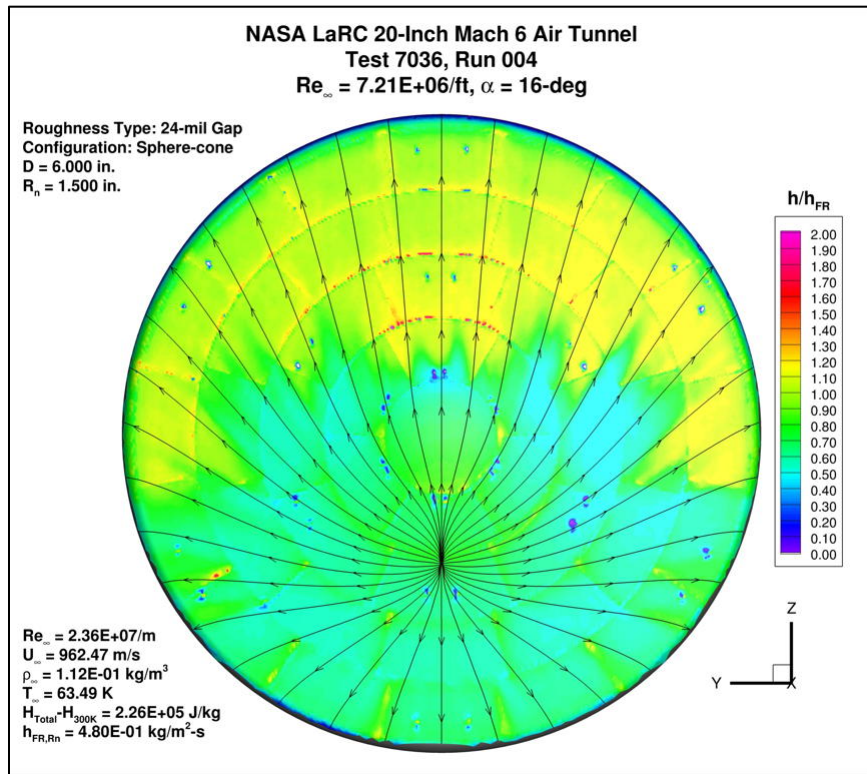


Figure 138. Test 7036, Run 4, $Re_\infty = 7.5 \times 10^6/ft$, sphere-cone 24 mil gap.

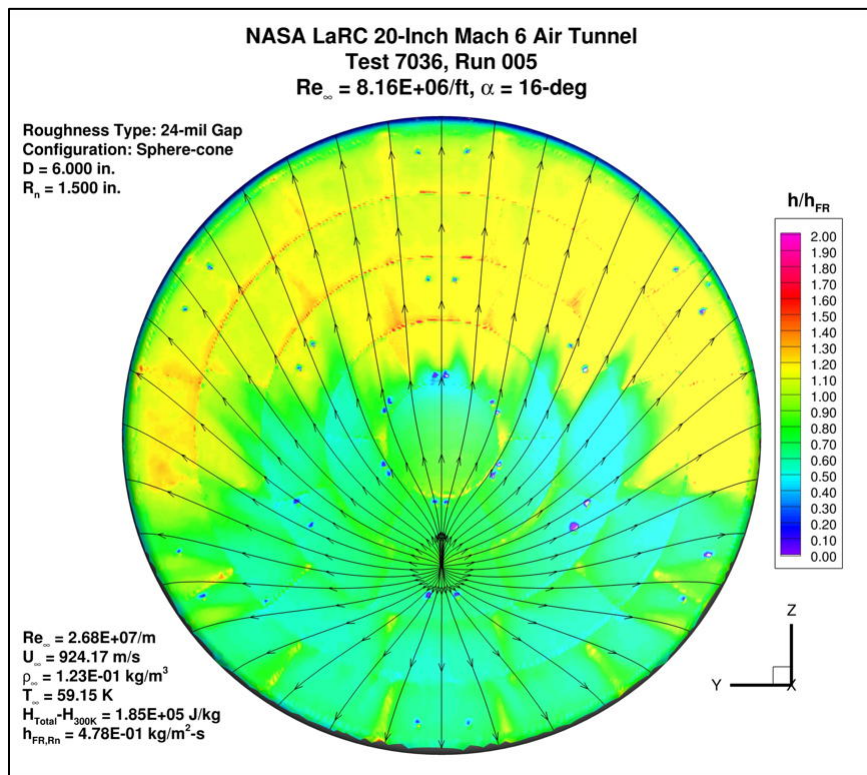


Figure 139. Test 7036, Run 5, $Re_\infty = 8.3 \times 10^6/ft$, sphere-cone 24 mil gap.

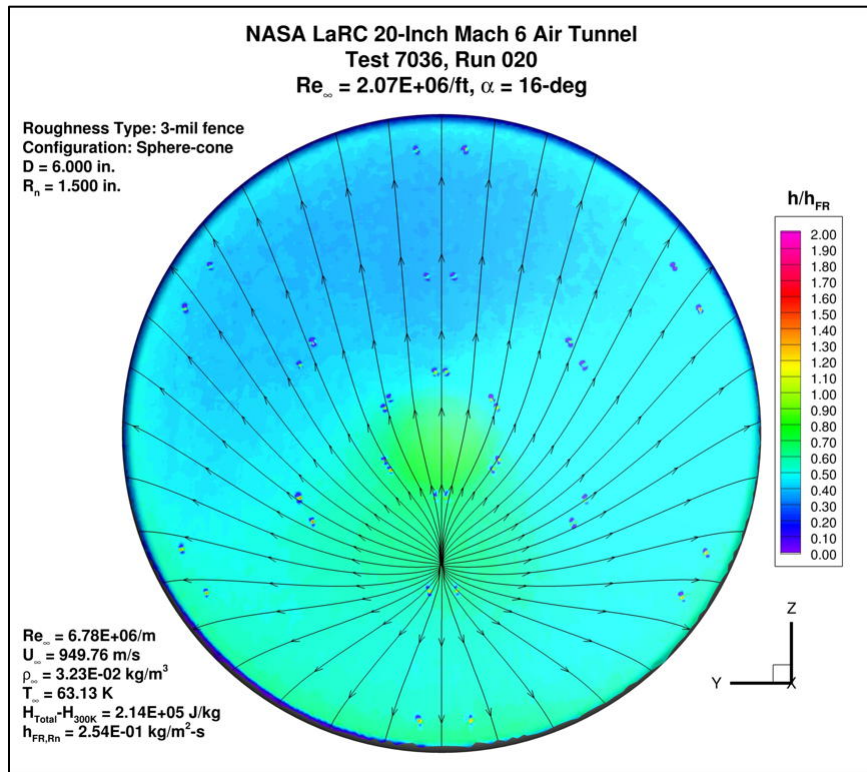


Figure 140. Test 7036, Run 20, $Re_{\infty} = 2.1 \times 10^6/ft$, sphere-cone 3 mil fence.

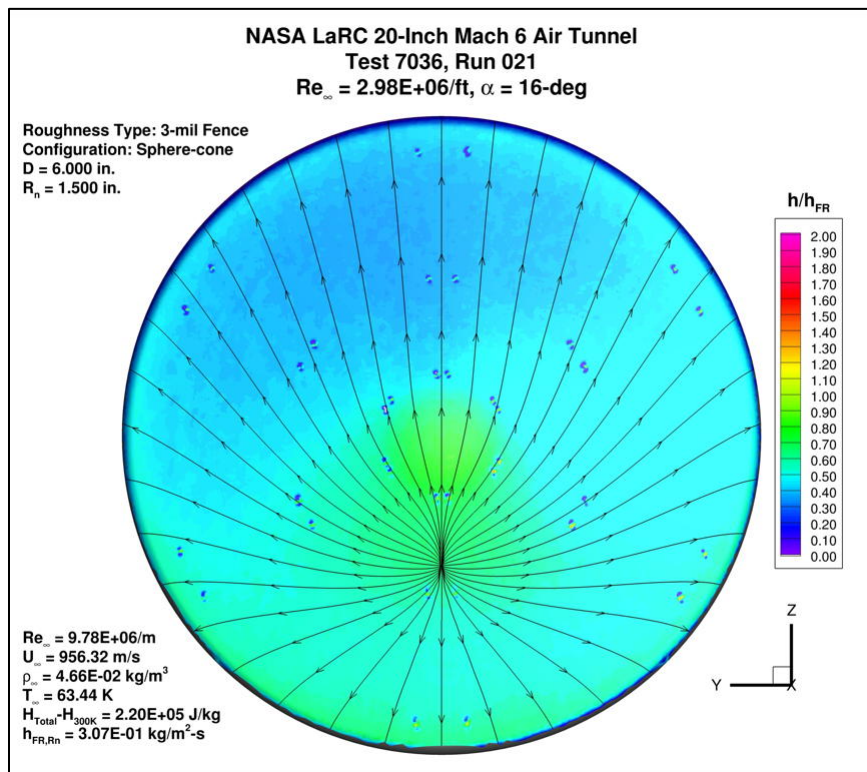


Figure 141. Test 7036, Run 21, $Re_{\infty} = 3.0 \times 10^6/ft$, sphere-cone 3 mil fence.

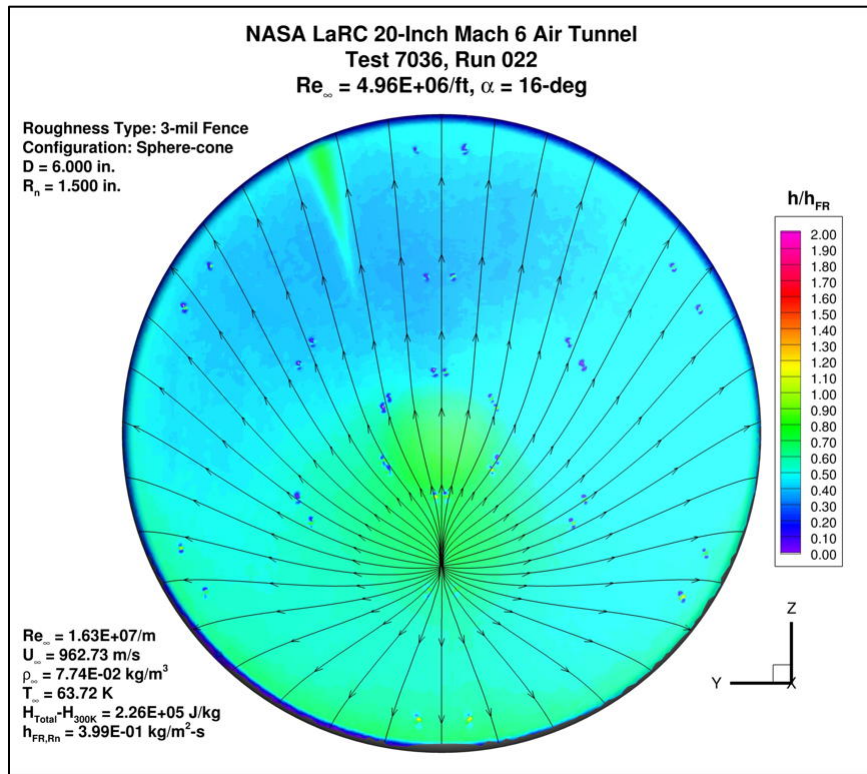


Figure 142. Test 7036, Run 22, $Re_{\infty} = 5.0 \times 10^6/ft$, sphere-cone 3 mil fence.

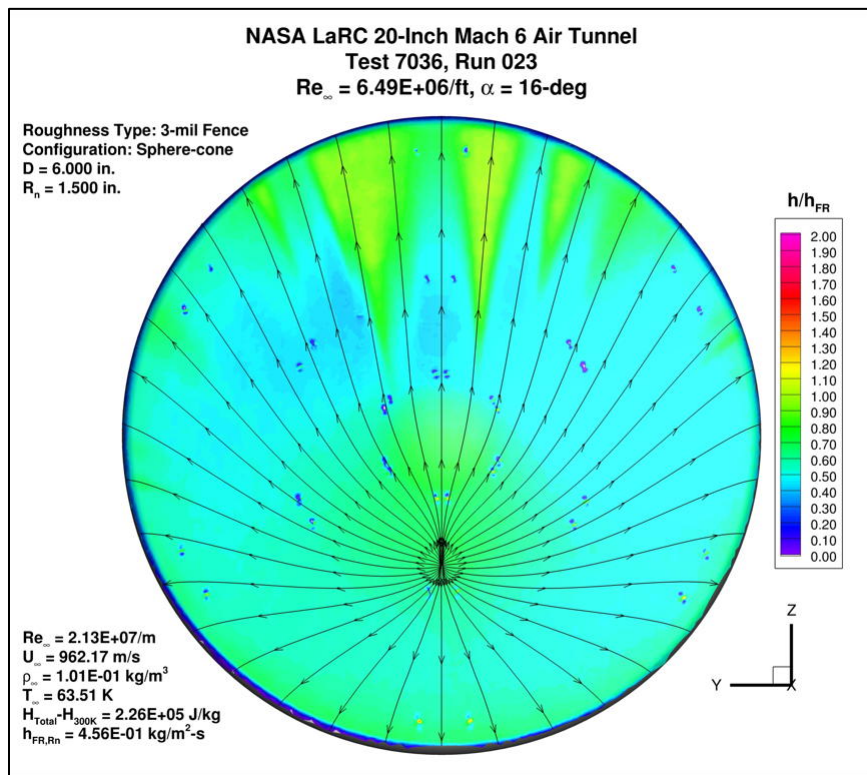


Figure 143. Test 7036, Run 23, $Re_{\infty} = 6.6 \times 10^6/ft$, sphere-cone 3 mil fence.

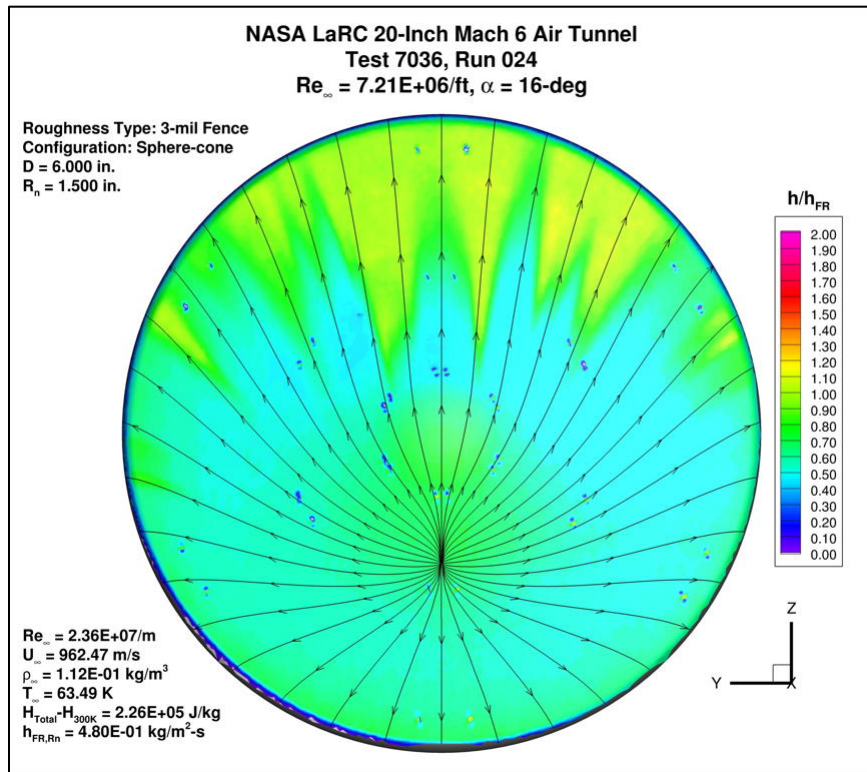


Figure 144. Test 7036, Run 24, $Re_{\infty} = 7.5 \times 10^6/ft$, sphere-cone 3 mil fence.

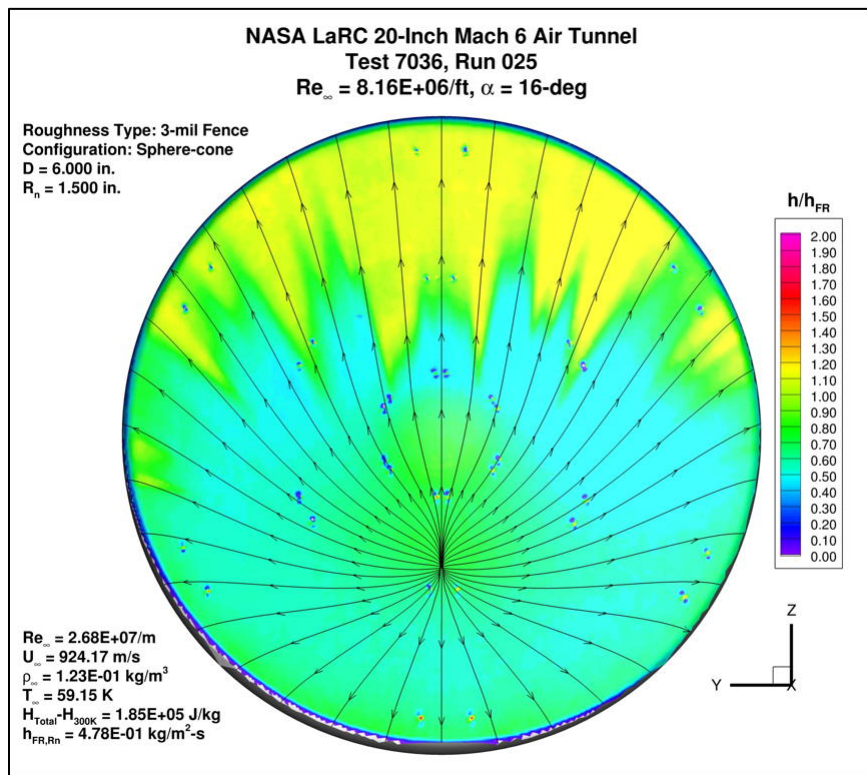


Figure 145. Test 7036, Run 25, $Re_{\infty} = 8.3 \times 10^6/ft$, sphere-cone 3 mil fence.

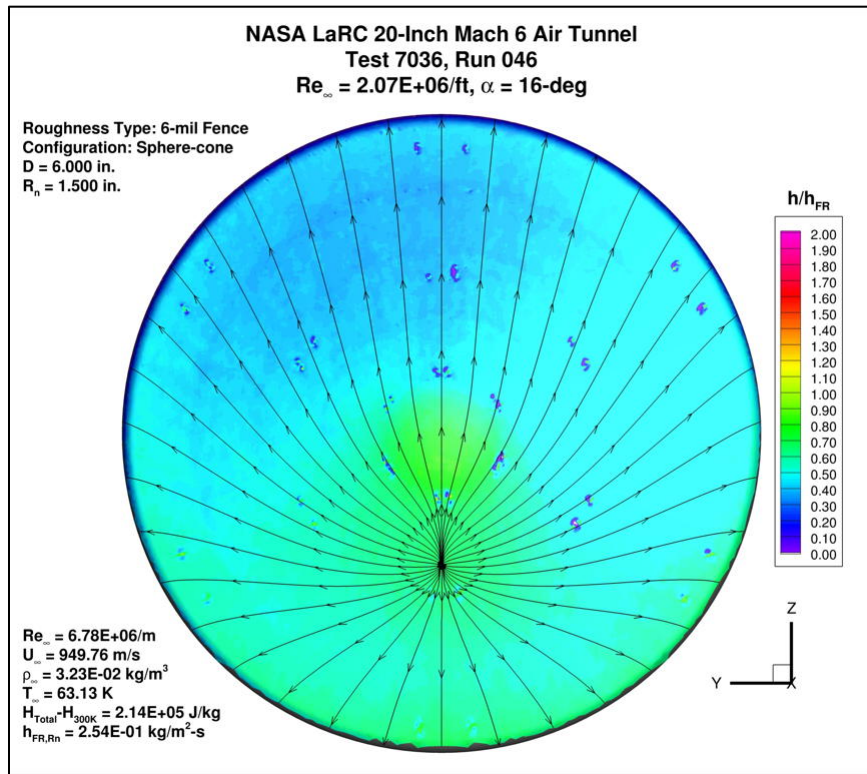


Figure 146. Test 7036, Run 46, $Re_{\infty} = 2.1 \times 10^6/ft$, sphere-cone 6 mil fence.

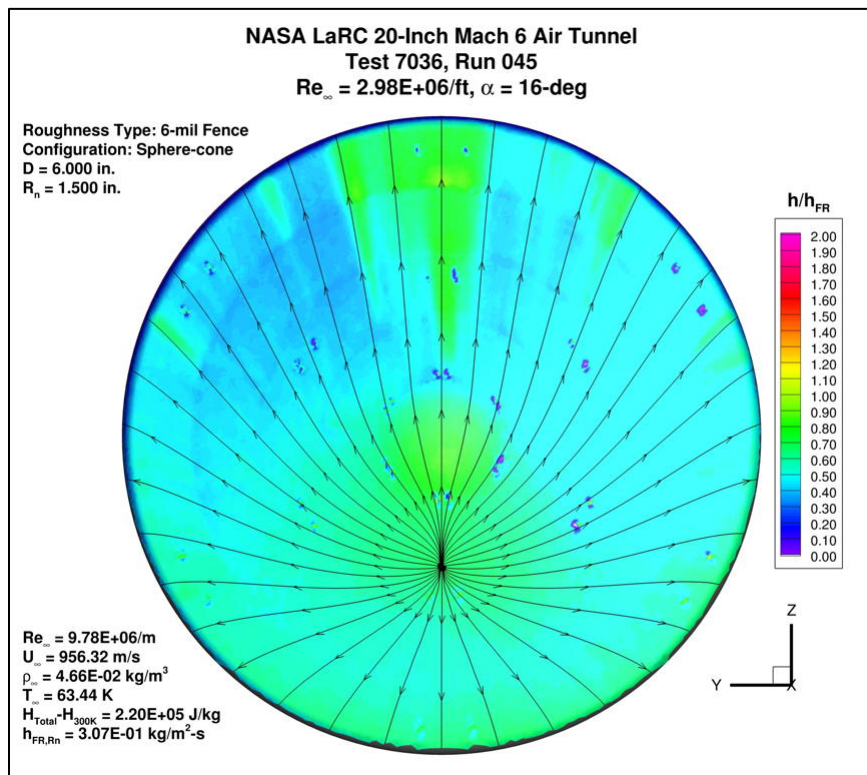


Figure 147. Test 7036, Run 45, $Re_{\infty} = 3.0 \times 10^6/ft$, sphere-cone 6 mil fence.

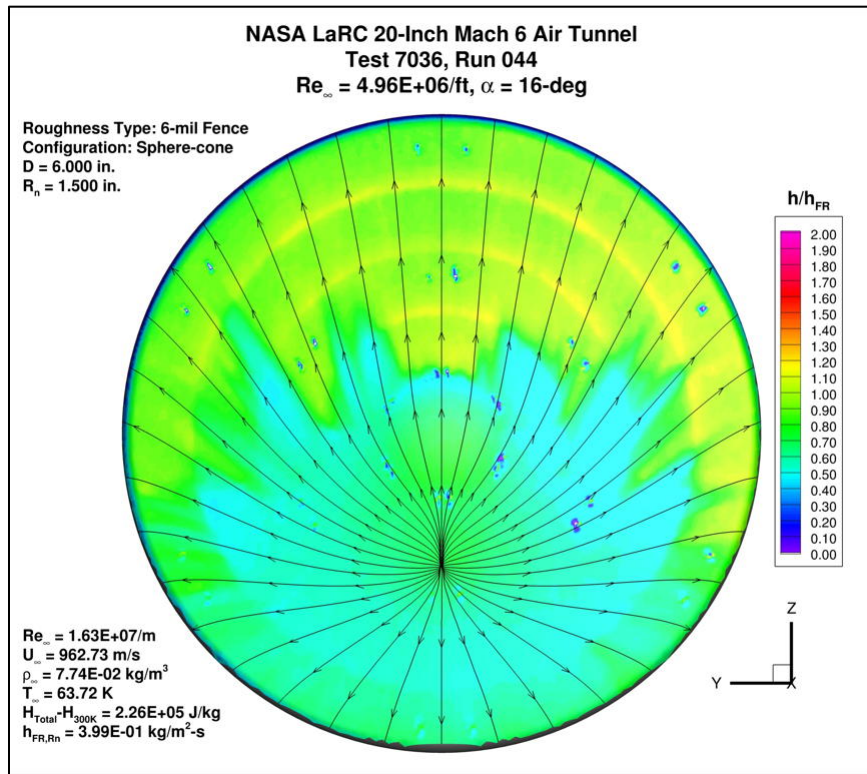


Figure 148. Test 7036, Run 44, $Re_{\infty} = 5.0 \times 10^6/ft$, sphere-cone 6 mil fence.

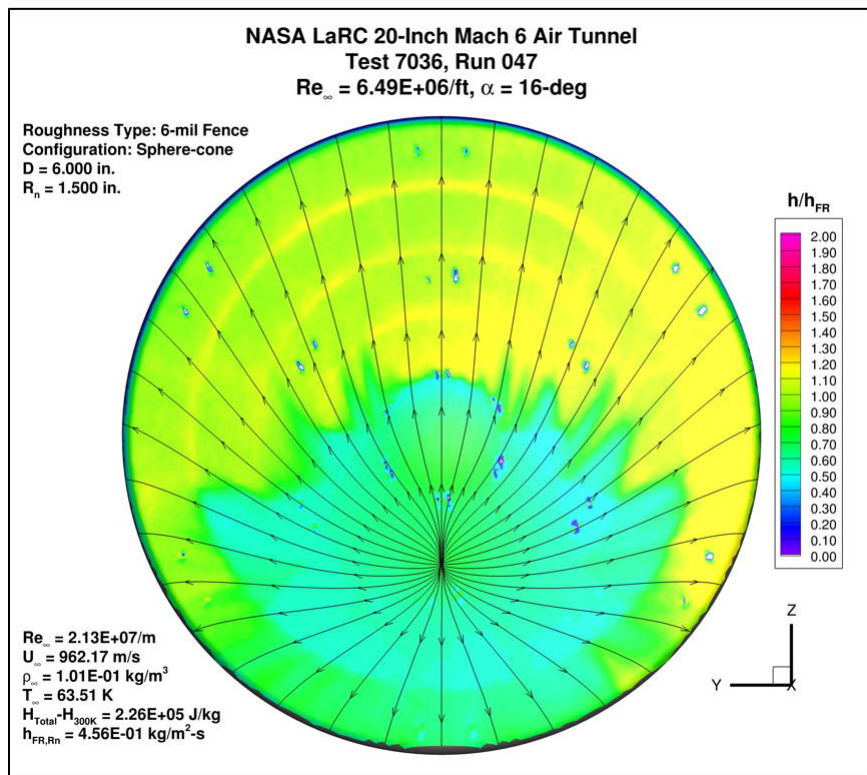


Figure 149. Test 7036, Run 47, $Re_{\infty} = 6.6 \times 10^6/ft$, sphere-cone 6 mil fence.

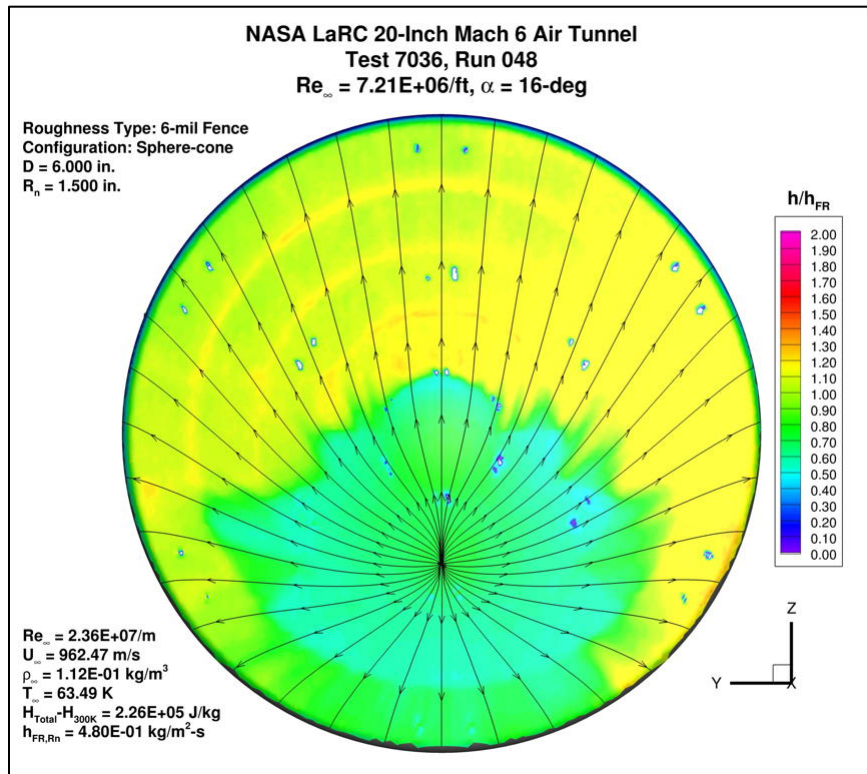


Figure 150. Test 7036, Run 48, $Re_{\infty} = 7.5 \times 10^6/ft$, sphere-cone 6 mil fence.

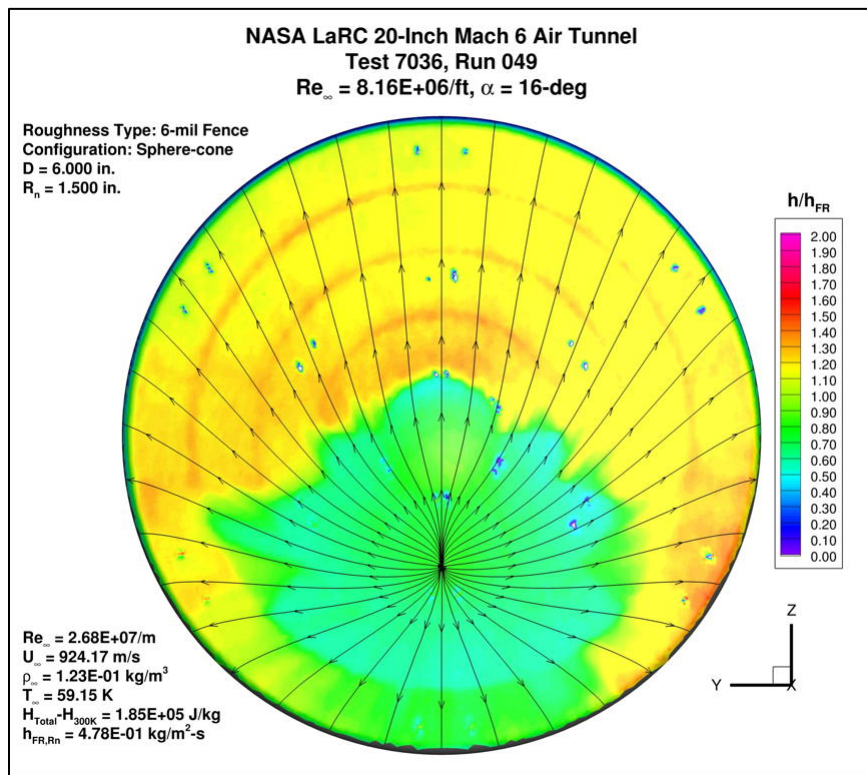


Figure 151. Test 7036, Run 49, $Re_{\infty} = 8.3 \times 10^6/ft$, sphere-cone 6 mil fence.

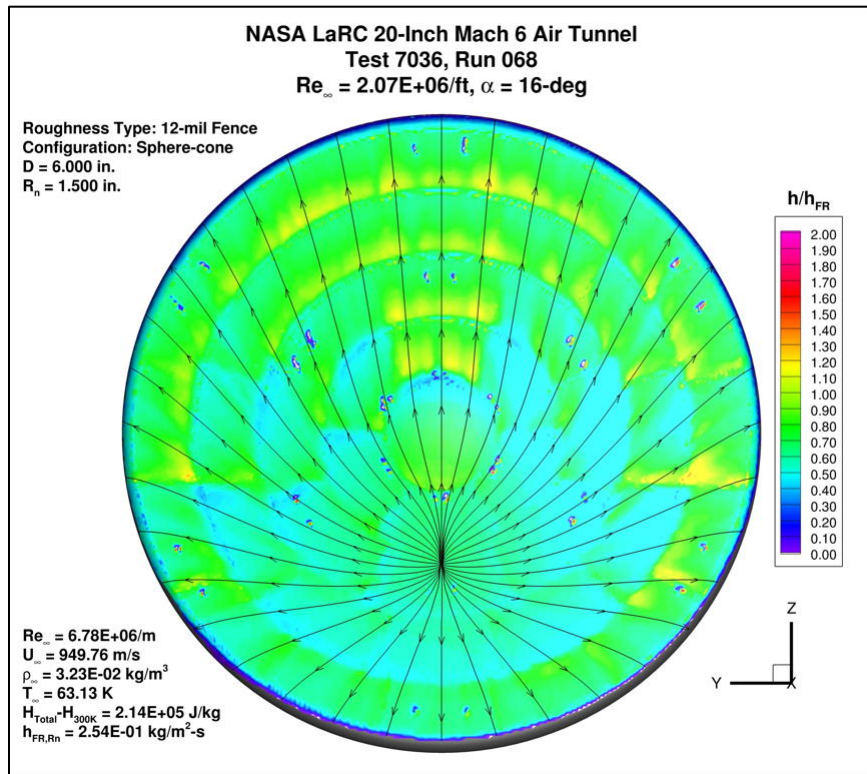


Figure 152. Test 7036, Run 68, $Re_\infty = 2.1 \times 10^6/ft$, sphere-cone 12 mil fence.

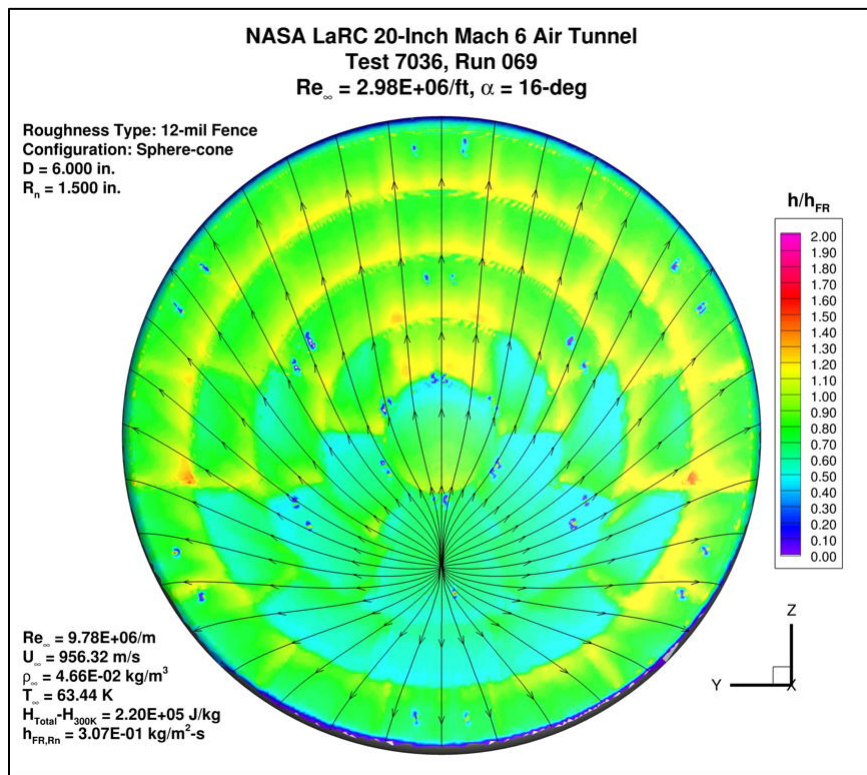


Figure 153. Test 7036, Run 69, $Re_\infty = 3.0 \times 10^6/ft$, sphere-cone 12 mil fence.

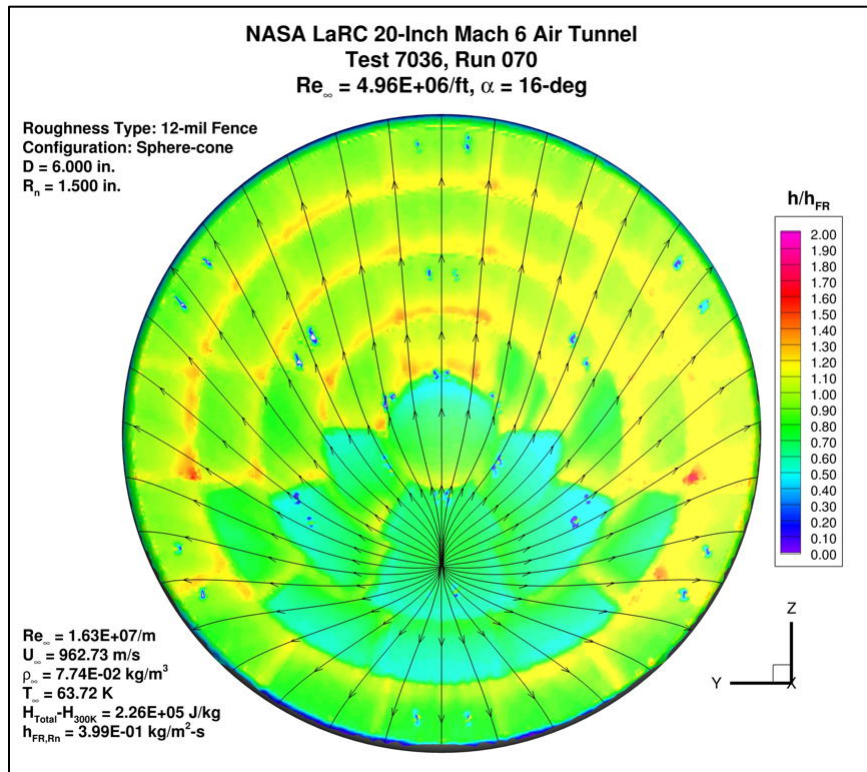


Figure 154. Test 7036, Run 70, $Re_\infty = 5.0 \times 10^6/ft$, sphere-cone 12 mil fence.

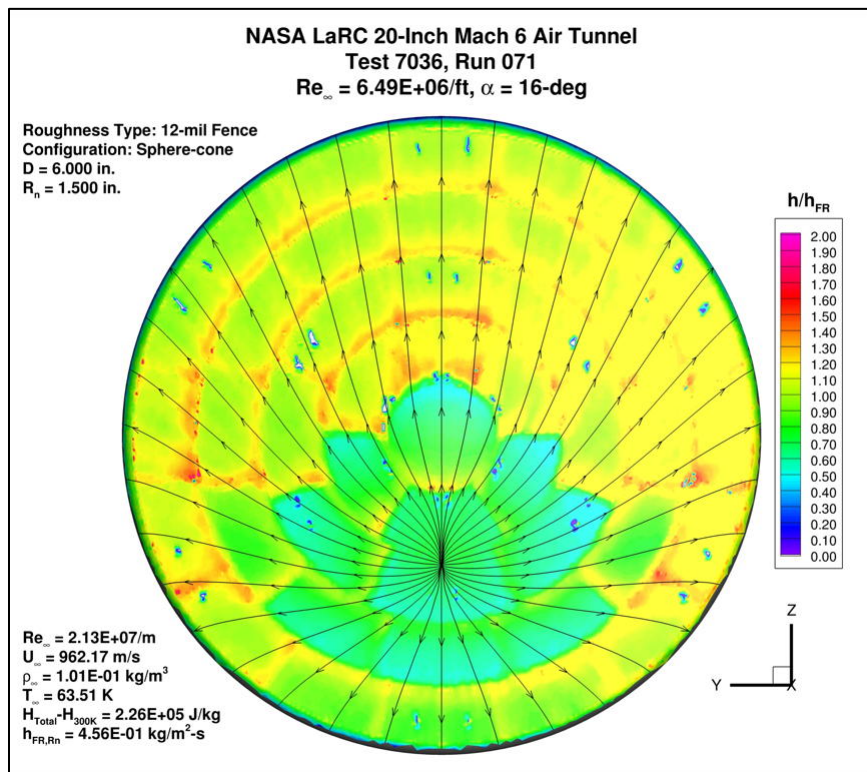


Figure 155. Test 7036, Run 71, $Re_\infty = 6.6 \times 10^6/ft$, sphere-cone 12 mil fence.

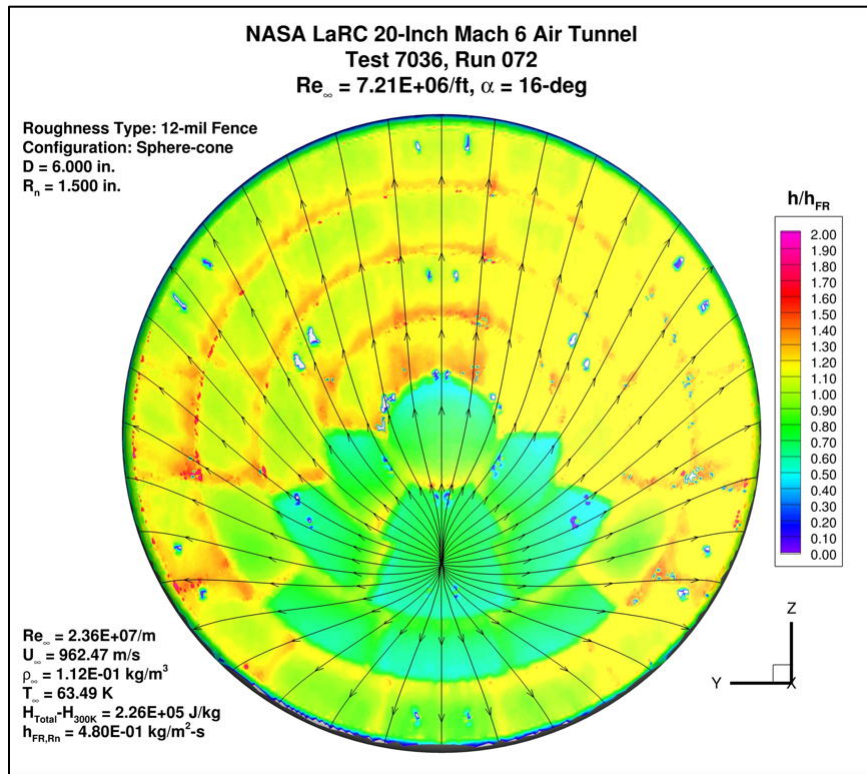


Figure 156. Test 7036, Run 72, $Re_\infty = 7.5 \times 10^6/ft$, sphere-cone 12 mil fence.

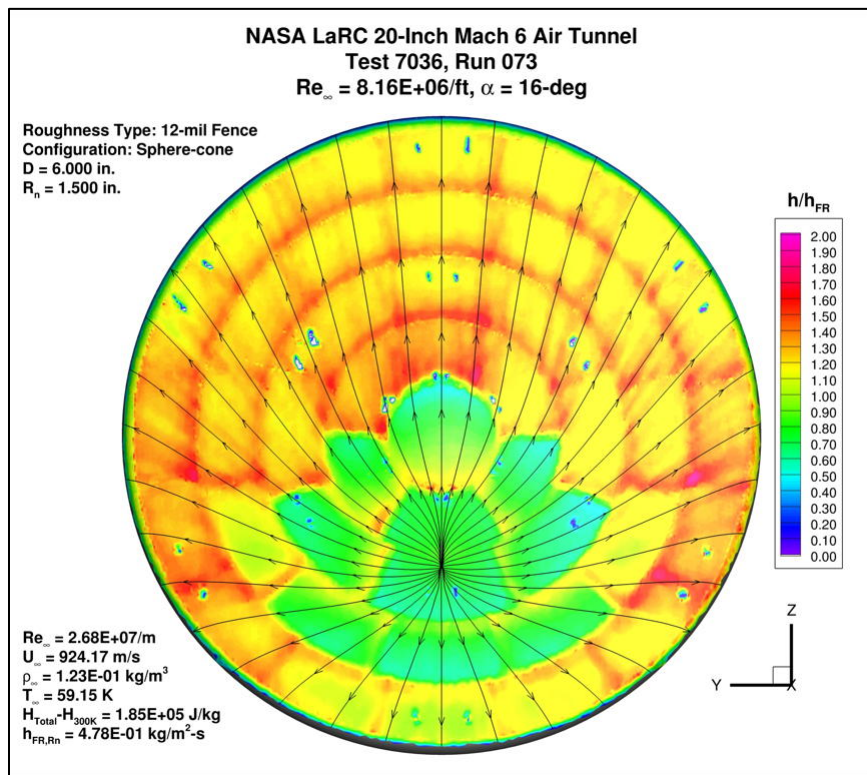


Figure 157. Test 7036, Run 73, $Re_\infty = 8.3 \times 10^6/ft$, sphere-cone 12 mil fence

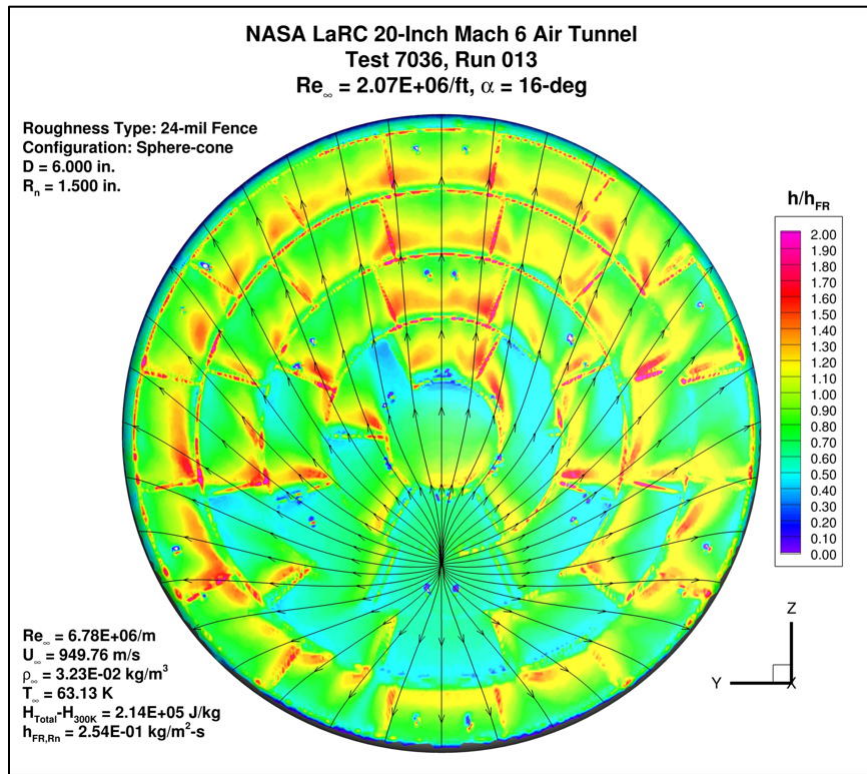


Figure 158. Test 7036, Run 13, $Re_\infty = 2.1 \times 10^6/ft$, sphere-cone 24 mil fence.

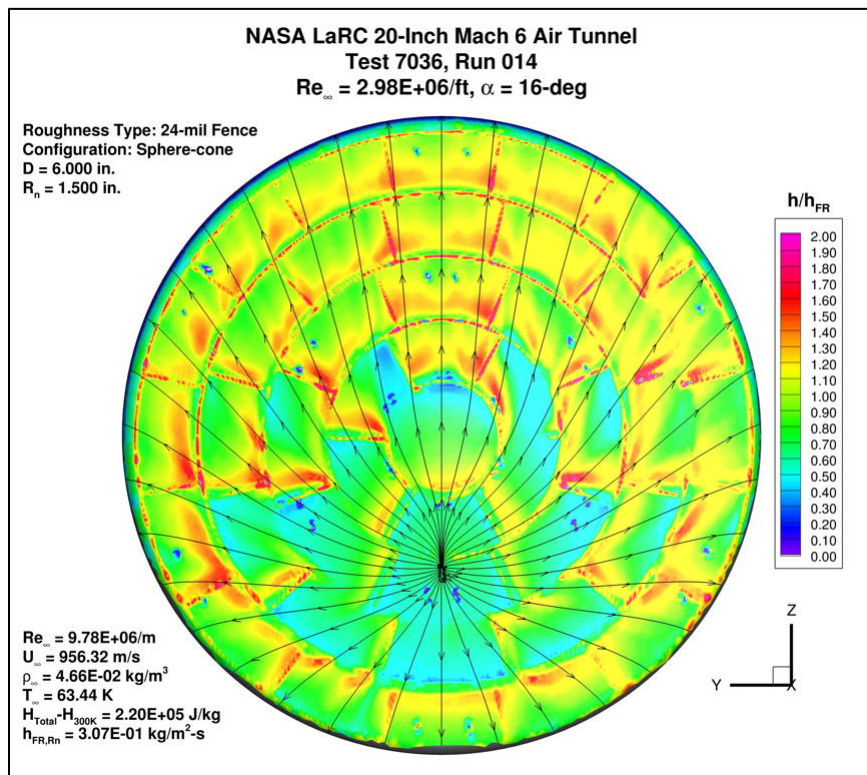


Figure 159. Test 7036, Run 14, $Re_\infty = 3.0 \times 10^6/ft$, sphere-cone 24 mil fence.

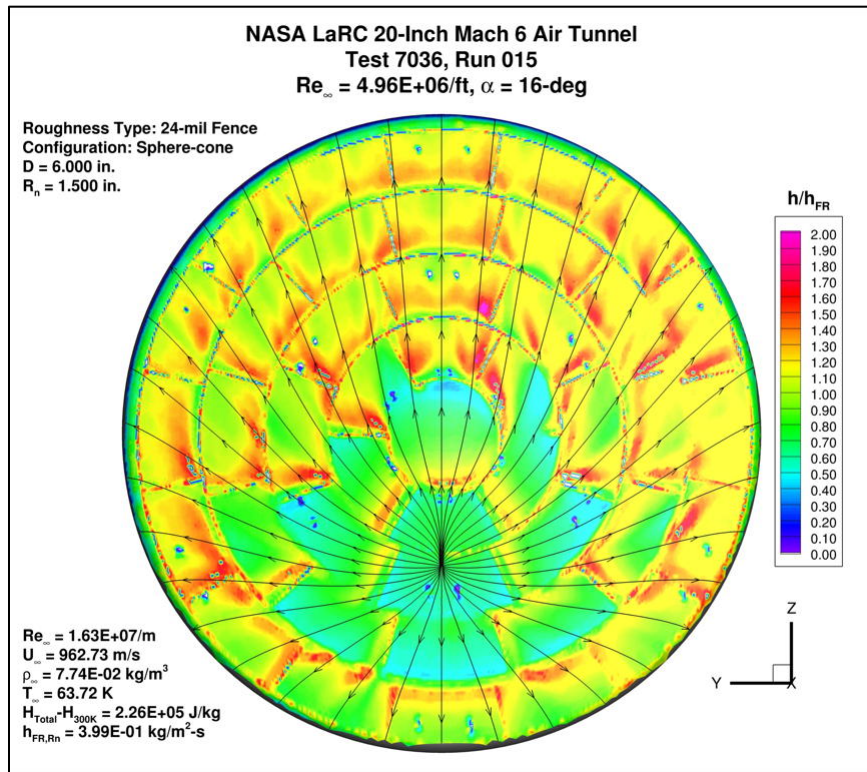


Figure 160. Test 7036, Run 15, $Re_\infty = 5.0 \times 10^6/ft$, sphere-cone 24 mil fence.

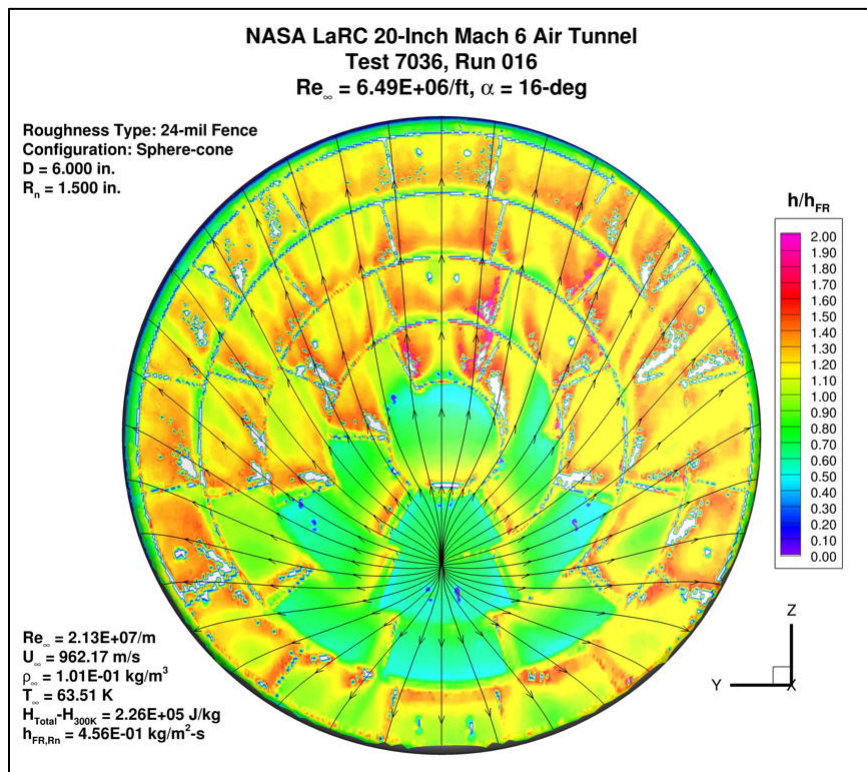


Figure 161. Test 7036, Run 16, $Re_\infty = 6.6 \times 10^6/ft$, sphere-cone 24 mil fence.

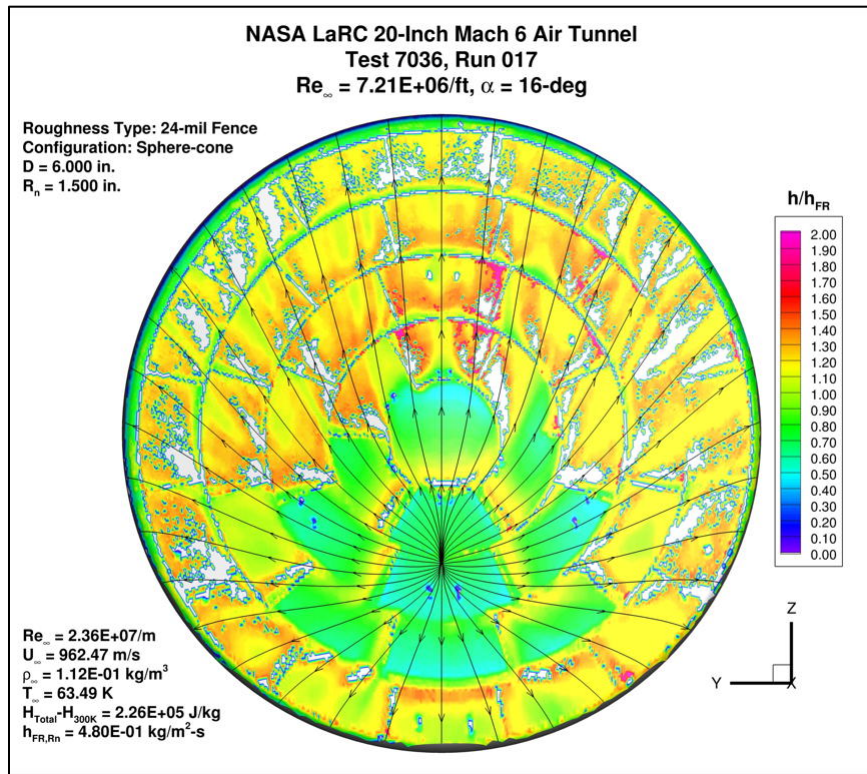


Figure 162. Test 7036, Run 17, $Re_\infty = 7.5 \times 10^6/ft$, sphere-cone 24 mil fence.

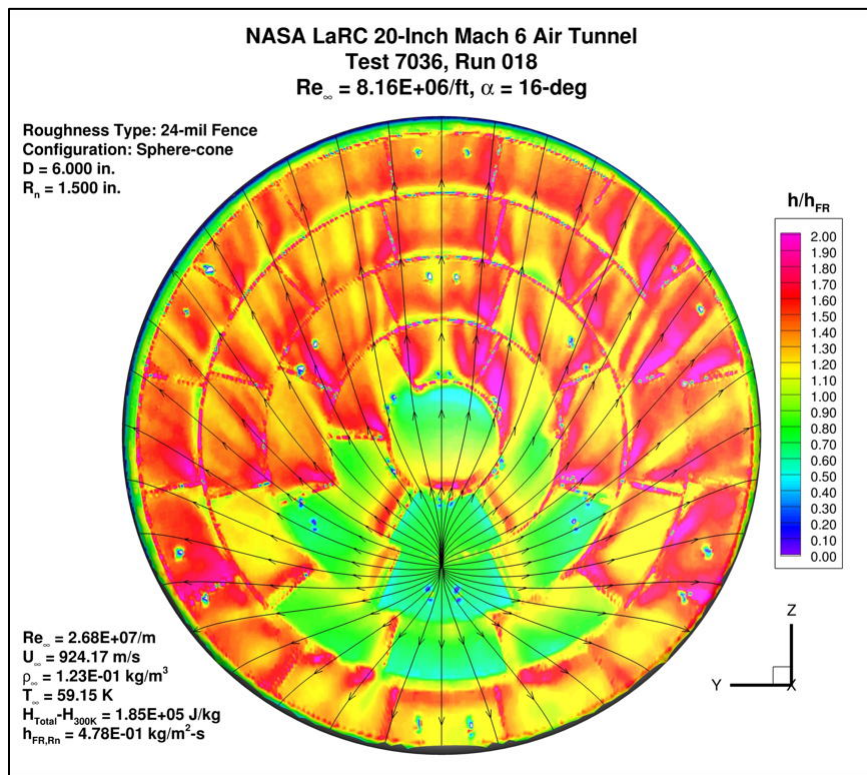


Figure 163. Test 7036, Run 18, $Re_\infty = 8.3 \times 10^6/ft$, sphere-cone 24 mil fence

Appendix B. Spherical-Cap Geometry Global Heating Images

Global heating images for the sphere-cone geometry from Test 7057 in the LAL 20-Inch Mach 6 Air Tunnel are presented in this Appendix. Smooth wall data are shown in Figure 164 to Figure 169, gap model data are shown in Figure 170 to Figure 193, and fence model data are presented in Figure 194 to Figure 217. In these images, boundary-layer edge streamlines determined from laminar, smooth-surface LAURA simulations have been superimposed to illustrate the nature of the flow field.

At higher Reynolds numbers and/or larger fence heights, white patches on the images indicate areas where the measured surface temperatures exceed the calibrated range of the phosphor thermography (approximately 460 K) and no valid data were obtained

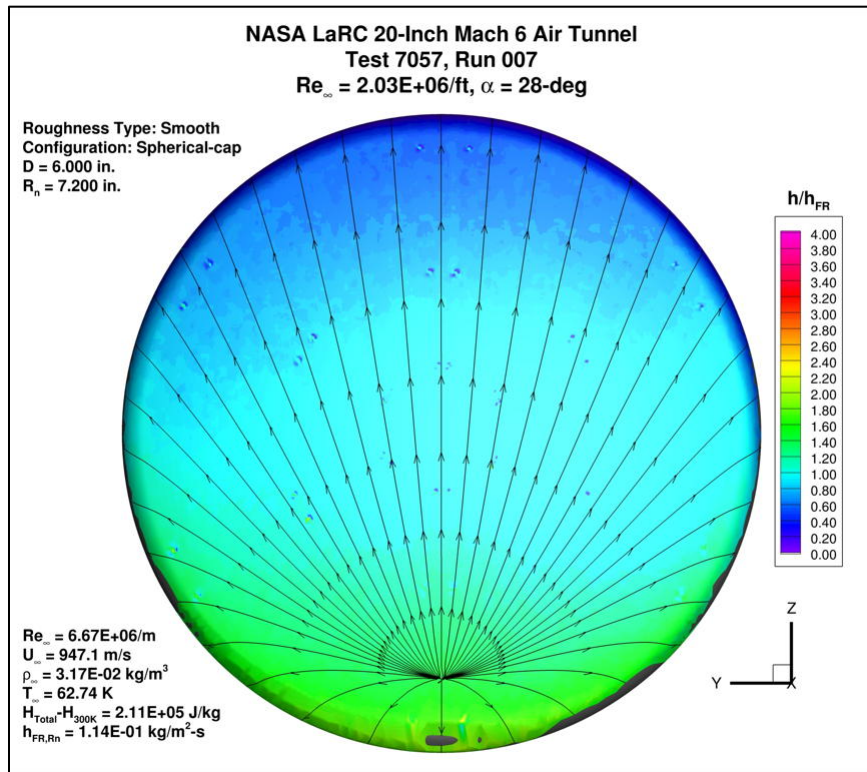


Figure 164. Test 7057, Run 7, $Re_{\infty} = 2.1 \times 10^6/ft$, spherical-cap, smooth OML.

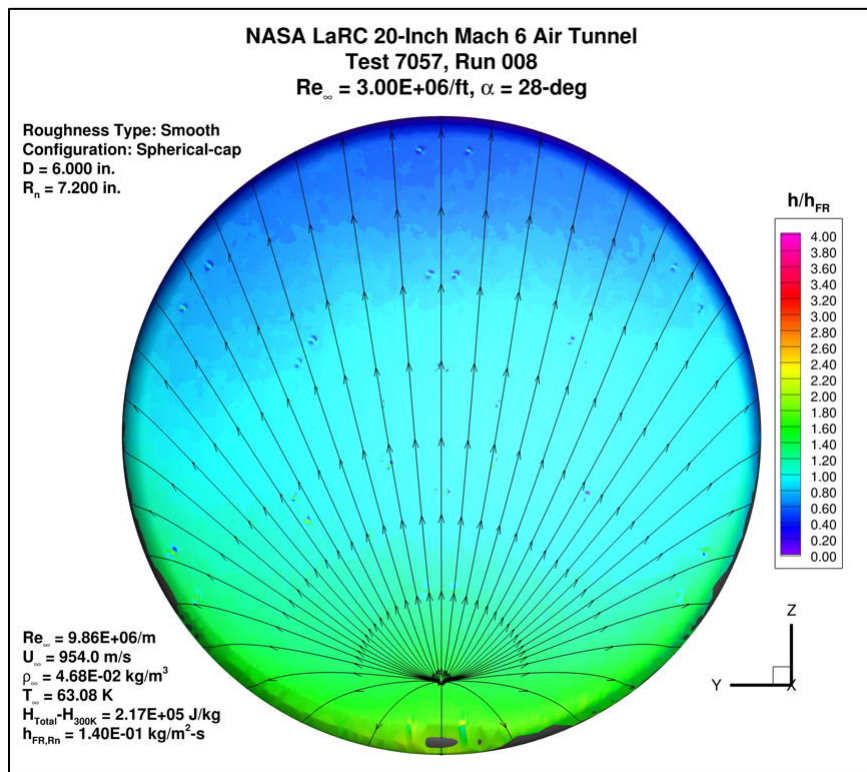


Figure 165. Test 7057, Run 8, $Re_{\infty} = 3.0 \times 10^6/ft$, spherical-cap, smooth OML.

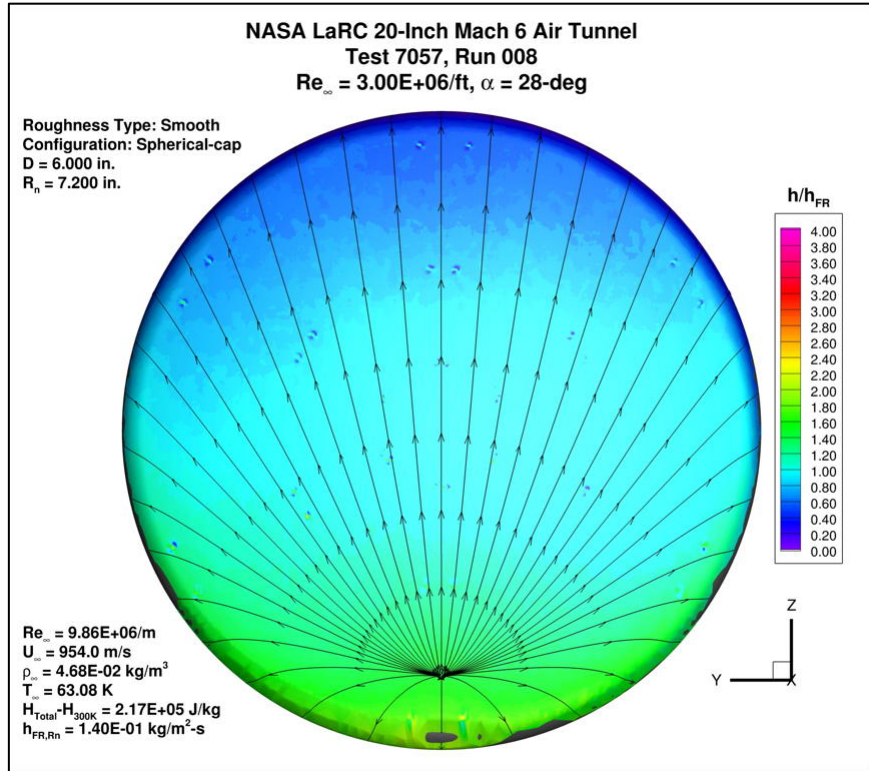


Figure 166. Test 7057, Run 9, $Re_\infty = 5.0 \times 10^6/ft$, spherical-cap, smooth OML.

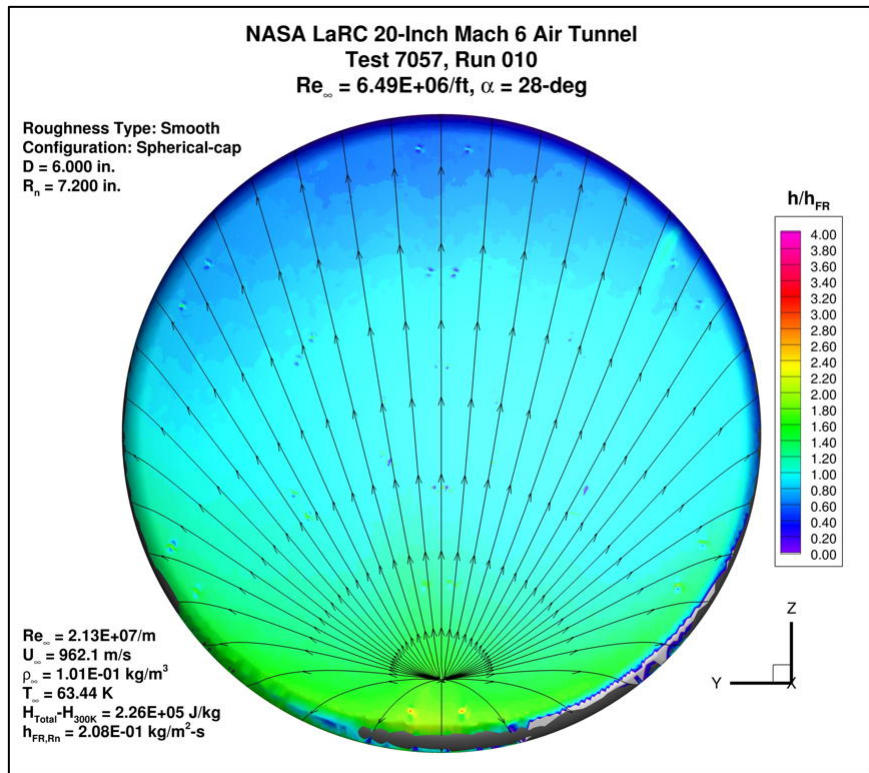


Figure 167. Test 7057, Run 10, $Re_\infty = 6.6 \times 10^6/ft$, spherical-cap, smooth OML.

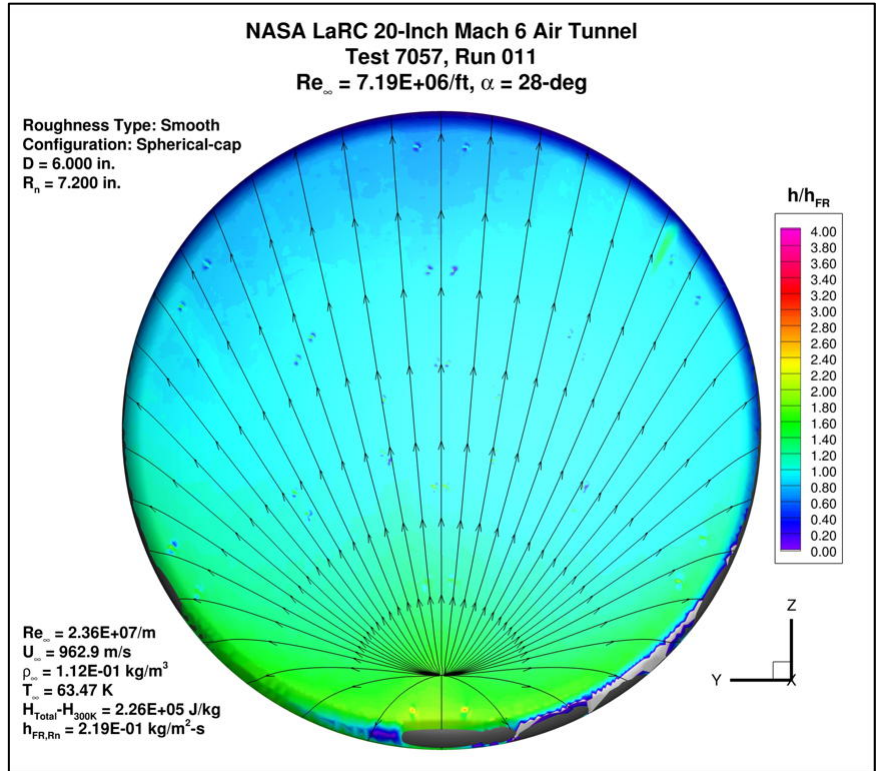


Figure 168. Test 7057, Run 11, $Re_\infty = 7.5 \times 10^6/ft$, spherical-cap, smooth OML.

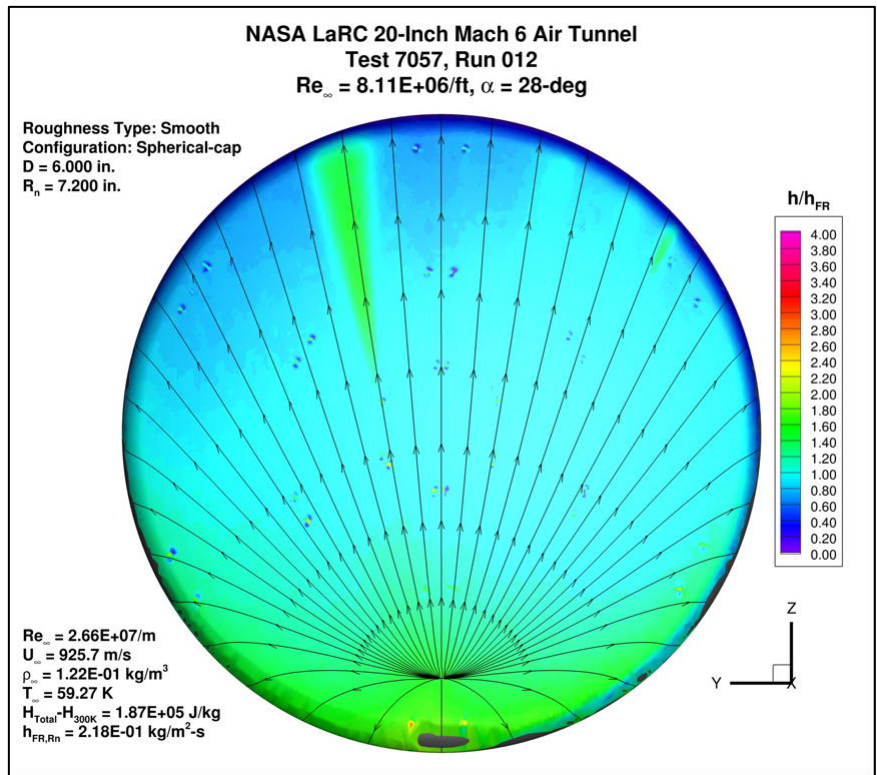


Figure 169. Test 7057, Run 12, $Re_\infty = 8.3 \times 10^6/ft$, spherical-cap, smooth OML.

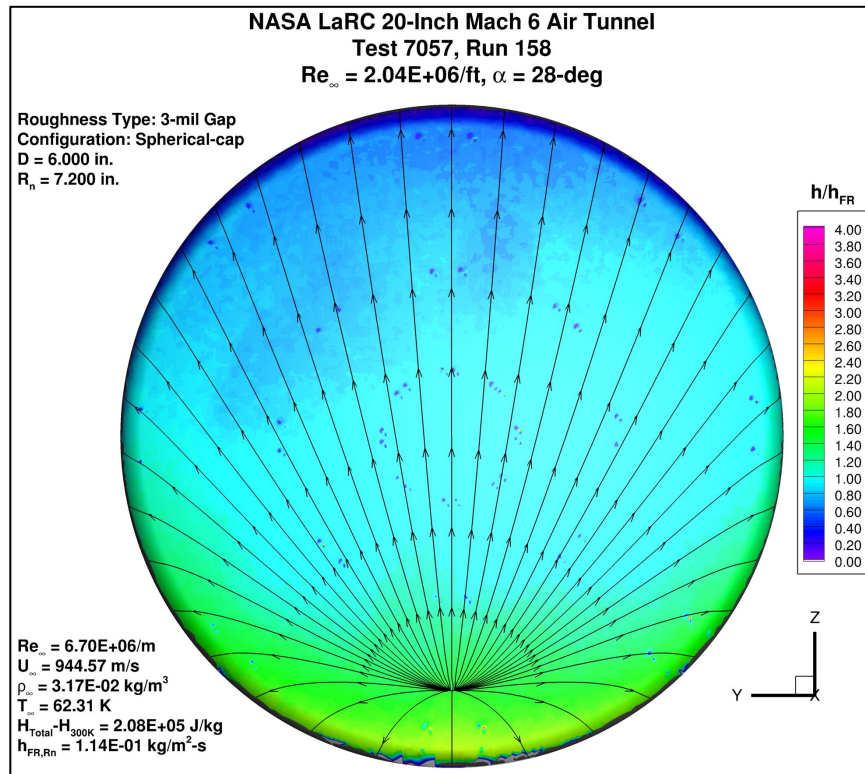


Figure 170. Test 7057, Run 158, $Re_\infty = 2.1 \times 10^6/ft$, spherical-cap 3 mil gap.

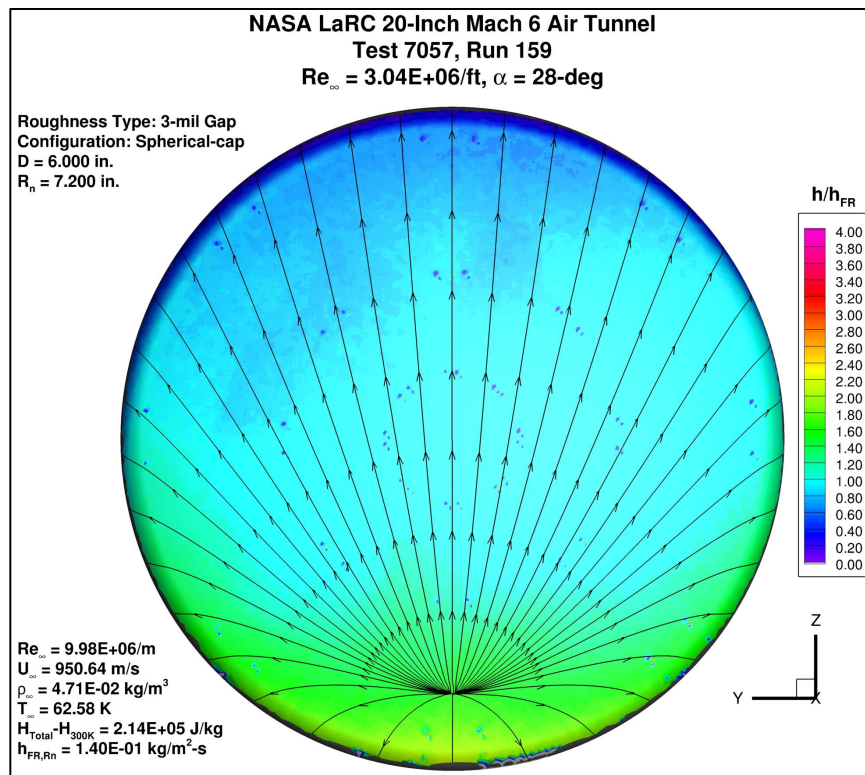


Figure 171. Test 7057, Run 159, $Re_\infty = 3.0 \times 10^6/ft$, spherical- cap 3 mil gap.

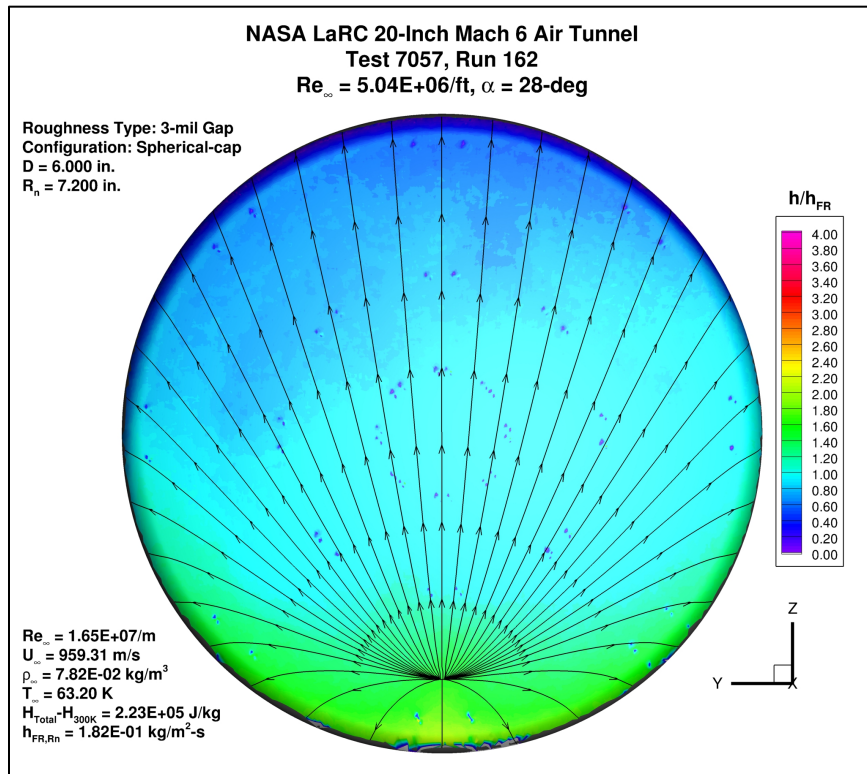


Figure 172. Test 7057, Run 162, $Re_\infty = 5.0 \times 10^6/ft$, spherical-cap 3 mil gap.

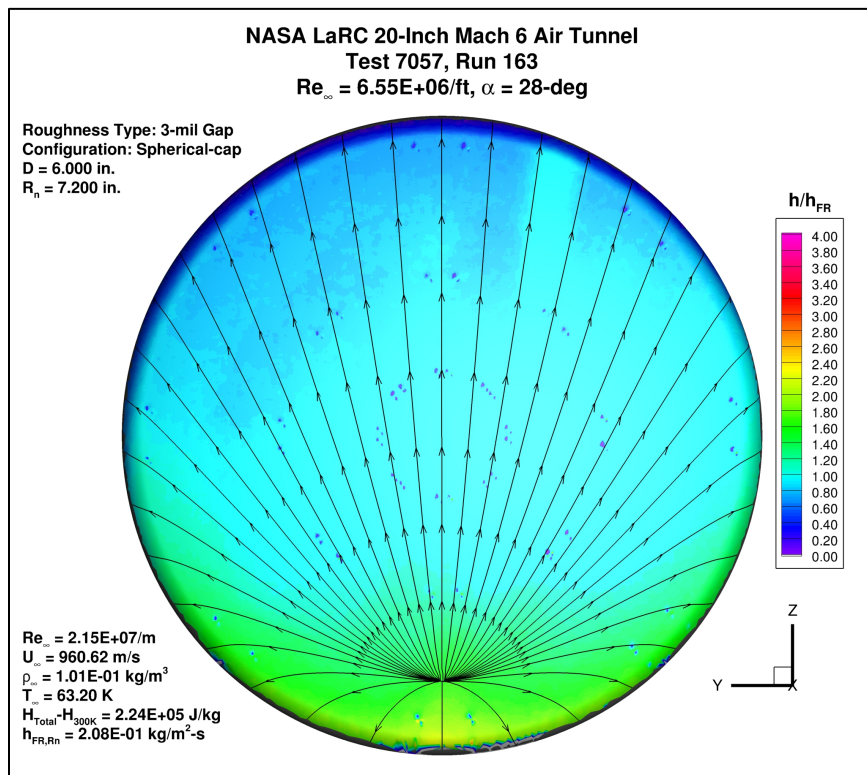


Figure 173. Test 7057, Run 163, $Re_\infty = 6.6 \times 10^6/ft$, spherical-cap 3 mil gap.

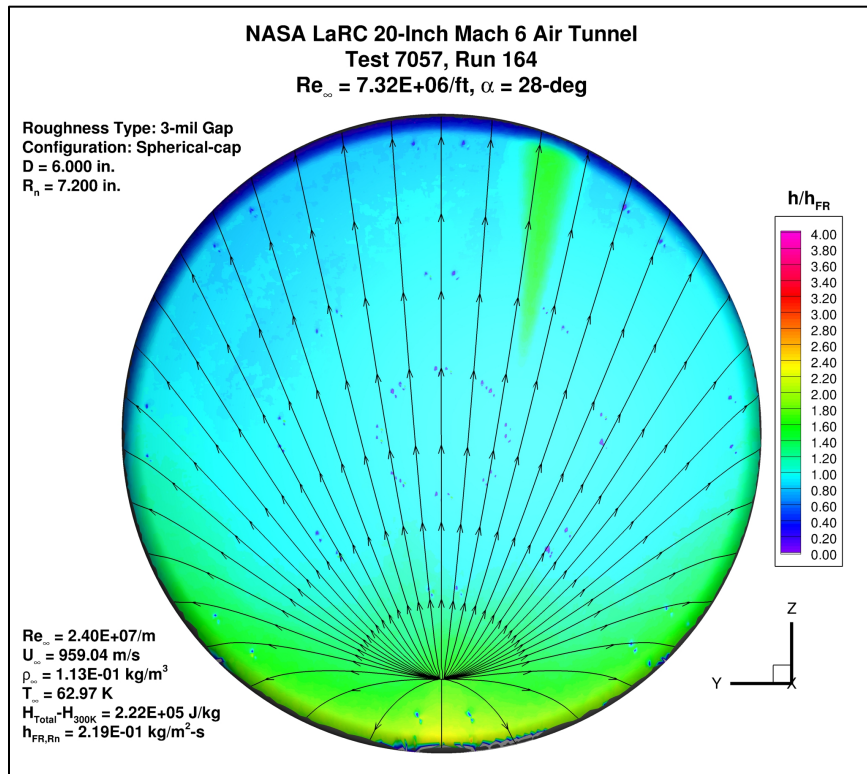


Figure 174. Test 7057, Run 164, $Re_\infty = 7.5 \times 10^6/ft$, spherical-cap 3 mil gap.

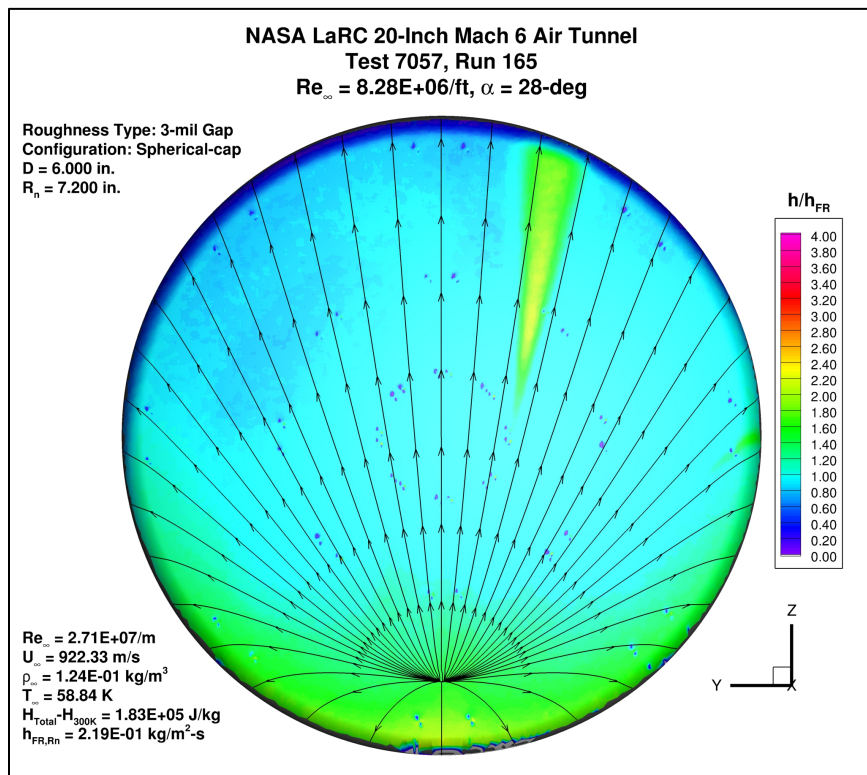


Figure 175. Test 7057, Run 165, $Re_\infty = 8.3 \times 10^6/ft$, spherical-cap 3 mil gap.

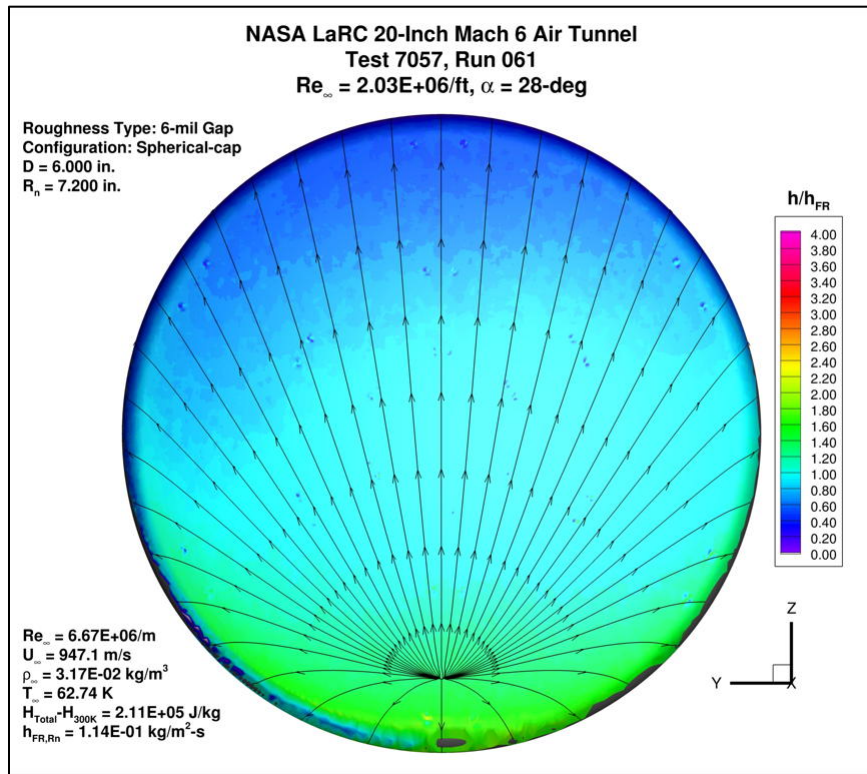


Figure 176. Test 7057, Run 61, $Re_{\infty} = 2.1 \times 10^6/ft$, spherical-cap 6 mil gap.

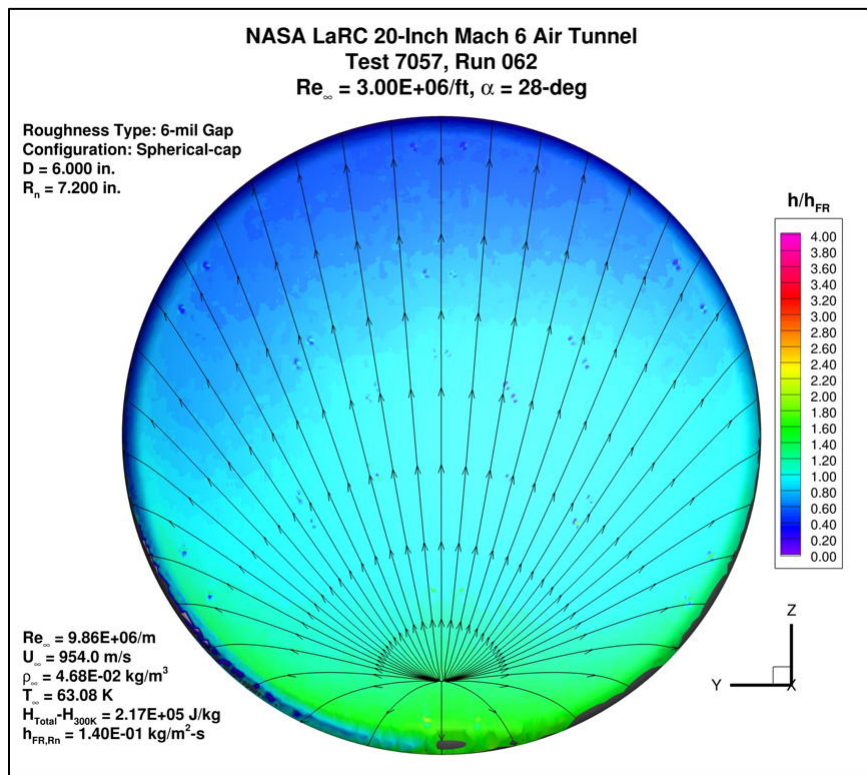


Figure 177. Test 7057, Run 62, $Re_{\infty} = 3.0 \times 10^6/ft$, spherical-cap 6 mil gap.

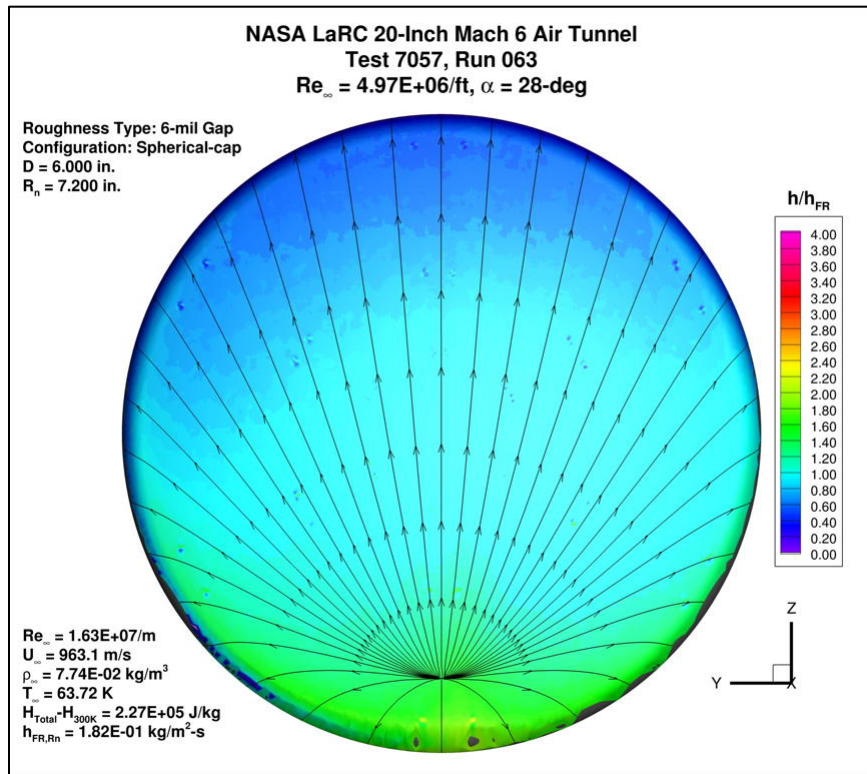


Figure 178. Test 7057, Run 63, $Re_{\infty} = 5.0 \times 10^6/ft$, spherical-cap 6 mil gap.

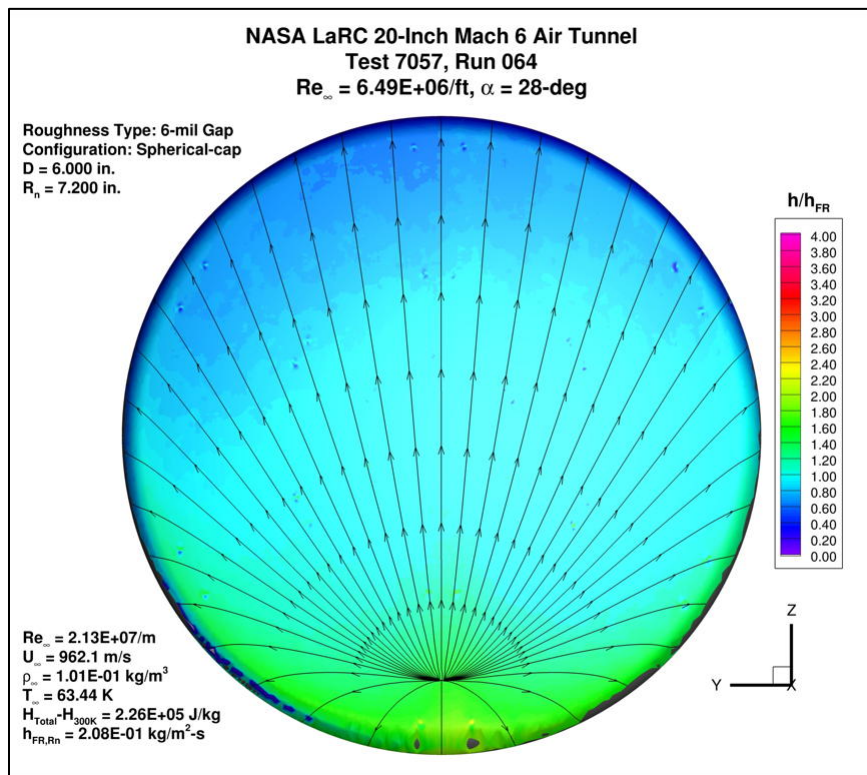


Figure 179. Test 7057, Run 64, $Re_{\infty} = 6.6 \times 10^6/ft$, spherical-cap 6 mil gap.

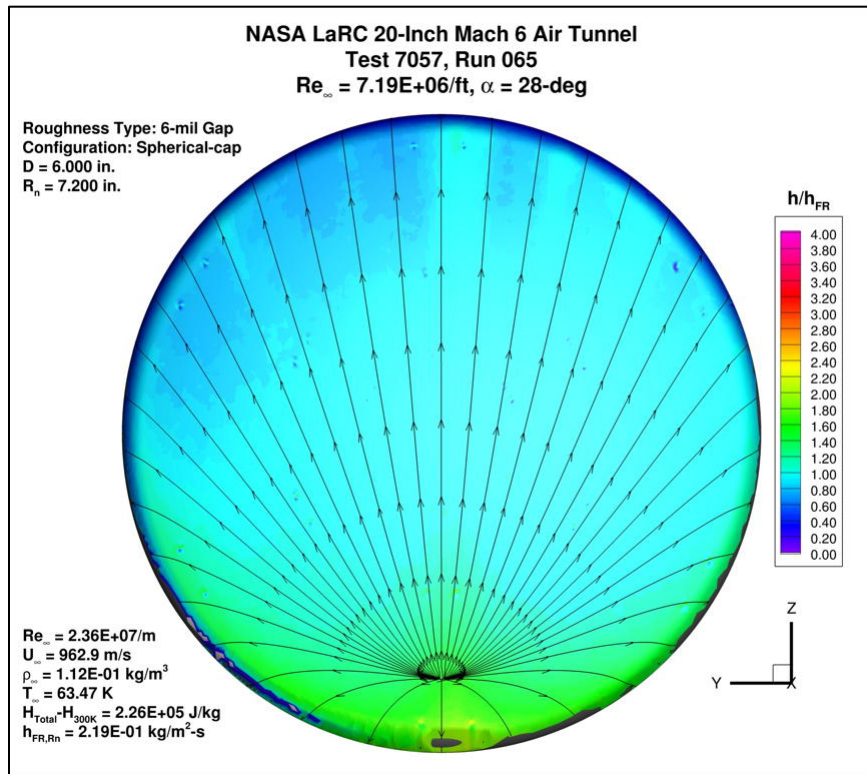


Figure 180. Test 7057, Run 65, $Re_{\infty} = 7.5 \times 10^6/ft$, spherical-cap 6 mil gap.

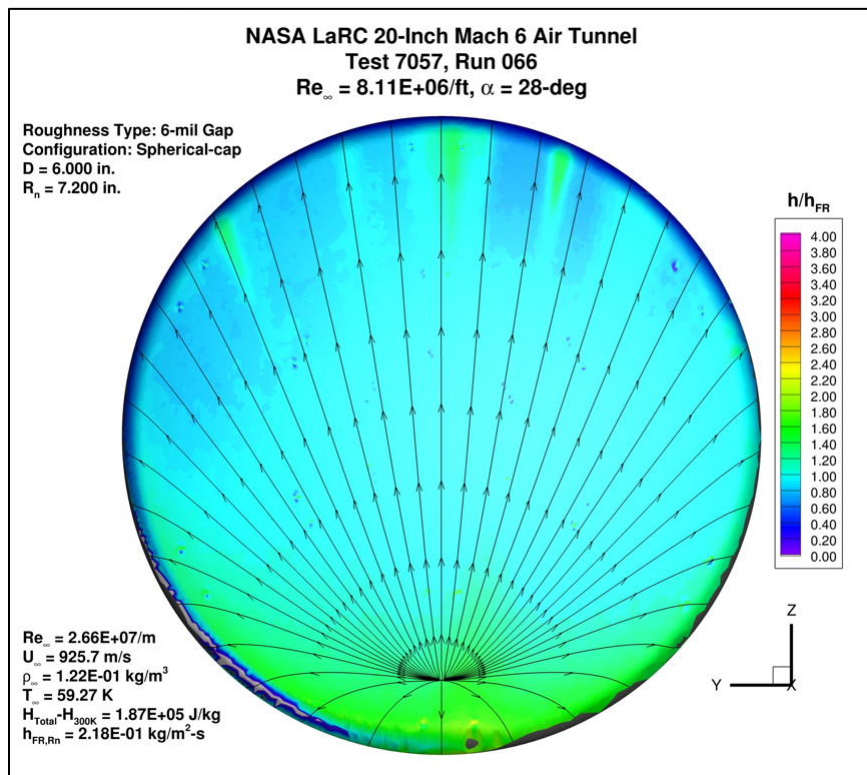


Figure 181. Test 7057, Run 66, $Re_{\infty} = 8.3 \times 10^6/ft$, spherical-cap 6 mil gap.

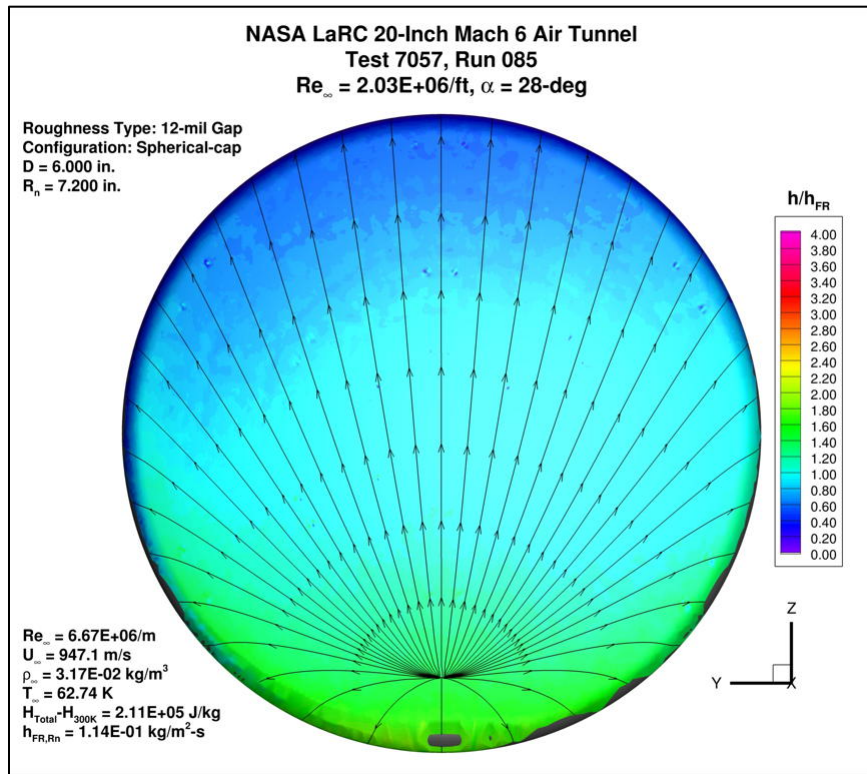


Figure 182. Test 7057, Run 85, $Re_\infty = 2.1 \times 10^6/\text{ft}$, spherical-cap 12 mil gap.

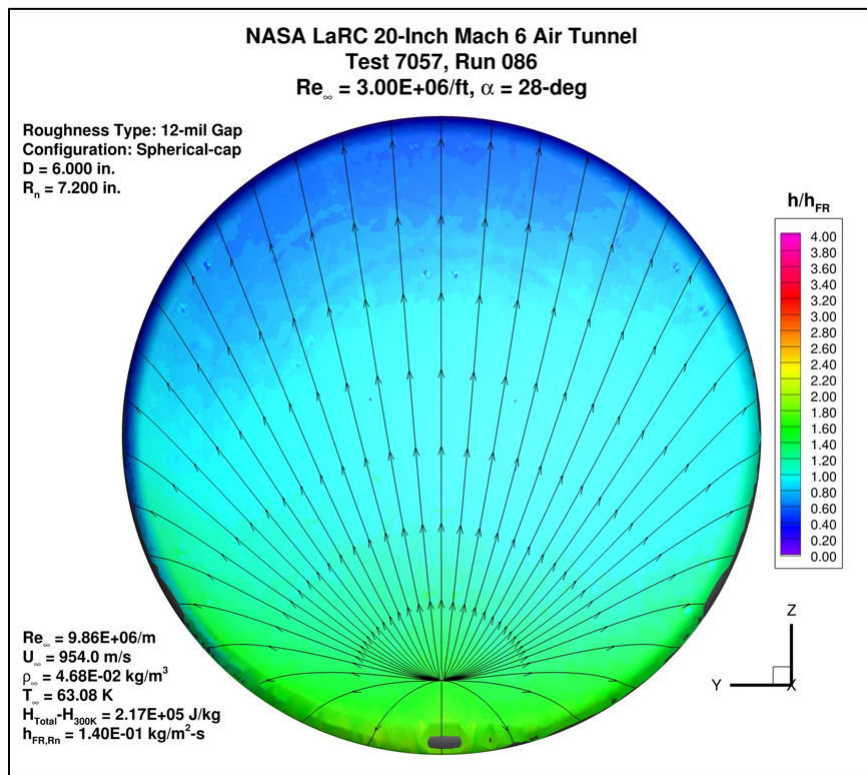


Figure 183. Test 7057, Run 86, $Re_\infty = 3.0 \times 10^6/\text{ft}$, spherical-cap 12 mil gap.

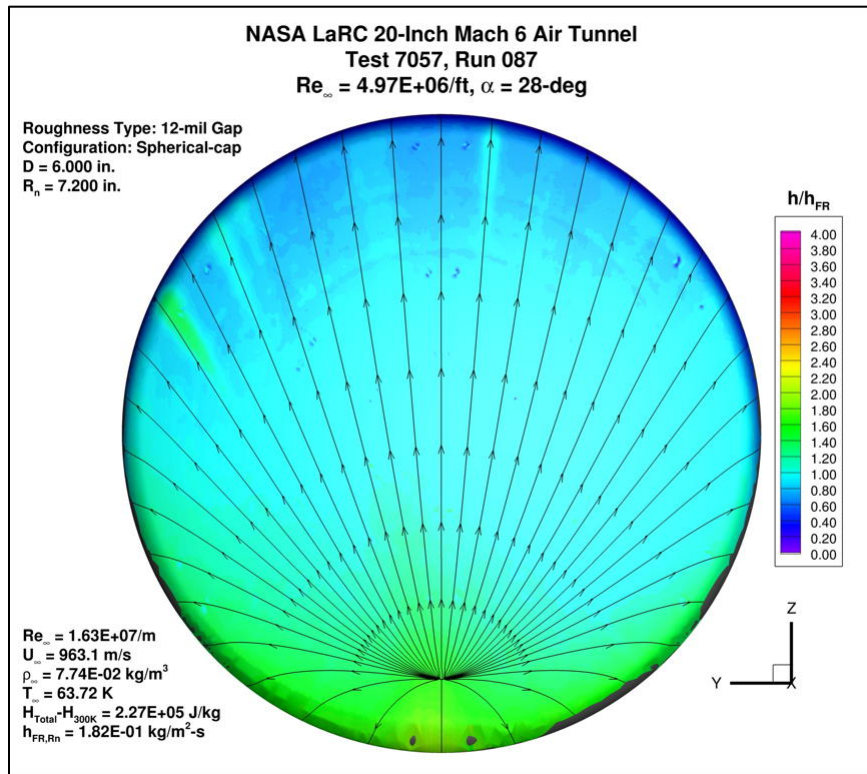


Figure 184. Test 7057, Run 87, $Re_\infty = 5.0 \times 10^6/ft$, spherical-cap 12 mil gap.

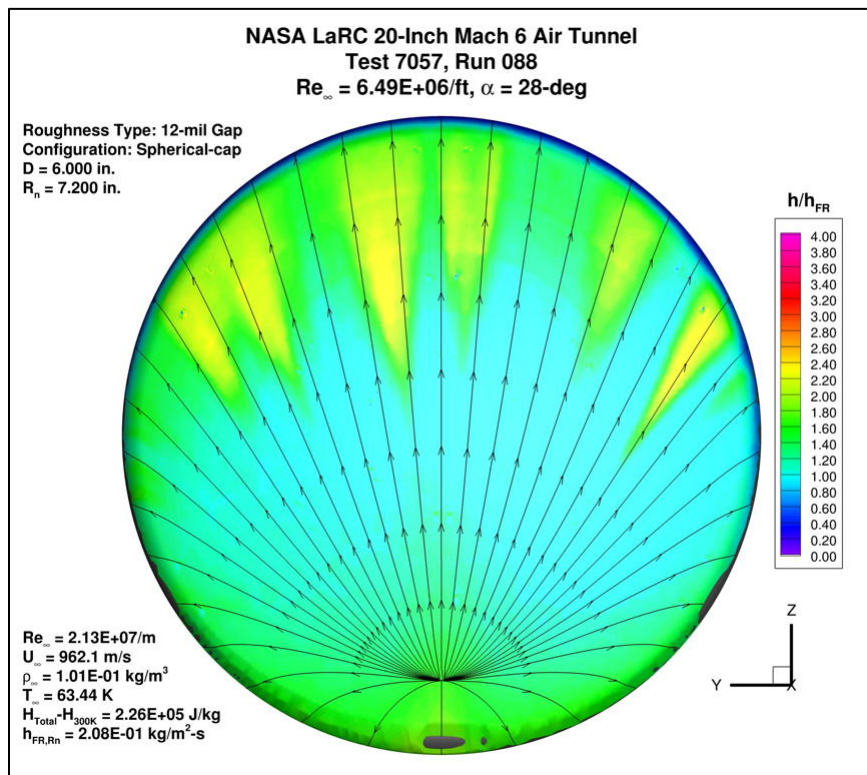


Figure 185. Test 7057, Run 88, $Re_\infty = 6.6 \times 10^6/ft$, spherical-cap 12 mil gap.

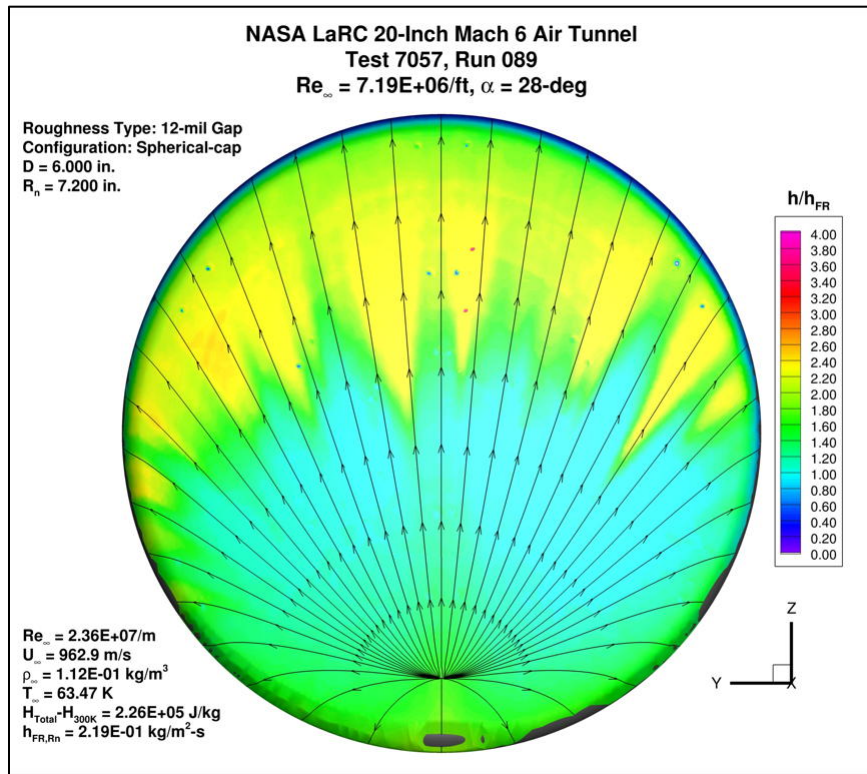


Figure 186. Test 7057, Run 89, $Re_\infty = 7.5 \times 10^6/ft$, spherical-cap 12 mil gap.

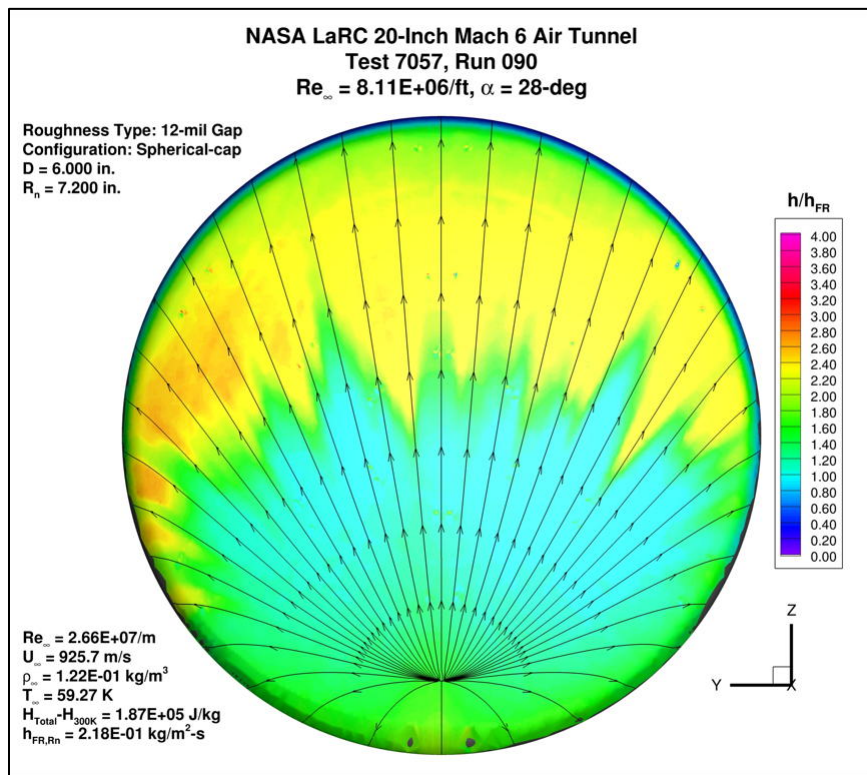


Figure 187. Test 7057, Run 90, $Re_\infty = 8.3 \times 10^6/ft$, spherical-cap 12 mil gap.

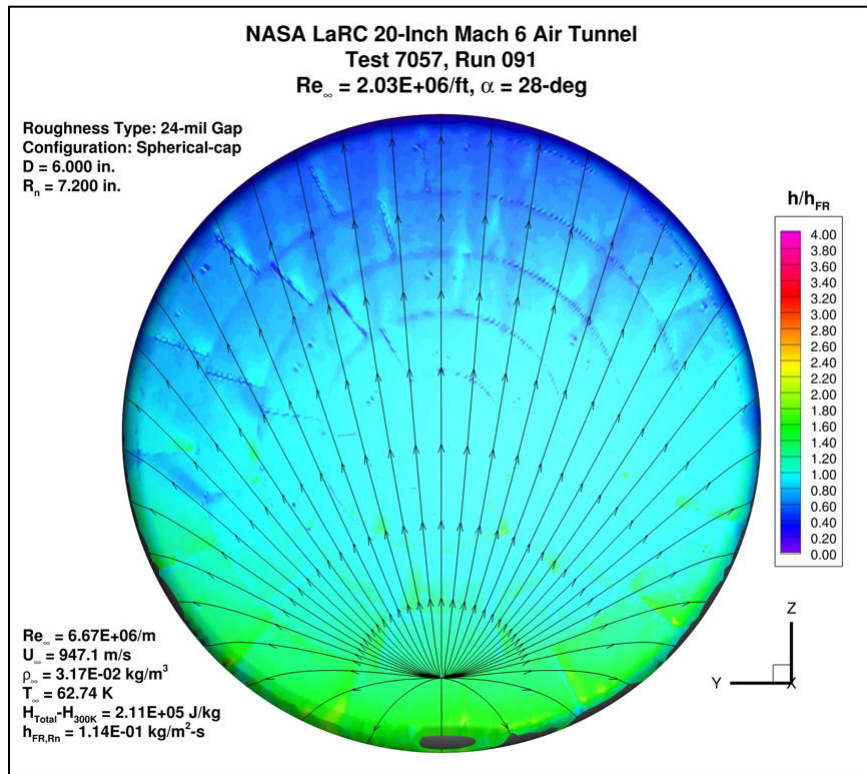


Figure 188. Test 7057, Run 91, $Re_\infty = 2.1 \times 10^6/\text{ft}$, spherical-cap 24 mil gap.

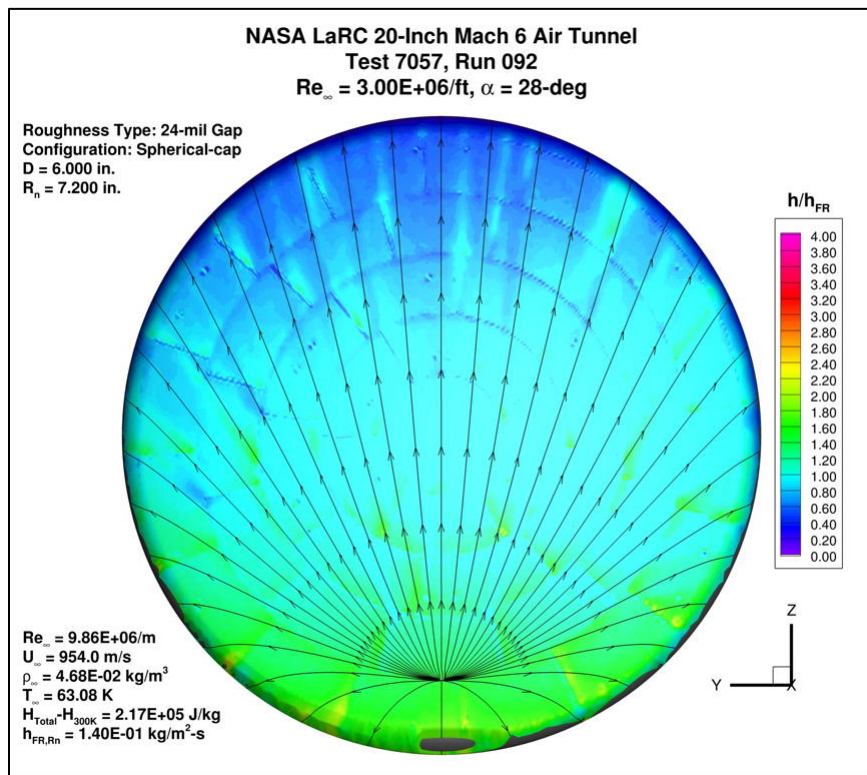


Figure 189. Test 7057, Run 92, $Re_\infty = 3.0 \times 10^6/\text{ft}$, spherical-cap 24 mil gap.

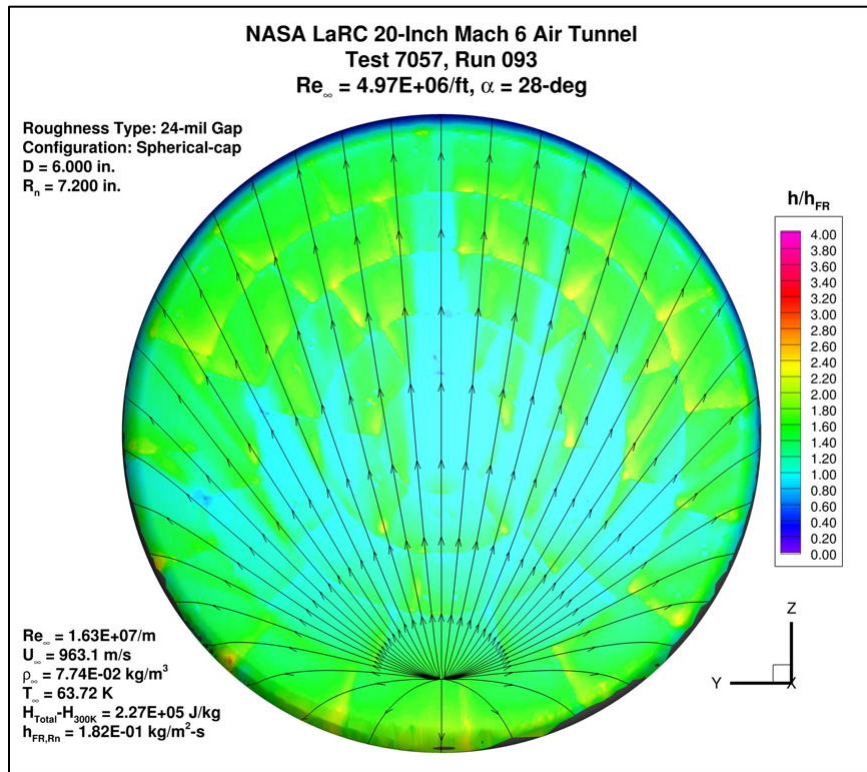


Figure 190. Test 7057, Run 93, $Re_\infty = 5.0 \times 10^6/ft$, spherical-cap 24 mil gap.

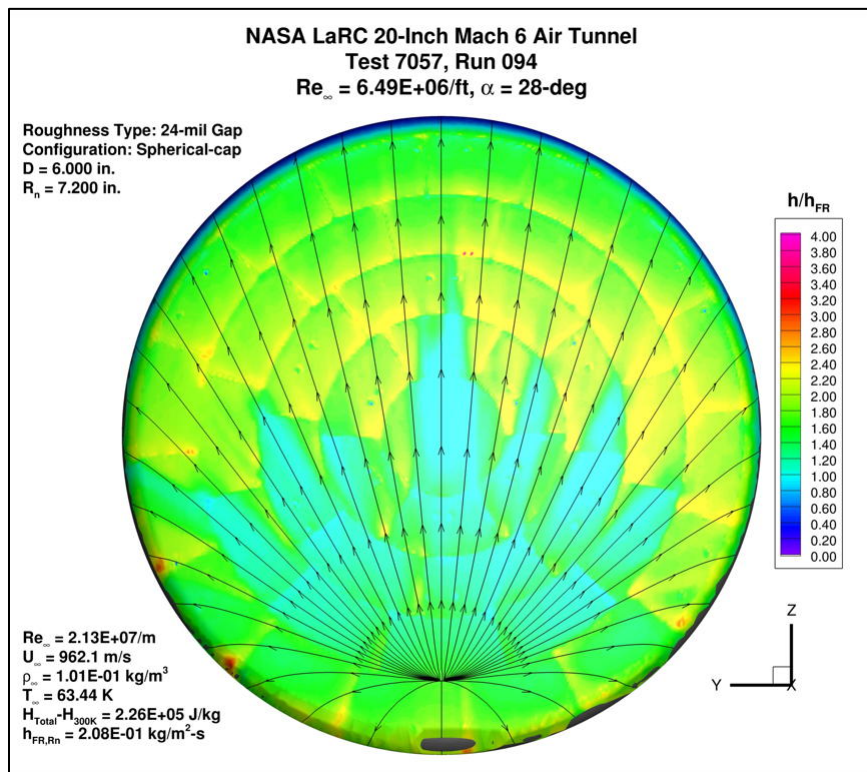


Figure 191. Test 7057, Run 94, $Re_\infty = 6.6 \times 10^6/ft$, spherical-cap 24 mil gap.

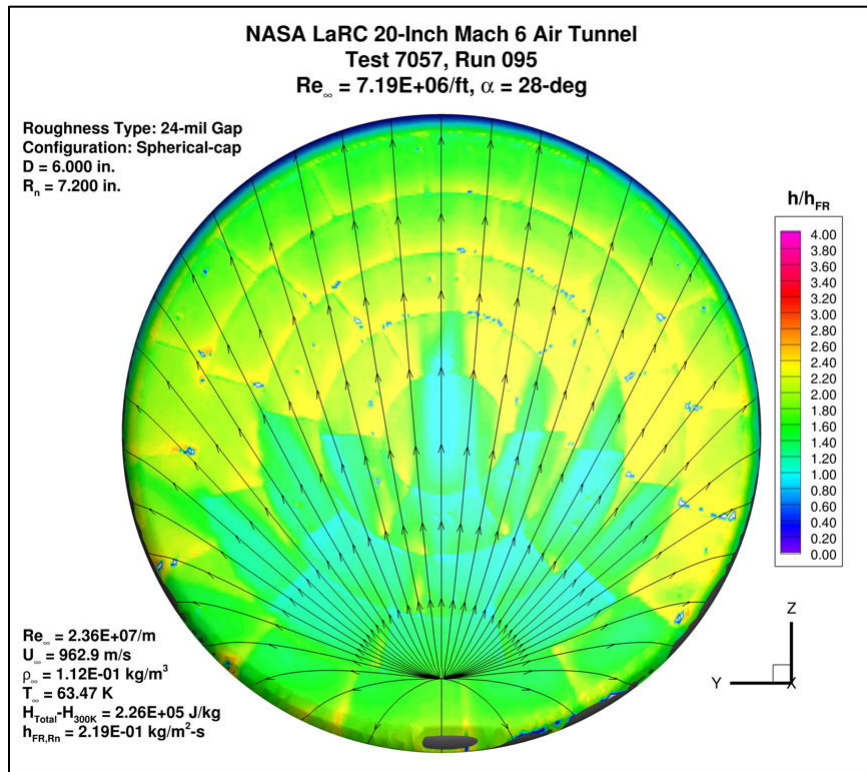


Figure 192. Test 7057, Run 95, $Re_\infty = 7.5 \times 10^6/ft$, spherical-cap 24 mil gap.

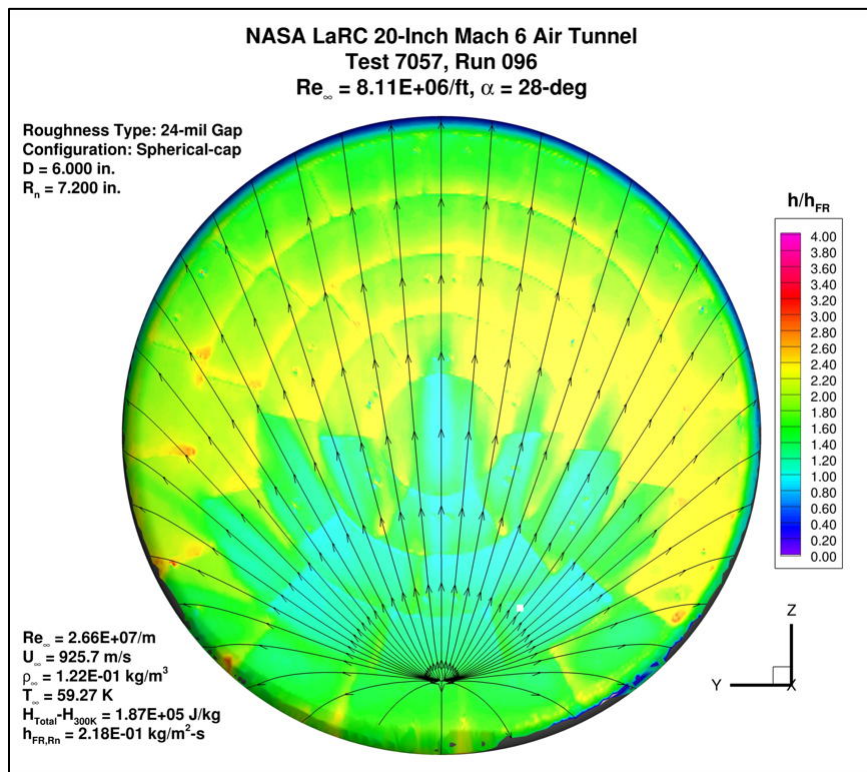


Figure 193. Test 7057, Run 96, $Re_\infty = 8.3 \times 10^6/ft$, spherical-cap 24 mil gap.

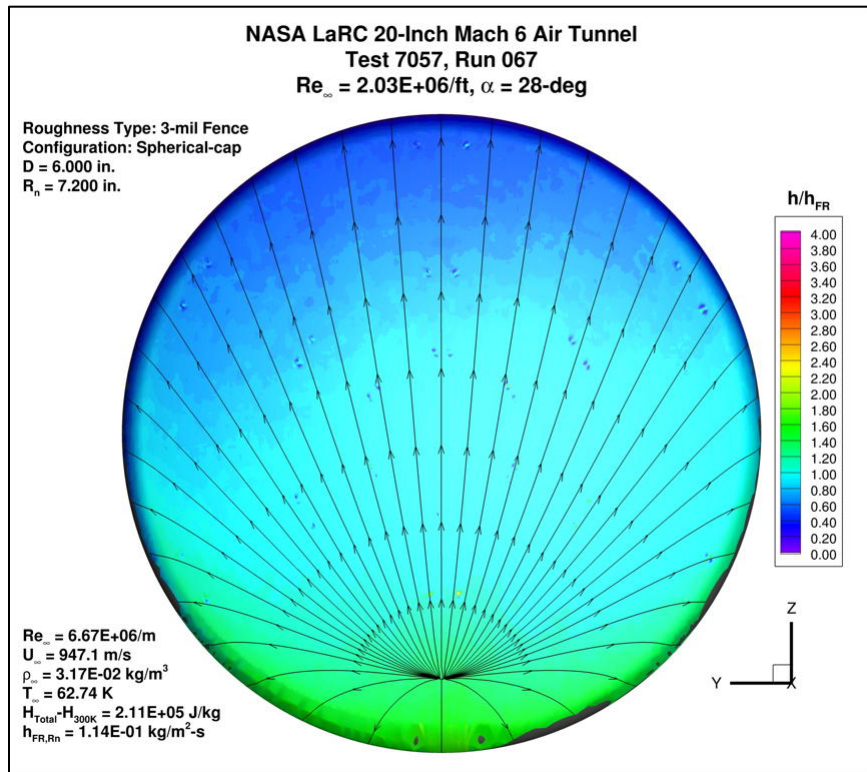


Figure 194. Test 7057, Run 67, $Re_\infty = 2.1 \times 10^6/ft$, spherical-cap 3 mil fence.

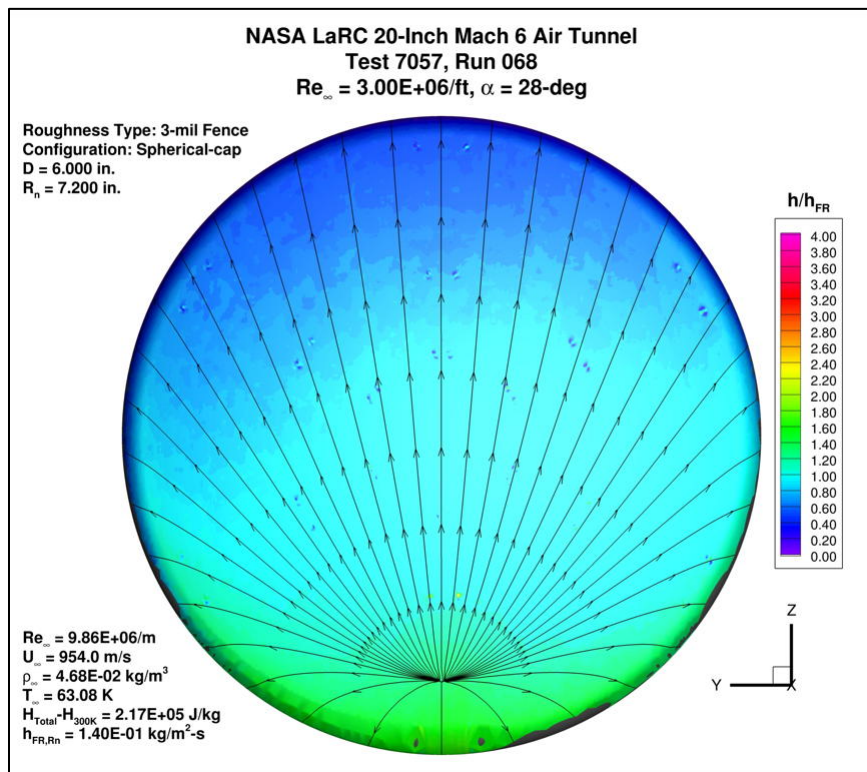


Figure 195. Test 7057, Run 68, $Re_\infty = 3.0 \times 10^6/ft$, spherical-cap 3 mil fence.

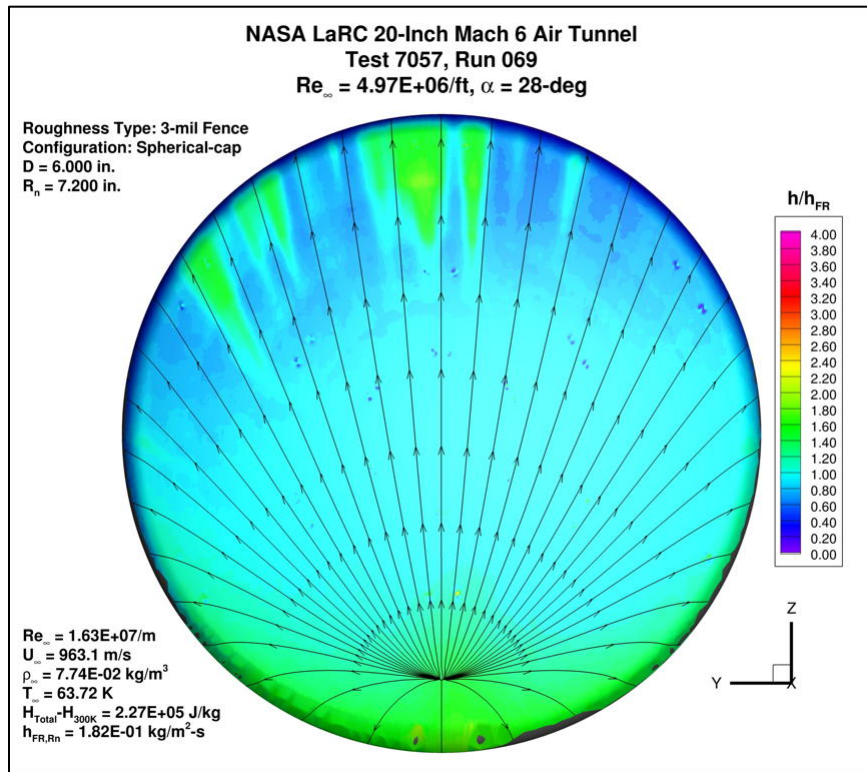


Figure 196. Test 7057, Run 69, $Re_\infty = 5.0 \times 10^6/ft$, spherical-cap 3 mil fence.

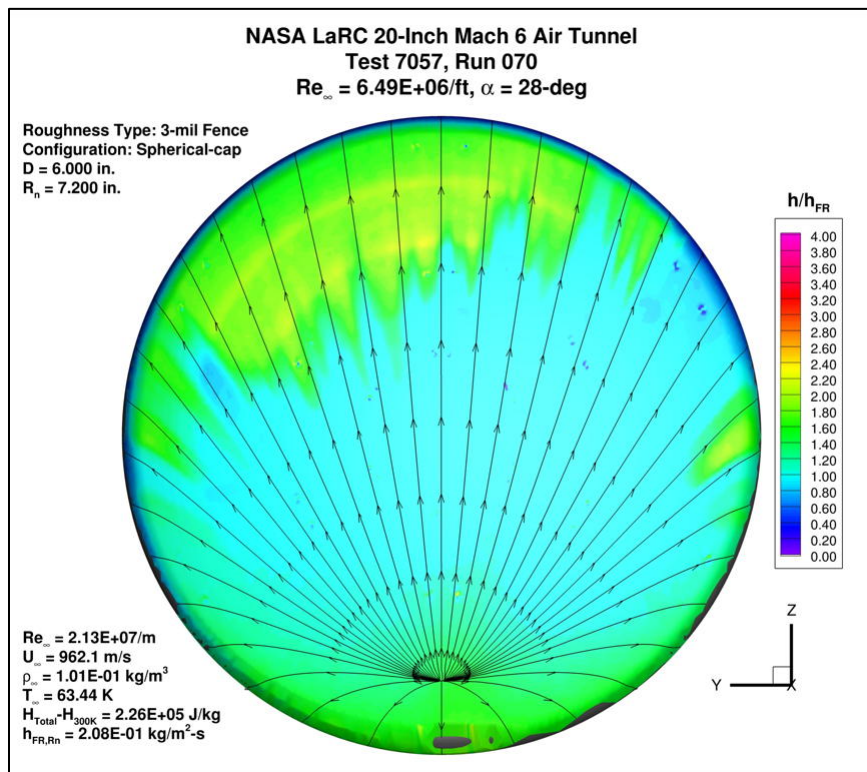


Figure 197. Test 7057, Run 70, $Re_\infty = 6.6 \times 10^6/ft$, spherical-cap 3 mil fence.

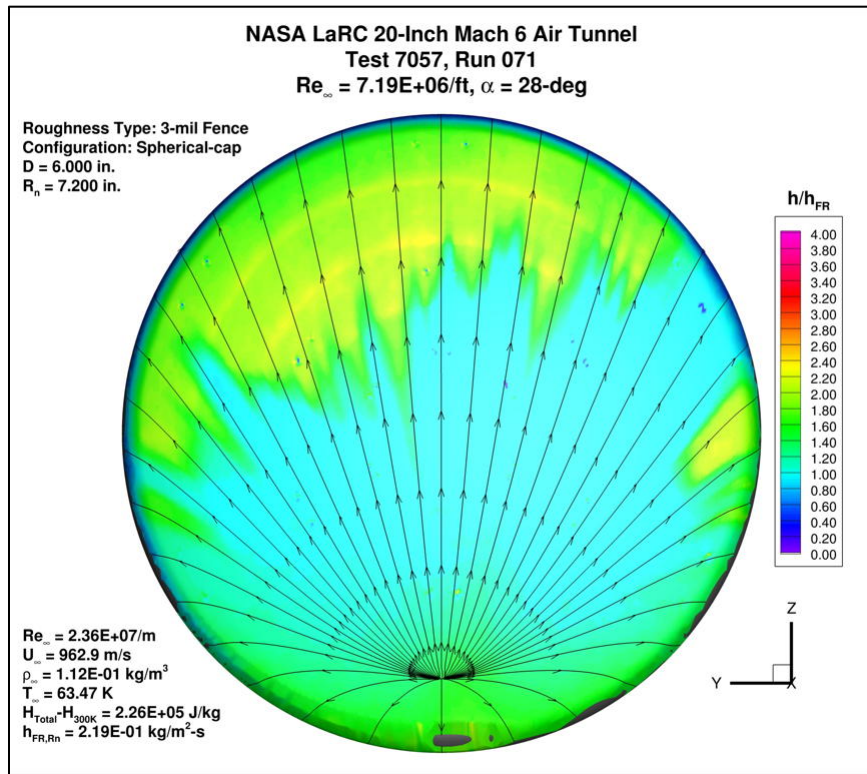


Figure 198. Test 7057, Run 71, $Re_\infty = 7.5 \times 10^6/ft$, spherical-cap 3 mil fence.

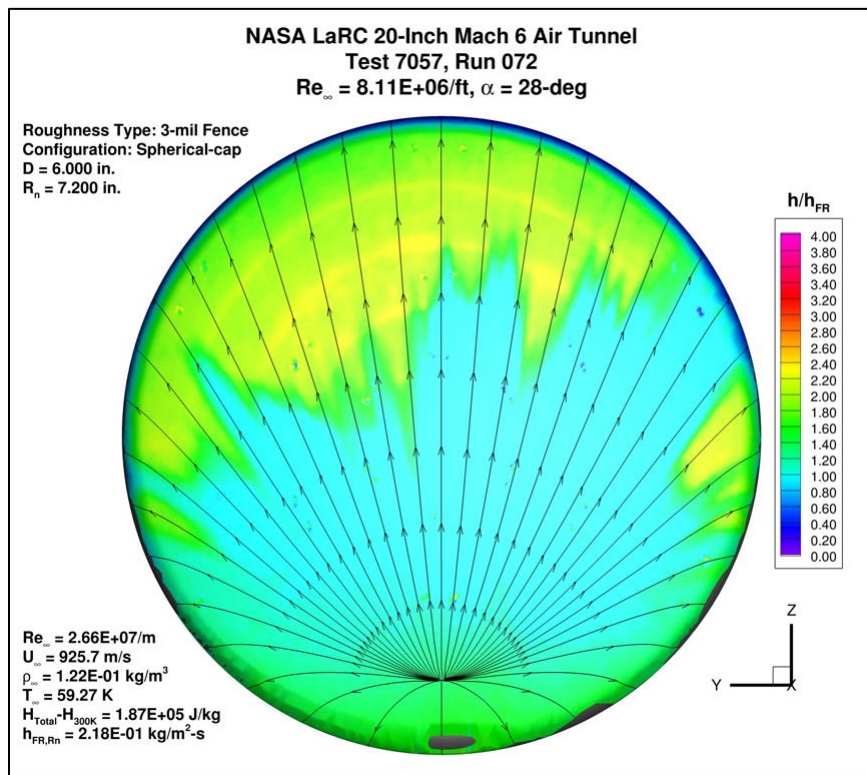


Figure 199. Test 7057, Run 72, $Re_\infty = 8.3 \times 10^6/ft$, spherical-cap 3 mil fence.

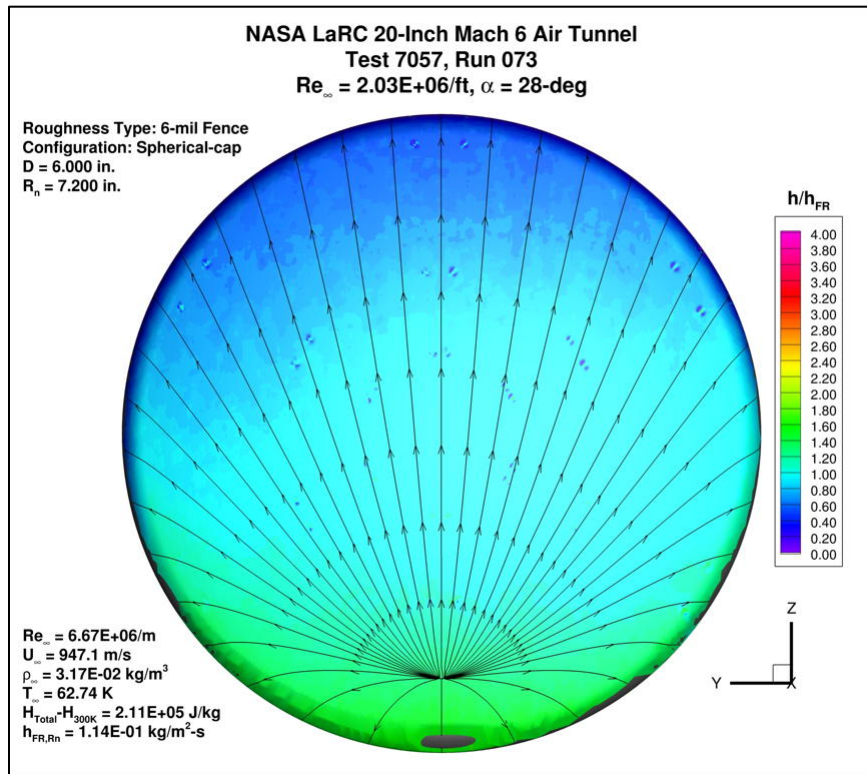


Figure 200. Test 7057, Run 73, $Re_\infty = 2.1 \times 10^6/ft$, spherical-cap 6 mil fence.

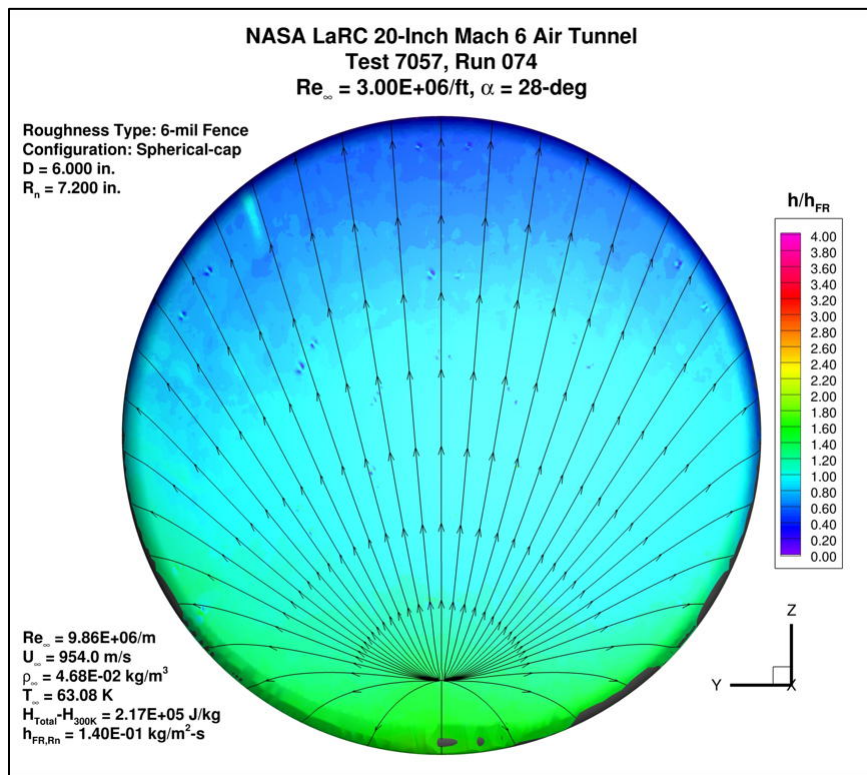


Figure 201. Test 7057, Run 74, $Re_\infty = 3.0 \times 10^6/ft$, spherical-cap 6 mil fence.

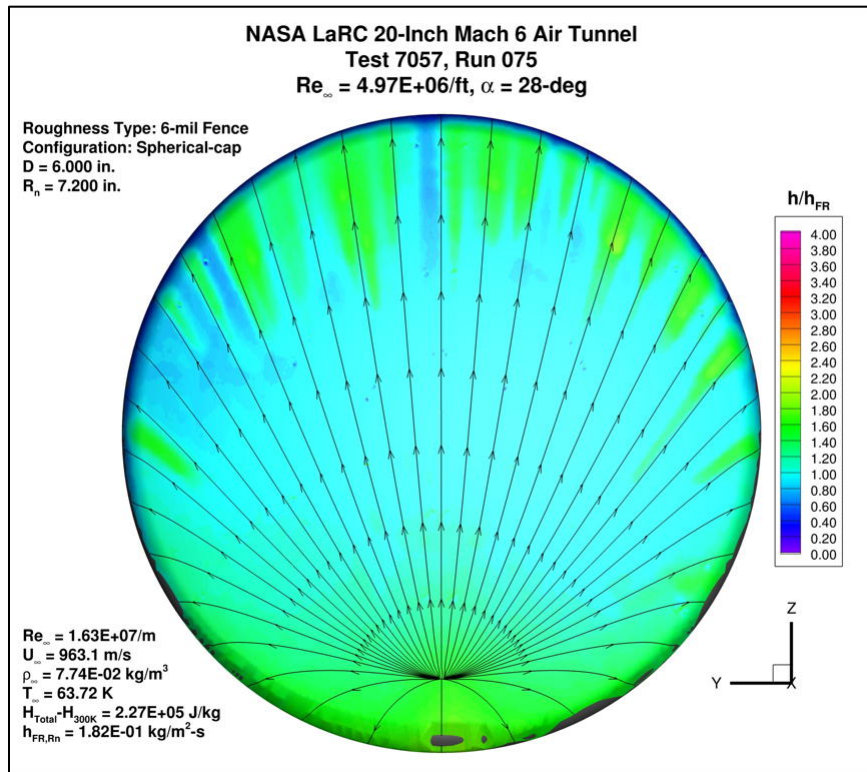


Figure 202. Test 7057, Run 75, $Re_{\infty} = 5.0 \times 10^6/ft$, spherical-cap 6 mil fence.

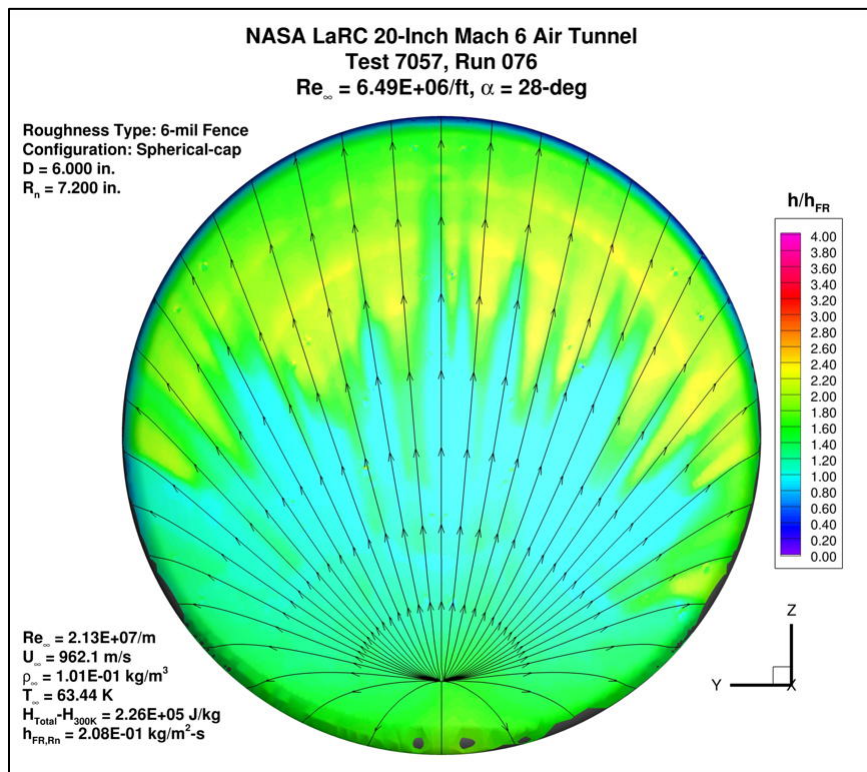


Figure 203. Test 7057, Run 76, $Re_{\infty} = 6.6 \times 10^6/ft$, spherical-cap 6 mil fence.

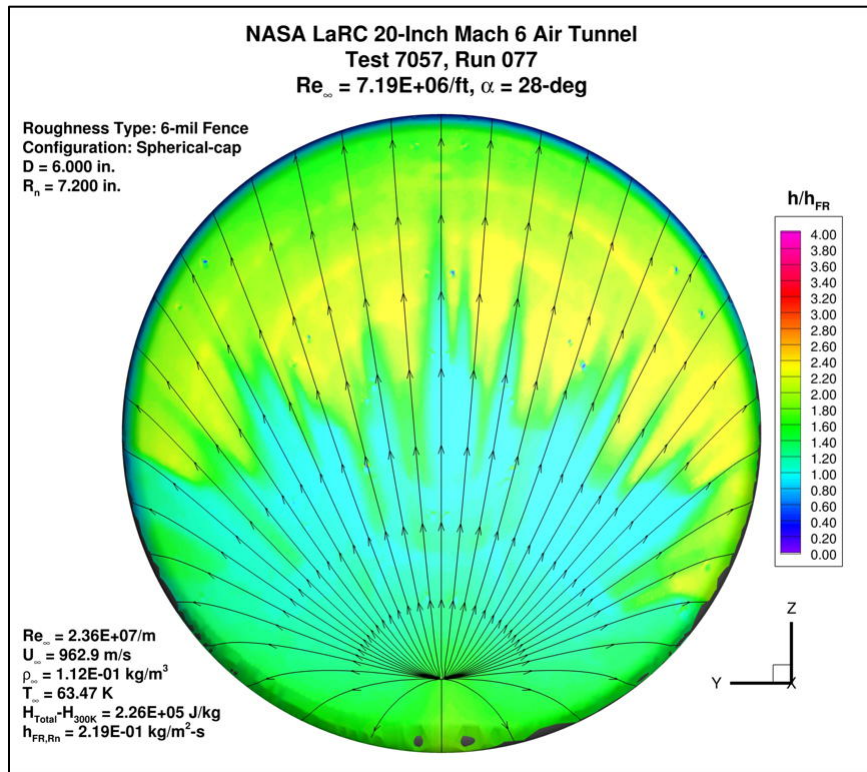


Figure 204. Test 7057, Run 77, $Re_\infty = 7.5 \times 10^6/ft$, spherical-cap 6 mil fence.

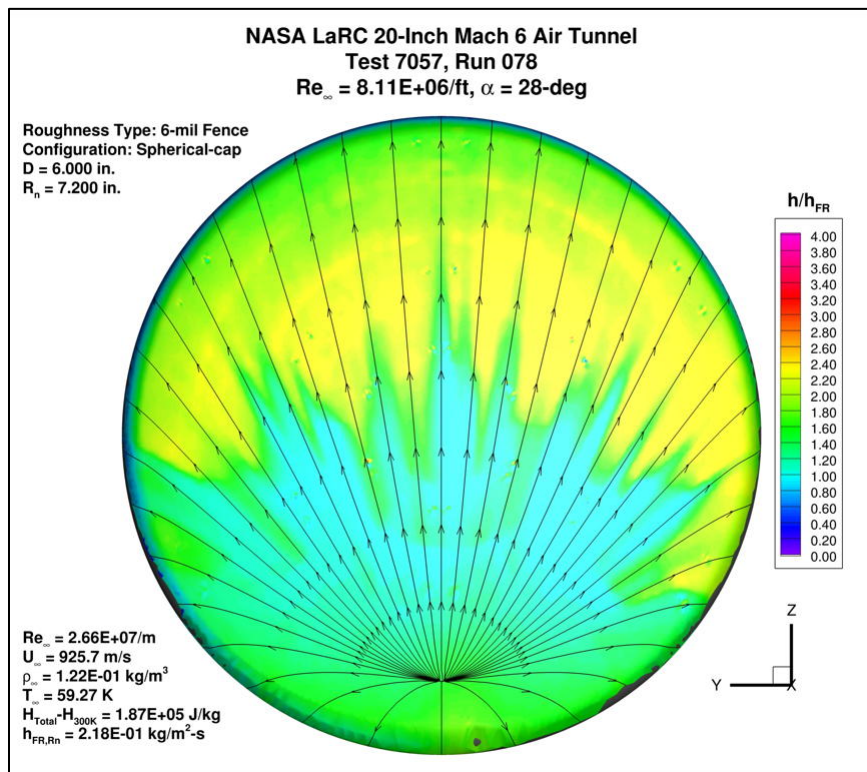


Figure 205. Test 7057, Run 78, $Re_\infty = 8.3 \times 10^6/ft$, spherical-cap 6 mil fence.

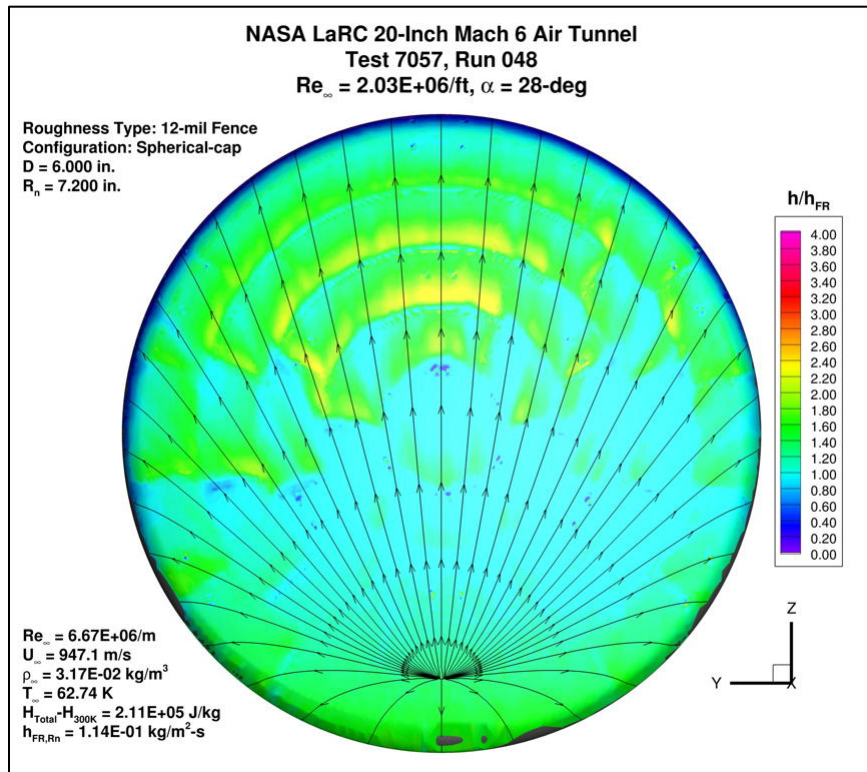


Figure 206. Test 7057, Run 48, $Re_{\infty} = 2.1 \times 10^6/ft$, spherical-cap 12 mil fence.

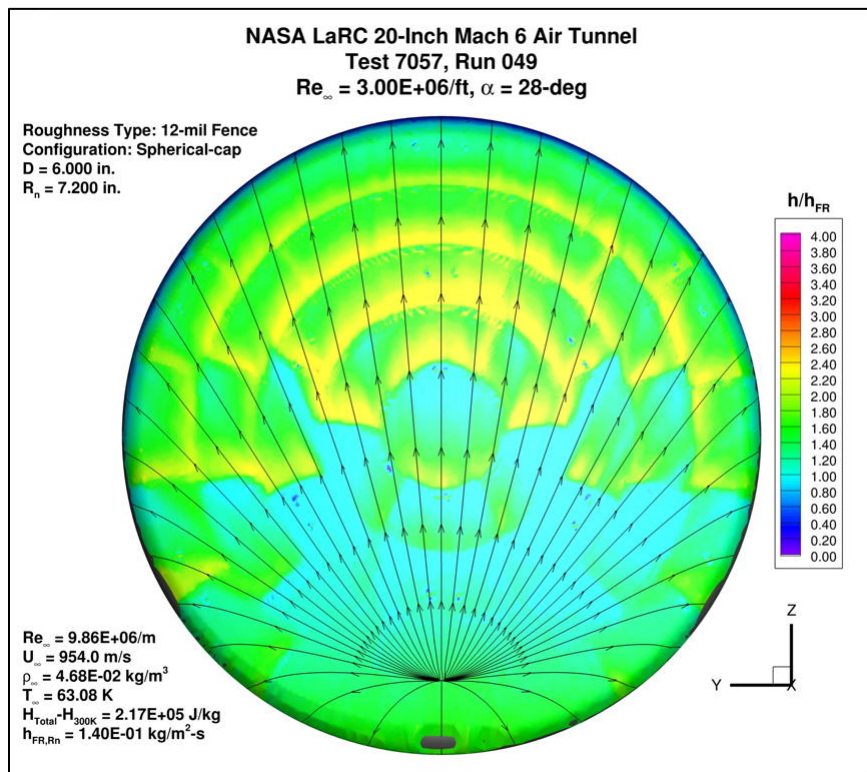


Figure 207. Test 7057, Run 49, $Re_{\infty} = 3.0 \times 10^6/ft$, spherical-cap 12 mil fence.

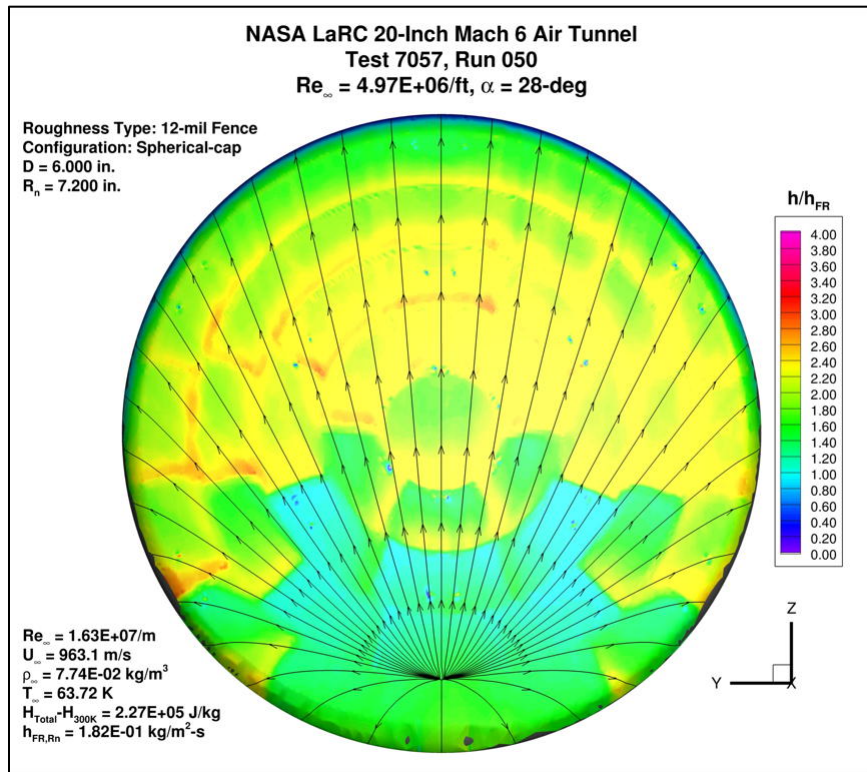


Figure 208. Test 7057, Run 50, $Re_{\infty} = 5.0 \times 10^6/ft$, spherical-cap 12 mil fence.

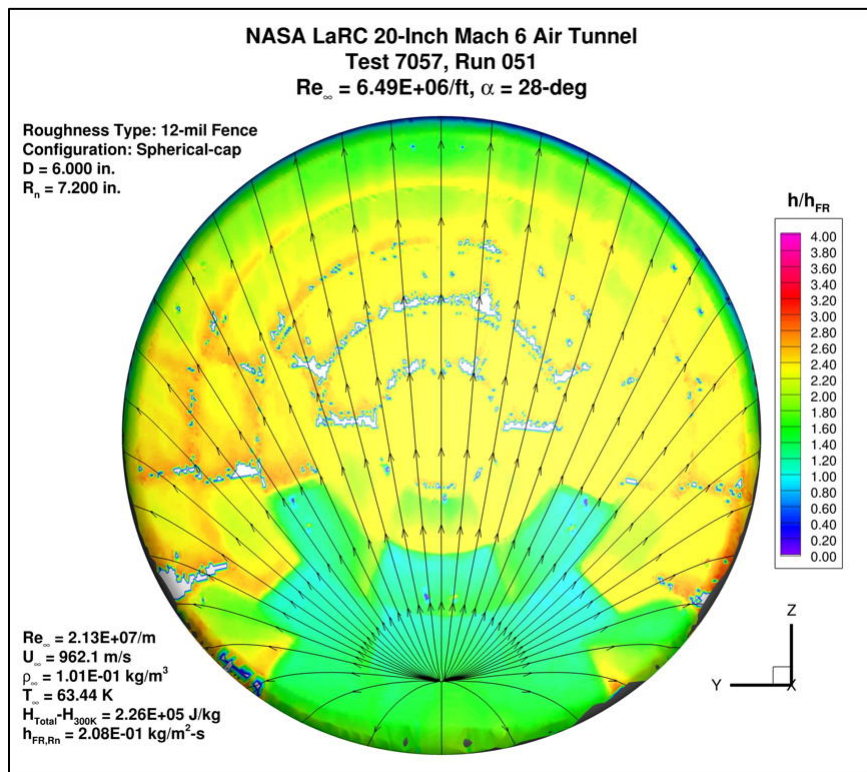


Figure 209. Test 7057, Run 51, $Re_{\infty} = 6.6 \times 10^6/ft$, spherical-cap 12 mil fence.

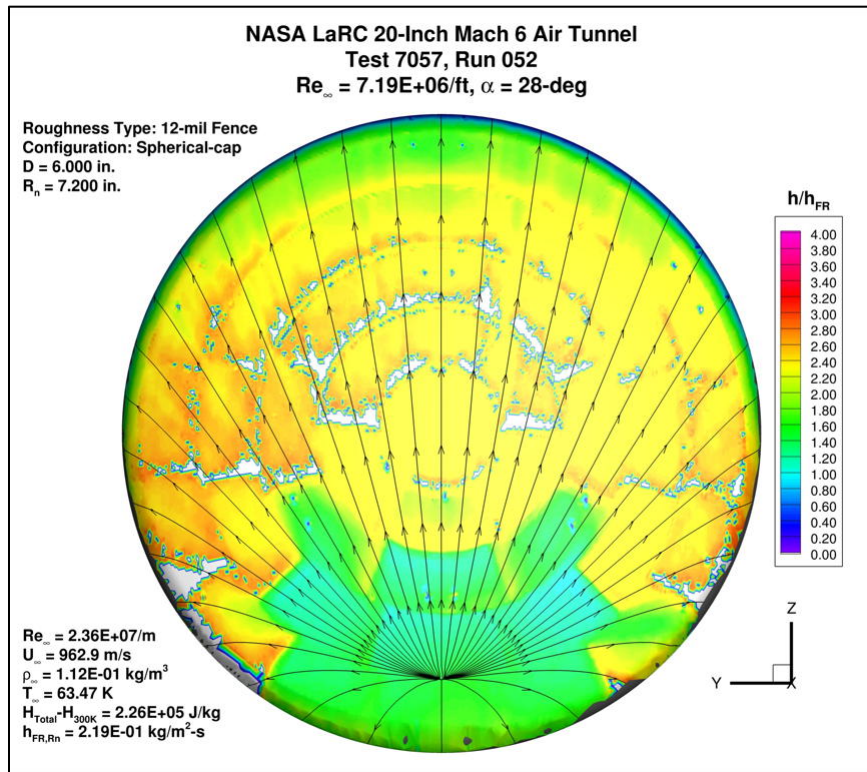


Figure 210. Test 7057, Run 52, $Re_{\infty} = 7.5 \times 10^6/ft$, spherical-cap 12 mil fence.

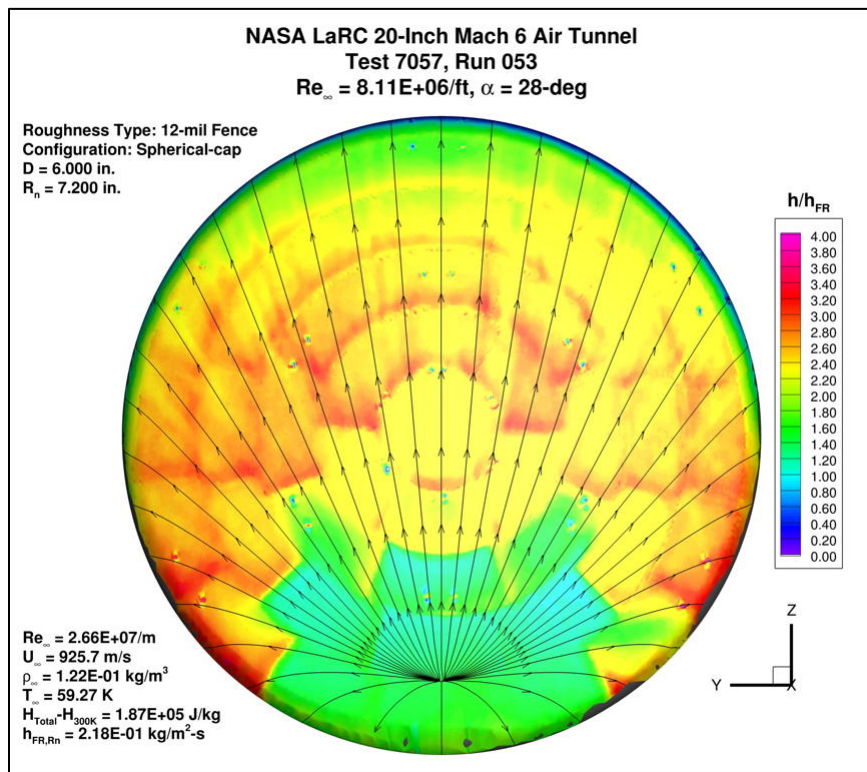


Figure 211. Test 7057, Run 53, $Re_{\infty} = 8.3 \times 10^6/ft$, spherical-cap 12 mil fence

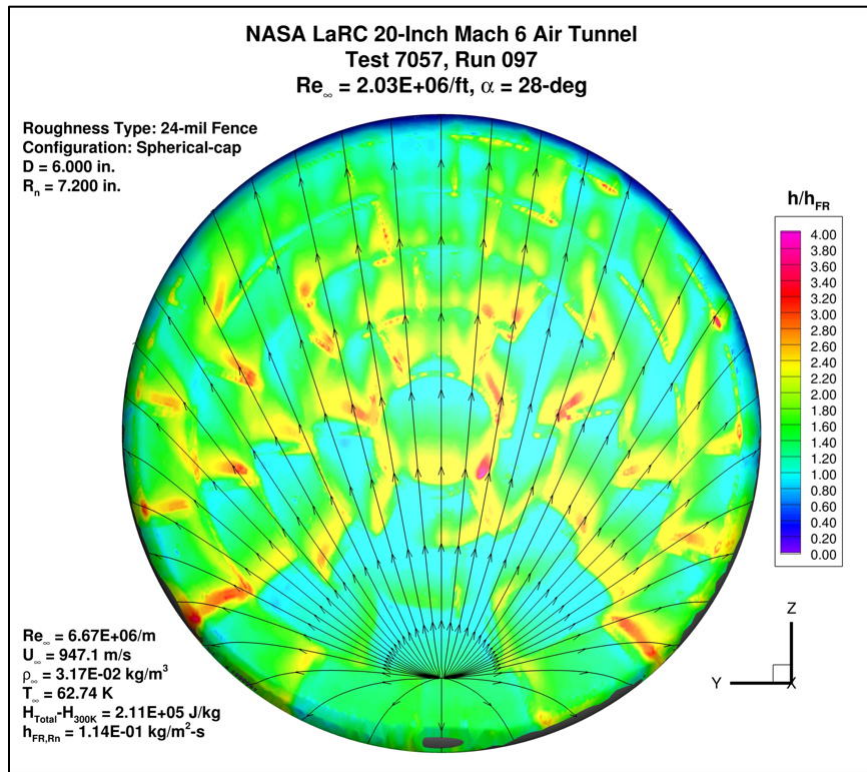


Figure 212. Test 7057, Run 97, $Re_{\infty} = 2.1 \times 10^6/ft$, spherical-cap 24 mil fence.

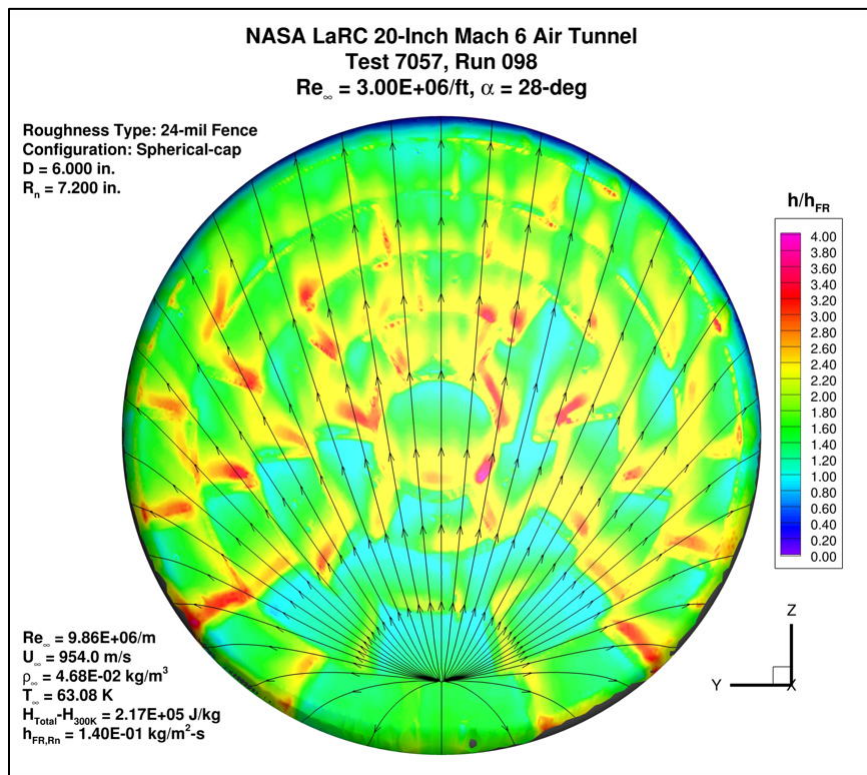


Figure 213. Test 7057, Run 98, $Re_{\infty} = 3.0 \times 10^6/ft$, spherical-cap 24 mil fence.

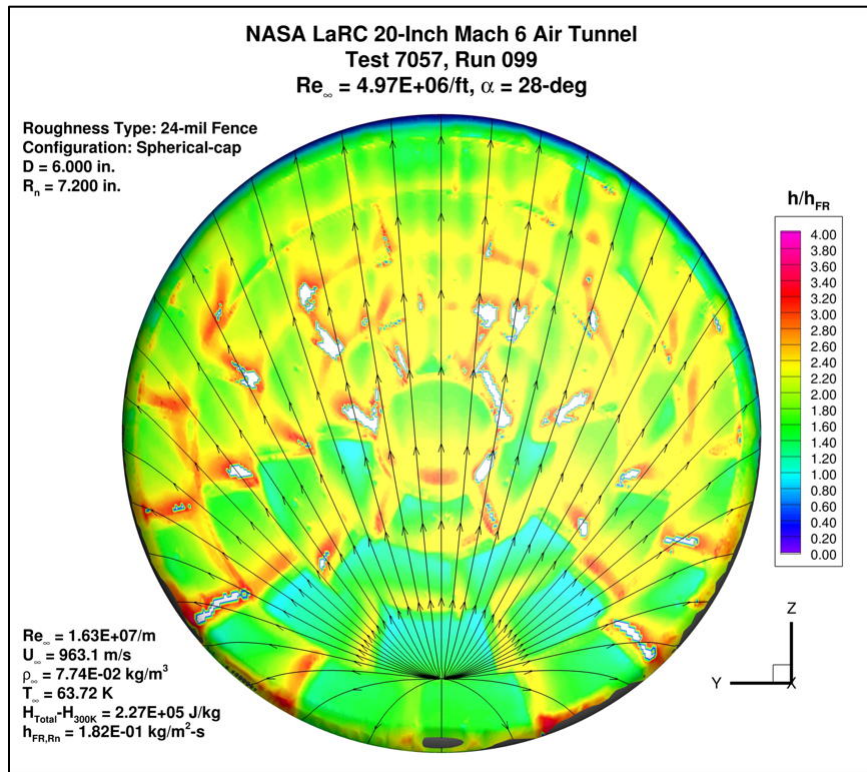


Figure 214. Test 7057, Run 99, $Re_{\infty} = 5.0 \times 10^6/ft$, spherical-cap 24 mil fence.

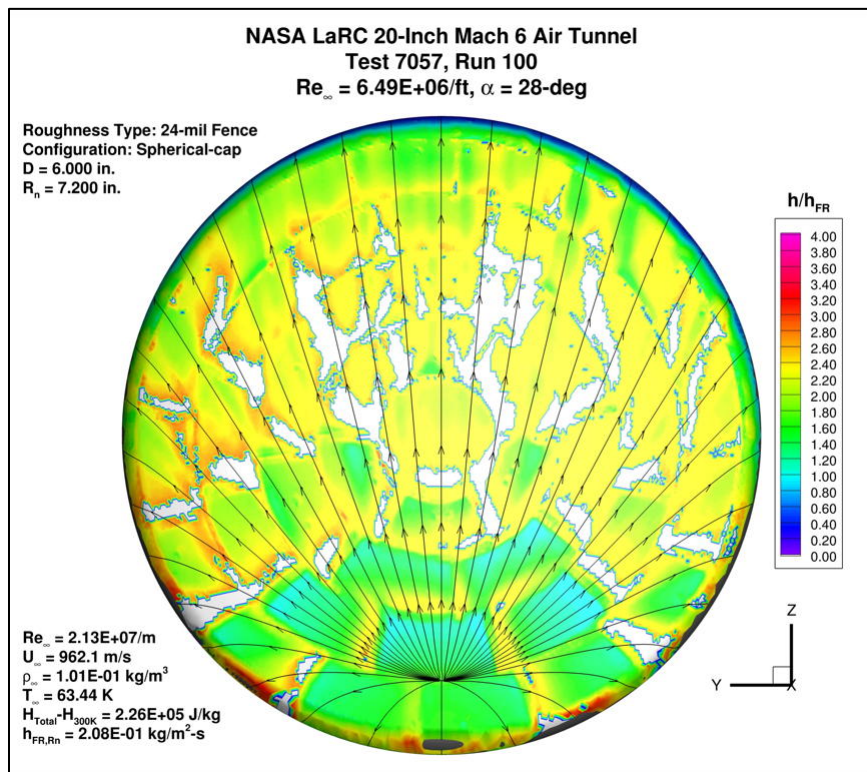


Figure 215. Test 7057, Run 100, $Re_{\infty} = 6.6 \times 10^6/ft$, spherical-cap 24 mil fence.

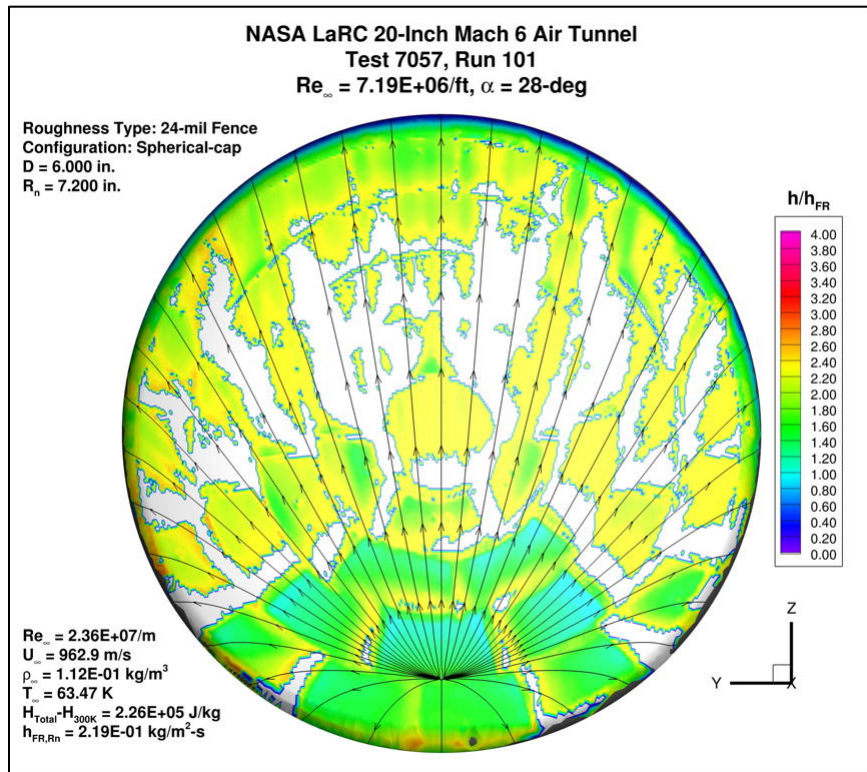


Figure 216. Test 7057, Run 101, $Re_\infty = 7.5 \times 10^6/ft$, spherical-cap 24 mil fence.

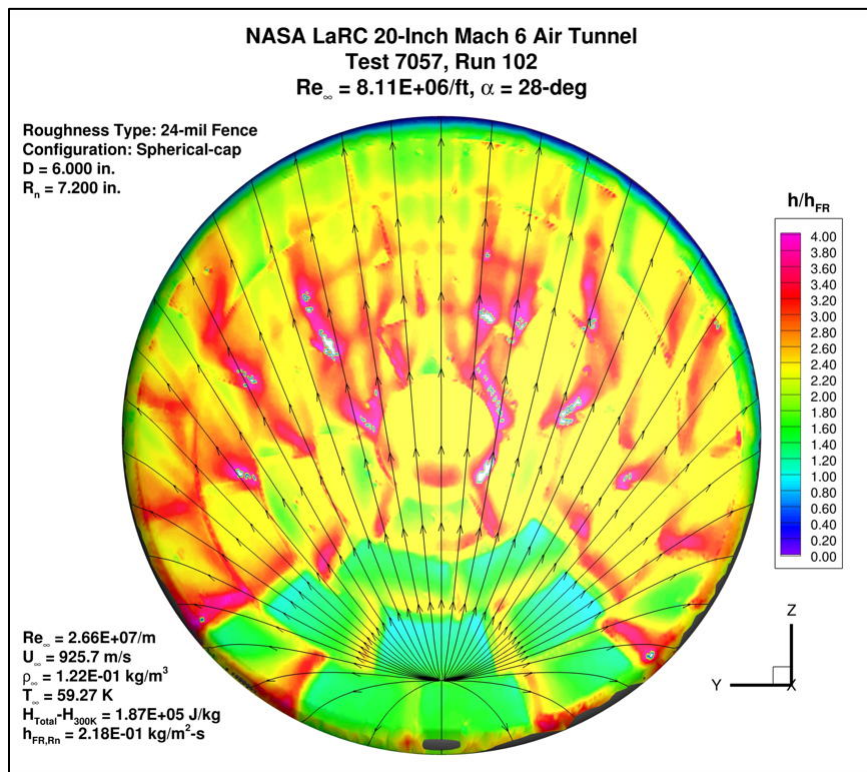


Figure 217. Test 7057, Run 102, $Re_\infty = 8.3 \times 10^6/ft$, spherical-cap 24 mil fence